

Search for double beta decay of  $^{96}\text{Zr}$   
with the NEMO-3 detector and  
ultra-low radioactivity measurements  
for the SuperNEMO experiment with  
the BiPo-3 detector

Guillaume Eurin  
University College London

Submitted to University College London in fulfilment  
of the requirements for the award of the  
degree of **Doctor of Philosophy**

October 12, 2015



# Declaration

I, Guillaume Eurin, confirm that the work presented in this thesis is my own. Where information has been derived from other sources, I confirm that this has been indicated in the thesis.

A handwritten signature in black ink, appearing to read 'Guillaume Eurin', is centered on the page. The signature is written in a cursive style with a long horizontal stroke extending to the right.

Guillaume Eurin



# Abstract

The double- $\beta$  decay of  $^{96}\text{Zr}$  was studied with data from NEMO-3, a unique experiment combining tracking and calorimetry. A total isotope mass of 9.4 g and a runtime of 5.25 y were available for this work. The half-life of the two-neutrino double- $\beta$  decay of  $^{96}\text{Zr}$  was measured to be  $T_{1/2}^{2\nu 2\beta} (^{96}\text{Zr}) = 2.41 \pm 0.11$  (stat.)  $^{+0.21}_{-0.18} \times 10^{19}$  y. A lower limit on the neutrinoless double-beta decay half-life was set at  $T_{1/2}^{0\nu 2\beta} (^{96}\text{Zr}) > 1.29 \times 10^{22}$  y @ 90% C.L. corresponding to a limit on the effective neutrino mass of  $|m_{\beta\beta}| < 3.8 - 12.1$  eV @ 90% C.L.. A first limit was set with NEMO-3 data on the two-neutrino double- $\beta$  decay to excited states half-life was set at  $T_{1/2}^{2\nu 2\beta} (^{96}\text{Zr}, 0_1^+) > 5.85 \times 10^{19}$  y @ 90% C.L..

SuperNEMO is the next-generation experiment based on NEMO-3 detection principle. The principle and the construction of the BiPo-3 detector for ultra-low contaminations are described. Developments of calibration procedures are exposed along with the validation of the Monte-Carlo simulations. The intrinsic background level has been proven acceptable for SuperNEMO isotopic source foils requirements. Measurements of the contamination of the first SuperNEMO source foils have been performed and the first results are very promising.



## Acknowledgements

First I would like to express my gratitude to my supervisors. David Waters helped me focus on the essential aspects of my work and provided me with an important external point of view. I want to thank him for his support and the time he spent answering my questions and correcting this thesis until the end. A special thought for Mathieu Bongrand for the endless hours spent discussing this thesis and so many other crucial points. I could not have gone that far without his support and I want to thank him for that. Learning from both of them was extremely interesting and I estimate myself lucky for the opportunity I was given to work in two great places.

I want to thank Achille Stochi and the direction of the Laboratoire de l'Accélérateur Linéaire for the support they provided me with and without whom this thesis would not have been possible. I am especially grateful for their understanding and trust. This time would not have been the same without the secretaries, the different services and other members of the administration of the laboratory. Many thanks go to Geneviève, for cheering me up when times were complicated and for her help in general. I also want to thank the administration staff of the Physics and Astronomy group at UCL. A special thought for Deborah who helped me going through the British administration.

These discussions about France, Italy, the UK and other countries in my office in UCL with Rob, David, Leigh, Stefano, Anastasia were always passionate and helped me enjoy my time in London. Working in the SuperNEMO group at UCL with James, Cristóvão, Ruben, Michele and Derek was very interesting and I thank them all for that. Thank you Pauline for introducing me to the UK in your special way and staying by my side the whole time. I also thank Tomas and Inês for providing me with a room when most needed. It has been enriching to meet everyone in UCL and especially Andrew, Rebecca, Patrick, Laura and I want to thank them all. A special thought for Xin Ran, thank you very much for all the support and help you

gave me, especially at the very end. Let us hope we meet again somewhere around the world.

Many thanks again to Mathieu for teaching me how to survive a collaboration meeting without anything planned but a flight. Xavier G., I always appreciated his jokes and I am happy he found a student to pass on his knowledge, good luck Steven and be careful in the future collaboration meetings. Sophie, I apologize for Just Dance, we need to get this done. Thanks to Serge for the long discussions about politics and the history of NEMO-3. Laurent it has been a pleasure to discuss with him about everything. Héctor, we built BiPo-3 together and I want to thank him for the good (and tough) times in Spain. I think that the BiPo team made a great work and he played an important role in this. I also thank our colleagues from Zaragoza and the LSC (especially Asun and Alfonso), their help was really precious. Xavier S., another eminent member of the BiPo team, I really want to thank him for all the time spent discussing, sometimes intensely, my work on BiPo. Pia arrived at the end of my time on BiPo so I wish her good luck and hope she will take good care of our detector. Stephane and Eric, essential members of our BiPo team, without them nothing would have been possible. Many thanks for the good times spent at the LSC and the tremendous amount of hours spent underground in good company.

Nothing would have been possible without moral support. The NPAC team has been essential: Marco, Asénath, Agnès, Samuel, Jérémy and Estelle. Vincent, although recently the situation got us far from each other, I wish the dream team will not split up after all these years. Pauline was always here although I was not always in touch, I thank her for that. Our many collaboration meetings also allowed me to meet great PhD students: Benjamin, Aivaras, Summer, John, Arnaud, Thibaut and senior members: Frederic, Christine, Dominique, Fabrice, Cédric, François, Christian, Benoit, Yves, Victor. May SuperNEMO live long and prosper. Magali, many thanks for organising our great Aussois meetings and for the tartiflette and other typical Savoy food. She has a great family and it was a great pleasure meeting them all.

Anja entered my life in the middle of my thesis but has always been a support and I want to thank her deeply for that. I hope I repay her for her thesis and more in the future years to come.

Lastly I would like to thank my family, for the incredible support I received through all that happened during these years. Maxime, although it has never been the easiest situation, many thanks for hosting me when I really needed it. Good luck for the rest, you are almost done. My parents are probably one of the biggest reasons how I managed to get going when times got hard and I will never be able to thank them enough for that, not only during this thesis but also all those years before. Many thanks also to my grand-mother, for trying to understand what I work on and always wishing me the best. Manande, thank you very much for all these Saturday's spent and sorry we lost so many times.



# Contents

<b>List of Figures</b>	<b>17</b>
<b>List of Tables</b>	<b>23</b>
<b>Introduction</b>	<b>25</b>
0.1. Author's Contributions . . . . .	26
<b>1. Neutrino phenomenology</b>	<b>29</b>
1.1. History of the neutrino . . . . .	29
1.2. Neutrino mixing and oscillations . . . . .	32
1.2.1. Two neutrino flavours model . . . . .	33
1.2.2. Generalization to three neutrino flavours . . . . .	33
1.3. Neutrinos masses and nature . . . . .	34
1.3.1. Dirac mass term . . . . .	34
1.3.2. Majorana mass term . . . . .	35
1.3.3. Combined Majorana and Dirac mass terms . . . . .	35
1.4. See-saw mechanism . . . . .	36
1.5. Experimental Status . . . . .	37
1.5.1. Oscillations . . . . .	37
1.5.2. Absolute mass measurement . . . . .	39
<b>2. Double-<math>\beta</math> decay</b>	<b>41</b>
2.1. Semi-empirical mass formula . . . . .	41
2.2. Two-neutrino double- $\beta$ decay . . . . .	41
2.2.1. Double- $\beta^-$ decay . . . . .	42
2.2.2. Double- $\beta^-$ decay to excited states . . . . .	43
2.2.3. Double- $\beta^+$ decay and double electron capture . . . . .	44
2.3. Neutrinoless double- $\beta$ decay . . . . .	45

2.4. Nuclear Matrix Elements . . . . .	47
2.4.1. Different models . . . . .	48
2.5. Neutrino mass hierarchy and effective neutrino mass . . . . .	49
2.5.1. Quasidegenerate Region . . . . .	50
2.5.2. Inverted Hierarchy . . . . .	50
2.5.3. Normal Hierarchy . . . . .	51
<b>3. Experimental status of neutrinoless double-<math>\beta</math> decay searches</b>	<b>53</b>
3.1. Principle of double- $\beta$ experiments . . . . .	53
3.2. Germanium experiments . . . . .	55
3.2.1. Operating principle . . . . .	55
3.2.2. Heidelberg-Moscow and IGEX . . . . .	57
3.2.3. GERDA & MAJORANA . . . . .	57
3.3. Bolometer experiments . . . . .	61
3.3.1. Operating principle . . . . .	61
3.3.2. CUORICINO . . . . .	62
3.3.3. CUORE-0 . . . . .	64
3.3.4. CUORE . . . . .	65
3.3.5. LUCIFER & LUMINEU . . . . .	66
3.4. TPC and Liquid Scintillator experiments . . . . .	67
3.4.1. EXO-200 . . . . .	67
3.4.2. KamLAND-Zen . . . . .	69
3.4.3. SNO+ . . . . .	71
3.5. Tracker-Calorimeter: NEMO experiments . . . . .	72
3.5.1. NEMO-3 . . . . .	72
3.5.2. SuperNEMO . . . . .	74
<b>4. The NEMO-3 detector</b>	<b>77</b>
4.1. Introduction . . . . .	77
4.2. Backgrounds to double-beta decay in NEMO-3 . . . . .	78
4.3. NEMO-3 at the LSM . . . . .	81
4.3.1. The <i>Laboratoire Souterrain de Modane</i> . . . . .	81
4.3.2. Strategies to reduce background . . . . .	82
4.4. Description of the NEMO-3 detector . . . . .	84
4.4.1. Source foils . . . . .	84
4.4.2. Tracker . . . . .	88

4.4.3.	Calorimeter . . . . .	93
4.4.4.	Electronics and acquisition system . . . . .	97
<b>5.</b>	<b>Double-<math>\beta</math> decay of <math>^{96}\text{Zr}</math> with NEMO-3</b>	<b>99</b>
5.1.	Analysis techniques and reconstruction . . . . .	99
5.1.1.	Simulations . . . . .	99
5.1.2.	Event reconstruction . . . . .	100
5.1.3.	Events selection . . . . .	102
5.1.4.	Time of flight Analysis . . . . .	103
5.1.5.	Data Analysis . . . . .	108
5.2.	Analysis context . . . . .	111
5.2.1.	NEMO-3 data sets . . . . .	111
5.2.2.	Isotopes constituting the background model . . . . .	112
5.3.	Background measurement . . . . .	112
5.3.1.	External Backgrounds . . . . .	113
5.3.2.	1 electron and 1 delayed $\alpha$ channel - $^{214}\text{Bi}$ - $^{214}\text{Po}$ background .	120
5.3.3.	Internal background . . . . .	123
5.3.4.	Summary of the internal background activities . . . . .	132
5.4.	Measurement of two-neutrino double- $\beta$ decay of $^{96}\text{Zr}$ to the ground state of $^{96}\text{Mo}$ . . . . .	133
5.4.1.	Background identification and rejection for two-neutrino double- $\beta$ decay to ground state . . . . .	136
5.4.2.	Optimisation for two-neutrino double- $\beta$ decay . . . . .	138
5.4.3.	Measurement of two-neutrino double- $\beta$ decay to ground state for the individual samples . . . . .	140
5.4.4.	Estimation of the systematic uncertainties . . . . .	142
5.5.	Search for neutrinoless double- $\beta$ decay of $^{96}\text{Zr}$ to the ground state of $^{96}\text{Mo}$ . . . . .	144
5.5.1.	Estimation of the systematic uncertainties . . . . .	147
5.6.	Search for two-neutrino double- $\beta$ decay to excited states . . . . .	148
5.6.1.	Estimation of the systematic uncertainties . . . . .	156
<b>6.</b>	<b>The SuperNEMO experiment</b>	<b>159</b>
6.1.	SuperNEMO and underground laboratories . . . . .	159
6.2.	From NEMO-3 to SuperNEMO . . . . .	161
6.2.1.	Goals . . . . .	161

6.2.2.	Design of SuperNEMO . . . . .	161
6.2.3.	Improvements . . . . .	162
6.3.	The SuperNEMO Demonstrator . . . . .	168
6.3.1.	Description of the detector . . . . .	168
6.3.2.	Demonstrator status . . . . .	168
6.4.	Future prospects . . . . .	169
<b>7.</b>	<b>BiPo prototypes and the BiPo-3 detector</b>	<b>171</b>
7.1.	Principle of the BiPo detectors . . . . .	172
7.1.1.	Detection principle . . . . .	172
7.1.2.	The data acquisition system . . . . .	173
7.1.3.	Event reconstruction . . . . .	175
7.1.4.	Background components . . . . .	176
7.2.	Quenching of alpha-particles . . . . .	177
7.3.	R&D for the BiPo detector . . . . .	178
7.3.1.	BiPo-1 . . . . .	179
7.3.2.	BiPo-2 . . . . .	179
7.3.3.	Preproduction BiPo-3 module . . . . .	180
7.4.	GEANT4 Simulations . . . . .	185
7.5.	The BiPo-3 detector . . . . .	185
7.5.1.	Design . . . . .	186
7.5.2.	Construction and commissioning . . . . .	188
7.6.	Uniformity of the surface response of the scintillators . . . . .	190
7.7.	Calibration of the BiPo detectors . . . . .	192
7.7.1.	Energy calibration and energy resolution . . . . .	193
7.7.2.	Choice of the energy calibration procedure . . . . .	194
7.7.3.	Time calibration . . . . .	196
7.7.4.	$\beta$ - $\alpha$ discrimination . . . . .	198
7.7.5.	Detector stability . . . . .	199
7.8.	Analysis techniques . . . . .	200
7.8.1.	Pulse shape analysis: noise rejection . . . . .	200
7.8.2.	Cross-talk rejection . . . . .	202
7.8.3.	Activity measurements . . . . .	203
7.8.4.	Fit of the delay time . . . . .	204

7.9. Measurements with BiPo-3 . . . . .	206
7.9.1. Aluminium foil . . . . .	206
7.9.2. Background level . . . . .	219
7.9.3. Selenium foils . . . . .	225
<b>Conclusion</b>	<b>233</b>
<b>A. NEMO-3 analysis tables</b>	<b>237</b>
<b>References</b>	<b>247</b>



# List of Figures

2.1.	Mass of an even $A$ nucleus as predicted by the SEMF. . . . .	42
2.2.	Feynman diagram for $2\nu\beta\beta$ . . . . .	43
2.3.	Feynman diagram for $0\nu\beta\beta$ . . . . .	45
2.4.	Energy spectrum of double- $\beta$ decays . . . . .	46
2.5.	Results of Nuclear Matrix Elements computations . . . . .	47
2.6.	Neutrino mass hierarchy . . . . .	49
2.7.	Effective neutrino masses depending on the mass hierarchy . . . . .	50
3.1.	Semi-coaxial and broad energy high purity germanium detectors . . . . .	56
3.2.	Schematic of the GERDA detector . . . . .	59
3.3.	Energy spectrum in the $0\nu\beta\beta$ region for GERDA . . . . .	60
3.4.	Schematic of the MAJORANA demonstrator . . . . .	61
3.5.	Views of the CUORICINO detector . . . . .	63
3.6.	Energy spectrum in the $0\nu\beta\beta$ region for CUORICINO . . . . .	63
3.7.	Background reduction between CUORICINO and CUORE-0 . . . . .	65
3.8.	Background identification for LUCIFER . . . . .	67
3.9.	Energy spectrum for EXO-200 . . . . .	68
3.10.	Energy spectrum for KamLAND-Zen . . . . .	70
3.11.	New energy spectrum for KamLAND-Zen . . . . .	71
3.12.	Expected energy spectrum for SNO+ . . . . .	73
3.13.	Latest results of the NEMO-3 experiment on $^{100}\text{Mo}$ . . . . .	74
3.14.	Schematic of the SuperNEMO demonstrator . . . . .	75

4.1.	Schematic principle of the NEMO detection technique . . . . .	77
4.2.	Natural radioactivity chains of $^{232}\text{Th}$ and $^{238}\text{U}$ . . . . .	79
4.3.	Internal background topologies in NEMO-3 . . . . .	80
4.4.	External background topologies in NEMO-3 . . . . .	81
4.5.	Location of the LSM . . . . .	81
4.6.	View of the shielding of the NEMO-3 detector . . . . .	82
4.7.	View of NEMO-3 in the LSM . . . . .	83
4.8.	Diagram displaying the components of NEMO-3 . . . . .	84
4.9.	$\beta\beta$ -isotopes in NEMO-3 sectors . . . . .	86
4.10.	Schematic of a composite source foil . . . . .	87
4.11.	Source frame of one of the NEMO-3 sectors . . . . .	88
4.12.	Views of the $^{96}\text{Zr}$ samples in NEMO-3 . . . . .	89
4.13.	Diagram of an elementary NEMO-3 Geiger cell . . . . .	90
4.14.	Schematic of a petal and the position of the drift cells . . . . .	92
4.15.	Schematic of a NEMO-3 sector . . . . .	93
5.1.	Example of a NEMO-3 event display . . . . .	102
5.2.	Possible topologies for two-track events . . . . .	104
5.3.	Time differences between the measured time and the expected time .	105
5.4.	$\chi^2$ probabilities for 2 electrons events. . . . .	107
5.5.	NLLR distributions for background only and signal plus background hypotheses. . . . .	110
5.6.	Total energy in the crossing electron channel . . . . .	115
5.7.	Control distributions in the crossing electron channel . . . . .	116
5.8.	Total energy in $1e1\gamma$ (external) events . . . . .	118
5.9.	Control distributions in $1e1\gamma$ (external) events . . . . .	118
5.10.	Delay time fit in $1e1\alpha$ events . . . . .	121
5.11.	$\alpha$ -track length in Phase 2 . . . . .	122

5.12.	$\alpha$ -track length in Phase 1 and Phase 1 + Phase 2 . . . . .	122
5.13.	Total energy in 1e1 $\gamma$ events . . . . .	126
5.14.	Control distributions in 1e1 $\gamma$ events . . . . .	127
5.15.	Total energy in 1e2 $\gamma$ events . . . . .	129
5.16.	Control distributions in 1e2 $\gamma$ events . . . . .	130
5.17.	Fit of the electron energy in 1e events . . . . .	132
5.18.	Total energy in 2e events . . . . .	134
5.19.	Control distributions in 2e events . . . . .	135
5.20.	Maximum energy as a function of minimum energy in 2e events . . . . .	136
5.21.	Total energy and control distributions in 2e events after $^{40}\text{K}$ selection . . . . .	137
5.22.	Fit of the total energy in 2e events with free $\mathcal{A}(^{40}\text{K})$ . . . . .	138
5.23.	Fit of the total energy in 2e events after $^{40}\text{K}$ rejection . . . . .	139
5.24.	Fit of the total energy in 2e events for the individual samples . . . . .	141
5.25.	Fit of the total energy in 2e events for the individual samples after $^{40}\text{K}$ rejection . . . . .	142
5.26.	Expected $0\nu\beta\beta$ half-life . . . . .	145
5.27.	High energy spectrum in 2e events . . . . .	147
5.28.	Energy scheme for the double- $\beta$ decay of $^{96}\text{Zr}$ to $^{96}\text{Mo}$ . . . . .	148
5.29.	Example of a NEMO-3 2eN $\gamma$ event . . . . .	149
5.30.	Illustration of $\gamma$ -tracking . . . . .	150
5.31.	Validation of $\gamma$ -tracking . . . . .	150
5.32.	Total energy in 2eN $\gamma$ events . . . . .	152
5.33.	Total $\gamma$ energy as a function of electron energy in 2eN $\gamma$ events . . . . .	153
5.34.	Total energy in 2eN $\gamma$ events after loose selection . . . . .	153
5.35.	Total energy in 2eN $\gamma$ events after strict selection . . . . .	154
5.36.	Total energy in 2eN $\gamma$ events for $^{232}\text{U}$ calibration source . . . . .	156
5.37.	Total energy in 2eN $\gamma$ events for $^{232}\text{U}$ after selections . . . . .	157

6.1.	Underground facilities throughout the world . . . . .	159
6.2.	20 SuperNEMO modules at the LSM . . . . .	160
6.3.	Schematic of a SuperNEMO module . . . . .	162
6.4.	Last results of the NEMO-3 experiment on $^{100}\text{Mo}$ . . . . .	163
7.1.	BiPo cascades in $^{238}\text{U}$ and $^{232}\text{Th}$ decay chains . . . . .	172
7.2.	Detection principle of the BiPo detectors and main backgrounds . . .	173
7.3.	Schematic of the acquisition chain used in BiPo detectors . . . . .	174
7.4.	Schematic of a sampled pulse in the BiPo detector . . . . .	175
7.5.	Digitized PMT pulses in BiPo-3 . . . . .	177
7.6.	Quenching factor of $\alpha$ 's in a plastic scintillator . . . . .	178
7.7.	Schematic of the BiPo-2 prototype . . . . .	180
7.8.	Views of the BiPo-3 preproduction module . . . . .	181
7.9.	$^{214}\text{BiPo}$ events during radon measurement with the preproduction module . . . . .	183
7.10.	Aluminium calibration foil in the BiPo-3 preproduction module . . .	184
7.11.	$\alpha$ surface background rejection . . . . .	185
7.12.	GEANT4 simulation of a BiPo-3 module . . . . .	186
7.13.	Schematic of a BiPo-3 module . . . . .	186
7.14.	Schematic of the gas flushing system of the BiPo-3 detector . . . . .	188
7.15.	Shielding of the BiPo-3 detector . . . . .	188
7.16.	View of the first BiPo-3 module at the LSC . . . . .	189
7.17.	$^{207}\text{Bi}$ electron energy spectrum in BiPo . . . . .	190
7.18.	Scan and qualification of the BiPo scintillators using electrons . . . .	191
7.19.	$^{241}\text{Am}$ $\alpha$ energy spectrum . . . . .	191
7.20.	Non-uniformity of BiPo-3 scintillators . . . . .	192
7.21.	Corrections to the simulated energy spectrum for $^{54}\text{Mn}$ $\gamma$ calibration .	194
7.22.	Example of $^{54}\text{Mn}$ energy calibration spectrum . . . . .	195

---

7.23.	Calibration scenarios for BiPo-3 . . . . .	195
7.24.	Homogeneity of the illumination for two calibration scenarios . . . . .	197
7.25.	Illumination of the BiPo-3 detector in two calibration scenarios . . . . .	197
7.26.	Time calibration events . . . . .	198
7.27.	Time calibration of a BiPo-3 optical submodule . . . . .	198
7.28.	Normal and noisy counting rates . . . . .	200
7.29.	Example of a noisy pulse . . . . .	200
7.30.	Successive $\gamma$ -calibrations of an optical submodule . . . . .	201
7.31.	Pulse-shape analysis in the BiPo-3 detector . . . . .	201
7.32.	Pulse shape analysis signal selection . . . . .	202
7.33.	Cross-talk event in BiPo-3 . . . . .	202
7.34.	$\alpha$ -particle energy spectra from Monte Carlo in BiPo-3 . . . . .	204
7.35.	Fit of the delay time . . . . .	205
7.36.	$^{214}\text{Bi}$ spectra for one aluminium foil before radon decay1 . . . . .	206
7.37.	Aluminium calibration foil in a BiPo-3 module . . . . .	207
7.38.	Determination of high-energy $\alpha$ -quenching . . . . .	208
7.39.	Optimisation of the determination of high-energy $\alpha$ -quenching . . . . .	209
7.40.	$^{208}\text{Tl}$ spectra for module 1 . . . . .	209
7.41.	$^{208}\text{Tl}$ spectra for module 2 . . . . .	210
7.42.	Simulated vertices distribution for one and two aluminium foils . . . . .	211
7.43.	One-foil sample $^{208}\text{Tl}$ individual optical submodules activity . . . . .	212
7.44.	Two-foil sample $^{208}\text{Tl}$ individual optical submodules activity . . . . .	212
7.45.	Calibration constant as a function of the $^{208}\text{Tl}$ activity . . . . .	213
7.46.	$\beta/\alpha$ discrimination factors . . . . .	214
7.47.	$^{214}\text{Bi}$ spectra for one aluminium foil after radon decay . . . . .	216
7.48.	$^{214}\text{Bi}$ spectra for one aluminium foil after delay time cut . . . . .	216
7.49.	$^{214}\text{Bi}$ spectra for one aluminium foil after $\beta/\alpha$ discrimination . . . . .	217

7.50.	Delay times in the $^{214}\text{BiPo}$ channel for two aluminium foils . . . . .	219
7.51.	Fit of the delay time in the $^{212}\text{BiPo}$ channel for background measurement	220
7.52.	Electron and $\alpha$ energies in $^{212}\text{BiPo}$ channel for background measurement	220
7.53.	Fit of the delay time in the $^{214}\text{BiPo}$ channel . . . . .	222
7.54.	Electron and $\alpha$ energies in $^{214}\text{BiPo}$ channel for background measurement	223
7.55.	Identification of external radon background . . . . .	224
7.56.	Expected sensitivities for BiPo-3 from background measurements . . .	225
7.57.	View of the first SuperNEMO source foils in BiPo-3 . . . . .	225
7.58.	Schematic of the $^{82}\text{Se}$ source foils . . . . .	226
7.59.	Distributions in $^{208}\text{Tl}$ for the SuperNEMO source foils . . . . .	227
7.60.	Distributions in $^{208}\text{Tl}$ for the SuperNEMO source foils after back- ground rejection . . . . .	228
7.61.	Distributions in $^{214}\text{Bi}$ for the SuperNEMO source foils . . . . .	229
7.62.	Distributions in $^{214}\text{Bi}$ for the SuperNEMO source foils after delay time cut . . . . .	230
7.63.	Distributions in $^{214}\text{Bi}$ for the SuperNEMO source foils after $\beta/\alpha$ dis- crimination . . . . .	230

# List of Tables

1.1. Recent oscillation parameters . . . . .	39
2.1. List of the main $\beta\beta$ isotopes and their properties . . . . .	44
2.2. Recent nuclear matrix elements computations for $^{96}\text{Zr}$ . . . . .	48
3.1. Comparison between NEMO-3 performance and SuperNEMO requirements	76
4.1. Properties of the $\beta\beta$ -isotopes studied in NEMO-3 . . . . .	85
5.1. Available data for $^{96}\text{Zr}$ analysis . . . . .	111
5.2. PMTs HPGe measurements . . . . .	114
5.3. Summary of the external background model . . . . .	119
5.4. Fit of the total energy in $1e1\gamma$ (external) events . . . . .	119
5.5. Summary of the $1e1\alpha$ measurements . . . . .	123
5.6. HPGe measurements of the $^{96}\text{Zr}$ samples . . . . .	124
5.7. Activity measurements in $1e1\gamma$ events . . . . .	128
5.8. Activity measurements in $1e2\gamma$ events . . . . .	129
5.9. Activity measurements in $1e$ events . . . . .	131
5.10. Summary of the measurements of the internal background model. . .	133
5.11. $^{40}\text{K}$ activity measurement in $2e$ events . . . . .	138
5.12. Results of the fit of the total energy in $2e$ events after $^{40}\text{K}$ rejection .	140
5.13. Systematic uncertainties for $2\nu\beta\beta$ half-life measurement . . . . .	143
5.14. Background contribution in the $0\nu\beta\beta$ region of interest . . . . .	146
5.15. Systematic uncertainties for the $0\nu\beta\beta$ measurement. . . . .	148

5.16. Fit in $2eN\gamma$ events after strict selection cuts . . . . .	155
5.17. Systematic uncertainties for $2\nu\beta\beta$ to excited states. . . . .	157
6.1. Comparison between NEMO-3 and SuperNEMO . . . . .	164
7.1. Characteristics of the BiPo cascades . . . . .	172
7.2. Exposure predictions for $^{54}\text{Mn}$ $\gamma$ calibration . . . . .	196
7.3. $^{208}\text{Tl}$ activity measurement in the aluminium foil . . . . .	210
7.4. Delay time selections results for $^{214}\text{Bi}$ in aluminium foil . . . . .	215
7.5. $^{214}\text{Bi}$ activities in the aluminium foil from energy spectrum fit . . . . .	218
7.6. Background measurement in $^{208}\text{Tl}$ . . . . .	221
7.7. Background measurement in $^{214}\text{Bi}$ . . . . .	223
7.8. Results of $^{214}\text{Bi}$ measurements for the SuperNEMO source foils . . . . .	231
A.1. Available Monte-Carlo simulations . . . . .	237
A.2. Decay modes and main $\gamma$ -rays for $^{96}\text{Zr}$ backgrounds . . . . .	238
A.3. Decay modes and main $\gamma$ -rays for $^{96}\text{Zr}$ backgrounds (continued) . . . . .	239
A.4. Summary of the $1e1\alpha$ measurements for the ITEP sample . . . . .	239
A.5. Summary of the $1e1\alpha$ measurements for the INR sample . . . . .	240
A.6. Activity measurements in $1e1\gamma$ for the ITEP sample . . . . .	240
A.7. Activity measurements in $1e1\gamma$ for the INR sample . . . . .	241
A.8. Activity measurements in $1e2\gamma$ for the ITEP sample . . . . .	241
A.9. Activity measurements in $1e2\gamma$ for the INR sample . . . . .	242
A.10. Activity measurements in $1e$ for the ITEP sample . . . . .	242
A.11. Activity measurements in $1e$ for the INR sample . . . . .	243
A.12. Fit of the $2e$ channel after $^{40}\text{K}$ rejection for the individual samples . . . . .	243
A.13. $2eN\gamma$ channel before selection cuts . . . . .	244
A.14. $2eN\gamma$ channel after loose selection cuts . . . . .	245

# Introduction

*“Well begun is half done.”*

- Aristotle

Neutrinoless double- $\beta$  decay ( $0\nu\beta\beta$ ) is a process beyond the Standard Model, that has been searched for in the past decades. If it exists and is discovered, it would solve one of the most fundamental questions about the nature of the neutrino. It would prove that the neutrino is the only fermion being a Majorana particle ( $\nu=\bar{\nu}$ ). It would also give access to the neutrino mass and help understanding its origin. The discovery of the non-zero neutrino mass by oscillation experiments implied the necessity to modify the Standard Model. This can be done adding Majorana mass terms in the massive neutrino Lagrangian. In the see-saw mechanism, this would explain the smallness of the neutrino mass. A quick description of neutrino phenomenology is given in Chapter 1. The double- $\beta$  decay processes are presented in Chapter 2. Many experiments have searched for these processes in recent years. A summary of different technological strategies and latest results is exposed in Chapter 3.

One of the most successful experiments of the past generation is NEMO-3. It combined a tracker and a calorimeter allowing full reconstruction of  $\beta\beta$ -events. It studied seven different double- $\beta$  isotopes allowing the first accurate measurements of two-neutrino double- $\beta$  decay ( $2\nu\beta\beta$ ) to be performed for some of these isotopes. It also enabled to set world’s best limits on  $0\nu\beta\beta$  for almost all of these isotopes. Chapter 4 is dedicated to the description of NEMO-3 and its advantages. This thesis contains the analysis of the double- $\beta$  decay of  $^{96}\text{Zr}$ . Chapter 5 covers the analysis techniques, the background measurements, the study of  $2\nu\beta\beta$  and  $0\nu\beta\beta$  to ground state. A first search of  $2\nu\beta\beta$  to excited states is also enclosed.

Due to the very good results of NEMO-3, a new experiment has been designed using the same *modus operandi*: SuperNEMO, aimed at measuring 100 kg of the double- $\beta$  isotope  $^{82}\text{Se}$ . The first module of SuperNEMO is now under construction

and should be completed in 2016. Chapter 6 describes the baseline and the current status of SuperNEMO. One of the crucial aspects of the SuperNEMO experiment is the radiopurity of the source foils. Constraints being set at levels currently unreachable by standard qualification means, a dedicated detector has been designed. The BiPo detector takes advantage of decay cascades in natural radioactivity, which is the source of most of the background for double- $\beta$  decay. Chapter 7 exposes the experimental principle and the R&D phases that were necessary to design this detector. Its performances and results after two years of operation are also encompassed ending with the measurement of the first SuperNEMO isotopic sources.

## 0.1. Author's Contributions

### NEMO-3

- Data analysis of  $^{96}\text{Zr}$ ;
  - Measurement of all of the backgrounds for the  $2\nu\beta\beta$  of  $^{96}\text{Zr}$  thanks to several analysis channels;
  - Improvement of the current half-life measurement of  $2\nu\beta\beta$ ;
  - Search for  $0\nu\beta\beta$  process;
  - Search for  $2\nu\beta\beta$  to excited states.
- Participation in the definition of an analysis module for  $\gamma$ -particles identification and reconstruction in a modular analysis framework, in particular in the correction of the energy resolution;
- Analysis of calibration sources data for systematic uncertainties estimations.

**SuperNEMO**

- SuperNEMO tracker
  - Development of a  $\gamma$ -calibration procedure;
  - Participation in the construction.
- Preproduction module of the BiPo-3 detector:
  - Operation and calibration of the detector;
  - Data analysis and analysis tools development;
  - Radon background reduction with the optimisation of a gas flushing system;
  - Participation in the validation for the construction of BiPo-3.
- BiPo-3 detector
  - Participation in the construction and commissioning ;
  - Development of the calibration procedure;
  - Participation in the design definition;
  - Optimisation of data quality studies;
  - Validation of the BiPo technique with a calibrated sample;
  - Participation in the data analysis of the intrinsic background of the detector and of the first samples for the SuperNEMO source foils.



# Chapter 1.

## Neutrino phenomenology

*“There is nothing like looking, if you want to find something. You certainly usually find something, if you look, but it is not always quite the something you were after.” - J.R.R. Tolkien, The Hobbit*

### 1.1. History of the neutrino

The history of neutrino started in 1914 when Chadwick observed that the energy spectrum of the electron in a  $\beta$  decay is continuous [1]. This result was later confirmed by Ellis and Wooster in 1927 [2].

Energy conservation requires that if only an electron is emitted in a  $\beta$  decay, its energy spectrum should be a line. In 1930, in order to explain the continuous spectrum, Pauli postulated the emission of a neutral particle along with the electron [3], calling it a “neutron”. After this theoretical proposition, Pauli said:

*“I have done something very bad today by proposing a particle that cannot be detected; it is something no theorist should ever do. [3]”*

It is worth noting that Bohr proposed a different solution, implying that the energy conservation might not be absolute but simply statistical [4].

As it was shown in  $\beta$  decays that mother and daughter nuclei have the same spin value, angular momentum conservation required the emission of a spin- $\frac{1}{2}$  particle, making of the “neutron” of Pauli a fermion. As Chadwick discovered the neutron in 1932, Fermi renamed it “neutrino” as we call it today.

The first step in the theory of weak interactions was made by Fermi in 1934. He postulated a theory of  $\beta$  decay, now called, the Fermi theory [5] analogous to quantum electrodynamics. This theory explains  $\beta$  decay as the point-like interaction of the 4 particles involved in the decay. The same year, Bethe and Peierls predicted thanks to this theory that inverse- $\beta$  decay could be observed:

$$\bar{\nu}_e + p \rightarrow e^+ + n \quad (1.1)$$

However, they concluded that given the strength of the interaction it might never be the case [6]. In spite of this, Cowan and Reines were ultimately successful [7]. After an inconclusive attempt in Hanford in 1953, they moved close to Savannah River improving it with underground detectors. The detection of the time coincidence between the  $\gamma$ 's from  $e^+$  annihilation and the nucleus de-excitation after the neutron capture successfully proved the existence of the neutrino.

Another step in the formulation of the theory of weak interaction was about parity conservation. At that time, the  $\theta$ - $\tau$  puzzle was still unsolved. It consisted in the comparison of the decays of two different particles:  $\theta$  into two pions and  $\tau$  into three pions.  $\theta$  and  $\tau$  were observed to have the exact same properties such as the spin or the mass and the only difference was the parity of the final state. This implied that  $\theta$  and  $\tau$  are same particle and the parity symmetry is violated in weak interaction. This was first proven by Lee and Yang in 1956 [8].

Given that parity is not conserved by weak interaction, parity-violating couplings could be introduced, such as in the V-A theory by Feynman and Gell-Mann [9]. They postulated that neutrinos are only left-handed and antineutrinos right-handed. It was subsequently experimentally proven by Goldhaber, Grodzins and Sunyar in 1958 [10]. They inferred the helicity of the neutrinos emitted in the  $\beta$  decay of  $^{152m}\text{Eu}$  to  $^{152}\text{Sm}^*$  from the corresponding polarization of the  $\gamma$ -rays.

In order to favour neutrino detection, Pontecorvo suggested to detect a change in the nuclei after a neutrino interaction. A new isotope being produced after the decay, its observation would give access to the initial state of the reaction. In 1955 Davis tried to study reactor neutrinos through  $\nu_e + {}^{37}\text{Cl} \rightarrow {}^{37}\text{Ar} + e^-$ . As it was later discovered, reactors do not emit  $\nu_e$  but  $\bar{\nu}_e$ . Therefore the results from this experiment were only limits on the total lepton number violating process  $\bar{\nu}_e + {}^{37}\text{Cl} \rightarrow {}^{37}\text{Ar} + e^-$ . However this proved that neutrinos and antineutrinos have

different interaction probabilities. Davis re-used the same principle in the Homestake solar neutrino experiment detecting  $\nu_e$  from the Sun.

$\mu \rightarrow e + \gamma$  is theoretically allowed by total lepton number conservation in weak interaction. However experimental limits on this process (with a fraction  $< 5.7 \times 10^{-13}$  @ 90 % C.L. [11]) were much smaller than predicted. Pontecorvo suggested that if neutrinos from  $\pi^+ \rightarrow \mu^+ + \nu_\mu$  cannot produce electrons, then two different types, or flavours, of neutrinos must exist [12]. Therefore a new conservation law was introduced, *individual lepton number*. In 1962, Lederman, Schwartz and Steinberger used a  $\nu_\mu$  beam and observed less electrons than expected along with muons. This showed that at least two flavours of neutrino exist, now known as  $\nu_e$  and  $\nu_\mu$  [13].

In 1989, experiments at LEP experimentally determined the number of light left-handed neutrinos ( $m_\nu < \frac{m_{Z^0}}{2}$ ) from the invisible decay width of  $Z^0$  (to  $\nu \bar{\nu}$ ) [14]:

$$N_\nu = 2.984 \pm 0.008 \quad (1.2)$$

The third flavour is the tau neutrino,  $\nu_\tau$ , first detected in 2000 by the DONUT collaboration at Fermilab [15].

An important property of neutrinos is their mixing. The first mention of neutrino oscillations was made by Pontecorvo in 1957 [16]. In 1962, Maki, Nakagawa and Sakata assumed that  $\nu_e$  and  $\nu_\mu$  are a combination of mass eigenstates [17]. Pontecorvo proposed a first two-neutrino mixing model in 1967-1969, a full theory finally developed in 1975-1976 by several groups.

Atmospheric neutrinos played an important role in the observation of neutrino oscillations. They were first considered as a background for proton decay experiments. But they allowed the first model-independent indication of  $\nu_\mu$ 's oscillations in the Super-Kamiokande experiment in 1998 [18].

Today in the lepton sector of the Standard Model, three leptons exist: electron, muon and tau, each associated in a doublet to the neutrino with which they are produced by weak interaction,  $\nu_e$ ,  $\nu_\mu$  and  $\nu_\tau$  respectively. Neutrinos are supposed to be different from their antiparticles ( $\nu \neq \bar{\nu}$ ) and are massless (even if the oscillations proved it wrong). All neutrinos are left-handed and all antineutrinos are

right-handed. Sterile neutrinos could exist as a singlet of weak interactions, have any possible mass and be Majorana particles ( $\nu = \bar{\nu}$ ) as they carry no weak charge.

## 1.2. Neutrino mixing and oscillations

The neutrino mixing can be treated using an analogy to the quarks mixing through the CKM matrix. A neutrino with flavour  $\alpha$  can be described by equation 1.3 (left) and a mass eigenstate  $i$  can be defined as in 1.3 (right) [19].

$$|\nu_\alpha\rangle = \sum_i U_{\alpha i} |\nu_i\rangle, \quad |\nu_i\rangle = \sum_\alpha (U^\dagger)_{i\alpha} |\nu_\alpha\rangle = \sum_\alpha U_{\alpha i}^* |\nu_\alpha\rangle \quad (1.3)$$

U is a unitary matrix linking the mass eigenstates  $|\nu_i\rangle$  ( $i \in \{1, 2, 3\}$ ) and the flavour eigenstates  $|\nu_\alpha\rangle$  ( $\alpha \in \{e, \mu, \tau\}$ ). In neutrino oscillations total lepton number is conserved but not individual lepton number.

The transition probability is defined as the probability to observe a neutrino with flavour  $|\nu_\beta\rangle$  that was originally emitted as  $|\nu_\alpha\rangle$ . This probability can be written, by solving Schrödinger's equation, as:

$$\begin{aligned} P(|\nu_\alpha\rangle \rightarrow |\nu_\beta\rangle)(t) &= |\langle \nu_\beta | \nu_\alpha \rangle|^2 \\ &= \sum_{i,j} U_{\alpha i} U_{\beta i}^* U_{\alpha j}^* U_{\beta j} e^{-i(E_i - E_j)t} \end{aligned} \quad (1.4)$$

Given that neutrinos are relativistic ( $m \ll p$ ), one can write [19]:

$$E_i \simeq E + \frac{m_i^2}{2E} \quad \text{and} \quad t = L \text{ in natural units} \quad (1.5)$$

As will be showed in the following, experiments are sensitive to the squared-mass differences. This quantity can be defined using equation 1.5 as in 1.6.

$$E_1 - E_2 \simeq \frac{\Delta m_{12}^2}{2E} = \frac{m_1^2 - m_2^2}{2E} \quad (1.6)$$

This formalism will be applied to a simplified two-neutrino scenario in the following section.

### 1.2.1. Two neutrino flavours model

The first two discovered flavours will be considered in this section:  $\nu_e$  and  $\nu_\mu$ . It is a good approximation of the real mixing as the squared-mass differences are very different between the three mass eigenstates as will be showed in section 1.5.1. In this case, the unitary matrix  $U$  can be represented as a two-dimensional rotation matrix. It connects the flavour eigenstates  $\nu_e$  and  $\nu_\mu$  to the mass eigenstates  $\nu_1$  and  $\nu_2$  as follows:

$$\begin{pmatrix} \nu_e \\ \nu_\mu \end{pmatrix} = \begin{pmatrix} \cos \theta & \sin \theta \\ -\sin \theta & \cos \theta \end{pmatrix} \begin{pmatrix} \nu_1 \\ \nu_2 \end{pmatrix} \quad (1.7)$$

A mixing angle  $\theta$  is introduced and represents one of the observables for oscillation experiments. The two neutrino masses are also combined into a squared-mass difference  $\Delta m^2$  which is the second experimental observable.

Experiments studying the appearance of a neutrino flavour take into consideration the transition probability, simplified in the two-neutrino scenario:

$$P(|\nu_e\rangle \rightarrow |\nu_\mu\rangle) = \sin^2(2\theta) \times \sin^2\left(\Delta m^2 \times 1.27 \times \frac{L}{E}\right) \quad (1.8)$$

In this example, an experiment will search for the amount of  $|\nu_\mu\rangle$  detected after the neutrinos travelled a distance  $L$  (in km) having an energy  $E$  (in GeV). Equation 1.8 shows that oscillations are possible only if  $\theta$  and  $\Delta m^2$  are both different from zero.

### 1.2.2. Generalization to three neutrino flavours

Nowadays, the results of experiments studying neutrino oscillations can be explained by a three-neutrino mixing. Therefore the oscillation formalism from section 1.2.1 has to be extended. The  $U$  matrix is the PMNS (Pontecorvo-Maki-Nakagawa-Sakata [17]) matrix and can be written as:

$$U = \begin{pmatrix} c_{12}c_{13} & s_{12}c_{13} & s_{13}e^{-i\delta} \\ -s_{12}c_{23} - c_{12}s_{23}s_{13}e^{i\delta} & c_{12}c_{23} - s_{12}s_{23}s_{13}e^{i\delta} & s_{23}c_{13} \\ s_{12}s_{23} - c_{12}s_{23}s_{13}e^{i\delta} & -c_{12}s_{23} - s_{12}c_{23}s_{13}e^{i\delta} & c_{23}c_{13} \end{pmatrix} \quad (1.9)$$

where  $c_{ij} = \cos \theta_{ij}$  and  $s_{ij} = \sin \theta_{ij}$  ( $i, j \in 1, 2, 3$ ). The PMNS matrix is analogous to the CKM mixing matrix in the quark sector. Three mixing angles  $\theta_{ij}$  have been introduced to quantify the mixing between the flavour eigenstates. A CP-violating Dirac phase  $\delta$  exists in this matrix, being equal to zero if no CP-violation is observed. Three masses have also been introduced and since experiments are only sensitive to the squared-mass differences, they can be reduced to two squared-mass differences. If neutrinos are Majorana particles, Majorana phases  $\lambda_2$  and  $\lambda_3$  are introduced under the form of the diagonal matrix  $(1, e^{-i\lambda_2}, e^{-i\lambda_3})$ .

### 1.3. Neutrinos masses and nature

As already explained, neutrinos are postulated to be massless in the Standard Model. The observation of neutrino oscillations demonstrates that neutrinos are massive. Depending on the nature of neutrinos, there are several ways to give them a mass, with Dirac mass terms, Majorana mass terms or a combination of both.

#### 1.3.1. Dirac mass term

The Lagrangian for neutrinos assuming a free field without interaction can be written from the Dirac equation for fermions as in 1.10.

$$\mathcal{L} = \bar{\psi}(i\gamma^\mu \frac{\partial}{\partial x^\mu} - m_D)\psi \quad (1.10)$$

The first term corresponds to the kinetic energy of the neutrino and the second one is the Dirac mass term of the neutrino. This mass term can be decomposed using the chirality operators as:

$$\mathcal{L} = -m_D(\bar{\psi}_L\psi_R + \bar{\psi}_R\psi_L) \quad (1.11)$$

where  $m_D$  is the Yukawa coupling for massive Dirac neutrinos to the Higgs field.

Under this form, neutrinos would have a left-handed and a right-handed Dirac state like all of the other fermions in the Standard Model. Given that in the Standard Model the neutrino is only left-handed, the Dirac mass has to be zero.

### 1.3.2. Majorana mass term

The neutrino being neutral, it can be a Majorana particle so that  $\nu = \nu^C$ . Therefore neutrinos are unique as they are the only elementary particles potentially having Majorana mass terms. In that case, an additional term can be added to the neutrino Lagrangian as follows:

$$\mathcal{L} = \frac{1}{2}m_M(\bar{\psi}\psi^c) + h.c. \quad (1.12)$$

For simplification we are only considering one neutrino generation here.

Assuming that only the left-handed chiral field  $\psi_L$  exists, one can write a Majorana mass term as:

$$\mathcal{L}_{Majorana}^L = \frac{1}{2}m_L\psi_L^T\mathcal{C}^\dagger\psi_L + h.c. \quad (1.13)$$

In this case, the neutrino can acquire a mass from this Majorana mass term. It implies that the neutrino is a Majorana particle named after Ettore Majorana [20], with a Dirac mass equal to zero.

### 1.3.3. Combined Majorana and Dirac mass terms

Let us assume that the right-handed chiral field forbidden in the Standard Model also exists, a Dirac mass term can then be written as in equation (1.11). This also allows us to write another Majorana mass term as in (1.14).

$$\mathcal{L}_{Majorana}^R = \frac{1}{2}m_R\psi_R^T\mathcal{C}^\dagger\psi_R + h.c. \quad (1.14)$$

This allows to write the following Lagrangian for the neutrino:

$$\mathcal{L}_{Majorana+Dirac} = L_{Dirac} + L_{Majorana}^L + L_{Majorana}^R \quad (1.15)$$

From the Majorana mass terms, total lepton number violating processes beyond the Standard Model could exist such as the see-saw mechanism (see 1.4).

The combined mass term can be written as in (1.16).

$$\mathcal{L}_{Majorana+Dirac} = \frac{1}{2} N_L^T C^\dagger M N_L + h.c. , \quad (1.16)$$

where:

$$N_L = \begin{pmatrix} \psi_L \\ \psi_R^C \end{pmatrix} \quad \text{and} \quad M = \begin{pmatrix} m_L & m_D \\ m_D & m_R \end{pmatrix} \quad (1.17)$$

Assuming  $M$  is a real mass matrix, which requires CP-invariance, it can be diagonalized as in (1.18).

$$M = \begin{pmatrix} m_1 & 0 \\ 0 & m_2 \end{pmatrix} \quad (1.18)$$

The eigenvalues of  $M$  defined in (1.18) are therefore:

$$m_{1,2} = \frac{1}{2} \left( m_L + m_R \mp \sqrt{(m_L - m_R)^2 + 4m_D^2} \right) \quad (1.19)$$

A mixing angle  $\theta$  is defined as

$$\tan 2\theta = \frac{2m_D}{m_R - m_L} \quad (1.20)$$

From these eigenvalues, several limit cases are possible. The case where  $m_D \ll m_R$  and  $m_L = 0$  is called the see-saw mechanism.

## 1.4. See-saw mechanism

One of the most important questions about the neutrino is why its mass is so small compared to the other elementary particles. A possible explanation can be provided considering the see-saw mechanism.

With  $m_D \ll m_R$  and  $m_L = 0$ , the eigenvalues of the mass matrix defined in (1.19) become:

$$m_1 \simeq \frac{m_D^2}{m_R}, \quad m_2 \simeq m_R \quad (1.21)$$

From the values of the neutrino masses in (1.21), one can understand the origin of the name of the see-saw mechanism. Indeed, the larger  $m_R$ , the larger  $m_2$  and the smaller  $m_1$ . Therefore the heaviness of neutrino  $\nu_2$  can explain the lightness of neutrino  $\nu_1$ . The mixing angle in 1.20 becomes:

$$\tan 2\theta \simeq 2 \frac{m_D}{m_R} \ll 1 \quad (1.22)$$

This mixing angle is very small which makes  $\nu_1$  a state mainly composed of the active left-handed chiral field  $\psi_L$ :  $\nu_1 \simeq -i\psi_L$ . Conversely  $\nu_2$  is mainly constituted of the sterile right-handed chiral field  $\psi_R$ :  $\nu_2 \simeq \psi_R^C$ . Thanks to this mechanism, the small mass of the active neutrinos can be explained. We can assume a Dirac mass of the order of the electroweak scale at 100 GeV and  $m_R$  of the order of the grand unification scale at  $10^{14}$ - $10^{16}$  GeV. Therefore the ratio of  $m_D$  over  $m_R$  is around  $10^{-14}$ - $10^{-12}$  GeV which highly suppresses the mass of the light neutrinos compared to the Dirac mass and gives  $m_1 \sim O(\text{meV})$ .

## 1.5. Experimental Status

In the past decades, many experiments contributed to determine the properties of neutrinos. Oscillations experiments have been successful at identifying the mixing angles and the squared-mass differences. The absolute neutrino mass and the mass hierarchy still have to be determined. This section describes the latest results on the oscillations parameters and absolute mass measurements.

### 1.5.1. Oscillations

Three neutrino sectors have been defined along with a mixing angle, depending on the origin of the neutrinos that are studied: atmospheric ( $\theta_{23}$ ), solar ( $\theta_{12}$ ) and reactors ( $\theta_{13}$ ). Isolating the contributions from the different sectors, the PMNS

matrix can be written as follows (assuming no Majorana phase):

$$U = \begin{pmatrix} 1 & 0 & 0 \\ 0 & c_{23} & s_{23} \\ 0 & -s_{23} & c_{23} \end{pmatrix} \times \begin{pmatrix} c_{13} & 0 & s_{13}e^{-i\delta} \\ 0 & 1 & 0 \\ -s_{13}e^{-i\delta} & 0 & c_{13} \end{pmatrix} \times \begin{pmatrix} c_{12} & s_{12} & 0 \\ -s_{12} & c_{12} & 0 \\ 0 & 0 & 1 \end{pmatrix} \quad (1.23)$$

In each of these sectors, it is possible to use a two-neutrino formalism due to the large differences in the squared-mass differences. However global fits of the oscillation parameters give more precise results by taking smaller effects into consideration.

Many experiments have investigated the different neutrino sectors. Equation 1.1 summarizes recent results on these parameters obtained with a global fit of all of the oscillation parameters.

For solar neutrinos, Borexino, SNO and Super-Kamiokande have contributed to the measurement of  $\theta_{12}$ .  $\Delta m_{21}^2$  corresponding to the solar sector has been measured by the KamLAND experiment from the disappearance of  $\bar{\nu}_e$  combined with data from solar neutrino experiments. The sign of  $\Delta m_{21}^2$  was accessible thanks to the matter effects that occur in the Sun. In its centre the matter effects are so important that only the heaviest mass eigenstate is produced. Therefore the neutrinos detected from the Sun are only  $\nu_2$  (assuming the convention  $m_1 < m_2$ ).

Super-Kamiokande performed a measurement of the angle from the atmospheric neutrinos  $\theta_{23}$ . The atmospheric squared-mass difference  $\Delta m^2 (= m_3^2 - \frac{m_2^2 + m_1^2}{2})$  has been measured by several long-baseline accelerator experiments such as T2K (disappearance of  $\nu_\mu$ ) and MINOS (disappearance of  $\nu_\mu$  and  $\bar{\nu}_\mu$ ). The sign of this squared-mass difference still needs to be determined to have access to the complete neutrino mass hierarchy (see Chapter 2).

The mixing angles measurements have recently been completed by the measurement of non-zero  $\theta_{13}$  by Daya Bay, RENO and Double Chooz in the reactor sector. These results on neutrino oscillations are in very good agreement with the three-neutrino mixing scenario. Some anomalies in the neutrino sector could exist, as pointed out by the LSND experiment [21], requiring an extension of this scenario.

Parameter	best-fit ( $\pm 1\sigma$ )
$\Delta m_{21}^2$	$7.54^{+0.26}_{-0.22} \times 10^{-5} \text{ eV}^2$
$\Delta m^2$ (NH)	$2.43 \pm 0.06 \times 10^{-3} \text{ eV}^2$
$\sin^2\theta_{12}$	$0.308 \pm 0.017$
$\sin^2\theta_{23}$ (NH)	$0.437^{+0.033}_{-0.023}$
$\sin^2\theta_{13}$ (NH)	$0.0234^{+0.0020}_{-0.0019}$

**Table 1.1.:** *Recent results on squared-mass differences and mixing angles [11]*

### 1.5.2. Absolute mass measurement

As already mentioned, neutrino oscillations can only measure the squared-mass differences. However the absolute neutrino mass scale is still unknown. Several handles exist in order to constrain and possibly determine it. Absolute mass measurement of  $\nu_e$  are possible from single- $\beta$  decay and cosmological constraints can be set on the sum of the neutrino masses. In the case of a Majorana neutrino, the search for  $0\nu\beta\beta$  can provide information on the effective Majorana mass. The current status of the search for  $0\nu\beta\beta$  will be presented in Chapter 3.

#### Direct neutrino mass measurement from $\beta$ decay

Several experiments have studied single- $\beta$  decay in order to measure the electron neutrino mass [22]. The principle is to use kinematics to determine the average electron neutrino mass. Challenging  $\beta$ -spectroscopy is applied in order to have enough statistics around the end-point of the  $\beta$  decay. Short-lived isotopes are favoured to maximise the number of detected events. Tritium is the most often used candidate because of its low  $Q_\beta$  value and its simple atomic structure.

After 10 years of running completed in 2004, in 2011 data from the Troitsk experiment enabled to set the current best limit on the neutrino mass at [23]:

$$m_\beta < 2.05 \text{ eV (95\% CL)} \quad (1.24)$$

The KATRIN project, successor to Troitsk, is aimed at improving its energy resolution to reach the level of 200 meV with a  $5\sigma$  discovery potential at 350 meV. This experiment is currently under commissioning and data taking will start in 2015.

## Cosmology

Neutrinos are one of the most abundant particles in the Universe. They are thought of as candidates for dark matter although light neutrinos cannot comprise a large fraction of  $\Omega_{DM}$ , the density of non-baryonic dark matter in the Universe. The observable accessible from cosmology is the sum of neutrino masses. In the Standard Model, the number of relic neutrinos and the fraction of the total matter density in the Universe are well known. Combining these values allows to set an upper limit on neutrino masses to explain the content of the Universe. The general method for that purpose is large-scale structure surveys. Several types of probes are accessible such as the Cosmic Microwave Background, galaxies lensing, spectroscopy of hydrogen lines or baryon acoustic oscillations. The current model-dependent range of values for the sum of neutrino masses is [24]:

$$\sum_i m_i \leq (0.2 - 1.3) \text{ eV (95\% C.L.)} \quad (1.25)$$

# Chapter 2.

## Double- $\beta$ decay

*“If we knew what it was we were doing, it would not be called research, would it?”- A. Einstein*

The search for  $0\nu\beta\beta$  is the most promising way to investigate the Majorana nature of neutrinos.  $2\nu\beta\beta$  is a second order process of the weak interaction conserving lepton number. It exists in the Standard Model and has already been observed for several isotopes. No observation has yet been reported of  $0\nu\beta\beta$ , with the exception of a single claim (see Chapter 3). This would be a process beyond the Standard Model since it violates total lepton number conservation by two units.

### 2.1. Semi-empirical mass formula

The Semi-empirical mass formula (SEMF) can be used to compute an approximation of the mass of a nucleus [25]. Considering nuclei with the same number of nucleons, the masses display parabolas as a function of the number of protons as visible in Figure 2.1.

### 2.2. Two-neutrino double- $\beta$ decay

In a single- $\beta^-$  decay, a nucleus  $(A, Z)$  decays into its daughter nucleus  $(A, Z + 1)$ . As visible in Figure 2.1, for some nuclei the single- $\beta$  decay of nucleus  $(A, Z)$  (a) to nucleus  $(A, Z + 1)$  (b) is energetically forbidden. It is also possible that the energy level of the nucleus  $(A, Z + 1)$  is lower but single- $\beta$  decay is strongly suppressed. It is the case for  $^{96}\text{Zr}$  due to the difference in angular momentum between the different energy states.

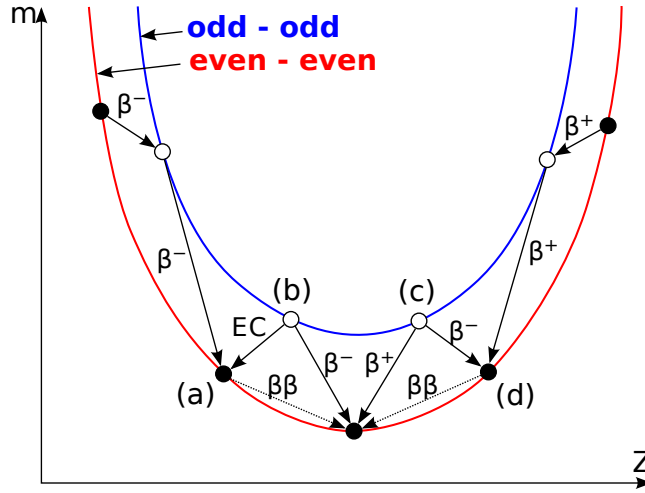
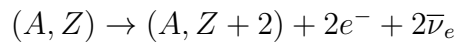


**Figure 2.1.:** Mass of an even  $A$  nucleus as predicted by the SEMF. Two parabolas are visible, the blue one for odd-odd nuclei and the red one for even-even nuclei.

### 2.2.1. Double- $\beta^-$ decay

For some nuclei for which single- $\beta$  decay is impossible,  $2\nu\beta\beta$  can occur naturally. This requires a ground state energy for the decaying isotope higher than the ground state energy of the decay product plus two electrons and two neutrinos.  $2\nu\beta\beta$  was first suggested by Goeppert-Mayer in 1935 [26], postulating that it can be mediated by second-order terms in the perturbation theory of weak interaction.

$2\nu\beta\beta$  is the decay of a nucleus  $(A, Z)$  to its daughter nucleus  $(A, Z + 2)$ . This Standard Model process results in the emission of two electrons and two electron antineutrinos (see Figure 2.2) :



As illustrated on Figure 2.1, nuclei decaying through  $2\nu\beta\beta$  have an even number of neutrons and protons since the odd-odd nuclei will predominantly decay via a single- $\beta$  decay. 35 natural isotopes can decay via a double- $\beta^-$  decay, with their properties available in [27] and summarised in Table 2.1.

The electron energy spectra (both their individual and total energies) are continuous (see Figure 2.4) since neutrinos take away part of the energy of the four-body final state of the decay.

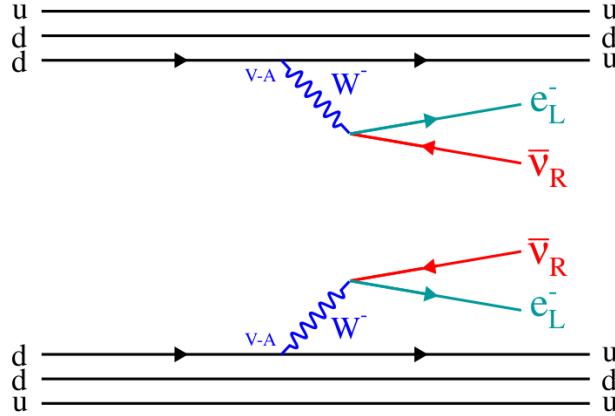


**Figure 2.2.:** Feynman diagram for  $2\nu\beta\beta$ .

The maximum energy available to the decay products,  $Q_{\beta\beta}$ , ranges from 100 keV to 4.3 MeV depending on the isotope and is defined as:

$$Q_{\beta\beta} = M(A, Z) - M(A, Z + 2) - 2m_e \quad (2.1)$$

The half-life of  $2\nu\beta\beta$  is given by equation 2.2.

$$(T_{1/2}^{2\nu})^{-1} = G^{2\nu}(Q_{\beta\beta}, Z)|\mathcal{M}^{2\nu}|^2 \quad (2.2)$$

The phase space factor for  $2\nu\beta\beta$ ,  $G^{2\nu}(Q_{\beta\beta}, Z)$ , can be accurately computed and is expressed in  $[y^{-1}]$ . The nuclear matrix elements,  $\mathcal{M}^{2\nu}$ , can only be approximately determined (see section 2.4), giving rise to a large error on their values.

### 2.2.2. Double- $\beta^-$ decay to excited states

Double- $\beta$  decay can lead to the ground state or an excited state of the daughter nucleus. Because of smaller energy transitions, the probabilities to decay to excited states is theoretically lower than the decay to the ground state. This has been experimentally observed for several nuclei such as  $^{100}\text{Mo}$  [30]. Due to the large excitation energy observed for  $1^+$  and negative parity states, only  $2^+$  and  $0^+$  transitions are relevant [19]. If the decay occurs to excited states, the energy available for the electrons is the difference between the ground state of the parent nucleus and the excited state of the daughter nucleus. The available energy for the electrons in this

Transition	$Q_{\beta\beta}$ [keV]	nat. abund. [%]	$G^{2\nu}$ [ $y^{-1}$ ]	$G^{0\nu}$ [ $y^{-1}$ ]
$^{48}\text{Ca} \rightarrow ^{48}\text{Ti}$	$4272 \pm 4$	$0.187 \pm 0.021$	$1.55 \cdot 10^{-17}$	$2.49 \cdot 10^{-14}$
$^{76}\text{Ge} \rightarrow ^{76}\text{Se}$	$2039.006 \pm 0.050$	$7.61 \pm 0.38$	$4.39 \cdot 10^{-20}$	$2.34 \cdot 10^{-15}$
$^{82}\text{Se} \rightarrow ^{82}\text{Kr}$	$2995.8 \pm 1.5$	$8.73 \pm 0.22$	$1.48 \cdot 10^{-18}$	$1.01 \cdot 10^{-14}$
$^{96}\text{Zr} \rightarrow ^{96}\text{Mo}$	$3350.4 \pm 2.9$	$2.80 \pm 0.09$	$5.94 \cdot 10^{-18}$	$2.03 \cdot 10^{-14}$
$^{100}\text{Mo} \rightarrow ^{100}\text{Ru}$	$3034 \pm 6$	$9.63 \pm 0.23$	$2.91 \cdot 10^{-18}$	$1.57 \cdot 10^{-14}$
$^{110}\text{Pd} \rightarrow ^{110}\text{Cd}$	$2000 \pm 11$	$11.72 \pm 0.09$	$1.20 \cdot 10^{-19}$	$4.79 \cdot 10^{-15}$
$^{116}\text{Cd} \rightarrow ^{116}\text{Sn}$	$2805.0 \pm 3.8$	$7.49 \pm 0.18$	$2.58 \cdot 10^{-18}$	$1.66 \cdot 10^{-14}$
* $^{124}\text{Sn} \rightarrow ^{124}\text{Te}$	$2287.0 \pm 1.5$	$5.79 \pm 0.05$	$5.530 \cdot 10^{-19}$	$9.040 \cdot 10^{-15}$
$^{128}\text{Te} \rightarrow ^{128}\text{Xe}$	$867.2 \pm 1.0$	$31.74 \pm 0.08$	$2.53 \cdot 10^{-22}$	$5.55 \cdot 10^{-16}$
$^{130}\text{Te} \rightarrow ^{130}\text{Xe}$	$2528.8 \pm 1.3$	$34.08 \pm 0.62$	$1.46 \cdot 10^{-18}$	$1.41 \cdot 10^{-14}$
$^{136}\text{Xe} \rightarrow ^{136}\text{Ba}$	$2468 \pm 7$	$8.87 \pm 0.16$	$1.37 \cdot 10^{-18}$	$1.46 \cdot 10^{-14}$
* $^{148}\text{Nd} \rightarrow ^{148}\text{Sm}$	$1928.8 \pm 1.9$	$5.7 \pm 0.1$	$3.248 \cdot 10^{-19}$	$1.010 \cdot 10^{-14}$
$^{150}\text{Nd} \rightarrow ^{150}\text{Sm}$	$3367.5 \pm 2.2$	$5.6 \pm 0.2$	$3.42 \cdot 10^{-17}$	$6.20 \cdot 10^{-14}$
* $^{154}\text{Sm} \rightarrow ^{154}\text{Gd}$	$1251.0 \pm 1.3$	$22.75 \pm 0.29$	$9.591 \cdot 10^{-21}$	$3.015 \cdot 10^{-15}$
* $^{160}\text{Gd} \rightarrow ^{160}\text{Dy}$	$1729.7 \pm 1.3$	$21.86 \pm 0.19$	$1.938 \cdot 10^{-19}$	$9.559 \cdot 10^{-15}$
* $^{198}\text{Pt} \rightarrow ^{198}\text{Hg}$	$1047 \pm 3$	$7.163 \pm 0.055$	$1.536 \cdot 10^{-20}$	$7.556 \cdot 10^{-15}$
* $^{232}\text{Th} \rightarrow ^{232}\text{U}$	$842.2 \pm 2.5$	100	$1.131 \cdot 10^{-20}$	$1.393 \cdot 10^{-14}$
$^{238}\text{U} \rightarrow ^{238}\text{Pu}$	$1145.0 \pm 1.3$	$99.2745 \pm 0.0106$	$1.15 \cdot 10^{-19}$	$3.11 \cdot 10^{-14}$

**Table 2.1.:**  $Q_{\beta\beta}$ , natural abundance and phase space factors for  $2\nu\beta\beta$  ( $G^{2\nu}$ ) and  $0\nu\beta\beta$  ( $G^{0\nu}$ ). Values with \* come from [28] and others from [29].

process is lower than the decay to ground state. However de-excitation  $\gamma$ -rays are also emitted, often in a cascade of several  $\gamma$ 's.  $^{96}\text{Zr}$  is one of the double- $\beta$  decaying nuclei able to undergo a decay to excited states although it has never been observed.

It was suggested that decays to excited states can provide additional information on nuclear matrix elements [31]. A possibility considered in the past was the study of  $0\nu\beta\beta$  to excited states. The lower energy is compensated with a clear topological signature. Recent searches showed that these matrix elements are much smaller than required for next-generation experiments to detect a potential signal [32].

### 2.2.3. Double- $\beta^+$ decay and double electron capture

$0\nu\beta\beta^-$  is not the only process available to search for the nature of neutrinos. Other processes involving  $\beta^+$  decays and electron captures (EC) are investigated such as  $0\nu\beta\beta^+$ ,  $0\nu\beta^+\text{EC}$  and  $0\nu2\text{EC}$  for a smaller number of isotopes [19].

### 2.3. Neutrinoless double- $\beta$ decay

Supposing that the neutrino is a Majorana particle, Furry first introduced  $0\nu\beta\beta$  in 1939 [33]. This process can be understood as two simultaneous  $\beta$  decays in which one neutrino is exchanged, instead of two neutrinos being emitted. As a result, there would be only the emission of two electrons by the nucleus (see Figure 2.3):

$$(A, Z) \rightarrow (A, Z + 2) + 2e^- \quad (2.3)$$

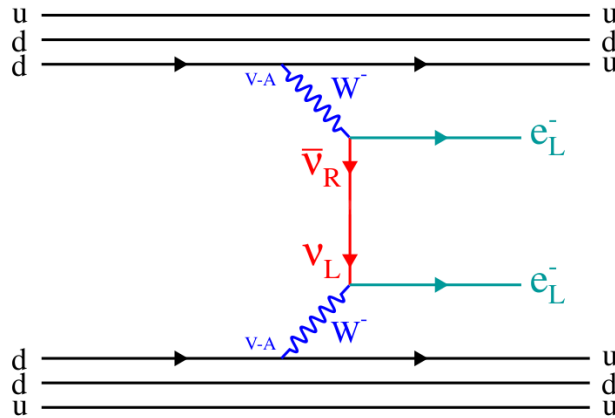


**Figure 2.3.:** Feynman diagram for  $0\nu\beta\beta$ .

In this case, the energy spectrum of the electrons should be a line at the  $Q_{\beta\beta}$  value, since they take away almost all of the available energy in the reaction (see Figure 2.4). Indeed the nucleus has a small recoil but the energies involved are negligible by several orders of magnitude [34].

All of the isotopes that can undergo  $2\nu\beta\beta$  can theoretically decay through  $0\nu\beta\beta$ . However the half-life of this process would be higher than for  $2\nu\beta\beta$ .

Total lepton number is violated by two units in  $0\nu\beta\beta$ . Hence this process is forbidden by the Standard Model. From the Feynman diagram for  $0\nu\beta\beta$  shown in Figure 2.3, two issues can be identified. Firstly, the emitted right-handed anti-neutrino must be absorbed in the other vertex as left-handed in order to produce an electron. Secondly, for Majorana neutrinos,  $\nu$  and  $\bar{\nu}$  differ only in their helicities, requiring a helicity flip. This is only possible as neutrinos are massive [19]. The half-life of  $0\nu\beta\beta$  is defined as in 2.4.

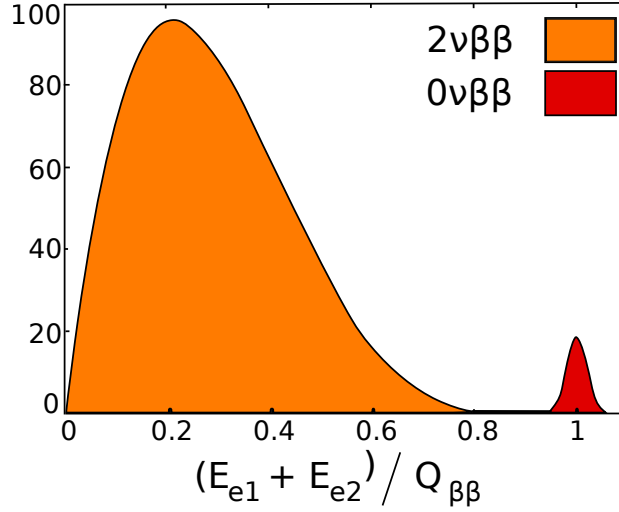


**Figure 2.4.:** Energy spectrum of the two electrons for  $2\nu\beta\beta$  and  $0\nu\beta\beta$  normalized to the  $Q_{\beta\beta}$  value. The energy resolution of the detector has been accounted for.

$$(T_{1/2}^{0\nu})^{-1} = G^{0\nu}(Q_{\beta\beta}, Z) |\mathcal{M}^{0\nu}|^2 \frac{|m_{\beta\beta}|^2}{m_e^2} \quad (2.4)$$

$G^{0\nu}(Q_{\beta\beta}, Z)$  corresponds to the two-electron phase space factor and  $\mathcal{M}^{0\nu}$  is the nuclear matrix element (see section 2.4). The effective neutrino mass for  $0\nu\beta\beta$ ,  $m_{\beta\beta}$ , is defined, using the formalism of equation 1.9, as:

$$m_{\beta\beta} = \sum_{i=1}^3 U_{ei}^2 m_i = c_{12}^2 c_{13}^2 m_1 + e^{2i\lambda_2} s_{12}^2 c_{13}^2 m_2 + e^{2i(\lambda_3 - \delta)} s_{13}^2 m_3 \quad (2.5)$$

$0\nu\beta\beta$  has been assumed here as the mass mechanism process corresponding to the exchange of massive Majorana neutrino. It could also occur by other mechanisms such as the exchange of right-handed weak currents (V+A) that can account for the helicity mismatch [35]. Due to the lepton number violation necessary for  $0\nu\beta\beta$ , the (B-L) symmetry is also broken. If one considers the spontaneous breaking of a global (B-L) symmetry, a Goldstone boson can be associated with it. This boson is called Majoron and could be emitted in  $0\nu\beta\beta$  along with the two electrons [36]. The NEMO technique providing full kinematics, individual energies and the angle between the two electrons allows these processes to be distinguished. Supersymmetric theories can also give rise to Feynman diagrams for  $0\nu\beta\beta$  [37].

## 2.4. Nuclear Matrix Elements

One of the main sources of uncertainty on the effective neutrino mass comes from nuclear matrix elements. The exchange of massive neutrinos involves nucleon-nucleon interactions at short distances. The first step is the creation of a many-body Hamiltonian describing these interactions. Several observables have been considered in order to constrain the best theoretical models such as  $2\nu\beta\beta^+$ , single- $\beta$  decay or muon capture on nuclei [38]. However the accuracy of these measurements is still limited due to the large number of energy states to simulate. In [39] different methods are detailed based on two basic strategies, the nuclear shell model or the quasi random particle approximation (QRPA). Figure 2.5 displays recent results on the calculation of nuclear matrix elements performed with several models. The ranges of predicted values for one isotope are large and are the main uncertainty on the limits on the effective neutrino mass provided by an experiment. All of these models try to describe accurately the structure of the nuclei thanks to the introduction of a mean field and differ in the approximations required to account for the extremely numerous intermediate nuclear states existing in each nucleus.

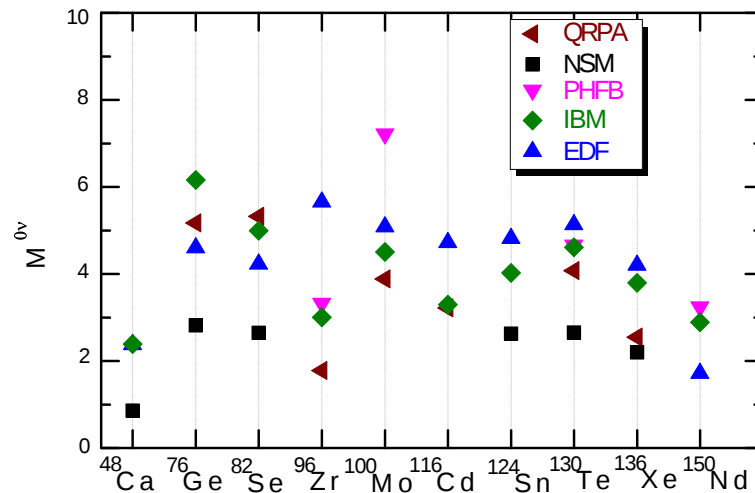


**Figure 2.5.:** Nuclear Matrix Elements computed with different models: Quasi-Random Particle Approximation (QRPA), Nuclear Shell Model (NSM), Projected Hartree-Fock-Bogoliubov (PHFB), Interacting Boson Model (IBM) and Energy-Density Functional (EDF). Adapted from [40].

### 2.4.1. Different models

Quasi-Random Particle Approximation (QRPA) is based on the simulation of a very large number of nuclear orbitals but considering simpler interactions between nucleons. Experimental inputs are given in order to modify the Hamiltonian describing the nucleus. Recently,  $2\nu\beta\beta$  results have been used to tune the value of  $g_{pp}$ , the strength of the isoscalar particle-particle interaction, parametrising the proton-proton interactions. This reduces the uncertainties for this method; however this may not be accurate to describe  $0\nu\beta\beta$ . QRPA is commonly accepted to be more suitable for the description of large nuclei.

Nuclear Shell Model(NSM) is complementary to QRPA being adapted for small nuclei, therefore it is not of use for the description of  $^{96}\text{Zr}$ . This method is based on the complete description of a few nuclear orbitals in the valence shell. A complete description of the interactions in these orbitals is performed and the Hamiltonian is adjusted to describe the spectroscopy of the nucleus. This method tends to estimate smaller than average values for the nuclear matrix elements which may be due to the small number of orbits that are considered.

Interacting Boson Model(IBM) only builds pairs of nucleons with a total momentum equals 0 or 2 and models them as bosons. Shell-model calculations are performed with this approximation. This method has been employed for small and large nuclei.

Projected Hartree-Fock Bogoliubov (PHFB) describes the nuclear matrix elements of  $2\nu\beta\beta$  and  $0\nu\beta\beta$  with few parameters. It only describes pairs of neutrons with even angular momenta and positive parity. Only quadrupole interactions are included.

Energy-Density Functional (EDF) is similar to QRPA since any intermediate single-particle state is available. It is seen as an improvement of the PHFB method on which it is based in that respect thanks to the inclusion of the Gogny interaction [41].

Due to the large number of nucleons in  $^{96}\text{Zr}$ , NSM is not available. Recent results from [40] are presented in Table 2.2:

Framework	NSM	QRPA (Tübingen)	IBM	EDF	PHFB
NME	-	1.77	3.00	5.65	3.32

**Table 2.2.:** Recent results on nuclear matrix elements computations for  $^{96}\text{Zr}$ . [40]

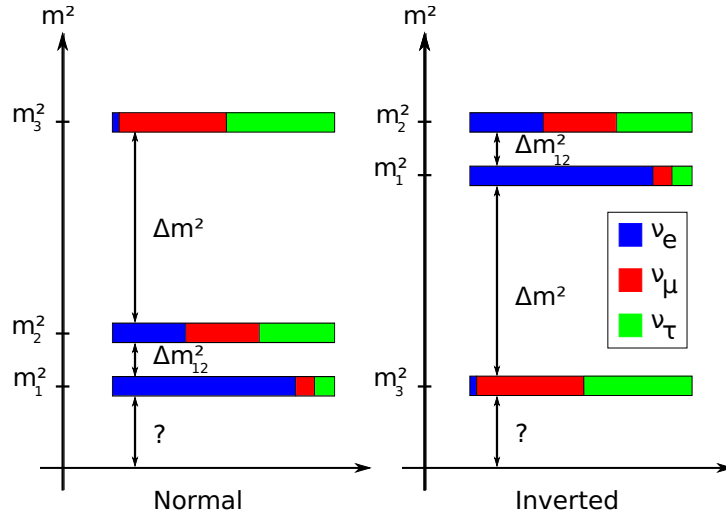


**Figure 2.6.:** Neutrino mass scale in the two different mass hierarchy scenarios. The individual contribution of each flavour to the mass eigenstates is also illustrated.

## 2.5. Neutrino mass hierarchy and effective neutrino mass

Thanks to neutrino oscillation experiments, the squared-mass differences are now accurately measured (see Table 1.1). The sign of  $\Delta m_{12}^2$  implies that  $m_1 < m_2$ . However two scenarios are still possible for the mass eigenstates, the so-called *normal*:  $m_1 < m_2 < m_3$  and *inverted*:  $m_3 < m_1 < m_2$  hierarchy schemes (see Figure 2.6). Figure 2.7 displays the available values for the effective Majorana mass as a function of the mass of the lightest neutrino  $m_{Min}$  ( $m_1$  or  $m_3$ ). It is important to note that any result on the neutrino masses from  $0\nu\beta\beta$  is only relevant if the neutrino is a Majorana particle.

Three regions of interest can be defined in the plane  $(m_{Min}, |m_{\beta\beta}|)$ , known as quasidegenerate, normal hierarchy and inverted hierarchy regions. CP is assumed to be conserved. In addition to having  $\delta = 0$ , only four possible cases exist in which CP is conserved for the Majorana phases:  $(\alpha_2, \alpha_3) = (0,0), (\pi,\pi), (0, \pi)$  and  $(\pi, 0)$ . In that case, the effective neutrino mass can be written from equation 2.5 (with  $\alpha_2 = 2\lambda_2$  and  $\alpha_3 = 2(\lambda_3 - \delta)$ ) as:

$$m_{\beta\beta} = |U_{e1}|^2 m_1 + e^{i\alpha_2}|U_{e2}|^2 m_2 + e^{i\alpha_3}|U_{e3}|^2 m_3 \quad (2.6)$$

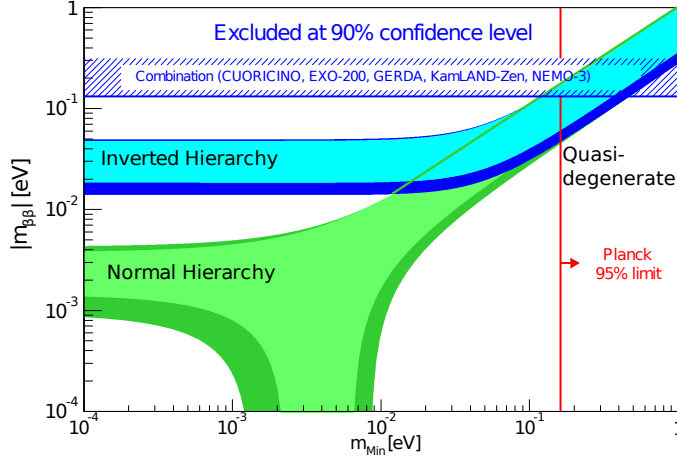


**Figure 2.7.:** Effective neutrino mass  $|m_{\beta\beta}|$  as a function of the lightest neutrino mass, with  $3\text{-}\sigma$  allowed ranges of  $\Delta m_{31}^2$ ,  $\Delta m_{21}^2$ ,  $\sin^2 \theta_{21}$  and  $\sin^2 \theta_{13}$ . The Normal Hierarchy corresponds to the green bands and the Inverted Hierarchy corresponds to the blue bands. The width of the bands is due to the experimental uncertainties on the nuclear matrix elements. The light blue and light green bands correspond to the range of  $\alpha_2$  and  $\alpha_3$ . The Quasi Degenerate region corresponds to the overlap between the two bands. Adapted from [42].

### 2.5.1. Quasidegenerate Region

The lightest neutrino mass obeys  $m_{\min} \gg \sqrt{\Delta m_{21}^2}$  and only two cases remain. If  $\alpha_2 = 0$  and  $\alpha_3 = (0, \pi)$ ,  $m_{\beta\beta} \simeq m_{\min}$ . Otherwise, with  $\alpha_2 = \pi$ ,  $m_{\beta\beta} \simeq m_{\min} \cos(2\theta_{12})$ . A range of values is available for  $m_{\beta\beta}$  due to the uncertainty on  $\theta_{12}$ . Current experiments are exploring the quasidegenerate region and will soon be able to start probing the inverted hierarchy region.

### 2.5.2. Inverted Hierarchy

Here  $m_1 \simeq m_2 \simeq \sqrt{m_3^2 + \Delta m_{31}^2}$ . Due to the small mass of  $m_3$ , a lower bound can be set for  $m_{\beta\beta}$  for any value of  $m_{\min}$ . If  $\alpha_2 = 0$ ,  $m_{\beta\beta} \simeq \sqrt{\Delta m_{31}^2}$  and if  $\alpha_2 = \pi$  then  $m_{\beta\beta} \simeq \sqrt{\Delta m_{31}^2} \cos(2\theta_{12})$ . The possible values for  $m_{\beta\beta}$  are:

$$19 \times 10^{-3} \leq |m_{\beta\beta}| \leq 5 \times 10^{-2} eV, \quad \text{with } m_3 \leq 10^{-2} eV \quad (2.7)$$

### 2.5.3. Normal Hierarchy

In this region we have  $m_1 \ll m_2 \ll m_3$ . The other masses are then  $m_2 \simeq \sqrt{\Delta m_{21}^2}$  and  $m_3 \simeq \sqrt{\Delta m_{31}^2}$ . An upper bound on  $m_{\beta\beta}$  exists at:

$$|m_{\beta\beta}| \leq 4 \times 10^{-3} eV, \quad \text{with } m_1 \leq 10^{-3} eV \quad (2.8)$$

It is possible to have a vanishing value for  $m_{\beta\beta}$  for  $m_1$  around  $4 \times 10^{-3}$  eV. Therefore,  $0\nu\beta\beta$  might never be experimentally measured even if it exists. On the other hand, observing a  $0\nu\beta\beta$  signal would determine at the same time the neutrino nature and mass hierarchy. If the hierarchy is normal, next-generation experiments will not have the required sensitivity to reach it.



# Chapter 3.

## Experimental status of neutrinoless double- $\beta$ decay searches

*“If you want a thing done well, do it yourself.”* - N. Bonaparte

### 3.1. Principle of double- $\beta$ experiments

In the past decades, several experiments have been competing to try and discover a signal for  $0\nu\beta\beta$ . Today the experiments of the previous generation: Heidelberg-Moscow, NEMO-3, CUORICINO, etc. have stopped, but new generation ones have started or are about to start. Even if the experimental techniques are different, the principle remains equal. All of them try to meet these requirements:

- measure with a very good energy resolution the energy of the two emitted electrons. This allows then the  $0\nu\beta\beta$  line to be distinguished from the  $2\nu\beta\beta$  spectrum (see Figure 2.4) and from other backgrounds;
- achieve high spatial resolution or use segmented sources. This is important to identify the origin of the events as the two electrons must come from the same nucleus and help rejecting background;
- maximise the isotope mass in the detector. It increases the experiment sensitivity. It can be done by enriching the isotopes or using a large mass of isotopes with large natural abundance;

- reduce the background to access higher sensitivities. The rareness of the process makes it critical to suppress as many background counts as possible. This can be done thanks to material selections for radiopurity and source purification;
- identify the two emitted electrons and access their full kinematics. Other particles, such as  $\alpha$ 's or  $\gamma$ 's can mimic the two-electron events if the events topologies are not properly identified;
- identify the daughter nucleus produced in double- $\beta$  decay to completely characterize the process. This has not been done so far, but it would provide a clear signature of the process.

Compromises have to be made on these criteria and several technologies have been explored by different experiments. Semi-conductors, bolometers and scintillating bolometers have an excellent energy resolution. Their detection efficiency is high as the source is the detector itself. One of the limitations of germanium detectors is the low  $Q_{\beta\beta}$  value of  $^{76}\text{Ge}$  compared to the main backgrounds from natural radioactivity (see section 3.2).

Liquid scintillators experiments have also been designed with a large mass enabling to define a fiducial volume. These experiments reuse large existing detectors but have a lower energy resolution compared to germanium detectors for example.

Other technologies have been investigated such as time projection chambers (TPC, consisting of a large container filled with a gas or a liquid ionized by the passage of a charged particle) or a combination of a tracker and a calorimeter which is the principle behind the NEMO experiments. Their strength is their capability to identify the two electrons and their kinematics (individual energies, angle of emission, track curvature,...) although their energy resolution is lower.

The lowest background is required for double- $\beta$  decay experiments. Since the energies considered here are around a few MeV, background mainly come from natural radioactivity and cosmic rays. To greatly reduce cosmic backgrounds, experiments are installed in underground laboratories. Extensive shielding is used in order to isolate the detectors from their environment.

Today, the lower limits on half-lives of the  $0\nu\beta\beta$  process range from  $10^{24}$  to  $10^{26}$  years, depending on the isotope. However, all of the technologies previously mentioned have comparable sensitivities on the effective neutrino mass.

We tried to quote the latest results published by the experiments that are described in the following. Some results only quoted the value of the half-life. In the following, results quoted as “recalculated” will refer to calculations of the effective neutrino mass assuming a reference measurement. When available, this reference measurement is another result published by the same collaboration. If not the values that are displayed come from a calculation performed independently in [43].

## 3.2. Germanium experiments

### 3.2.1. Operating principle

In the past, several experiments studied the  $0\nu\beta\beta$  of  $^{76}\text{Ge}$  to  $^{76}\text{Se}$  and this process is still studied today. In these experiments, the sources are constituted of Ge semiconductor diodes enriched at about 86 % in  $^{76}\text{Ge}$ , which have a high detection efficiency. The  $Q_{\beta\beta}$  of 2039 keV makes of the highest energy  $\gamma$  of  $^{208}\text{Tl}$  ( $E_\gamma = 2.615$  MeV) a possible background for Ge experiments due to Compton scattering.  $\alpha$ -particles from the surface of the detector structure are another source of background. Therefore the energy resolution has to be excellent to be able to identify  $0\nu\beta\beta$  signal. Combined with a cooling system (e.g. liquid argon), it can be as small as a few keV at the  $Q_{\beta\beta}$  value.

A particle interaction inside the detector produces charge carriers. The electrodes collect them and a preamplifier converts this charge into a voltage pulse proportional to the energy deposited in the detector. There are several types of germanium detectors. The first ones are semi-coaxial detector. They consist of a cylinder of germanium with an n-type contact on the outer surface, and a p-type contact on the surface of an axial well (see Figure 3.1). In semiconductors, electrons and holes act as charge carriers. N-type semiconductors have an excess of electrons over holes which makes of electron the majority carriers. In contrast, p-type semiconductors have an excess of holes.

A new type of germanium detector has also been developed, Broad-Energy Germanium detectors (BEGe), with improved performances. The BEGe is designed with an electrode structure (see Figure 3.1) that improves the energy resolution. It is fabricated from selected germanium having an enhanced charge collection (thus resolution and peak shape) at high energies. In addition to higher efficiency for typical

samples, the BEGe exhibits lower background than typical coaxial detectors. They are also very stable as they have no charge collection loss.

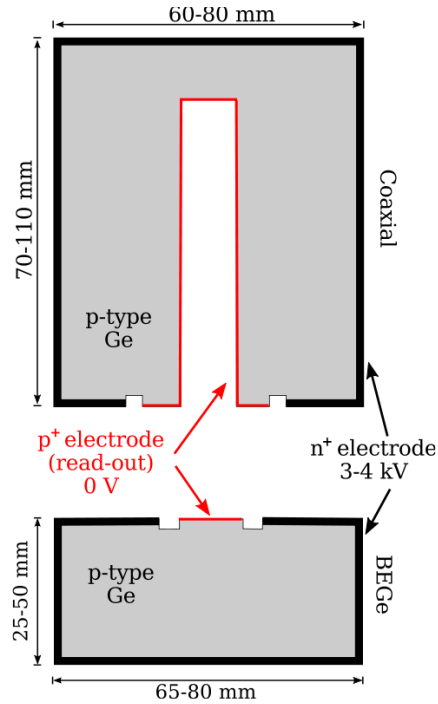


**Figure 3.1.:** Schematic of semi-coaxial and broad energy HPGe [44].

In Germanium detectors, two topologies can be observed when searching for  $0\nu\beta\beta$ . The two electrons are emitted from the same vertex implying that their energies are deposited at a unique position in the detector. These events are called *single-site* events. A  $\gamma$ -particle loses its energy typically through several spatially separated Compton scatters. Therefore *multi-site* events can be observed.

It is crucial to discriminate between the two events topologies in order to reject  $\gamma$ -background from  $\beta$ - $\gamma$  emitters in natural radioactivity. For that purpose a Pulse Shape Discrimination (PSD) has been developed. BEGe detectors appear to have better performance concerning this pulse shape analysis. It has been observed that the pulses shapes are different for single-site and multi-site events. Similarly, pulses from  $\beta$ 's or  $\alpha$ 's near the surface of the crystals can be identified [45]. The amplitude over energy (A/E) ratio of the pulse is computed and the amplitude is globally linear with the energy for the single-site events and not for multi-site events.

### 3.2.2. Heidelberg-Moscow and IGEX

Two experiments ran during the 1990s using  $^{76}\text{Ge}$  as a  $\beta\beta$  isotope. Heidelberg-Moscow (HdM) and International Germanium EXperiment (IGEX) were respectively located in the *Laboratori Nazionali del Gran Sasso* (LNGS, Italy) and in the *Laboratorio Subterráneo de Canfranc* (LSC, Spain). The data acquisition started in 1990 for HdM and in 1991 for IGEX and stopped in 2003 and 2000 respectively. The total exposures were 71.7 kg.y for HdM and 8.9 kg.y for IGEX. PSD was already used at that time and allowed  $\gamma$ -induced background to be reduced.

When considering the entire dataset for the two experiments, no excess has been observed. The accepted exclusion values for the half-life and for the effective neutrino mass for these two experiments are:

$$\begin{aligned} \text{HdM} : T_{1/2}^{0\nu} &> 1.9 \times 10^{25} \text{ years and } |m_{\beta\beta}| < 0.35 - 1.05 \text{ eV @ 90\% C.L. [46]} \\ \text{IGEX} : T_{1/2}^{0\nu} &> 1.57 \times 10^{25} \text{ years and } |m_{\beta\beta}| < 0.33 - 1.35 \text{ eV @ 90\% C.L. [47]} \end{aligned}$$

There has been a controversy between these experiments and inside the HdM collaboration. Indeed, part of the HdM collaboration announced the observation of a  $0\nu\beta\beta$  signal. The results published in 2005 by part of the HdM collaboration are:

$$T_{1/2}^{0\nu} = 1.19_{-0.23}^{+0.37} \times 10^{25} \text{ years @ } 4.2 \sigma \text{ and } |m_{\beta\beta}| = 0.44 \text{ eV} \in [0.24, 0.58] \text{ eV [48]}$$

Although the IGEX experiment did not observe any excess at the expected energy for  $0\nu\beta\beta$ , it has also not been able to prove that the excess was not due to this signal. Today this result is still controversial and several experiments are currently investigating further into refuting or confirming it. Indeed no absolute rejection is yet possible because of the error on the nuclear matrix elements unless considering the same isotope. However, it is now generally admitted that the GERDA experiment has made a clear statement about this claim.

### 3.2.3. GERDA & MAJORANA

#### GERDA (GERmanium Detection Array)

GERDA is the next-generation experiment following Heidelberg-Moscow and IGEX and is located in the LNGS. Several phases are scheduled in which the isotope mass will be progressively increased.

The aim of phase I was to verify the claim from part of the HdM collaboration. It was also designed to reach higher sensitivity than previous Ge experiments. Eight enriched semi-coaxial detectors (four from HdM, one from GENIUS-Test-Facility and three from IGEX have been re-used). In total, 20.7 kg of detector (of which 17.7 kg are enriched) were available. For phase II, a higher  $\beta\beta$  isotope mass is scheduled along with a background reduction to increase further the sensitivity.

Ge diodes cooled by ultra-pure liquid argon (LAr) are part of the detection technique of this experiment. Compared to HdM, important improvements have been made on two critical parts of the experiment: the shielding and the supports of Ge diodes. The supports of the Ge diodes have been optimized by reducing their dimensions removing as much material as possible close to the Ge diodes.

In the GERDA detector, bare enriched  $^{76}\text{Ge}$  detectors are contained in a cryostat filled with liquid argon (see Figure 3.2). The Ge detectors are held by an array of individual strings each capable of being equipped with up to 5 detectors. In addition to being a very efficient coolant, liquid argon acts as an external  $\gamma$  shield and a scintillator. The cryostat is a 4 m-diameter stainless steel vessel with a copper lining aiming at reducing the  $\gamma$  flux from the vessel. It has a total mass of about 25 tons and contains 100 tons of liquid argon. The detectors are also isolated from radon with a 3 m high, 750 mm diameter and 30  $\mu\text{m}$  thick copper cylindrical shroud placed inside the cryostat.

A shield of ultra-pure water surrounds the cryostat in a 8.5 m high and 10 m diameter tank. This provides a 3 m thick water buffer around the cryostat which can absorb the neutrons and attenuate the external  $\gamma$  flux (along with LAr), provide a Cherenkov medium as a muon veto and contain the argon in case of an emergency.

A clean room and a lock have been installed on top of the vessel. This makes it possible to insert the detectors strings and the calibration sources without contaminating the liquid argon, preserving the radiopurity.

Background measurements started in June 2011 with three natural Ge detectors. Data taking started in November 2011 with the eight enriched semi-coaxial detectors. In July, 2012 five enriched BEGe diodes were installed (as first tests for phase II) with a total mass of 3.6 kg.

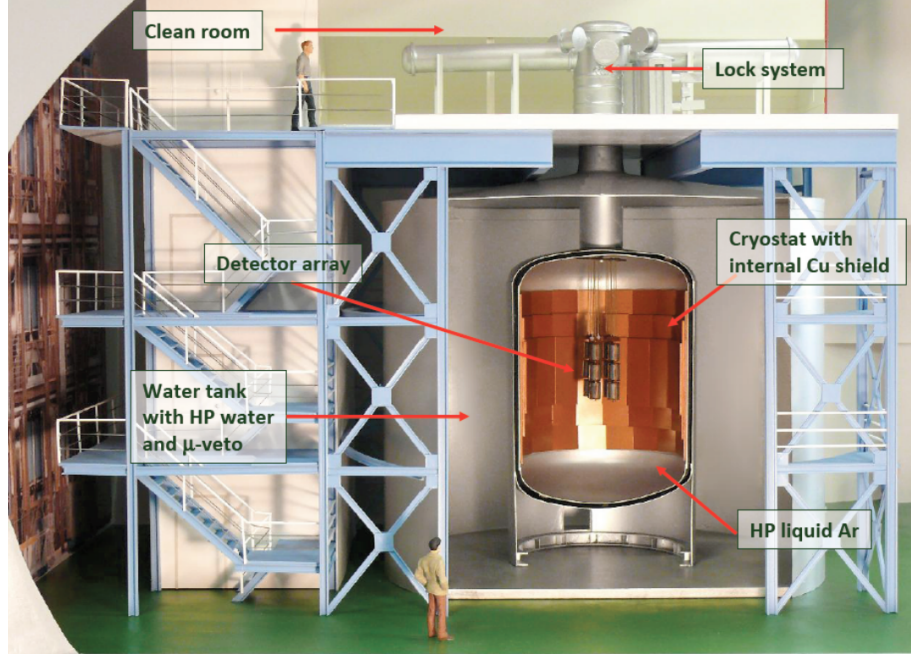


**Figure 3.2.:** Schematic of the GERDA detector.

During the first phase, the background was very high, at  $18 \times 10^{-2}$  cts/(keV · kg · y)) coming mainly from radon ( $^{208}\text{Tl}$  and  $^{214}\text{Bi}$ ). A background from  $^{42}\text{K}$ , a daughter nucleus of  $^{42}\text{Ar}$  cosmogenically activated, was also detected in LAr.

Further studies, mainly on the  $^{42}\text{K}$  contribution with a dedicated detector (LArGe) resulted in the addition of mini-shrouds around the strings, efficiently reducing this background for the semi-coaxial detectors. This enabled the background to be reduced to  $6 \times 10^{-2}$  cts/(keV · kg · y) in the  $\beta\beta$  region.

The energy resolution, weighted by the exposure, was found to be  $4.8 \pm 0.2$  keV (FWHM) for the semi-coaxial detectors and  $3.2 \pm 0.2$  keV (FWHM) for the BEGes at  $Q_{\beta\beta}$ .

The result of the  $2\nu\beta\beta$  half-life measurement is:

$$T_{1/2}^{2\nu} = 1.84_{-0.10}^{+0.14} \times 10^{21} \text{ y [49]}$$

An exposure of 21.6 kg.y was available for the  $T_{1/2}^{0\nu}$  search. Figure 3.3 displays the energy spectrum in the  $0\nu\beta\beta$  region where no excess is observed.

A lower limit was set by the Phase I at:

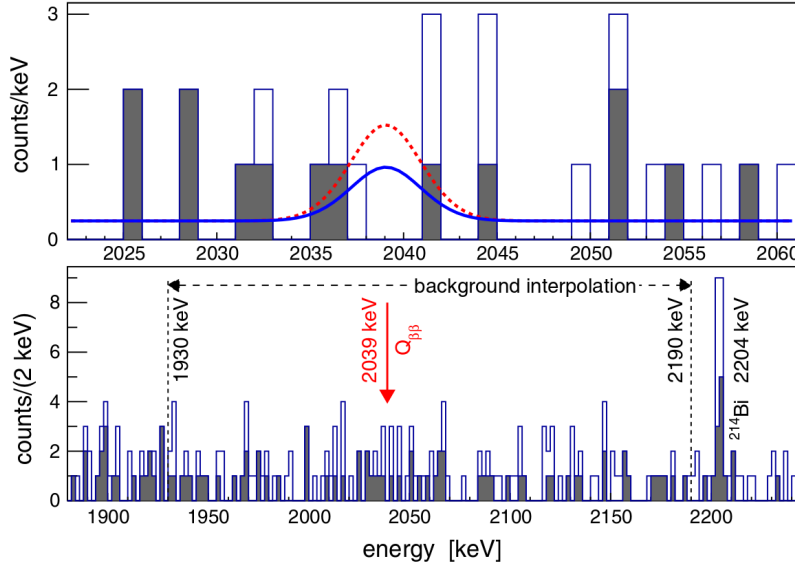


**Figure 3.3.:** Energy spectrum in the  $0\nu\beta\beta$  region for GERDA [50]. The top plot is a zoom of the bottom plot in the region of interest. No excess is observed. The blue line corresponds to the 90 % upper limit. The dashed red line is the expected spectrum assuming the central value from the HdM claim.

$$T_{1/2}^{0\nu} > 2.1 \times 10^{25} \text{ y (@ 90 \% C.L.) [50] and } |m_{\beta\beta}| < 0.29 - 0.57 \text{ eV @ 90 \% C.L.}$$

(recalculated from [50])

No support for the previous claim was announced. Indeed these limits were not yet able to completely rule out this claim and only to strongly disfavour it.

A combination of this measurement and the results of the previous experiments allowed a higher limit on the  $0\nu\beta\beta$  process half-life to be set:

$$T_{1/2}^{0\nu} > 3.0 \times 10^{25} \text{ y (@ 90 \% C.L.) and } |m_{\beta\beta}| < 0.2 - 0.4 \text{ eV @ 90 \% C.L. [50]}$$

The transition to the second phase of the GERDA experiment is already ongoing. In order to have a larger mass of Ge detector, a new set of enriched material is being produced. Special care has been taken in order to avoid cosmogenic activation, from the transportation to the storage of the isotopes in the underground laboratory.

Natural BEGe detectors have been installed in a cryostat and studies of background reduction in  $^{214}\text{Bi}$  and  $^{208}\text{Tl}$  have been performed showing promising results [51]. The new BEGe detectors have an energy resolution improved by about a factor of 2 compared to phase I. A total enriched mass of approximately 20 kg will be available for the phase II in the form of 20 BEGe detectors. Another improvement in phase

II of GERDA will be the use of the liquid argon as a scintillating veto. Tests have been performed at the LNGS with the LArGe detector for that purpose. Given the success of these tests and the current background level in phase I, the liquid argon cryostat will be equipped with scintillation detectors.

The target sensitivity for phase II, with a background of  $10^{-3}$  cts/(keV · kg · y) is:

$$T_{1/2}^{0\nu} > 1.4 \times 10^{26} \text{ y (@ 90 \% C.L.) [52] and } |m_{\beta\beta}| < 0.04 - 0.09 \text{ eV @ 90 \% C.L.} \\ \text{(recalculated from [52])}$$

## MAJORANA

MAJORANA is another experiment under construction based on the Ge technology (see Figure 3.4). It aims at employing 40 kg of Ge of which 20 kg will be enriched at 86 % and is installed in the Sanford Underground Laboratory on the Davies campus next to the Homestake mine (South Dakota, USA). A low background shielding made of copper, electroformed in the underground laboratory, and lead has already been installed. A collaboration between the GERDA and MAJORANA experiments is currently discussed and could be the third phase of operation of GERDA.

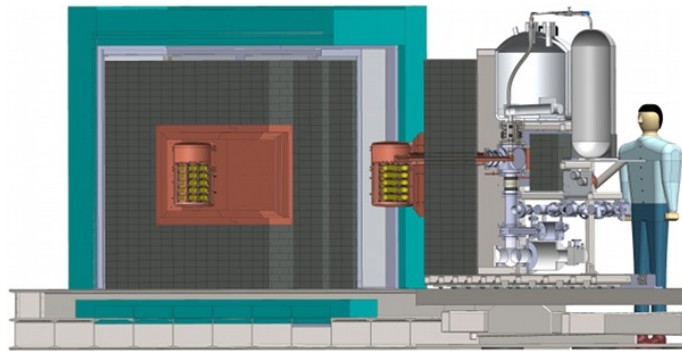


**Figure 3.4.:** *Schematic of the MAJORANA demonstrator.*

## 3.3. Bolometer experiments

### 3.3.1. Operating principle

Bolometers are very-low temperature calorimeters. When a particle passes through the detector, it creates heat (phonons) proportionally to its energy. An absorber collects the heat and its temperature increases by the ratio of the energy deposit over

its heat capacity. Semiconductor thermistors measure this temperature increase. To detect an energy deposit in a bolometer detector, it is necessary to cool it down at a temperature around 10 mK to reduce the heat capacity. Thermistors are required as they are sensitive thermometers. In bolometers, the efficiency of the energy deposition detection is very high but the collection of the data is slow.

### 3.3.2. CUORICINO

Located in the LNGS (*Laboratori Nazionali del Gran Sasso*), this bolometric experiment ran from March 2003 to July 2008. CUORICINO experiment was comprised of enriched and natural  $\text{TeO}_2$  crystals made of around 75 % and 33.8 % respectively of the  $\beta\beta$ -emitter  $^{130}\text{Te}$ . In spite of its high natural abundance,  $^{130}\text{Te} \rightarrow ^{130}\text{Xe}$  has a  $Q_{\beta\beta}$  value of 2527.5 keV which makes the  $\gamma$  line of  $^{208}\text{Tl}$  a critical background.

Thanks to the design of the detector, 85% of two-electron events are fully contained. The event signature is a monochromatic peak in the energy spectrum. This allows most of the background to be rejected by defining a narrow region of interest. The difficulty is to reject events that mimic two-electron events. These fake events can come from the detector itself (electronics or thermal noise). An efficient rejection is achieved via a pulse shape analysis. They can also be produced by particles interacting in the detector (from natural radioactivity or cosmic rays).

The first source of background is  $\gamma$ 's from inside the detector, mainly from  $^{208}\text{Tl}$  in natural radioactivity below 2.615 MeV. An efficient shielding is necessary in order to reduce this background. The second one is  $\alpha$ 's dominating above 2.615 MeV. The  $\alpha$ 's originate from the natural radioactivity chains of  $^{238}\text{U}$  and  $^{232}\text{Th}$ . These isotopes can be found on the surface of the elements of the detector, and especially the copper structure holding the crystals. This can be dealt with thanks to a proper material selection and handling, and a careful surface preparation. The background levels have been estimated at 0.104 cts/(keV · kg · y) for  $\alpha$ 's and at 0.16 cts/(keV · kg · y) for  $\gamma$  [53].

The detector was designed as a tower array of 62  $\text{TeO}_2$  crystals with a total mass of 40.7 kg (see Figure 3.5). It was installed in a dilution refrigerator at the LNGS operating at a temperature of 8 mK. Four groups of crystals were placed in the experiment: 44 big crystals of 790 g, 14 small crystals of 330 g, 2  $^{130}\text{Te}$  enriched crystals of 330 g enriched at 75 % and 2  $^{128}\text{Te}$  enriched crystals of 330 g enriched at

82.3 %. The energy resolution (FWHM) was on average 7 keV (big crystals) and 9 keV (small crystals) at the  $Q_{\beta\beta}$  value.

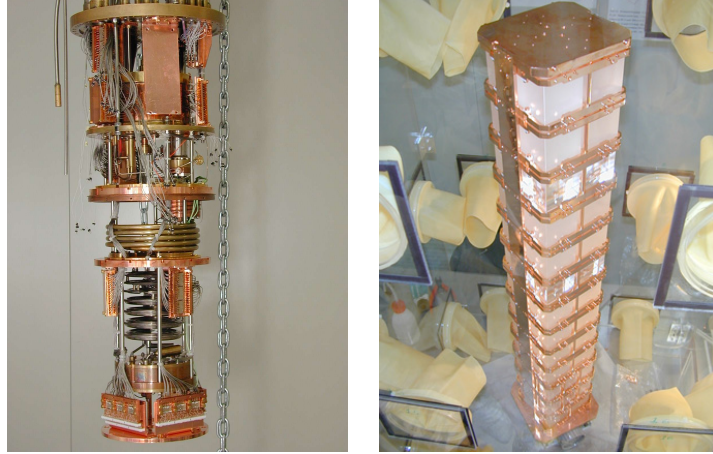


**Figure 3.5.:** Views of the CUORICINO tower array. On the left the cooling system. On the right the thirteen layers of crystals are visible in the copper structure.

Figure 3.6 displays the energy spectrum in the  $0\nu\beta\beta$  region. No excess is observed in the energy region of interest. A clear peak is observed at a slightly lower energy, associated to  $\gamma$ -events from  $^{60}\text{Co}$ .

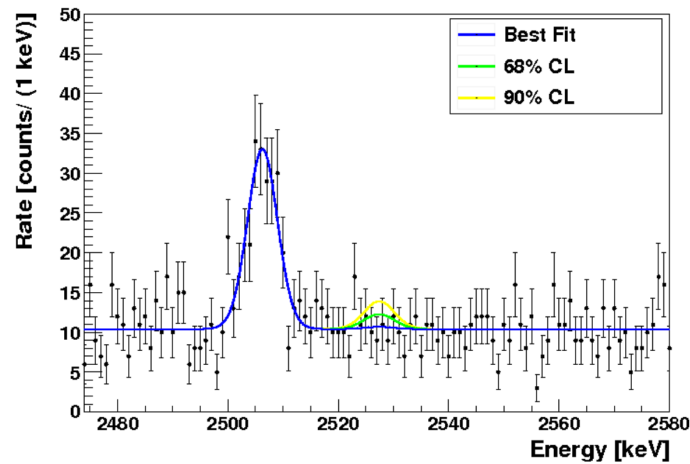


**Figure 3.6.:** Energy spectrum in the  $0\nu\beta\beta$  region [53]. The blue line corresponds to the background level. The peak in the blue line is associated to  $^{60}\text{Co}$ . The green and yellow lines correspond to the limits on the half-life at 68 % and 90 % respectively.

The current results on  $T_{1/2}^{0\nu}$  with an exposure of 19.75 kg.y are:

$$T_{1/2}^{0\nu} > 2.8 \times 10^{24} \text{ y @ 90 \% C.L. and } |m_{\beta\beta}| < 0.3 - 0.7 \text{ eV [53]}$$

The double- $\beta$  decay of  $^{130}\text{Te}$  to the  $0^+$  excited state of  $^{130}\text{Xe}$  was also investigated using time coincident events. The results of these studies were:

$$\begin{aligned} T_{1/2}^{2\nu, 0^+} &> 1.3 \times 10^{23} \text{ y @ 90 \% C.L. [54]} \\ T_{1/2}^{0\nu, 0^+} &> 9.4 \times 10^{23} \text{ y @ 90 \% C.L. [54]} \end{aligned}$$

### 3.3.3. CUORE-0

CUORE-0 is the last step before the start of the full CUORE experiment [55]. It consists of a single CUORE-like tower made of 52 CUORE crystals with a total mass of 39 kg. Very strict cleanliness conditions were imposed during the assembly of the tower to test improvements on the background reduction from CUORICINO. CUORE-0 began its operation in September 2012 by the cooling down in the cryostat of CUORICINO. However the stable phase started only in March 2013 proving that the material could operate properly at low temperature. An energy resolution of  $5.1 \pm 0.3$  keV (FWHM) was measured at 2.615 MeV. Data unblinding has been performed in April 2015 when the sensitivity surpassed the one from CUORICINO. However data taking will continue until CUORE starts. The background levels have been decreased compared to CUORICINO as shown in Figure 3.7. A reduction of a factor of  $\sim 6$  has been measured on the  $\alpha$ -background. However some contributions remain, due to the use of the same cryostat, essentially on the  $\gamma$ -background. They correspond to the peaks visible on top of the continuum. This should be also reduced when using new cryostats for the final detector.

The latest results published with the CUORE-0 results on the half-life of the  $0\nu\beta\beta$  of  $^{130}\text{Te}$  are:

$$T_{1/2}^{0\nu} > 2.7 \times 10^{24} \text{ y @ 90 \% C.L. [57] and } |m_{\beta\beta}| < 0.4 - 1.1 \text{ eV (recalculated from [57])}$$

This result is of the same order as the one obtained by CUORICINO. A combination of both experiments has been performed, leading to the current best limit on the half-life of the  $0\nu\beta\beta$  of  $^{130}\text{Te}$ :

$$T_{1/2}^{0\nu} > 4.0 \times 10^{24} \text{ y @ 90 \% C.L. and } |m_{\beta\beta}| < 0.27 - 0.76 \text{ eV [57]}$$

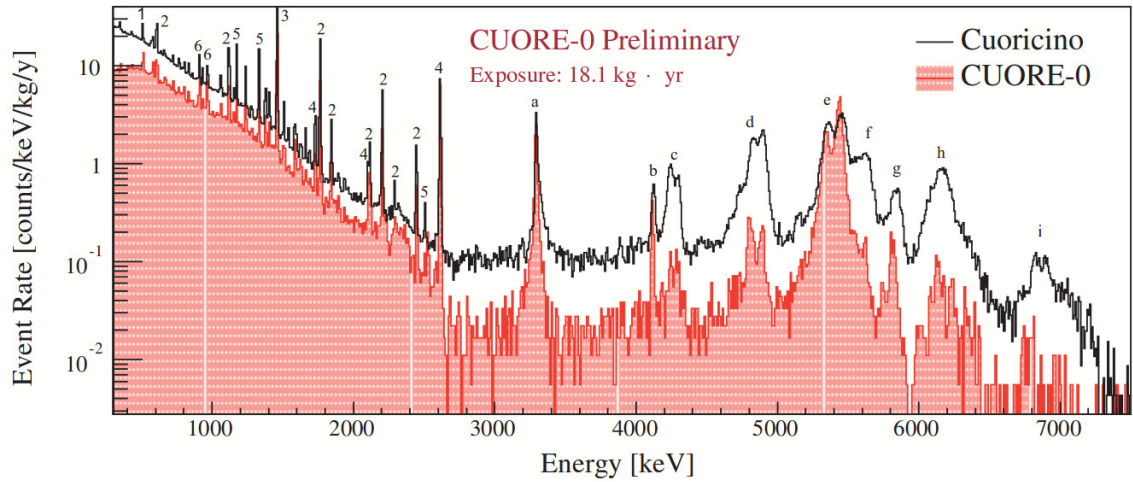


**Figure 3.7.:** Comparison of the energy spectra of CUORE-0 and CUORICINO. The  $\alpha$  background has clearly been reduced but  $\gamma$ -lines are still clearly visible (e.g. the line of  $^{208}\text{Tl}$  at 2.615 MeV) [56].

### 3.3.4. CUORE

CUORE is the next-generation experiment using bolometers and the successor of CUORICINO. It will also be located in the LNGS. The  $\beta\beta$  emitter will remain  $^{130}\text{Te}$  but the mass could be increased from 40.7 kg to up to 741 kg of natural Te corresponding to 206 kg of  $^{130}\text{Te}$ . 19 towers will be installed and operated at 10 mK. The expected energy resolution (FWHM) at  $Q_{\beta\beta}$  value is around 5 keV.

Since the sensitivity is a function of the background level, efforts have been made to reduce the two main backgrounds from CUORICINO. Ultra-pure materials have been selected and efficient shields have been installed in order to reduce the  $\gamma$  background. The crystals surface contamination targets are very low (10 - 100  $\mu\text{Bq}/\text{m}^2$ ) and required several crystals to be measured at the same time. These measurements enabled the best surface cleaning procedure to be selected in order to decrease the  $\alpha$  background by a factor of two compared to CUORICINO. Bulk contamination has been shown to be below the requirements for CUORE [58]. In order to reach the 0.01 cts/(keV · kg · y) required for CUORE, further improvements are needed. The radiopurity of the cryostat and the shield efficiency will be increased by a careful material selection.

The commissioning of the cryostat of CUORE started in Summer 2012 and the first cool down of the cryostat has already been performed. The 19 towers of the

detector have now been fully assembled and data taking is expected to start in 2015. Assuming a low background of 0.01 cts/(keV · kg · y) and five years of data taking, the expected sensitivity is:

$$T_{1/2}^{0\nu} > 9.5 \times 10^{25} \text{ y @ 90 \% C.L. and } |m_{\beta\beta}| < 0.05 - 0.13 \text{ eV (@ 90 \% C.L.) [58]}$$

### 3.3.5. LUCIFER & LUMINEU

LUCIFER (Low Background Cryogenic Installation For Elusive Rates) is another bolometer experiment. It will study  $^{82}\text{Se}$  in the form of crystals of ZnSe. With a  $Q_{\beta\beta}$  of 2995 keV, the external  $\gamma$  background will be strongly reduced as it is above the  $\gamma$  line of  $^{208}\text{Tl}$  at 2.615 MeV.

The operating principle will be similar to that of CUORE, with the addition of the detection of a small fraction of the energy deposition converted into scintillation light in the ZnSe crystals. The remaining energy is converted into heat as for every bolometer experiment. As already explained, the two main backgrounds in CUORE are coming from  $\gamma$ 's and surface  $\alpha$ 's. Combining scintillation light and temperature signals allows the  $\alpha$  background to be reduced. Indeed the scintillation quenching factor is different for  $\alpha$  and  $\beta - \gamma$ . The detected light as a function of the energy of these particles are displayed in Figure 3.8. It is clearly visible that  $\alpha$ 's and  $\gamma$ 's have different behaviours, allowing a discrimination considering the ratio of the signal from scintillation over the one from phonons (see Figure 3.8 (right)). This technology was first developed for Dark Matter searches. It is worth noting that  $^{130}\text{Te}$  could not be employed as a scintillating bolometer due to the low light yield.

LUCIFER will be made of an array of dozens of individual bolometers. A demonstrator will be built using  $\sim 15$  kg of enriched  $^{82}\text{Se}$  through 36 individual crystals of a few hundred grams. This will also provide a granularity useful for background identification. Important studies on the production and radiopurity of the crystals will be carried out.

The expected sensitivity after 5 years of running and a background level of  $10^{-3}$  cts/(keV · kg · y) is:

$$T_{1/2}^{0\nu} > 6.0 \cdot 10^{25} \text{ y @ 90 \% C.L. and } |m_{\beta\beta}| < 0.07 - 0.19 \text{ eV [59]}$$

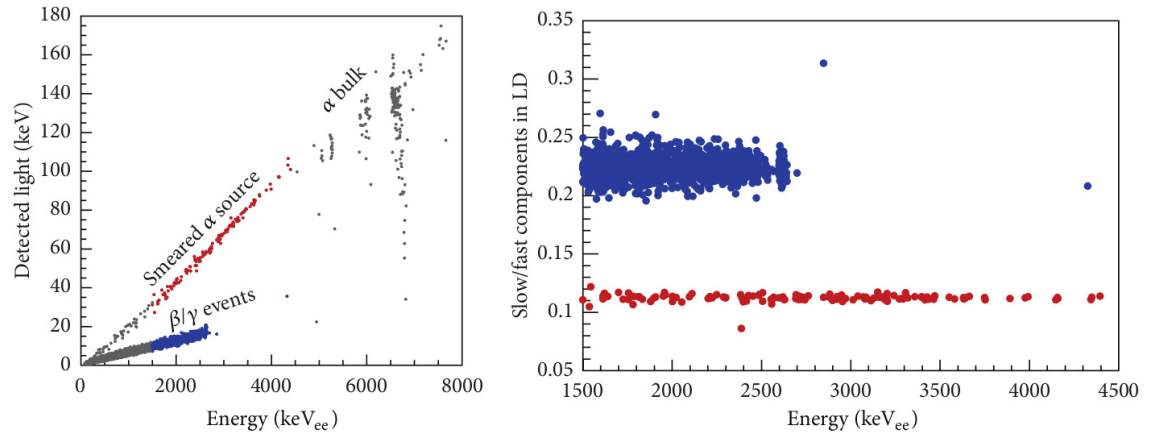


**Figure 3.8.:** *On the left, the light emitted by the ZnSe crystal as a function of the energy. On the right, the shape of events selected in the light detector (LD) around the ROI for  $0\nu\beta\beta$ . The energy scales are different for  $\alpha$ 's and  $\gamma$ 's enabling to discriminate between the two contributions. [59].*

Another experiment aiming at using scintillating bolometers is the Luminescent Underground Molybdenum Investigation for NEUtrino mass and nature (LUMINEU) experiment. As opposed to LUCIFER experiment, the goal here is to make  $\text{Zn}^{100}\text{MoO}_4$  crystals. The first step of this experiment is the production of four crystals for a total mass of  $^{100}\text{Mo}$  of 675 g.

The first crystal produced proved to have an energy resolution (FWHM) of 6 keV at 2.615 MeV. Pulse shape analysis has been demonstrated to successfully distinguish  $\alpha$ 's from  $\beta$ 's/ $\gamma$ 's. The radiopurity of the crystals was also proven excellent.

## 3.4. TPC and Liquid Scintillator experiments

### 3.4.1. EXO-200

EXO-200 is a cylindrical liquid xenon TPC. Data taking started in May 2011. The experiment has been installed in an underground clean room (1585 m.w.e.) in the Waste Isolation Pilot Plant, Carlsbad, New Mexico, USA. 200 kg of  $^{136}\text{Xe}$  ( $Q_{\beta\beta} = 2.458$  MeV) with an enrichment at 80.6% are studied. The detector has a diameter of 40 cm and is 44 cm high. Shielding is comprised of 50 cm of cryofluid at 167 K in a vacuum-insulated copper cryostat. 25 cm of lead have also been installed in order to reduce the external  $\gamma$  flux in the detector.

The TPC provides with three-dimensional coordinates. Avalanche photodiodes measure the scintillation light. Wire grids placed at the ends of the TPC provide energy and transverse coordinates. The detection of the scintillation light provides an initial time  $t_0$  which enables the measurement of the longitudinal coordinate. The possibility to reconstruct the energy deposits positions enables the discrimination of different events topologies. Single-site deposits are associated with single- $\beta$ , double- $\beta$  or  $\alpha$  events. On the other hand  $\gamma$ 's interact at several positions and produce multi-site energy depositions. A fiducial volume of 76.5 kg of  $^{136}\text{Xe}$  has also been defined removing the edges of the TPC from the analysis in order to decrease the background level. Cosmic ray muons are detected by plastic scintillator panels. The energy resolution (FWHM) at the  $Q_{\beta\beta}$  value is 3.3 % combining ionization and scintillation information.

As displayed in Figure 3.9, no excess has been observed in the region of interest. The latest results on the half life measurements are:

$$T_{1/2}^{2\nu} = 2.165 \pm 0.016(\text{stat.}) \pm 0.059(\text{syst.}) \times 10^{21} \text{ y [60]}$$

$$T_{1/2}^{0\nu} > 1.1 \times 10^{25} \text{ y and } |m_{\beta\beta}| < 0.19 - 0.45 \text{ eV [61]}$$

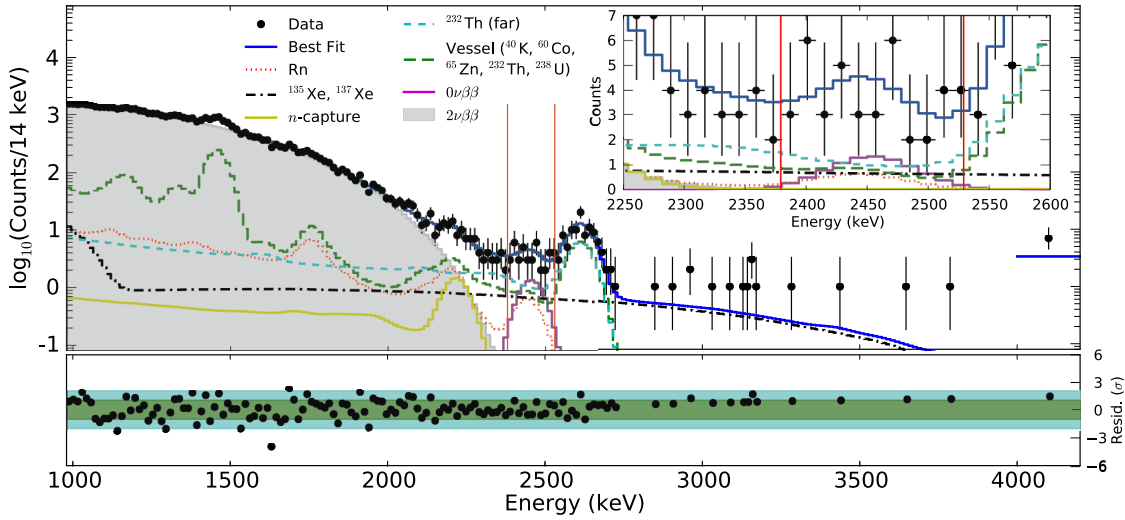


**Figure 3.9.:** *Single-site events energy spectra for the EXO-200 experiment [61]. A zoom on the ROI is displayed on the top right corner. No excess is visible over the background.*

The target for the background level was at  $10^{-3}$  cts/(keV · kg · y) in the  $0\nu\beta\beta$  energy region and was measured to be  $(1.7 \pm 0.2) \times 10^{-3}$  cts/(keV · kg · y) [61]. Background levels improvement are required for a ton-scale experiment. A possible solution to

increase sensitivity would be the tagging of the  $^{136}\text{Ba}$ ,  $^{136}\text{Xe}$  double- $\beta$  daughter nucleus. A gaseous TPC could also be designed to add tracking information.

### 3.4.2. KamLAND-Zen

The KamLAND-Zen (KamLAND-**Z**ero neutrino) experiment started using the previously existing KamLAND detector in Summer 2011. It is installed in the 1000 m deep Kamioka mine (2700 m.w.e.). The isotope studied here is also  $^{136}\text{Xe}$  in the form of 13 tons of Xe-loaded liquid scintillator with 330 kg of Xe enriched at  $90.93 \pm 0.05$  % in  $^{136}\text{Xe}$ .  $^{136}\text{Xe}$  was selected for its relatively low cost, its high  $2\nu\beta\beta$  half-life (around  $2 \times 10^{21}$  y) and its good solubility in liquid scintillator with a mass fraction of a few %.

An inner balloon (IB) has been introduced in KamLAND. It is a 3.08 m diameter spherical balloon made of a 25  $\mu\text{m}$  thick transparent nylon film and suspended in the already existing device. An outer balloon (OB) surrounds the IB with 1 kton of liquid scintillator. The OB has a diameter of 13 m and is made of a 135  $\mu\text{m}$  thick nylon/EVOH film. The liquid scintillator in the OB is an active shield for  $\gamma$ 's and can also detect the internal radiation emitted from the IB or the Xe-loaded liquid scintillator. Buffer oil is placed in a stainless-steel containment tank (SST) 18 m diameter balloon and serves as an external shield. 1325 17" PMTs and 554 20" PMTs provide a 34 % solid angle coverage. The SST is surrounded by a 3.2 kton water-Cherenkov detector used as a veto. The energy resolution (FWHM) is about 6.5 % at 1 MeV and 4.1 % at the  $Q_{\beta\beta}$  value. A fiducial volume of 129 kg of  $^{136}\text{Xe}$  was defined for the analysis.

An unexpected background was observed in the  $0\nu\beta\beta$  energy region (see Figure 3.10). It appeared to be coming from a contamination in  $^{110\text{m}}\text{Ag}$  ( $T_{1/2} = 249$  d) from the Fukushima fall out in March 2011. Tests were performed around the detector and the production facilities showing the presence of this isotope in the detector premises.

No excess was observed in the region of interest, apart from the background coming from  $^{110\text{m}}\text{Ag}$ . The current half-life measurement results are:

$$T_{1/2}^{2\nu} = 2.30 \pm 0.02(\text{stat}) \pm 0.12(\text{syst}) \times 10^{21} \text{ y [63]}$$

$$T_{1/2}^{0\nu} > 1.9 \times 10^{25} \text{ y and } |m_{\beta\beta}| < 0.12 - 0.25 \text{ eV [64]}$$

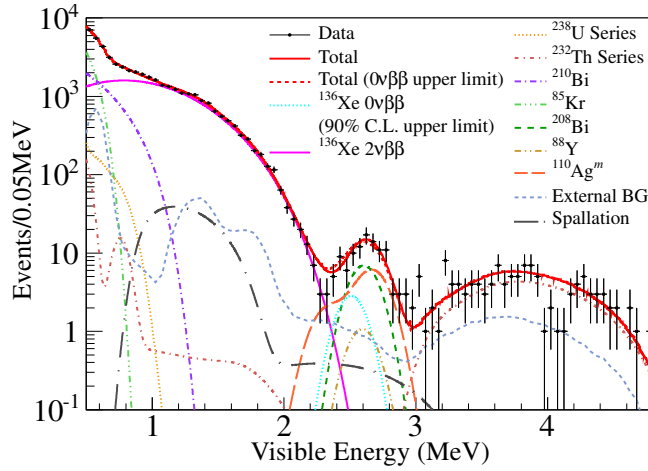


**Figure 3.10.:** Results of the 77 days data taking of the KamLAND-Zen experiment. Energy spectrum of  $\beta\beta$ -candidates together with the best-fit backgrounds, and the 90% C.L. upper limit for  $0\nu\beta\beta$ . The coincident  $\beta/\gamma$  events from  $^{208}\text{Tl}$  give the main contribution from 3 to 5 MeV. [62].

These results are in good agreement with the results of EXO-200. The limits set for the  $0\nu\beta\beta$  is slightly better for KamLAND-Zen but improvements are being performed on both experiments.

A second phase of the data taking started in December 2013 and scheduled to be completed by the end of 2015. The liquid scintillator and the xenon were purified before this second phase in order to remove  $^{110\text{m}}\text{Ag}$ . This rejection has been successful, with a reduction factor of 10 (see Figure 3.11). However an increase in the background coming from  $^{214}\text{Bi}$  has been observed leading to the definition of fiducial volumes. Figure 3.11 has been obtained with a fiducial volume corresponding to a sphere with a radius of 1 m in the centre of the IB. This selected a mass of approximately 88 kg of  $^{136}\text{Xe}$ .

A third phase is already planned and should start in 2016 with about 600 kg of Xe. Preliminary results combining the two phases of data taking provide an updated limit as no data excess was visible in the region of interest:

$$T_{1/2}^{0\nu} > 2.6 \times 10^{25} \text{ y @ 90 \% C.L. and } |m_{\beta\beta}| < 0.14 - 0.28 \text{ eV [63]}$$

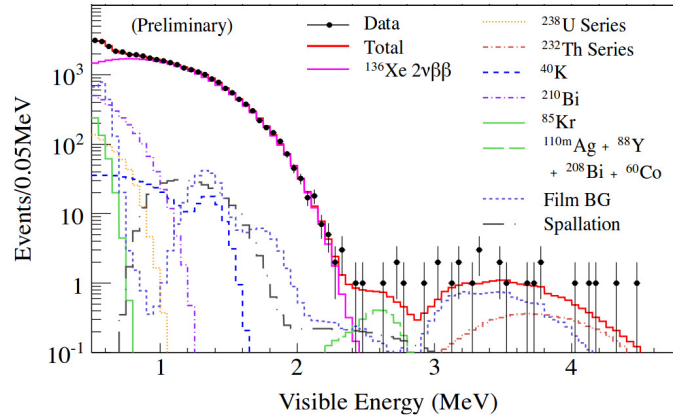


**Figure 3.11.:** *Preliminary energy spectrum of 115 days of data taking selected  $\beta\beta$  candidates within 1.0 m fiducial radius corresponding to 88 kg of  $^{136}\text{Xe}$ . A clear reduction of the  $^{110m}\text{Ag}$  background is visible in the region of interest [63].*

### 3.4.3. SNO+

The SNO+ experiment aims at building the world's largest liquid scintillator detector: the Sudbury Neutrino Observatory. SNOLAB is a 2 km deep underground laboratory inside Vale's Creighton nickel mine near Sudbury, Ontario, Canada. It is one of the deepest underground facility at 6000 m.w.e.

The detector is comprised of a 17.8 m suspended stainless steel frame forming the PSUP (PMT SUPport structure) equipped with 9500 8" PMTs. An acrylic vessel (AV) with a diameter of 12 m and made of 5.5 cm thick acrylic for a total volume of 907 m<sup>3</sup> is placed in the PSUP. The heavy water from SNO has been replaced for the SNO+ phase by a scintillating solution: LAB (Linear AlkylBenzene). The PMTs are located 3 m away from the scintillator in the acrylic vessel, which provides 1700 tonnes of shielding against external backgrounds. Outside the PSUP, 5700 tonnes of water play the role of shielding against the backgrounds coming from the rocks of the laboratory. The cavity where the detector is installed has also been lined with a radon-tight material. 780 tonnes of LAB scintillator will be installed combined with 2,5-adiphenyloxazol (PPO) as a wavelength shifter. LAB + PPO is a suitable scintillator for SNO+ due to its chemical compatibility with the acrylic vessel, the high light yield of about 10000 photons/MeV, the good optical transparency, the low scattering and the fast decay time. The levels of purification of the LAB are aiming at being similar to those reached by the Borexino experiment. To accomplish this purity the scintillating solution will be distilled during the filling of the detector.

This operation will need one to two months to complete the filling of the detector. The primary goal will be the search for  $0\nu\beta\beta$  of  $^{130}\text{Te}$  that be loaded in high quantities in the scintillator volume. The main background contributions to the search for  $0\nu\beta\beta$  with tellurium are  $^{208}\text{Tl}$  and  $^{212}\text{BiPo}$  pile-up from the  $^{232}\text{Th}$  chain and  $^{214}\text{Bi}$  from the  $^{238}\text{U}$  chain.

Several steps are already planned. The detector response and background will be studied using only liquid scintillator. After the pure liquid scintillator phase, natural tellurium at 0.3 % loading will be deployed in 2015.

Even if, as a liquid scintillator experiment, SNO+ will suffer from a relatively low energy resolution of 6.4 % at  $Q_{\beta\beta}$ , this may be compensated for by the high loading level, the low intrinsic background and background rejection techniques (such as fiducial volume definition). The SNO+ experiment initially investigated  $^{150}\text{Nd}$  as potential candidate. However, after a first internal suggestion in autumn 2011 and nearly two years of investigation and development, the collaboration has decided to focus on  $^{130}\text{Te}$ . This was mainly due to the difficulties in enriching a high mass of  $^{150}\text{Nd}$ .  $^{130}\text{Te}$  has a high isotopic abundance of 34.08% and a Q-value of 2.53 MeV. Its  $2\nu\beta\beta$  half-life of  $7.0 \times 10^{20}$  y is nearly a factor 100 longer than the  $^{150}\text{Nd}$  one, which will reduce the  $2\nu\beta\beta$  signal. In addition, the Te-loaded scintillator cocktail, in contrast with Nd, does not show any strong absorption line in the region where the PMTs are sensitive (350 nm - 550 nm).

A method for loading a relatively high concentration of tellurium in the liquid scintillator has been developed by the SNO+ collaboration. Loading up to 0.3% has been proven stable over one year. SNO+ is expected to reach a sensitivity to  $0\nu\beta\beta$  at a level lower than 0.1 eV. The expected energy spectrum for a 0.3% Te-loading, 2 years of running with a fiducial volume cut of 3.5 m in diameter is shown in Figure 3.12.

## 3.5. Tracker-Calorimeter: NEMO experiments

### 3.5.1. NEMO-3

The NEMO-3 experiment started on February 14<sup>th</sup>, 2003 and stopped on January 11<sup>th</sup>, 2011 in the *Laboratoire Souterrain de Modane* (LSM) in France. Several isotopes were measured simultaneously and the full kinematics of the decays could be

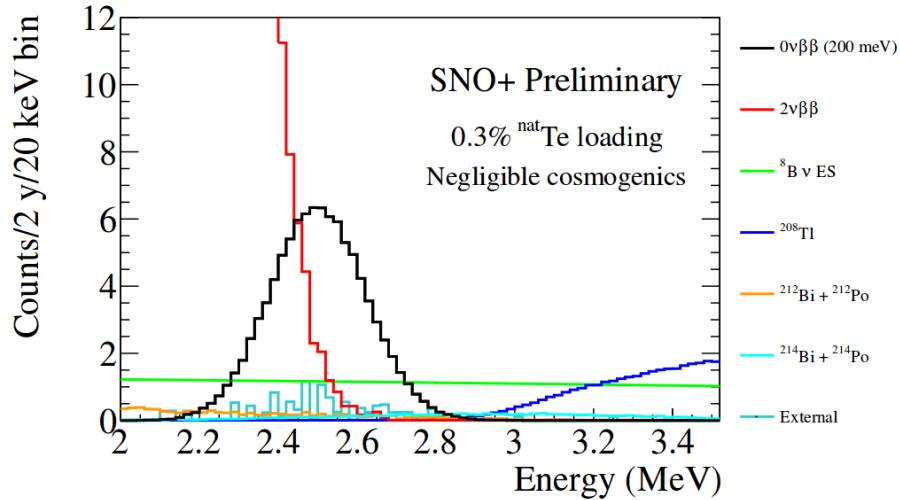


**Figure 3.12.:** *Expected energy spectrum for SNO+ after two years of running, a fiducial volume of 20% and 0.3% of Te-loading. The expected  $0\nu\beta\beta$  signal, assuming an effective Majorana neutrino mass of 200 meV, is shown for comparison.*

reconstructed. The  $\beta\beta$  isotopes were installed under the form of thin source foils. The calorimeter was made of plastic scintillators coupled to light guides and low radioactivity photomultiplier tubes of 5" and 3". Three dimensional tracks were reconstructed thanks to a vertical drift wire chamber. A magnetic field of 2.5 mT was applied over the whole tracking volume by a coil to distinguish electrons from positrons. The detector is described in details in Chapter 4.

Thanks to the depth of the LSM where NEMO-3 was installed, muon background is highly reduced. Different shielding of borated water and iron were used to avoid background from neutrons and external gammas. Very important constraints have been imposed for the radiopurity of the detector and especially for the source foils. The glass of NEMO-3 PMTs has been selected to have the lowest possible contamination but it is still the dominant contribution to the external background since it is located inside the detector shielding. One of the strength of the NEMO experiments is their capability to measure their own background using several control channels such as one electron events, one electron one  $\gamma$  events, crossing electrons, etc. For this reason, an estimation of the contribution of the different kinds of background for the double- $\beta$  decay events is possible.

After 7 years of  $0\nu\beta\beta$  searches, NEMO-3 has produced a lot of results: lower limits on the  $0\nu\beta\beta$  half life corresponding to upper limits on the neutrino mass, measure-

ment of  $T_{1/2}^{2\nu}$ . This was obtained for all of the 7 isotopes used in NEMO-3 and provided an unrivalled comprehension of the background for double- $\beta$  decay processes. Figure 3.13 shows the latest results obtained on the main isotope,  $^{100}\text{Mo}$ . For  $^{100}\text{Mo}$ , background simulations expected  $18.0 \pm 0.6$  events and 15 events have been observed in the  $[2.8, 3.2]$  MeV energy range. The total exposure was  $34.2 \text{ kg} \cdot \text{y}$  for a total mass of 6.9 kg. There is a good agreement between expected background and experimental results, and the final results are:

$$T_{1/2}^{0\nu} \geq 1.1 \times 10^{24} \text{ years and } |m_{\beta\beta}| \leq 0.3 - 0.9 \text{ eV [65].}$$

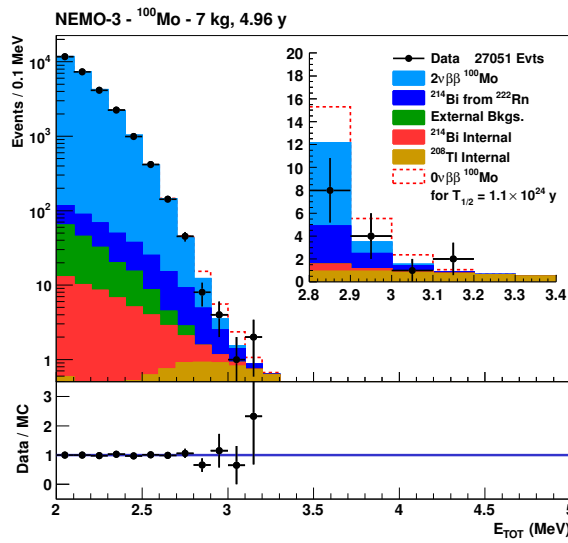


**Figure 3.13.:** Latest results of the NEMO-3 experiment on  $^{100}\text{Mo}$ . The dashed red line corresponds to the limit on  $0\nu\beta\beta$  [65].

For  $^{82}\text{Se}$ , with a total exposure of  $4.9 \text{ kg} \cdot \text{y}$  and a total mass of 0.9 kg, a limit on the  $0\nu\beta\beta$  half-life has been set at :

$$T_{1/2}^{0\nu} \geq 2.18 \times 10^{23} \text{ years, and } |m_{\beta\beta}| \leq 1.0 - 2.8 \text{ eV [66]}$$

### 3.5.2. SuperNEMO

The construction of the successor to NEMO-3, the experiment SuperNEMO, has begun as a first module (demonstrator) is under construction (see chapter 6). Even if the *modus operandi* is the same for NEMO-3 and SuperNEMO, numerous improvements are anticipated. Shielding is going to be installed in order to reduce the external background as was done in NEMO-3 (see Figure 3.14). 7 kg of  $^{82}\text{Se}$  will be measured in the demonstrator. More details will be given in Chapter 6.

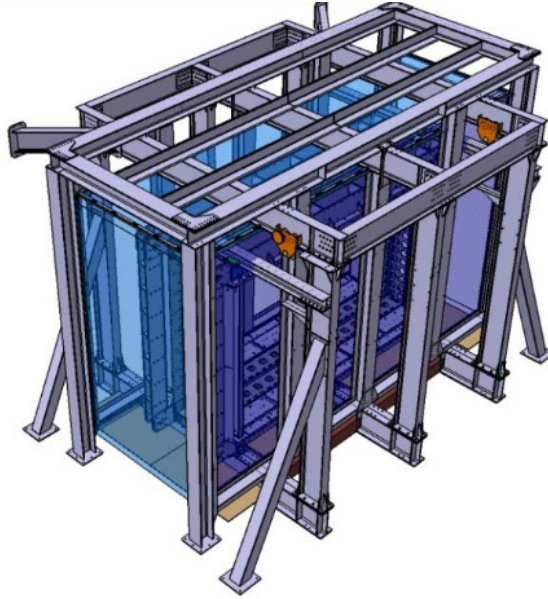


**Figure 3.14.:** *Schematic of the SuperNEMO demonstrator and the structure supporting the shielding.*

Several important aspects have been optimised in order to increase the half-life sensitivity. The goals of this improvement are displayed in table 3.1, mainly aiming at a global background reduction. First the mass of isotope has been increased from 10 kg to 100 kg. This increases the sensitivity of the experiment by increasing the potential number of  $0\nu\beta\beta$  events occurring in the detector. Then  $^{82}\text{Se}$  has been chosen because of its longer  $2\nu\beta\beta$  half-life compared to  $^{100}\text{Mo}$ . Given that  $2\nu\beta\beta$  is one of the main backgrounds for  $0\nu\beta\beta$ , this will contribute to the global background reduction. Another main point of refinement in SuperNEMO regards the contamination of source foils (internal background) and of radon contamination in the detector. Indeed these two backgrounds are responsible for most of the events in the region of interest. The level of radiopurity that must be achieved here is so challenging that dedicated detectors have been designed in order to measure the remaining contamination. Finally the energy resolution has been increased by a factor 2 thanks to the improvement of the calorimeter such as the use of 8" PMTs with a better quantum efficiency.

The expected sensitivity of SuperNEMO for  $^{82}\text{Se}$  is:

$$T_{1/2}^{0\nu} > 1.0 \times 10^{26} \text{ y @ 90 \% C.L. } |m_{\beta\beta}| < 0.040 - 0.10 \text{ eV}$$

	SuperNEMO	NEMO-3
Energy resolution	FWHM = 8% at 1 MeV	FWHM = 14% at 1 MeV
Isotope mass	100 kg	10 kg
Isotope	$^{82}\text{Se}$ , $^{150}\text{Nd}$	7 isotopes of which $^{100}\text{Mo}$ , $^{82}\text{Se}$
$^{208}\text{Tl}$ and $^{214}\text{Bi}$ contamination	$A(^{208}\text{Tl}) < 2 \mu\text{Bq/kg}$ $A(^{214}\text{Bi}) < 10 \mu\text{Bq/kg}$	$A(^{208}\text{Tl}) = 100 \mu\text{Bq/kg}$ $A(^{214}\text{Bi}) \sim 300 \mu\text{Bq/kg}$
Radon contamination	$\mathcal{A}(^{222}\text{Rn}) < 0.15 \text{ mBq/m}^3$	$\mathcal{A}(^{222}\text{Rn}) = 5 \text{ mBq/m}^3$

**Table 3.1.:** Comparison between NEMO-3 performance and SuperNEMO requirements

# Chapter 4.

## The NEMO-3 detector

*“Three things are to be looked to in a building: that it stand on the right spot; that it be securely founded; that it be successfully executed.” -*

Goethe

### 4.1. Introduction

NEMO-3 was a tracker-calorimeter detector designed to search for  $0\nu\beta\beta$ . Data taking started on February 14<sup>th</sup> 2003 and stopped on January 11<sup>th</sup> 2011.

The full kinematic reconstruction of two-electron events is one of the crucial and unique advantages of the NEMO technique. A  $\beta\beta$ -event is identified by two electrons coming from the same vertex in the source foil (see Figure 4.1). Three-dimensional tracks are reconstructed combining information coming from the different tracking cells. The magnetic field inside the tracker allows electrons to be distinguished from positrons via the track curvature. The  $e^-$  energies (individual and total) and their times of arrival are then measured in the segmented calorimeter.

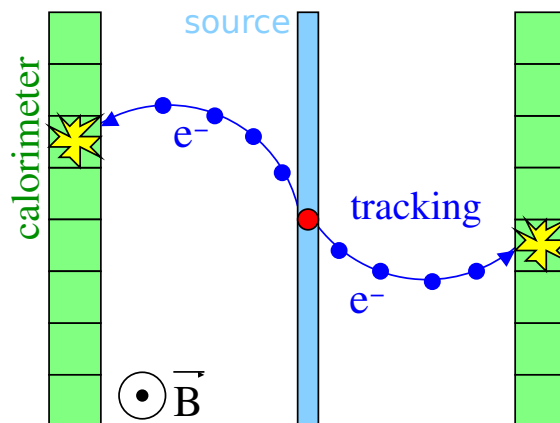


Figure 4.1.: Principle of the NEMO detection technique.

The detector is able to discriminate  $\gamma$ ,  $\alpha$ ,  $e^+$ ,  $e^-$  and  $\mu^\pm$ . First,  $e^+$  and  $e^-$  produce long tracks with a curvature due to the magnetic field. A  $\gamma$  particle will be seen as a hit in the calorimeter without any associated track. An  $\alpha$  particle coming from the source will only produce a short track and no calorimeter hit. Finally  $\mu^\pm$  are observed as a straight track as they are too energetic to be deflected by the magnetic field. They trigger two opposite calorimeter blocks, saturating the electronics with an energy  $> 12$  MeV.

## 4.2. Backgrounds to double-beta decay in NEMO-3

If it exists,  $0\nu\beta\beta$  is a very rare process. Therefore it is crucial to have the lowest background [67]. The most important background in NEMO-3 is due to several isotopes in natural radioactivity:  $^{232}\text{Th}$ ,  $^{235}\text{U}$ ,  $^{238}\text{U}$  and  $^{40}\text{K}$ . All of these elements have a lifetime greater than the age of the Earth implying they are still present in every material. For the first three, a decay chain exists but the natural abundance of  $^{235}\text{U}$  (0.72 %) and the decay times of the daughter nuclei in its decay chain are not high enough to constitute a background. In the decay chains of  $^{232}\text{Th}$  and  $^{238}\text{U}$ , a few isotopes represent the main backgrounds for NEMO-3 (see Figure 4.2).  $^{214}\text{Bi}$  and  $^{208}\text{Tl}$ , descending from  $^{238}\text{U}$  and  $^{232}\text{Th}$  respectively, are  $\beta\gamma$ -emitters with large Q-values ( $Q_\beta(^{214}\text{Bi}) = 3.27$  MeV and  $Q_\beta(^{208}\text{Tl}) = 4.992$  MeV).  $^{214}\text{Bi}$  and  $^{208}\text{Tl}$  also produce high-energy  $\gamma$ 's, the highest energy line in natural radioactivity at 2.615 MeV coming from  $^{208}\text{Tl}$ . It is therefore possible for these isotopes to contribute to the background above 3 MeV. This has to be compared to the energy of the  $0\nu\beta\beta$  line which is around 3 MeV, depending on the considered  $\beta\beta$ -isotope.

Radon exists in both the decay chains of  $^{238}\text{U}$  ( $^{222}\text{Rn}$ ) and  $^{232}\text{Th}$  ( $^{220}\text{Rn}$ ) with different half-lives:  $T_{1/2}(^{220}\text{Rn}) = 56$  s and  $T_{1/2}(^{222}\text{Rn}) = 3.8$  d. The short half-life of  $^{220}\text{Rn}$  prevents it from diffusing before it decays leaving  $^{222}\text{Rn}$  as the only problematic isotope for contaminations outside the detector. It is worth noting that radon itself does not directly contribute to the background. As it is a noble gas, it has the possibility to diffuse inside the tracking volume without any chemical interaction. Its daughter nuclei can deposit on every surface inside the detector (wires, foils, scintillators). As  $^{208}\text{Tl}$  and  $^{214}\text{Bi}$  are daughter nuclei of radon, it is a possible source of background from everywhere inside and outside the detector.

The so-called ‘‘BiPo’’ cascades are unique successions of decays existing in the two decay chains as will be explained in Chapter 7. They correspond to the emission

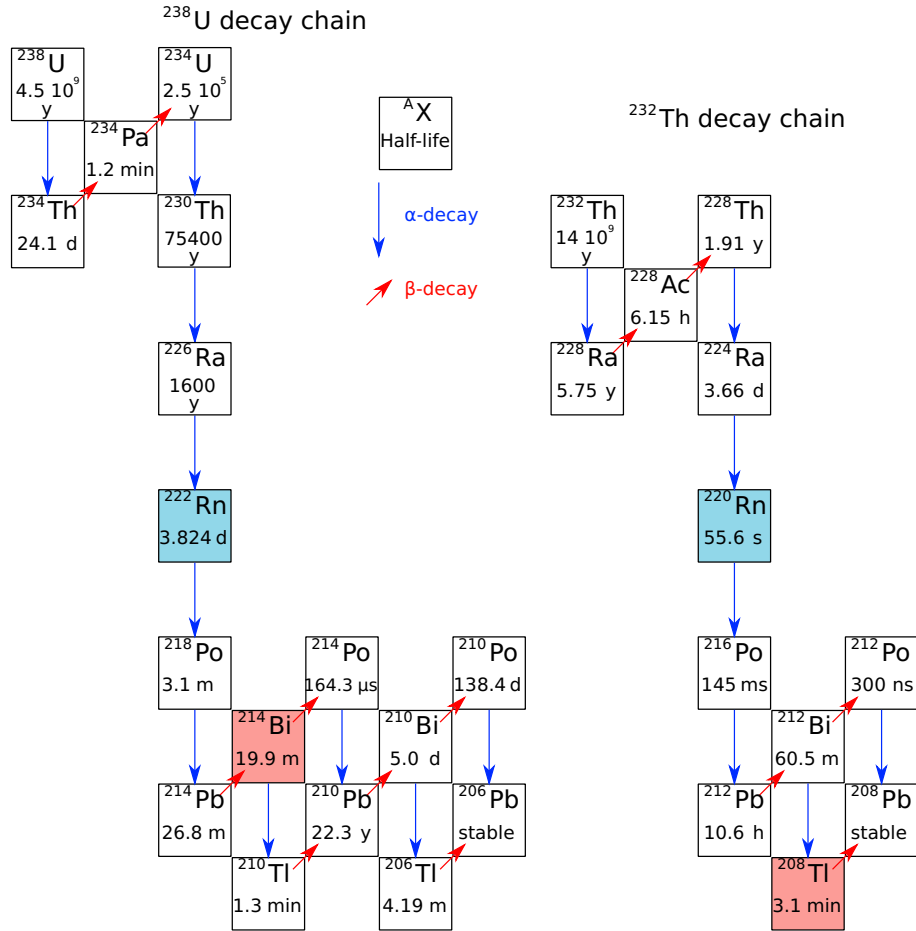


**Figure 4.2.:** Natural radioactivity chains of  $^{232}\text{Th}$  and  $^{238}\text{U}$  displaying in red the most important backgrounds for NEMO-3 and in blue the isotopes of radon.

of an  $e^-$  followed by a delayed  $\alpha$  with a characteristic time. Detecting these  $\alpha$ 's provides efficient rejection capabilities for  $^{214}\text{Bi}$  (see Chapter 5).

Two background origins can be identified. Any event from the source foil itself will be defined as *internal background*. Any other contribution will be referred to as *external background*. The time of flight (t.o.f.) measurement allows a distinction between these events (see Chapter 5).

When searching for  $0\nu\beta\beta$ , the high-energy tail of  $2\nu\beta\beta$  is a possible background. In an ideal detector, the fraction of  $2\nu\beta\beta$  events reconstructed in the  $0\nu\beta\beta$  energy region would be negligible. However in a detector such as NEMO-3, the energy resolution is not small enough. Internal backgrounds can mimic two-electron events

in three different ways, all of them starting with a single  $\beta$ -decay (see Figure 4.3). The second electron can be produced as follows:

- internal conversion of a de-excitation  $\gamma$  from the daughter nucleus;
- electron-electron scattering (Møller scattering) in the foil;
- nucleus de-excitation followed by a Compton scattering in the foil

In order to reduce internal contamination, every  $\beta\beta$  sources has been purified (see section 4.4.1) and their radiopurity was screened with HPGe.

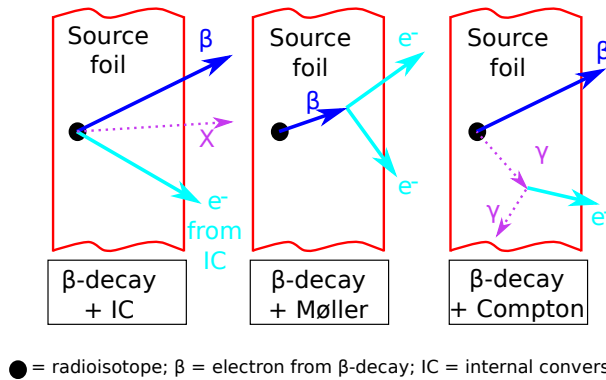


**Figure 4.3.:** *Internal background topologies in NEMO-3 [68]*

External  $\gamma$ 's can come from natural radioactivity outside the detector, from neutron captures and from any material inside the detector (mainly from PMT glass). Glass is naturally highly contaminated in uranium and thorium because it is made of silicon dioxide. Cosmic muons themselves are not a background given their topological signature in the detector. However they can produce neutrons through spallation reactions. Neutrons are also naturally emitted in the environment around the detector. They can produce  $\gamma$ 's with energies up to 10 MeV via radiative captures in the frame of the detector or its shielding, the PMT glass or the rocks surrounding the laboratory.

For these external backgrounds, three processes can give rise to the emission of two electrons from the source foil (see Figure 4.4). All of them are due to the interaction of an external  $\gamma$  inside the foil followed by:

- electron-positron pair creation by interaction of the photon in the foil, where the positron charge is misidentified;
- double Compton scattering in the foil close to each other;

- Compton scattering in the foil followed by a Møller scattering of the electron.

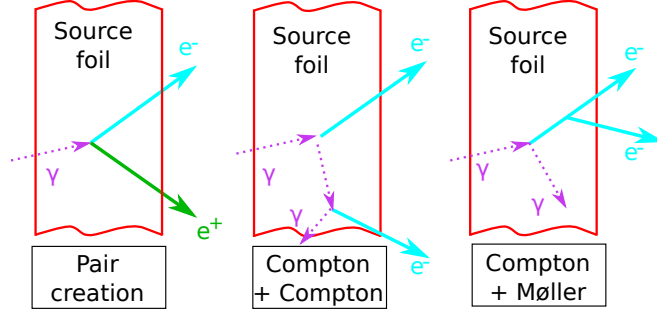


**Figure 4.4.:** *External background topologies in NEMO-3 [68]*

### 4.3. NEMO-3 at the LSM

Placing detectors underground provides shielding against cosmic rays. Additional shielding is required against external neutrons and  $\gamma$ 's. The material constituting the detectors also needs to be selected for its radiopurity. Radon (inside and outside) has to be carefully taken into consideration while designing the experiment.

#### 4.3.1. The *Laboratoire Souterrain de Modane*

The *Laboratoire Souterrain de Modane (LSM)* is an underground laboratory in the French Alps (see Figure 4.5). The cosmic-ray background at the LSM is reduced by a factor of about  $3 \times 10^6$  from  $10^7 \mu \cdot \text{m}^{-2} \cdot \text{d}^{-1}$  at sea level to only  $4 \mu \cdot \text{m}^{-2} \cdot \text{d}^{-1}$  thanks to 1700m of rocks or 4800 metres water equivalent (m.w.e.).

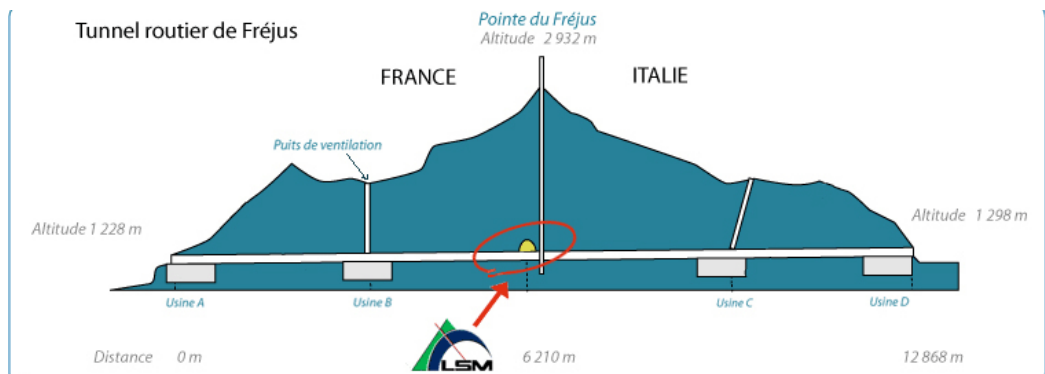


**Figure 4.5.:** *Location of the LSM in the Alps. The laboratory is located on the French-Italian border, under the Frejus peak (2932 m). Access is provided by the road tunnel joining Modane (Fr.) to Bardonecchia (It.).*

The neutron flux in the laboratory is about  $1 \times 10^{-6} \text{ neutron} \cdot \text{cm}^{-2} \cdot \text{s}^{-1}$ ,  $1 \times 10^5$  times lower than at sea level. The average level of radon is  $15 \text{ Bq/m}^3$  which is comparable to the level in open air. Thanks to this level of background, the NEMO-3 detector was installed at the LSM along with other detectors employed by the collaboration, like BiPo-1 and BiPo-2 (see Chapter 7) and HPGe.

### 4.3.2. Strategies to reduce background

The detector was shielded with 20 cm thick iron assembled in ten sections plus two end-caps for a total mass of 177 tons to reduce the  $\gamma$  flux entering the detector (see Figure 4.6). Neutrons are slowed down and captured by nuclei that have a high interaction cross-section with neutrons, such as boron. Ten borated water tanks 35 cm thick were put outside this iron shielding. Wood was used to reduce  $\gamma$  and neutron fluxes where water could not be safely placed (e.g. on top of the detector). Thanks to this shielding neutrons up to few MeV could be stopped.

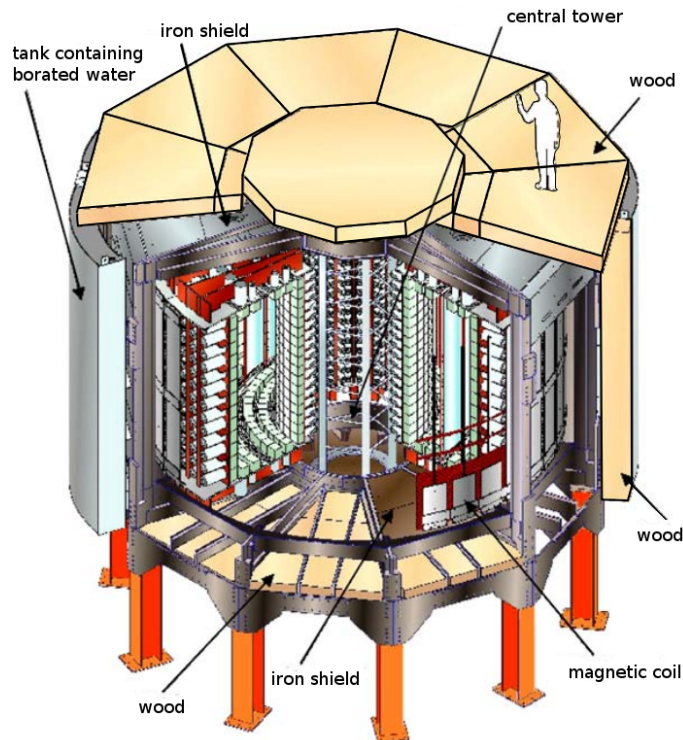


**Figure 4.6.:** *View of the NEMO-3 detector and its shielding.*

In order to control the detector intrinsic background, a  $\gamma$ -spectroscopy program of material selection was performed at the LSM with HPGe detectors according to their

contamination in  $^{214}\text{Bi}$ ,  $^{208}\text{Tl}$  and  $^{40}\text{K}$ . Studies in NEMO-2 proved that the glass of the PMTs (bulb and entrance window) are the dominant external background thanks to the external shielding [69]. A major effort was made on the selection of this glass.

The radon level is high in the laboratory, coming from rocks, although reduced to 10-20  $\text{Bq/m}^3$  by the ventilation systems. At the beginning of the data taking, the radon level inside the tracker volume was 10 times too high to meet the sensitivity requirements. A radon-free air factory was constructed to reduce it around the detector. It was made of 1 ton of active charcoal cooled down to  $-50\text{ }^\circ\text{C}$  and had flushing capabilities up to  $150\text{ m}^3/\text{h}$  for the detector operation. Combined with the low operation temperature, charcoal can efficiently adsorb radon.

An anti-radon tent was assembled (see Figure 4.7) to wrap the detector and was filled with radon-free air. Its ceiling was made of iron and its walls of 2 layers of  $200\text{ }\mu\text{m}$ -thick polyethylene. The tent was installed in September 2004 and significantly reduced the radon level. This made it necessary to define two phases in the analysis as the radon background was very different.

Thanks to the flushing, the activity went down from  $15\text{ Bq/m}^3$  to  $150\text{ mBq/m}^3$  inside the tent. In addition, the radon level decreased from  $37.7 \pm 0.1\text{ mBq/m}^3$  to  $6.46 \pm 0.02\text{ mBq/m}^3$  inside the tracking volume (only statistical errors [67]). This reduction factor of 6 inside the detector was not as high as the reduction factor observed in the anti-radon tent. The hypothesis is that both residual diffusion from outside and radon emanation from the detector were still significant.



**Figure 4.7.:** *View of the NEMO-3 detector and the anti-radon tent as it was in the LSM.*

## 4.4. Description of the NEMO-3 detector

The NEMO-3 detector was cylindrically shaped (see Figure 4.8), creating a continuous tracking detector for the 20 mechanically independent sectors. The detector had a radius of 2.5 m and was 3.1 m high. The sources occupied the centre of the sectors and consisted of 10 kg of  $\beta\beta$ -isotopes in total. The tracking system was made of 6180 drift cells operating in Geiger mode, providing three-dimensional reconstruction of the tracks of the particles. The calorimeter was comprised of 1940 scintillator blocks coupled to either 3" or 5" photomultiplier tubes (PMT).

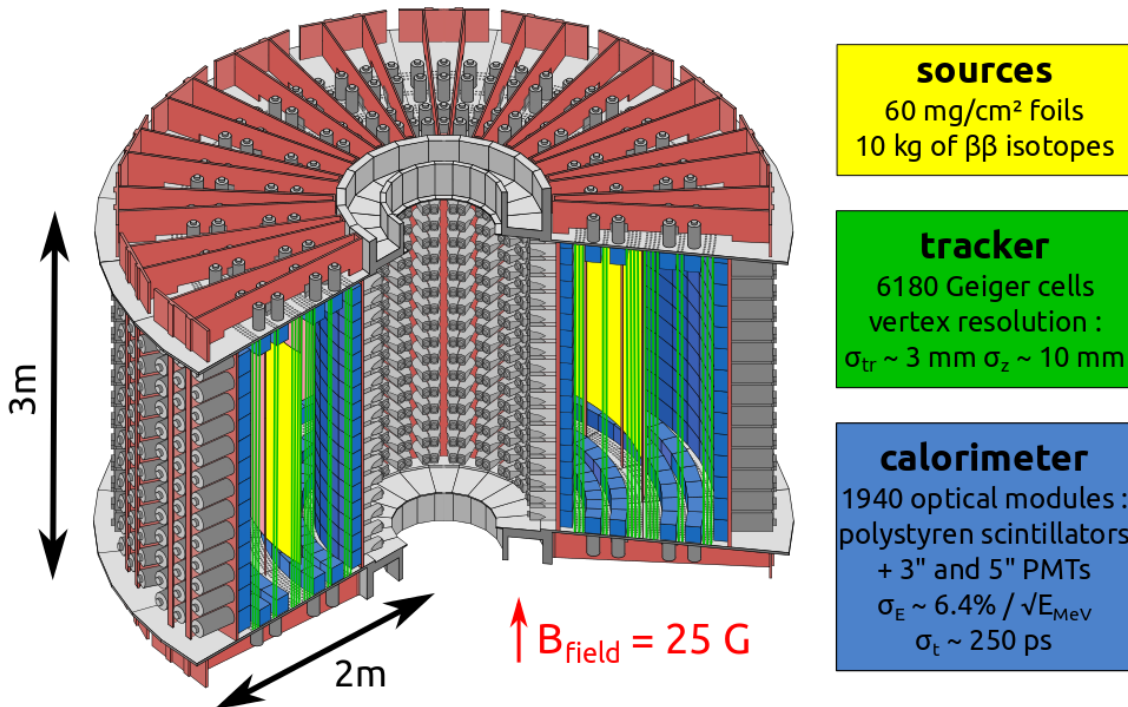


**Figure 4.8.:** Diagram of the NEMO-3 detector displaying the source foils, the tracker and the calorimeter.

### 4.4.1. Source foils

As opposed to most of other  $\beta\beta$ -decay experiments, the sources in NEMO-3 are independent from the detector itself. This allows different isotopes to be studied and a cross-check between the isotopes in case of a discovery. Having several isotopes also contributes to the background control. For instance, copper and natural tellurium have been installed where no  $0\nu\beta\beta$  is expected.

### Choice of isotopes for NEMO-3

Several criteria are defined for the selection of a suitable  $\beta\beta$ -isotope:

- The maximum energy available,  $Q_{\beta\beta}$ , should be larger than the energy of the 2.615 MeV  $\gamma$ -line of  $^{208}\text{Tl}$ ;
- $Q_{\beta\beta}$  should be larger than the  $Q_{\beta}$  of  $^{214}\text{Bi}$  at 3.27 MeV to reduce background in the  $0\nu\beta\beta$  energy range;
- The natural abundance should be high or the isotope should be easily enriched;
- The  $2\nu\beta\beta$  half-life has to be long in order to reduce the background coming from the high energy tail in the  $0\nu\beta\beta$  energy window. This is critical if the energy resolution is not good enough;
- The half-life of the  $0\nu\beta\beta$  process is inversely proportional to the square of the effective Majorana mass of the neutrinos, the phase space factor  $G^{0\nu}$  and the square of the nuclear matrix element  $M^{0\nu}$ . At a given effective Majorana mass, the higher  $G^{0\nu}$  and  $M^{0\nu}$ , the easier to observe  $0\nu\beta\beta$  (see equation (2.4)).

All of these properties could not be matched for the choice of the isotope in NEMO-3 and the best available isotopes have been investigated [70]. Seven isotopes were finally installed in NEMO-3 as presented in Table 4.1.

Isotope and transition	$Q_{\beta\beta}$ (keV)	Natural Abundance (%)	$T_{1/2}^{2\nu}$ (years)
$^{48}\text{Ca} \rightarrow ^{48}\text{Ti}$	$4271 \pm 4$	0.187	$4.4 \pm 0.6 \times 10^{19}$
$^{82}\text{Se} \rightarrow ^{82}\text{Kr}$	$2995 \pm 6$	9.2	$9.6 \pm 1.0 \times 10^{19}$
$^{96}\text{Zr} \rightarrow ^{96}\text{Mo}$	$3350 \pm 3$	2.8	$2.35 \pm 0.21 \times 10^{19}$
$^{100}\text{Mo} \rightarrow ^{100}\text{Ru}$	$3034 \pm 6$	9.63	$7.1 \pm 0.5 \times 10^{18}$
$^{116}\text{Cd} \rightarrow ^{116}\text{Sn}$	$2802 \pm 4$	7.49	$2.8 \pm 0.3 \times 10^{19}$
$^{130}\text{Te} \rightarrow ^{130}\text{Xe}$	$2529 \pm 4$	33.8	$7.0 \pm 1.4 \times 10^{20}$
$^{150}\text{Nd} \rightarrow ^{150}\text{Sm}$	$3367 \pm 2$	5.6	$9.0 \pm 0.7 \times 10^{18}$

**Table 4.1.:** Transition energy  $Q_{\beta\beta}$ , natural abundance and half-life of  $2\nu\beta\beta$  process for each isotope studied in NEMO-3.

The characteristics of the source strips for each NEMO-3 sector are displayed in Figure 4.9.  $^{100}\text{Mo}$  (6.9 kg) and  $^{82}\text{Se}$  (0.93 kg) are the isotopes of largest mass in NEMO-3 as they are relatively easy to enrich, have a high  $Q_{\beta\beta}$  value and their natural abundance is high.  $^{116}\text{Cd}$  (0.40 kg) also has a high natural abundance but its  $Q_{\beta\beta}$  value (2.8 MeV) is very close, regarding the energy resolution, to the 2.6 MeV line of  $^{208}\text{Tl}$ .  $^{96}\text{Zr}$  (9.43 g) and  $^{150}\text{Nd}$  (36.5 g) have a smaller abundance but their  $Q_{\beta\beta}$  values are higher than 3.27 MeV.  $^{48}\text{Ca}$  (6.99 g) was installed despite the very small mass available since it has a very high  $Q_{\beta\beta}$  (4.2 MeV). The small mass of the high  $Q_{\beta\beta}$  isotopes is due to the difficulty of enriching these isotopes.

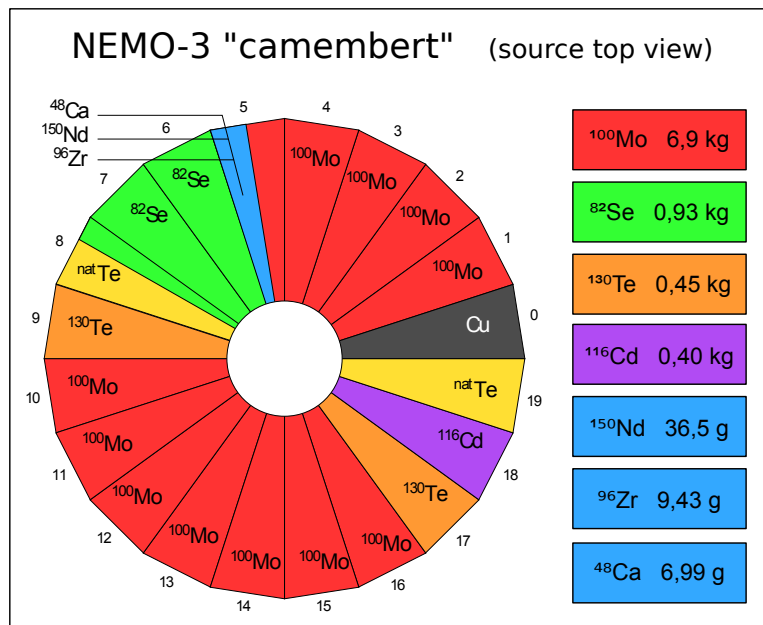


**Figure 4.9.:**  $\beta\beta$ -isotopes as they were installed in NEMO-3 sectors

### Enrichment, purification and production of the sources

The  $\beta\beta$ -isotopes measured in NEMO-3 have all been enriched. The general principle for enrichment is to produce a gas that is then centrifuged to separate the different isotopes. From these gas, a metallic powder can be produced (e.g.  $^{100}\text{Mo}$  and  $^{116}\text{Cd}$ ) or an oxide (e.g.  $^{96}\text{ZrO}_2$ ).

After the installation of the source foils in the detector, the internal background is irreducible requiring sources purification. A physical method was used consisting of the production of a monocrystal. During this process, the impurities migrate to the

edges and can be cut out. A chemical method was also employed aiming at breaking the secular equilibrium in the  $^{238}\text{U}$  and  $^{232}\text{Th}$  decay chains [71]. This method also allows  $^{226}\text{Ra}$  to be removed.

The final isotopic sources are thin foils with a density of 30-60 mg/cm<sup>2</sup>. The density has no impact on the sensitivity under about 60 mg/cm<sup>2</sup> as the calorimeter energy resolution is the limiting factor [68]. There were 7 strips 63-65 mm wide and 2.49 m high per sector. Two types of sources were realised depending on the isotope. Metallic foils were produced from a metal powder for  $^{116}\text{Cd}$  and part of the  $^{100}\text{Mo}$  after heating and rolling under vacuum. Composite foils, such as  $^{96}\text{Zr}$ , were made of sieved powder with grains smaller than 45  $\mu\text{m}$  mixed with ultra-pure water and a radiopure glue, PVA (PolyVinyl Alcohol) (see Figure 4.10). The mixture was placed in a 12  $\mu\text{m}$  thick plastic backing film, made of Mylar, which was irradiated with  $^{84}\text{Kr}$  ions to drill holes allowing the glue to dry. The sources were finally installed on a radiopure copper frame (see Figure 4.11).

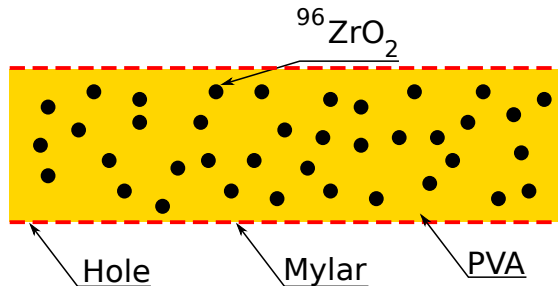


**Figure 4.10.:** Schematic of a  $^{96}\text{Zr}$  composite foil in NEMO-3. Holes were drilled in the Mylar to allow the PVA glue mixed with the  $^{96}\text{ZrO}_2$  powder to dry.

### The $^{96}\text{Zr}$ source foil in NEMO-3

There were two samples containing  $^{96}\text{Zr}$ , enriched at 57.3 %, in the NEMO-3 detector. The first one was used in the NEMO-2 detector and was produced at the ITEP in Russia. It was constituted of 4.1 g of  $^{96}\text{Zr}$ , had a total mass of 13.7 g and was 198.2  $\mu\text{m}$  thick. It was purified after its measurement in NEMO-2 as very localised contaminated regions (hotspots) were found [72].

The second sample was produced at the INR in Russia and contained 5.3 g of  $^{96}\text{Zr}$  for a total mass of 14.87 g and a thickness of 174.7  $\mu\text{m}$ . It was realised for NEMO-3.



**Figure 4.11.:** *One of the NEMO-3 sectors. The seven strips constituting the source foil can be seen as well as the copper frame they were installed on.*

These two samples were placed in one strip also containing nine disks of  $^{48}\text{Ca}$  and several layers of Mylar. This strip was installed in sector 5 along with other isotopes such as  $^{150}\text{Nd}$ . The ITEP sample was placed at the top above the INR one.

Figure 4.12 displays the vertices in the 1e channel (see Chapter 5). In this figure, the two samples are clearly visible, separated by an horizontal line used for the data analysis. It should be noted that the top sample shows less events than the bottom one. This will be associated to a much smaller contamination in  $^{40}\text{K}$  in this sample (see Chapter 5). The top and bottom limits of the samples have been defined close to the zirconium samples as they occupy the top of a strip and the  $^{48}\text{Ca}$  disks are right beneath them. The selections on the sides are not so strict in order not to reject events that would originate in the  $^{96}\text{Zr}$  samples but would not be accurately reconstructed due to the precision of the vertex reconstruction with the tracker.

#### 4.4.2. Tracker

The tracking system of the NEMO-3 detector was made of a vertical drift wire chamber. 6180 cells were installed, corresponding to 309 per sector or 39820 wires in

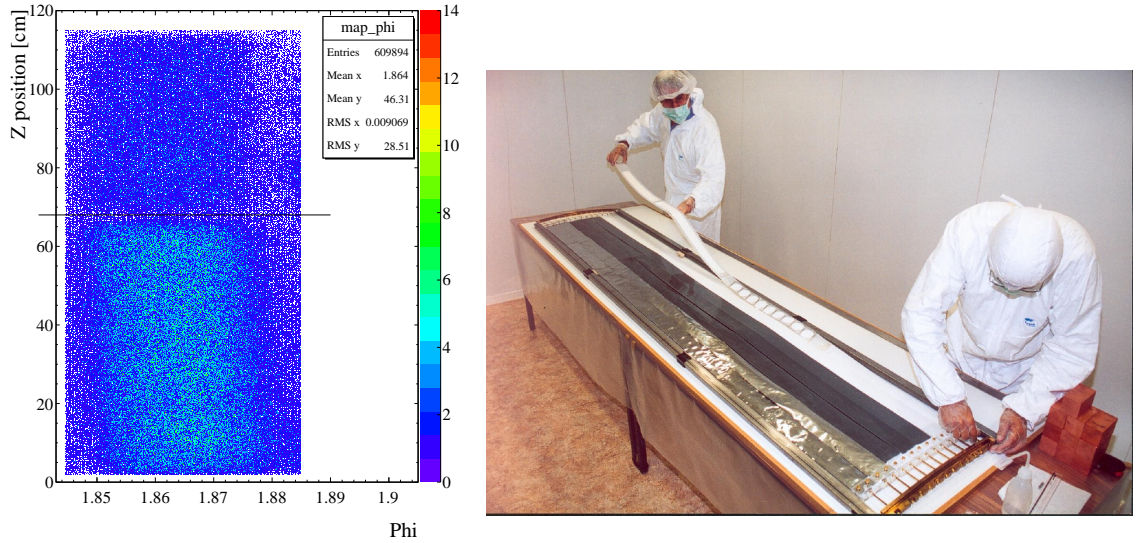


**Figure 4.12.:** *Left: Distribution of the vertices in the 1e channel in  $^{96}\text{Zr}$ . The two samples (INR at the top and ITEP at the bottom) have been separated along the black horizontal line. Right: Source frame for sector 5. The source holding  $^{96}\text{Zr}$  in which the  $^{48}\text{Ca}$  disks are also visible is being installed.*

total. The cells were operated in Geiger mode which simplified the tracker electronics compared to proportional mode [73]. All of the components of the tracker have been optimised to decrease the amount of material inside the detection volume.

### Drift Cells

The Geiger cells are octagonal with a diameter of 3 cm and 270 cm long (see Figure 4.13). They consist of an anode wire on which a high voltage of around 1600 V is applied. The outer part of the cells is made of nine grounded field wires. A copper cathode ring is installed at both ends surrounding the anode wire, both having a diameter of 2.3 cm, are 3 cm long and grounded. This creates an electric field allowing the detection of the arrival of the Geiger plasma. All of the wires are 50  $\mu\text{m}$  thick and made of a stainless steel selected for its radiopurity. The thickness of the wires is a compromise between the interaction probability of the particles (must be low) and mechanical constraints (must be strong enough).

A charged particle ionizes the gas it travels into as illustrated in Figure 4.13. On average an electron in helium creates 6 electron-ion pairs per cm it crosses, under NEMO-3 operating conditions of temperature and pressure. The electrons then

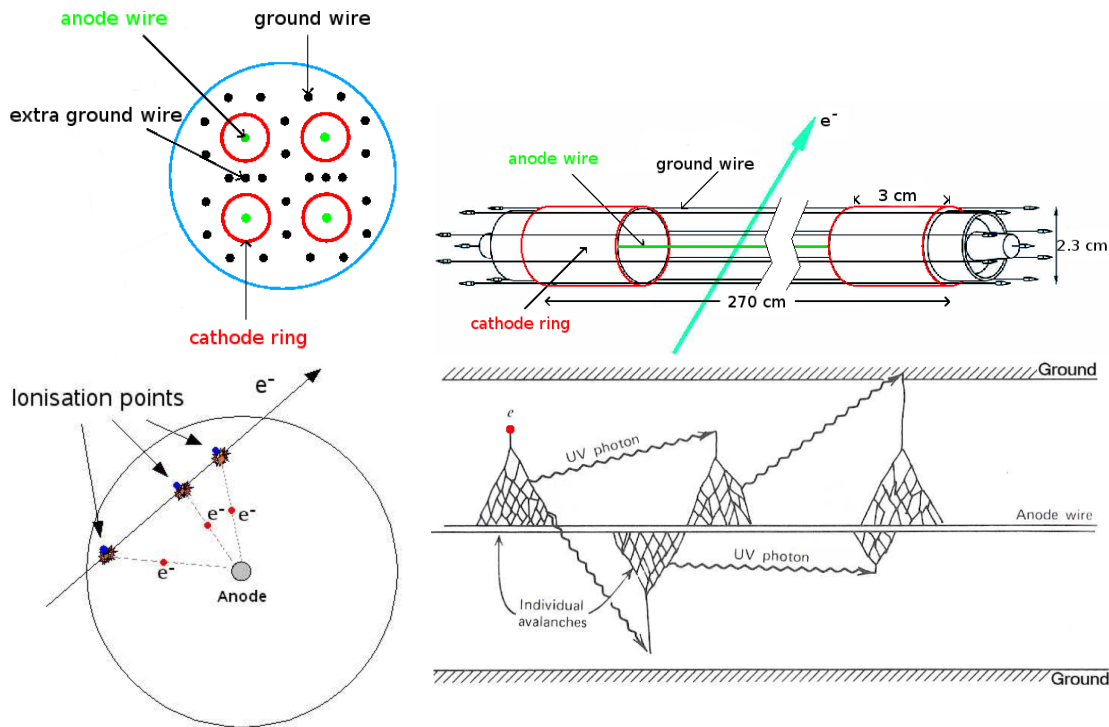


**Figure 4.13.:** *Top: Diagram of an elementary NEMO-3 Geiger cell. Bottom: Principle of a Geiger cell displaying transverse and longitudinal position reconstruction.*

travel toward the anode wire. Their speed increases from 1 to 2.3 cm/ $\mu$ s as they approach the wire. About 100  $\mu$ m away from the anode wire, secondary  $e^-$  are created because of the high electric field. These electrons will then create an avalanche producing more electrons and ions.

The primary avalanche also produces UV photons that in turn ionize the gas around the anode, creating photoelectrons generating further avalanches. In Geiger regime, the avalanche spreads along the anode wire and creates a plasma discharge propagating towards both extremities at a speed of around 5 cm/ $\mu$ s in the final gas mixture configuration (6-7 cm/ $\mu$ s without argon in the gas).

For each cell, three signals are detected, one coming from the anode wire and the other two from the cathode rings. The time difference between the cathode signals and the time difference between the anode and cathode signals provide the longitudinal position of the particle that triggered the cell with a resolution of 0.8 cm.

The transverse position comes from the measurement of the drift time of the ionisation towards the anode wire. It is performed by measuring the time difference

between the time of the hit in the calorimeter and that of the anode signal. The time for the electrons to travel from the closest ionisation point to the wire is measured to provide the circumference along whose tangent the particle passed. The resolution on the measured transverse position was 0.5 mm. A clustering of the hits in an event with a track reconstruction algorithm finally provides a three-dimensional track.

After a cell has been triggered there is a dead time of approximately 500  $\mu$ s. This corresponds to the time necessary for the gas around the wires to be neutralized. The trigger rate of the whole chamber of 6-7 Hz is dominated by single- $\beta$  decays.

Dust on a wire or a defect of its surface can stop the propagation of the plasma. Extremely clean conditions were needed when assembling the tracker and the wires were checked for defects while being unrolled.

### Gas in the tracker volume

The gas constituting the tracker volume was composed of helium (95 %), argon (1 %) and ethanol (4 %). Noble gases are a good medium in which the avalanche multiplication creating the plasma occurs at much lower fields than in others [74]. They are also used to avoid reactions with the material in the detector. Helium is a very transparent gas and has a low  $Z$  implying small energy losses. Many different particles can therefore be detected, including  $\alpha$ 's.

Ionizing the gas excites its atoms and produces UV photons. Quencher molecules, i.e. ethanol, are necessary to limit this process and their concentration allow the attenuation length of UV photons to be tuned to the size of a Geiger cell. Ethanol is an energy quencher at low energy (eV scale). It limits the photoionization and the triggering of the cells adjacent to the fired cell and neutralises helium ions which could produce new avalanches. Argon increases the gain (above  $10^6$  electrons per avalanche) since it has a smaller ionisation energy than helium.

### Configuration of the chamber

Nine cell layers in a 4-2-3 configuration (see Figure 4.14) constituted the NEMO-3 tracking device. The first four layers are close to the source foils and allow a precise vertex reconstruction (see Chapter 5). The two intermediate layers are designed to give a precise measurement of the track curvature. The last three layers are close to the scintillators to precisely reconstruct the impact point on the scintillator. This

enables a surface non-uniformity correction to be applied, since the light collection is lower if a particle enters the edges of the scintillator and not its centre.

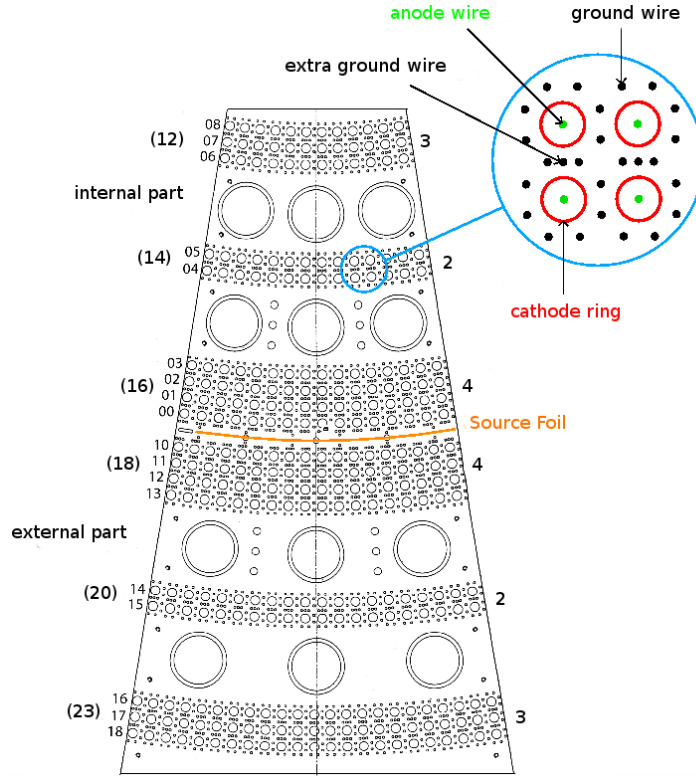


**Figure 4.14.:** Schematic of a petal of NEMO-3 displaying the positioning of the drift cells. The numbers in brackets on the left stand for the number of cells per layer, and on the right the number of cell layers.

## Magnetic field

In a  $\beta\beta$ -event, two tracks originate from the same vertex on the source foil.  $\gamma$ -rays emitted after a neutron capture produce  $e^+ e^-$  pairs. In order to reject these events, the tracking chamber is magnetised. A cylindrical coil generates a field of 25 G from a current of 29 A. The cylindrical coil weighs about 5 tons of which 3.1 tons are made of ultra-pure copper. In order to have a homogeneous field, backfield plates have been installed on the sides of the detector. The *petals* also play the role of backfield plates on top of the detector. In the magnetic field, electrons turn anti-clockwise from the source. Thanks to this, 95 % of  $e^+ e^-$  pairs are rejected at 3 MeV with better rejection at lower energies. Under this field, and considering the shortest track from the foil to the scintillators (55 cm), the maximum deviation of an electron of 3 MeV is close to 3 cm.

### 4.4.3. Calorimeter

1940 optical modules<sup>1</sup> constituted the calorimeter of the NEMO-3 detector. 3" PMTs with a flat photocathode were coupled to 1040 scintillator blocks. 5" PMTs with a hemispherical photocathode were coupled to 900 scintillator blocks. There were 97 optical modules per sector with 34 3" PMTs for the inner wall, 39 5" PMTs in three columns for the outer wall. 3 5" PMTs and 9 3" PMTs were on the top and bottom petals in 4 rows (see Figure 4.15).

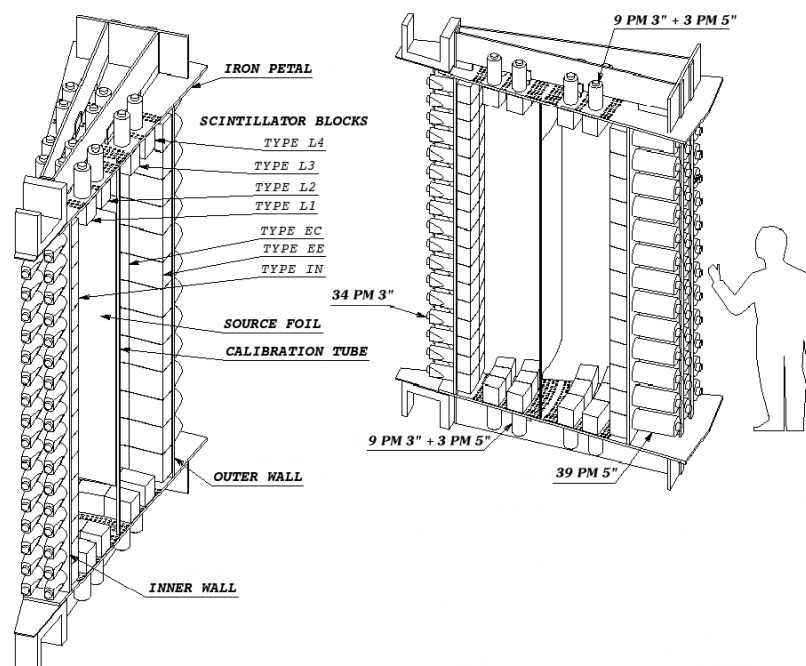


**Figure 4.15.:** Schematic of a NEMO-3 sector. The different types of scintillator blocks are presented in their respective positions.

A time resolution of about 250 ps at 1 MeV to be compared with the electron propagation time of a few ns and an average energy resolution of 16.5 % (FWHM) at 1 MeV for 3" PMTs and 13.7 % (FWHM) at 1 MeV for 5" PMTs were achieved.

### Scintillators

The scintillator blocks were made of polystyrene (PS) in which PTP (p-Terphenyl) and POPOP (1,4-di-(5-phenyl-2oxazolyl)benzene) were dissolved. This mixture was chosen for its short response time (few ns), its radiopurity and its low Z (3.7/atom

<sup>1</sup>An optical module is made of a scintillator, a light guide and a PMT.

on average). At an energy of around 3 MeV in PS, 2 cm are sufficient to contain an  $e^-$ . The small  $Z$  implies a small backscattering probability. The need for  $\gamma$  detection to reject some background requires at least a thickness of 10 cm to have a reasonable interaction probability. Even with this, it is only about 50 % at 500 keV.

The interaction of a particle in the scintillator excites its molecules. Scintillators re-emit incoming energy as an amount of light proportional to the deposited energy [75]. As the light emission happens within  $10^{-8}$  s, this process is called *fluorescence*. PTP is employed as a solid scintillating solution added to PS to convert the electron's energy deposition into scintillation light. POPOP is a wavelength shifter that re-emits the light in the most appropriate wavelength for the PMTs photocathode (maximum efficiency at 420 nm).

Because of their different sizes, the compositions of the blocks have been adapted for the main walls: 1.5 % of PTP and 0.01 % of POPOP and for the petals: 1.2 % of PTP and 0.05 % of POPOP. The blocks of the main walls were produced at INR and the petals were made in Kharkov. They were shaped according to the position they occupy in the detector and as shown in Figure 4.15, there were 7 different types.

Introducing part of the blocks inside the tracker volume reduced the energy loss as there is no extra material to cross for the particles before they enter the block. They can have a major impact on the background as they represent the most important part of the mass inside the drift chamber. Almost all of the walls were covered with scintillator blocks, except for the petals where the tracker cells were attached to the frame. This gave an almost full coverage of the volume surrounding the source foils.

The blocks were wrapped to increase light collection and to prevent UV light inside the scintillator from entering the tracking volume and triggering Geiger cells producing avalanches. The wrapping was made of 5 layers of 70  $\mu\text{m}$  thick Teflon combined with 2 layers of aluminised Mylar.

### Light guide and photomultiplier tube

The light guides were shaped to transfer light from the square scintillator blocks to the flat and spherical PMTs. They also isolate the tracker volume from the PMTs and prevent helium in the tracker from damaging the PMTs while altering their vacuum. The light guides are transparent at 98 % in [380, 420] nm, the maximum quantum efficiency range of the PMTs' photocathode. The light guides were glued

both to the scintillator blocks and the detector frame to ensure mechanical stability and good optical contact.

The PMTs were manufactured by Hamamatsu for NEMO-3 with a quantum efficiency (probability of an incoming photon to produce a photoelectron) of 20 % on average (with a maximum of 34 %). The high voltage to be applied on the PMTs was determined with a  $^{207}\text{Bi}$  source. Given the chosen gain for the PMTs and the dynamical range of the acquisition system, the maximum energy measurable was 12 MeV per optical module. The linearity has been proved to be better than 1 % up to 4 MeV. The PMTs installed in NEMO-3 were also chosen for their small dark rate and low counting rate (10 Hz at minimum threshold and 0.2 Hz above a 150 keV threshold). Hamamatsu produced PMTs with contamination 100 to 1000 times lower than standard PMTs. The radiopurity criteria for the PMTs selection were: 1.7 Bq/kg in  $^{40}\text{K}$ , 0.17 Bq/kg in  $^{208}\text{Tl}$  and 0.83 Bq/kg in  $^{214}\text{Bi}$ .

The PMTs were protected from the magnetic field by a mu-metal shielding, having a high permeability to magnetic fields. It therefore attracts the field lines and isolates the PMTs from the magnetic field.

### Calorimeter calibration and survey

**Qualification** All of the optical modules were qualified before their installation. The entrance face of the scintillator blocks was scanned with a  $^{90}\text{Sr}$  electron source based spectrometer. Thanks to this procedure, surface inhomogeneities were quantified and non-homogeneous blocks were rejected. This also allowed the “best” PMTs (good quantum efficiency and good electron collection) to be coupled to the “worst” scintillators (low light efficiency) in order to have a homogeneous energy resolution for the calorimeter.

*In situ*, a calibration procedure allowed the responses of the optical modules throughout the whole operation of NEMO-3 to be checked and corrected. Radioactive sources were inserted in the detector every month during one day ( $^{207}\text{Bi}$ ) or during long dedicated runs ( $^{90}\text{Sr}$ ). A laser survey was also regularly performed to correct PMT times and energies if necessary.

**Radioactive sources** Vertical calibration tubes made of copper with a section of  $24 \times 4 \text{ mm}^2$  were installed in all of the sectors. Three pairs of Kapton windows

were made in these tubes, each one in a pair oriented towards a calorimeter wall. They were vertically placed at -90, 0 and +90 cm for a uniform illumination of the detector. The radioactive sources were held by Delrin supports and inserted in these calibration tubes only for dedicated runs.

As all of the PMTs must have a common reference time, time calibrations with  $^{60}\text{Co}$  sources were chosen. This allowed differences in cables lengths, light guides, scintillator shape and PMT high voltage to be corrected.  $^{60}\text{Co}$  emits simultaneous  $\gamma$ 's of 1173 keV and 1332 keV. The time calibration of all of the optical modules was performed measuring the t.o.f. of these simultaneously emitted  $\gamma$ 's. They were done at the beginning and at the end of the running of the experiment.

For the energy calibration, two radioactive electron sources were necessary:  $^{207}\text{Bi}$  and  $^{90}\text{Sr}$ . In  $^{207}\text{Bi}$ , conversion electrons are emitted at 482 and 976 keV providing a calibration valid up to 1.5 MeV. Another electron line of  $^{207}\text{Bi}$  at 1682 keV was used to check the energy scale of the PMTs.  $^{90}\text{Y}$ , the daughter nucleus of  $^{90}\text{Sr}$ , has a  $\beta$ -spectrum with an end-point at 2.283 MeV. The fit of these three measurements provided a calibration for energies valid up to around 3 MeV. These calibrations allowed for an absolute energy calibration and the determination of the energy/ADC conversion factor.

Electrons only interact in 1 cm inside the blocks when  $\gamma$ 's can fully penetrate their volume. Therefore electron measurements are more sensitive to any inhomogeneity and have a smaller energy resolution compared to  $\gamma$ 's that can escape the block without depositing their entire energy. Hence, electron sources were necessary and the surface inhomogeneity was estimated to be about 2 % for 3" PMT and 10 % for 5" PMT coupled blocks.

**Laser survey system** The second part of the energy calibration developed for the NEMO-3 detector was a laser survey of the PMTs. A test of the PMTs gains was performed twice a day to check the stability of the energy scale between two  $^{207}\text{Bi}$  calibrations. This quantified the relative evolution of the gain of the PMTs with time. A laser correction was applied to the PMTs reference energy in case of a change in gain. Some PMTs were also rejected if there was an abrupt change in their gain. A complete test of the PMTs linearity response up to 12 MeV was also performed with the laser system.

6 reference blocks independent of the calorimeter were installed to compare  $^{207}\text{Bi}$  and laser spectra to provide an absolute measurement of the light intensity of the lasers. This was used as a reference for all of the optical modules of the calorimeter.

During calibration runs, laser tests were done every 2 hours. This allowed the gain of the PMTs to be corrected in a period of high activity inside the detector. More than 90 % of the PMTs were proven to have gain variations of less than 1 %.

#### 4.4.4. Electronics and acquisition system

The acquisition system of the NEMO-3 detector was made of two independent parts for the tracker and the calorimeter. The readout electronics, data acquisition and auxiliary trigger systems are inter-dependent of these two systems.

##### Trigger system

A three-level trigger was designed, with only two levels necessary for the data taking in  $\beta\beta$ -mode in the NEMO-3 detector. The first trigger level defined the minimum number of calorimeter hits to be recorded by the whole detector. At least one block was required to have a signal above 150 keV. The second level defined the minimum number of triggered tracker layers. At least three cell layers had to have recorded hits within the same half-sector. An extra condition required that two of these three layers belong to the same section of the tracker (see Figure 4.14).

The third trigger level was used when the running conditions were not appropriate for the  $\beta\beta$ -mode. It was designed for calibration runs to select  $e^-$  events coming from the radioactive calibration sources. It combined information from the second level with the calorimeter hit multiplicity at half-sector level.

##### Calorimeter electronics

The PMTs have been optimised for the linearity of their response at high current and their time resolution. Three PMTs are powered by one high voltage (HV) channel thus their gains have to be very similar (working HV lower than 80 V). Nine HV boards were necessary per sector each corresponding to four HV channels.

40 VME front-end mother boards were necessary, each of them associated to a half-sector. One front-end mother board was associated with 46 (for the inner part of a

sector) or 51 (for the outer part of a sector) daughter boards. The charge of the PMT pulse and the interaction time was collected by these individual daughter acquisition boards: the ANEMO boards. Two thresholds (low and high) were available for the ANEMO boards. A low threshold of 50 keV started the measurement. If the high threshold of 150 keV was passed, the time of the event is flagged.

The central trigger counts the number of triggers coming from the mother boards, one per PMT that passed the upper threshold. If the multiplicity level is reached (1 for the  $\beta\beta$ -mode) a signal is sent to the daughter boards. The charge of the counters involved in the events are then digitised and the acquisition of the TDC is stopped. The sampling performances of the NEMO-3 electronics provided an energy resolution of 3 keV/channel and a time resolution of 53 ps/channel. 200 ns after a PMT checked the high threshold condition, the system was reset.

### Tracking device electronics

Secondary voltage distribution cards supplied around 1600 V to the anode wires. These cards also collected anodes and cathodes signals. There were eight distribution cards per sector each associated with five sets of three daughters (one for each type of signal). Eight cells were connected per set of three daughter boards.

The acquisition boards amplified the signals and measured the times from the anode, the high and the low cathode. Eight of these were installed per sector with 40 cells per board. The signals were compared with the anode and cathode thresholds. If the thresholds were reached, the digital ASICs stored the TDCs. There were two possible time measurements with the TDCs. A window of 82  $\mu$ s was available for the anode and cathodes TDCs and a 2.6 ms window for the  $\alpha$  search. When the cathodes detected the Geiger plasma, the TDC was stopped and the times were stored. A resolution of 20 ns was achieved for the time measurement of the tracker.

# Chapter 5.

## Double- $\beta$ decay of $^{96}\text{Zr}$ with NEMO-3

*“Do not think about the goal, only think forward. Thus, by dint of thinking forward, you will reach or surpass your goals without even noticing.”* - B. Werber, La Révolution des Fourmis

### 5.1. Analysis techniques and reconstruction

The tracking and calorimetry capabilities of the NEMO-3 detector enables a good description of the backgrounds using control samples based on events topologies. Thanks to the comparison of data to Monte-Carlo simulations, a separate measurement of signal and backgrounds can be performed. In that way, double- $\beta$  decay can be studied in independent analysis channels.

#### 5.1.1. Simulations

The first step in the generation of GEANT-3.21 [76] Monte-Carlo simulations is the definition of the detector geometry and of the volumes in which decays can occur. Background can originate in many elements of the detector requiring the whole detector to be simulated to reproduce the processes of interest. The source foil is the most important, but others such as the surface of the foils, of the tracker wires, of the scintillators or the glass of the PMTs have also been simulated.

The standard DECAY0 package uses properties from nuclear databases to simulate isotopes and their energy levels or transition probabilities [77]. It produces primary

particles occurring in their decay and various processes such as double- $\beta$  decay or background processes ( $\alpha$  and  $\beta$ -decays) can be generated.

GEANT is then used to propagate the generated particles through the different volumes of the geometry. The results of their interactions with the detector (e.g. energy deposits in the calorimeter) are registered for comparison to data. In the next parts and if not specified, isotopes will be associated to a contamination of the source. Otherwise, their location will be specified as in: Mylar (plastic film around the  $^{96}\text{Zr}$ ), SFoil (surface of the source), SWire (surface of the tracker wires), SScint (surface of the scintillators) and PMTs. Table A.1 summarizes the contributions to the background with their locations and the available Monte-Carlo generated events.

The last part necessary for the simulations was the detector response. It implies to reproduce the behaviour of the different parts of the detector. The description of a particle crossing the tracker such as the distance from the anode wire and the tracking algorithm needs to be reproduced. The energy resolution and the correction of the scintillators surface non-uniformity have also to be applied to Monte-Carlo. The last part necessary for the simulations was the trigger (see section 4.4.4). The efficiency of this trigger, energy thresholds and time windows were simulated in order to accurately reproduce the behaviour of the detector.

### 5.1.2. Event reconstruction

Several algorithms are used for the reconstruction of data and Monte Carlo events. This allows raw data coming from the detector and from Monte-Carlo, such as the number and positions of triggered Geiger cells or the triggered calorimeter blocks, to be converted into physical observables.

The NEMO-3 database contains the properties and the running conditions of all of the elements of the detector throughout its operation. This enables criteria to be defined for the type of studied run, depending on the condition of the data taking.

#### Tracks

When a particle crosses the detector, several Geiger cells get a signal and can be clustered to construct a track. One of the important aspects of the reconstruction is the track fit. Two types of tracks are reconstructed in the NEMO-3 detector.

The first type is associated to electrons/positrons and are in time with a calorimeter hit. As previously stated, these tracks are curved by the magnetic field and connect the source foils to the calorimeter. A set of three helices is used to accurately fit the track. One of them fits the whole track providing a precise measurement of its curvature. The two others fit two half-tracks, one close to the scintillator and one close to the source foil. Precise measurements of the emission vertex and of the interaction point of the charged particles on the scintillators can therefore be performed. The vertex resolution is approximately 3 mm in the transverse plane and 10 mm in the longitudinal direction at 1 MeV. Another important parameter measured here is the length of the electron track  $l_e$ .

The second type corresponds to delayed tracks from  $\alpha$ -particles. These straight tracks are not associated to a calorimeter hit. They are fitted by a linear fit providing the length of the  $\alpha$  track.

## Energies

The measurement of the energy of the particles in the NEMO-3 detector is one of the most important reconstruction tasks. The charge of the PMT pulses is integrated and converted into an energy. This conversion is performed using the calibration parameters determined before the installation of the blocks in the calorimeter (see Chapter 4), checked during each  $^{207}\text{Bi}$  calibration and stored in the database.

Knowing the impact point of the electron on the surface of the scintillator allows the non-uniformity of the surface response to be accounted for and the energy measurement to be corrected. This cannot be performed for photons as their interaction point is not known. Therefore, the precision on the energy measurement of photons is smaller than for electrons. As a reminder, the energy resolution of the calorimeter is approximately 16.5% for 3" PMTs and 13.7% for 5" PMTs at 1 MeV.

## Times

The measurement of the arrival time of the particles in the calorimeter is essential for time of flight (t.o.f.) analyses (see section 5.1.4). The time measurement is performed when an energy measurement from a PMT reaches a low threshold around 50 keV. The time resolution of the calorimeter is of the order of 250 ps at 1 MeV and decreases with the energy.

### 5.1.3. Events selection

Specific properties have been identified for the three types of particles of interest, namely electrons,  $\gamma$ -particles and  $\alpha$ -particles. Figure 5.1 displays an event with each of these particles as detected by the NEMO-3 detector.

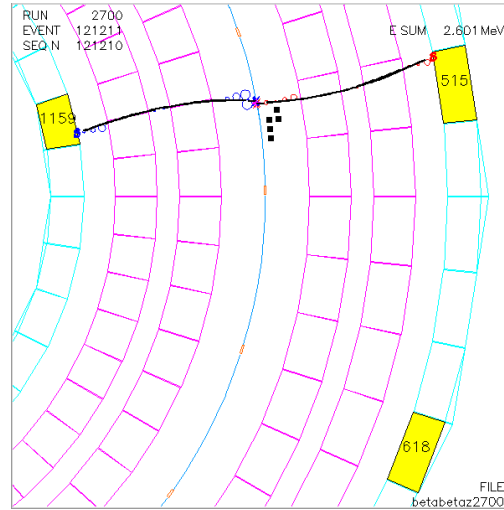


**Figure 5.1.:** *Example of a NEMO-3 event display. The two tracks correspond to two electrons. The squares correspond to delayed hits associated to an  $\alpha$ -particle. The energy deposit in the unassociated calorimeter hit (618 keV) is due to the interaction of a  $\gamma$ -particle.*

#### Selection of an electron

An electron is identified as a reconstructed track ending in a triggered calorimeter block. The curvature of the track is required to be negative, enabling 95 % of the tracks associated to a positron to be rejected.

Given its interaction with plastic scintillators and the wrapping of the blocks, an electron should deposit its energy in a unique calorimeter block. As a consequence the block must be *isolated*, i.e. no neighbouring calorimeter block should have measured a significant energy.

In order to have a correct estimation of the t.o.f. of the electrons, a lower cut at 200 keV is applied on their energy.

These criteria will be completed in the individual analysis channels by a specific set of cuts.

### Selection of a $\gamma$ -particle

$\gamma$ -particles do not produce a track in the detector but only an energy deposit in the calorimeter. Therefore the detection capabilities of NEMO-3 are as good as the calorimeter is efficient to detect them (around 50 %). It is however difficult to distinguish very low-energy  $\gamma$ -particles from the noise coming from PMTs or from the electronics. This made it necessary to apply lower energy cuts for the selection of energy deposits associated to  $\gamma$ 's. In most of the analysis channels a lower energy cut of 150 keV has been made to reconstruct a  $\gamma$ -particle. Due to the need to use low-energy  $\gamma$ 's for excited states, this constraint has been lowered to 100 keV in this search and further criteria have been applied for background rejection.

A  $\gamma$ -particle is able to interact in several locations inside the detector. A clustering algorithm is employed to treat  $\gamma$ -candidates. This algorithm takes into consideration the potential interactions of a  $\gamma$ -particle in several neighbouring blocks. A condition for a calorimeter block to be considered as part of a  $\gamma$  cluster is that it is not associated to a track. So far only a clustering in position has been developed and no clustering in time was available. It is worth noting that some developments have been made on a time-clustering algorithm [78] and are still under development for the SuperNEMO experiment.

### Selection of an $\alpha$ -particle

The possibility to detect  $\alpha$ -particles as short straight tracks gives a handle on the measurement of the radon background. As will be explained in section 5.3.2, delayed  $\alpha$ -particles are searched for within a time window of several times the half-life of  $^{214}\text{Po}$ . Given the high ionisation potential of  $\alpha$ 's, their tracks do not reach the calorimeter when originating from the source due to too small a mean free path. Therefore no energy measurement from the calorimeter is available.

#### 5.1.4. Time of flight Analysis

Electrons and  $\gamma$ 's t.o.f. measurement is another essential strength of the NEMO technique. It allows internal and external events to be identified, and has a very high rejection power for external backgrounds. However, it is worth noting that this cannot distinguish internal background events from double- $\beta$  events.

There is no direct way of measuring the exact time of a decay in the detector as the source foil is passive. The only time available is the trigger time of the calorimeter. From the energy of the electron measured in the calorimeter, it is possible to extrapolate the decay time. The relativistic properties of the electron are defined in equation 5.1.

$$\beta = \sqrt{1 - \frac{1}{\gamma^2}} \quad \text{where} \quad \gamma = \frac{E_{tot}}{m_e} = \frac{E + m_e}{m_e} \quad (5.1)$$

Thanks to this, the t.o.f. of the electron can be defined as equation 5.2.

$$t_{e,tof} = \frac{l_e}{\beta_e c} \quad (5.2)$$

The length  $l_e$  of the electron track is obtained at the reconstruction level (see section 5.1.2). The path length for electrons is precisely known therefore the error on  $l_e$  is very small. The error on the theoretical electron t.o.f. is dominated by the error on the energy. Given that  $\beta$  depends on the energy, the error can be written as:

$$\sigma_{t_{e,tof}}^2 = \left( \frac{l_e}{\beta_e c} \right)^2 \times \left( \frac{\sigma_{\beta_e}}{\beta_e} \right)^2 \quad (5.3)$$

The internal (2 electrons from the source) and external (a single electron crossing the detector) possibilities for a two-track events are illustrated in Figure 5.2.

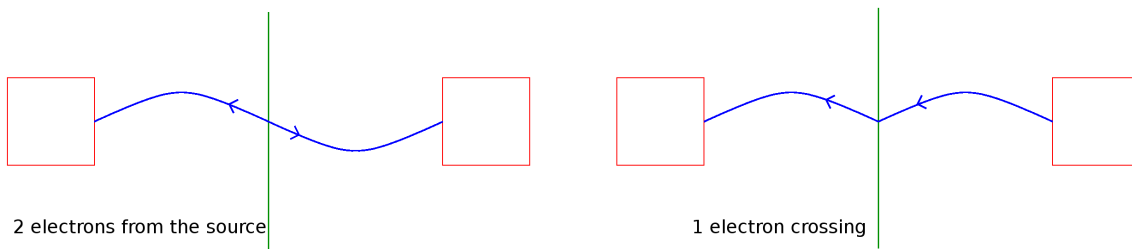


**Figure 5.2.:** *Left: double- $\beta$  event with two electrons originating from the source, the curvatures are both negative. Right: one electron originating from the calorimeter, the curvatures are opposite on the two sides of the source (in green).*

$\Delta t_{int}$  is the time difference between the two particles assuming they were emitted from the source foil and  $\Delta t_{ext}$  if they have an external origin. Figure 5.3 displays

$\Delta t_{ext}$  as a function of  $\Delta t_{int}$  for two-electron events (left) and 1 electron and 1  $\gamma$  events (right). Three populations are visible in this Figure for two-electron events. One of them is centred around 0 for the internal time difference and -5 ns for the external time difference. These events are real internal events such as double- $\beta$  events. The two other distributions are centred around  $\pm 5$  ns for the internal time difference and in 0 for the external time difference. These events have a time difference compatible with an external hypothesis. An important point to be noted is that these distributions are well separated. This will enable cuts to be performed in order to reject external events. The distributions are not as well defined for 1 electron and 1  $\gamma$  events due to larger uncertainties on the time measurement for  $\gamma$ 's.

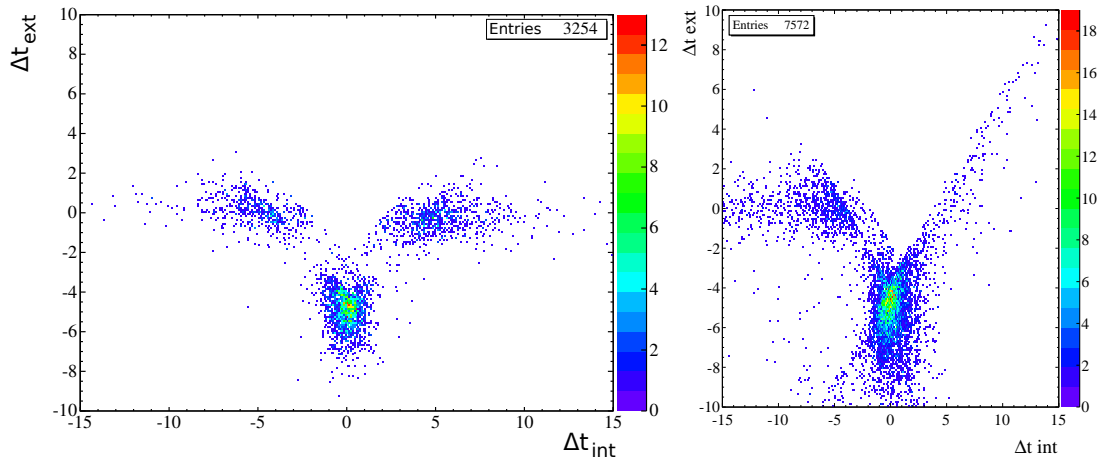


**Figure 5.3.:** Time differences between the measured time and the expected time. On the  $x$  axis in the internal scenario and on the  $y$  axis in the external scenario. Left: 2-electron events, Right: 1 electron 1  $\gamma$  events.

The same method is used to determine whether a  $\gamma$  particle was emitted in the foil or if an external  $\gamma$ -particle interacted first in a scintillator before producing a Compton electron in the foil. As it is impossible to track them, their path length is considered to be the straight-line distance between the reconstructed electron vertex on the source foil  $(x_{vert}, y_{vert}, z_{vert})$  and the centre of the unassociated calorimeter block that was triggered  $(x_{calo}, y_{calo}, z_{calo})$  and is defined as in equation 5.4.

$$l_{\gamma} = \sqrt{(x_{calo} - x_{vert})^2 + (y_{calo} - y_{vert})^2 + (z_{calo} - z_{vert})^2} \quad (5.4)$$

The interaction point inside the block is not known for  $\gamma$ 's, therefore their total path length is not known as precisely as for electrons. An extra time, named  $t_{scint}$ ,

is added to take into account the interaction depth of the  $\gamma$  inside the block. It depends on the block type and on the energy of the  $\gamma$ . It has been optimised along with its error on calibration data [79].

The t.o.f. of a  $\gamma$ -particle can be defined as in 5.5.

$$t_{\gamma,tof} = \frac{l_{\gamma}}{c} + t_{scint} \quad (5.5)$$

with its corresponding uncertainty:

$$\sigma_{t_{\gamma,tof}} = \sigma_{t_{scint}} \quad (5.6)$$

As for the two-electron case, the measured and theoretical time differences in a given hypothesis between the two particles are compared in order to determine if a  $\gamma$ -particle is internal or external. The correct hypothesis has been made if these time differences are close to each other.

A  $\chi^2$  method allows the most probable scenario to be defined with a  $\chi^2$  defined in equation 5.7.  $\Delta t_{meas}$  corresponds to the difference between the times measured by the calorimeter.  $\Delta t_{tof}$  is the difference in the expected arrival times from relativistic calculations, in a given time hypothesis (internal or external). The measured errors come from the error on the time measurement of the calorimeter, known for each optical module. The theoretical t.o.f. errors account for the error on the electrons energy measurement and on the path lengths.

$$\chi_{hyp}^2 = \frac{(\Delta t_{meas} - \Delta t_{tof})_{hyp}^2}{\sigma_{t_{meas}}^2 + \sigma_{t_{tof}}^2} \quad (5.7)$$

In the case of a 1 electron and 1  $\gamma$  event, the internal hypothesis can be written as in equation 5.8.

$$\chi_{int,e-\gamma}^2 = \frac{[(t_{\gamma,meas} - t_{\gamma,tof}) - (t_{e,meas} - t_{e,tof})]^2}{\sigma_{t_{\gamma,meas}}^2 + \sigma_{t_{\gamma,tof}}^2 + \sigma_{t_{e,meas}}^2 + \sigma_{t_{e,tof}}^2} \quad (5.8)$$

The external hypothesis can be written as in equation 5.9.

$$\chi_{ext,e-\gamma}^2 = \frac{[|t_{\gamma}^{meas} - t_e^{meas}| - (t_{\gamma,tof} + t_{e,tof})]^2}{\sigma_{t_{\gamma,meas}}^2 + \sigma_{t_{\gamma,tof}}^2 + \sigma_{t_{e,meas}}^2 + \sigma_{t_{e,tof}}^2} \quad (5.9)$$

In the same way,  $\chi^2$  can be written for a two-electron event for internal and external hypotheses.

Probabilities are derived from  $\chi^2$  computations. Figure 5.4 illustrating the logarithm of the  $\chi^2$  probabilities in the two hypothesis displays two different distributions, the vertical one corresponding to internal events. The standard cuts that are applied for the t.o.f. for internal events are:

- P(int) has to be greater than 4%
- P(ext) has to be less than 1%

These cuts are reversed for external events and other events are rejected.

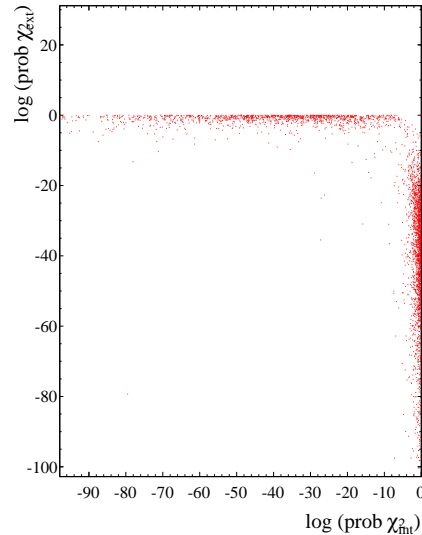


**Figure 5.4.:** *Logarithm of the external hypothesis  $\chi^2$  probability as a function of the internal hypothesis  $\chi^2$  probability for 2 electrons events. The horizontal distribution corresponds to external events, the vertical one to internal events.*

### 5.1.5. Data Analysis

Each channel for the NEMO-3 analysis is associated to a specific topology and allows a precise measurement of part of the contribution to background or signal. Data are fitted with Monte-Carlo simulations using a binned likelihood method. The best agreement between the histograms containing data and the sum of the backgrounds is used to set the activities of the different contributions. A  $1\sigma$  error from this fit is used as the uncertainty on these activities.

#### Likelihood method

The background model is supposed to be a good description of the data with only unknown scaling factors for each contribution. The binned likelihood method used here consists of maximising the likelihood to determine these scaling factors.

The probability  $p_i$  of observing  $n_i$  data events in bin number  $i$  when  $\theta_i$  events are expected in Monte-Carlo obeys a Poisson distribution such as :

$$p_i = \frac{\theta_i^{n_i} \times e^{-\theta_i}}{n_i!} \quad (5.10)$$

The likelihood is defined here as the product of the probabilities for each bin:

$$L = \prod_i p_i \quad (5.11)$$

Since the logarithm is a monotonically increasing function, maximising the likelihood is equivalent to maximising its logarithm in order to obtain the best Monte-Carlo to data agreement. One gets:

$$\ln L = \sum_i (n_i \times \ln(\theta_i)) - \sum_i \theta_i - \sum_i \ln(n_i!) \quad (5.12)$$

The logarithm of the likelihood is maximised as a function of  $\theta_i$  using the TMinuit package [80] from ROOT. This tool provides the best fitting set of scaling factors for each of the contributions, signal and/or backgrounds. A statistical uncertainty of one standard deviation is defined as the interval around the best fit in which the logarithm of the likelihood decreases by a maximum of 0.5.

### Limit setting

A limit has to be set on the signal strength when no significant amount of data allow a measurement. This will be used in this work for  $0\nu\beta\beta$  and  $2\nu\beta\beta$  to excited states.

The upper limits in this work have been obtained using Feldman-Cousins confidence intervals. It allows to define a number of excluded signal events at 90 % C.L. [81].

Another method has been employed, based on NLLR (negative log-likelihood ratio). It is built by taking the logarithm of the ratio of the likelihoods in the *signal plus background* hypothesis over the *background only* hypothesis:

$$Q(n) = -2 \ln \frac{L_{s+b}}{L_b} = 2 \sum_i \left( s_i - n_i \ln \left( 1 + \frac{s_i}{b_i} \right) \right) \quad (5.13)$$

where  $s_i$  is the number of predicted signal events,  $b_i$  the number of expected background events and  $n_i$  the number of observed data events.

With a large number of observed events, the NLLR follows a  $\chi^2$  distribution but this is not the case for small numbers as observed in this work [82] (see Figure 5.5). In our case, the distributions of the NLLR for both hypotheses are obtained by generating a large amount of pseudo-experiments and substituting  $n_i$  in the definition of the NLLR. For each hypothesis, a confidence level can be obtained considering situations where the NLLR  $Q$  would be larger for the *signal plus background* hypothesis:

$$CL_{s+b} = P_{s+b}(Q > Q(n)) = \int_{Q(n)}^{\infty} \frac{\partial P_{s+b}}{\partial Q} dQ \quad (5.14)$$

and for the *background only* hypothesis:

$$CL_b = P_b(Q > Q(n)) = \int_{Q(n)}^{\infty} \frac{\partial P_b}{\partial Q} dQ \quad (5.15)$$

From these definitions, the confidence level on the signal is defined as:

$$CL_s = \frac{CL_{s+b}}{CL_b} \quad (5.16)$$

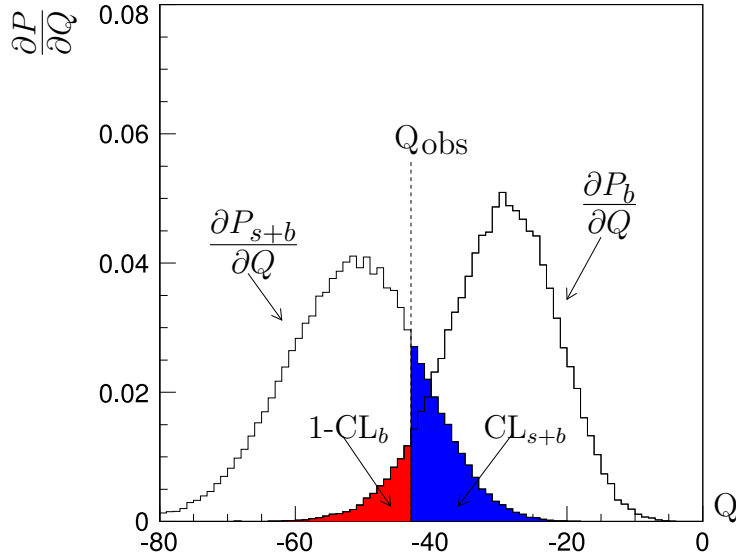


**Figure 5.5.:** Example of NLLR distributions for background only and signal plus background hypotheses.  $1-CL_b$  and  $CL_{s+b}$  are shown as colored areas. Adapted from [66].

and a limit on the signal strength at 90 % C.L. can be determined for  $CL_s = 10\%$ . If specified, the limits reported in this thesis have been obtained with ROOT TLimit package [83].

### Half-life measurement

As for every nuclear decay, double- $\beta$  decay obeys a radioactive decay law. The half-life  $T_{1/2}$  can be obtained from equation 5.17 where  $N_{obs}$  is the number of observed events,  $\mathcal{E}$  is the efficiency of the process,  $m_{^{96}\text{Zr}}$  is the isotope mass,  $N_A$  is Avogadro's constant and  $M_{^{96}\text{Zr}}$  is the isotope atomic mass.

$$N_{obs} = \frac{\mathcal{E} \times m_{^{96}\text{Zr}} \times N_A}{M_{^{96}\text{Zr}}} \left[ 1 - \exp\left(-\ln 2 \times \frac{t_{observation}}{T_{1/2}}\right) \right] \quad (5.17)$$

Given the very rare processes studied in double- $\beta$  decay experiments, equation 5.17 can be simplified since  $T_{1/2}$  is large. After reversing this equation, the half-life of the process can be obtained as in equation 5.18.

$$T_{1/2} = \frac{\mathcal{E} \times \ln 2 \times m_{^{96}\text{Zr}} \times N_A \times t_{\text{observation}}}{M_{^{96}\text{Zr}} \times N_{\text{obs}}} \quad (5.18)$$

## 5.2. Analysis context

### 5.2.1. NEMO-3 data sets

The NEMO-3 detector operated during almost 8 years. Due to various operations such as calibrations or technical stops, the whole time is not available for data analysis. The acquisition system splits the measurement time in runs. Several status of runs define the behaviour of the detector throughout its operation. So-called *standard runs* have been considered in this analysis. They contain all of the runs when the detector was fully operational and stable, and in addition some runs in which part of the detector was turned off.

As already mentioned in Chapter 4, two phases have been defined in the data analysis due to the radon background. Phase 1 refers to the time before the installation of the anti-radon tent while Phase 2 refers to data taken after the tent was setup.

Table 5.1 summarises the runtime that has been used for the  $^{96}\text{Zr}$  analysis. With only 9.4 g measured during 1919 days, the available exposure for this analysis is 49.4 g · y. This exposure is very small compared to the latest results published on  $^{100}\text{Mo}$  for instance with 6.9 kg and an exposure of 34.7 kg · y [65].

Phase	Run time [days]	Dead time [days]	Available time [days]
1	392	5	387
2	1548	16	1532
<b>Total</b>	1940	21	1919

**Table 5.1.:** Summary of the data available for the  $^{96}\text{Zr}$  analysis in the different phases of operation of the NEMO-3 detector.

### 5.2.2. Isotopes constituting the background model

Tables A.2 and A.3 summarize the different isotopes that will be considered in this analysis. These tables detail the decay modes, the total energy available in the decays, the branching ratio for each decay mode and the main  $\gamma$ -rays produced during the decays along with their individual intensities (with a minimum of a few %). It is clear from this table that many different isotopes can contribute and in various ways to the background of the NEMO-3 experiment. One of the main challenges of the analysis presented in the next sections has been to identify the individual contributions of each of these isotopes.

## 5.3. Background measurement

An important part of this work is the search for  $0\nu\beta\beta$  of  $^{96}\text{Zr}$  to the ground state of  $^{96}\text{Mo}$ .  $^{96}\text{Zr}$  is also one of the isotopes for which the decay can occur to excited states. A dedicated study has been performed in order to search for this process, never seen before for this isotope. The background measurements for elements inside the source foil as much as the ones from the detector are therefore crucial. Another challenge for this study is due to the fact that the enrichment fraction is lower than compared to the main double- $\beta$  isotopes studied in NEMO-3 at only 53.7%. This section is dedicated to the measurement of the background levels inside and outside the detector.

The next sections will start with the description of the external background model. It is known to have only a small contribution in the signal channels and does not require to take into consideration internal background mainly thanks to t.o.f. cuts. On the other hand, external background contributes in the analysis channels dedicated to the measurement of the internal background. Their activities will be used as input for the other channels. An independent analysis channel is dedicated to the measurement of the contributions from  $^{214}\text{Bi}$  in the source foil and in the tracking chamber. These contributions also take part in the fit of the internal background channels. The description of internal backgrounds follows with the precise measurement of  $^{208}\text{Tl}$  in electron- $\gamma$  channels. Pure  $\beta$ -emitters also produce  $\beta\gamma$ -events via Bremsstrahlung, however an issue in the description of  $^{40}\text{K}$  prevents us from using its dedicated 1 electron analysis channel. Therefore this channel will be pre-

sented last and solutions discussed in following sections before the description of the measurement of  $2\nu\beta\beta$ .

### 5.3.1. External Backgrounds

As already defined in Chapter 4, an external event can originate in any part of the detector or its surroundings with the exception of the source foil itself. Several analysis channels are available for the measurement of these backgrounds, namely the crossing electron channel and the 1 electron 1 external  $\gamma$  channel (1e1 $\gamma$  (external)). An effective background model has been chosen in order to describe the external backgrounds. The shielding in NEMO-3 is very efficient and the selection of radiopure materials has been very strict. Therefore all of the contamination will be assumed to come from the glass of the PMTs and the surface of the scintillators. The volume of the scintillators has not been considered here as the residual contamination after selections is negligible compared to the background coming from the PMTs. On the other hand, the surface can be contaminated during the installation of the detector, although great care was taken. This effective model is a valid approximation as it does not represent the dominant background contribution for the search for double- $\beta$  decay (see section 5.4.2).

#### Crossing electron channel

This channel studies events in which an electron has deposited part of its energy in a first calorimeter block before crossing the tracker and the source foil to deposit the rest of its energy in another calorimeter block.

A crossing electron can be produced via several mechanisms. A Compton electron can be emitted after the interaction of a  $\gamma$ -particle near the surface of the scintillator block.

They can also be produced after a  $\beta$ -decay on the surface of a scintillator. The electron enters the scintillator and is then back-scattered toward the tracking chamber.

Along with the emission of an electron,  $\gamma$ -particles can also be produced after a  $\beta$ -decay. For a surface contamination, the electron can be emitted towards the centre of the detector and the  $\gamma$  enter the scintillator where the decay occurred.

Due to the very good efficiency of NEMO-3 to reconstruct electrons, the crossing-electron channel is very efficient for the measurement of the external background (coming from the whole detector except the sources). Several isotopes have an energy high enough to produce events in the energy range of  $0\nu\beta\beta$  (see Table A.2), including  $^{40}\text{K}$ ,  $^{228}\text{Ac}$ ,  $^{208}\text{Tl}$  and  $^{214}\text{Bi}$ . They are the dominant external background for  $2\nu\beta\beta$ . The HPGe measurements of the PMTs are displayed in Table 5.2.

Activities [Bq]	$^{40}\text{K}$	$^{214}\text{Bi}$	$^{208}\text{Tl}$
1040 - 3" PMT R6091 (230 g/PMT)	354	86	14.4
900 - 5" PMT R6594 (385 g/PMT)	477	216	3.5
<b>Total</b>	831	302	17.8

**Table 5.2.:** Results of the HPGe measurements extrapolated to all of the PMTs in NEMO-3 [68].

For the scintillator surface contamination, HPGe detectors have shown the presence of two isotopes:  $^{40}\text{K}$  and  $^{152}\text{Eu}$ . As already stated,  $^{40}\text{K}$  is naturally present in any material. The contamination in  $^{152}\text{Eu}$  probably happened during the moulding of the scintillator blocks in INR.

Given that tracks reconstruction in NEMO-3 is performed from the source, two electron-like particles have to be reconstructed in this channel, according to the criteria defined in section 5.1.3 and 5.1.4. Further criteria have been applied:

- The track vertices are within 2 cm in x,y and 4 cm in z;
- Two different calorimeter blocks have been hit;
- The two tracks have opposite curvature;
- The two tracks are on opposite sides of the source foil;
- The tracks are longer than 50 cm;
- There is no  $\alpha$  in the event.

The total energy, corresponding to the sum of the two energy deposits, is the variable that is fitted. The parameters of the fit are the activities of each background. The

other kinematic variables available are the individual energies, the initial and the final energy and the angle between the two tracks.

As can be seen in Figure 5.6, the high energy part of the distribution corresponds mainly to  $^{208}\text{Tl}$  and  $^{214}\text{Bi}$ . This enables a precise measurement of the contamination of these two isotopes. In this channel, activities are considered not to evolve with time given the long-lived isotopes that exist in the decay chains. This was not true for  $^{152}\text{Eu}$ , which activity decreased during the operation of the detector, therefore an average activity over time is measured here. This analysis has not been separated in the two different phases of data taking.

The validity of the effective external background model is illustrated in Figure 5.7 with good agreement between the data and Monte-Carlo simulations for all of the topological variables. The activities of the backgrounds in these plots are the one obtained from the fit to the total energy of the event.

The results of the activity measurements will be detailed in section 5.3.1 and compared to the measurement in the  $1e1\gamma$  (external) channel.

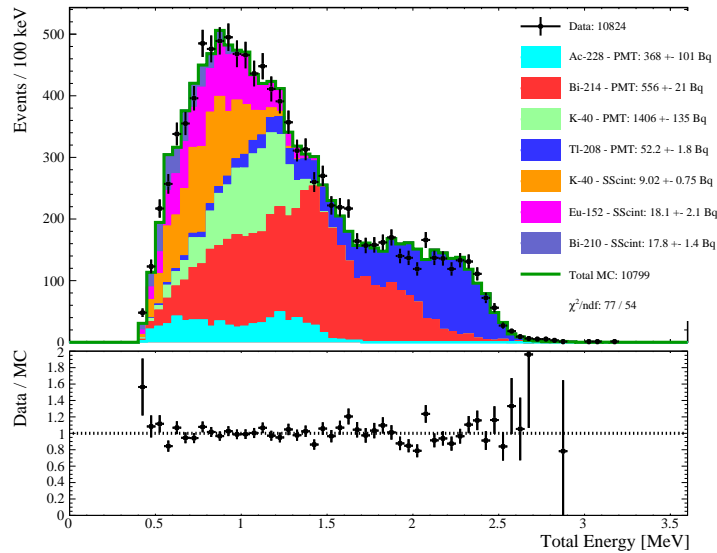


**Figure 5.6.:** *Fit of the total energy in crossing-electron events showing the data compared to the various external background contributions. The bottom plot shows the ratio of data to the total number of fitted Monte-Carlo events.*

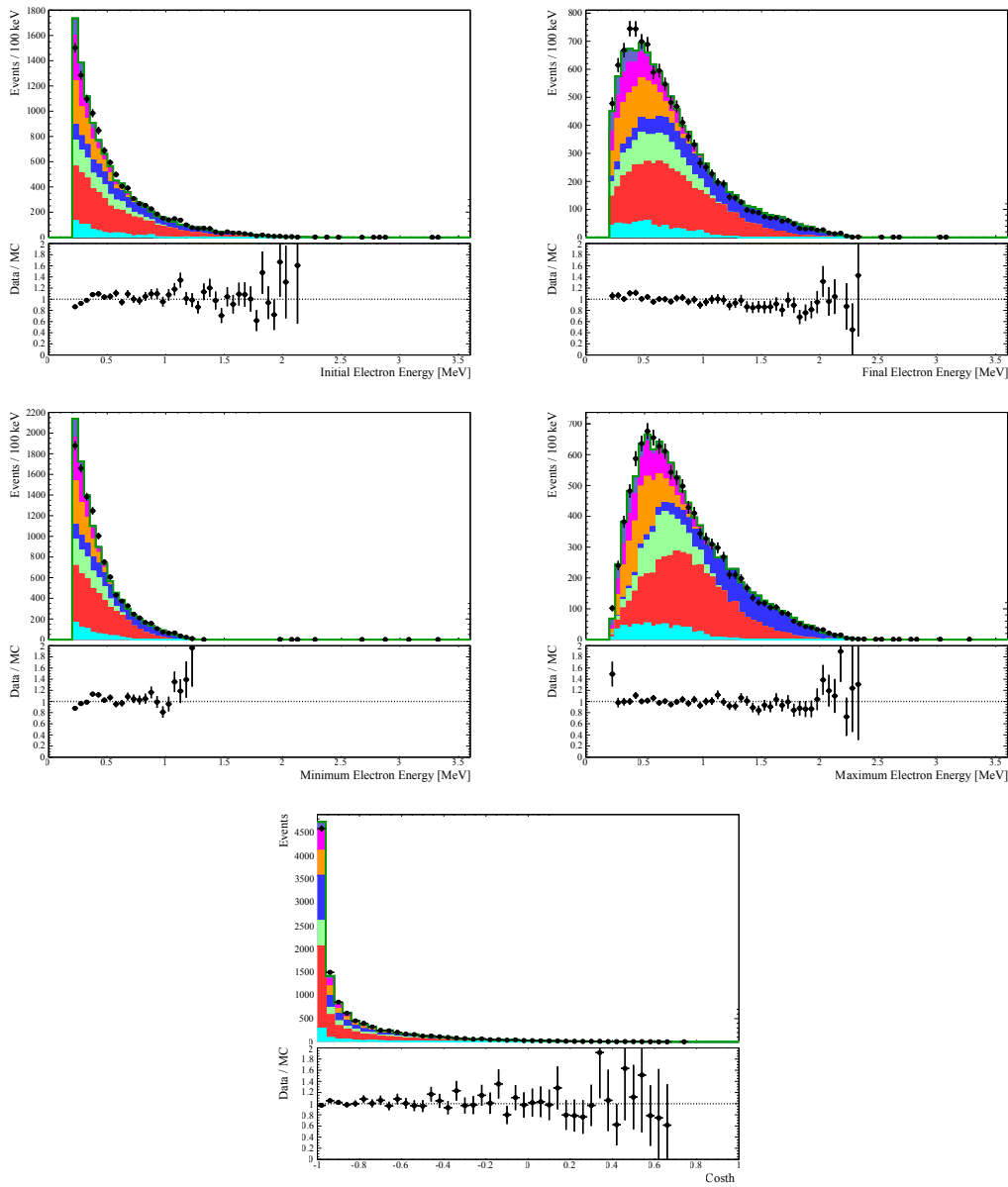


**Figure 5.7.:** Control distributions in the crossing electron channel: initial electron energy (top left), final electron energy (top right), minimum electron energy (middle left), maximum electron energy (middle right), angular distribution (bottom)

### 1 electron and 1 external $\gamma$ channel

The  $1e1\gamma$  (external) channel can also be used in order to measure the external background. However this channel is not as accurate as the crossing electron channel due to the lower detection efficiency for  $\gamma$ 's (50 %) compared to electrons. Two Compton scatterings are also necessary to produce these events reducing the proba-

bility of such an event to occur. This channel is used as a cross-check of the validity of the measurements performed in the crossing electron channel and for systematic uncertainty estimations.

One electron and one  $\gamma$ -particle have to be reconstructed in this channel, according to the selection defined in sections 5.1.3 and 5.1.4. Further criteria have been applied:

- The electron track is longer than 50 cm;
- There is no non-associated Geiger cell within 15 cm in  $x, y$  of the electron vertex;
- The  $\gamma$ -particle hit has an energy above 300 keV in order to reduce the noise existing below this threshold;
- There is no  $\alpha$  in the event.

All of the background activities are constrained at  $1\sigma$  around the previously measured values in the crossing electron channel and a fit is performed. The distribution of the total energy in this channel is displayed in Figure 5.8, and the individual electron and  $\gamma$  energies are displayed in Figure 5.9.

In spite of the low statistics, the agreement in this channel is good although not perfect. The discrepancies could be a hint for a missing contribution in the effective background model.

### Summary of the external background model

The effective external background model has been determined using the crossing electron channel. The measured activities have been used as input for the  $1e1\gamma$  (external)a channel. These activities are summarised in Table 5.3. As expected, the activities measured here are higher than the results of Table 5.2. Indeed the external background model is effective, assuming that all of the backgrounds come from the PMTs or the surface of the scintillators.

As already explained, the fit of the  $1e1\gamma$  (external) channel has been performed with constrained activities. A free fit has also been performed with the results displayed in Table 5.4 in order to quantify the systematic uncertainty on the external background. These uncertainties are all smaller than 20 %.

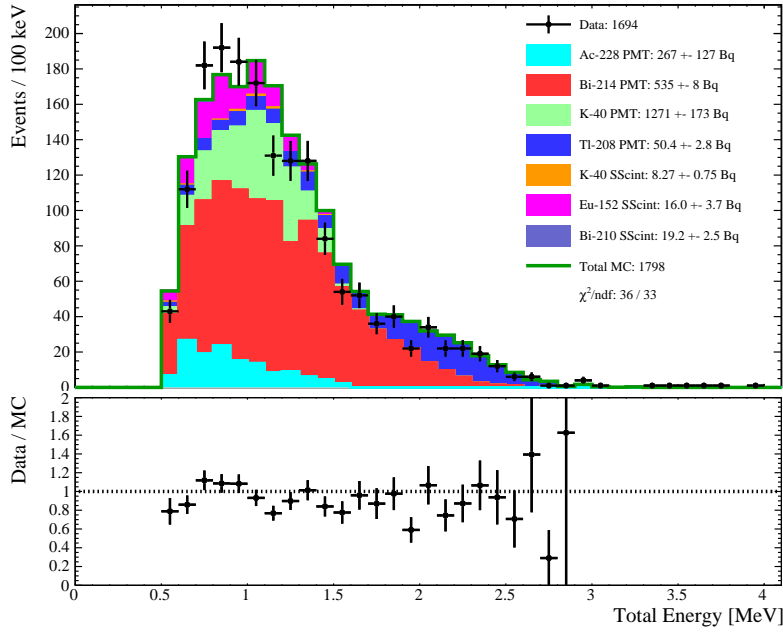


**Figure 5.8.:** *Distribution of the total energy in the 1 electron 1 external  $\gamma$  channel. The activities considered here are constrained at  $1\sigma$  around the values measured in the crossing electron channel.*

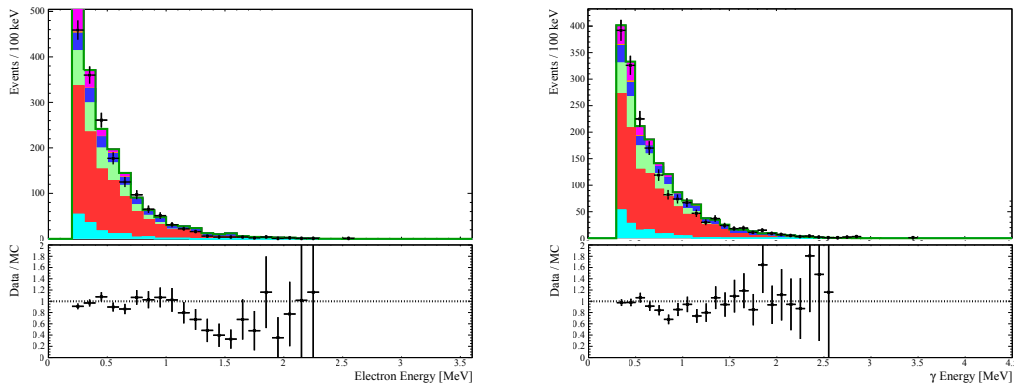


**Figure 5.9.:** *Control distributions in the 1 electron 1 external  $\gamma$  channel: electron energy (left) and  $\gamma$  energy (right).*

It is important to remind that the  $Q_{\beta\beta}$  of  $^{96}\text{Zr}$  is high enough for external backgrounds to have almost no impact on  $0\nu\beta\beta$  and only a negligible one for  $2\nu\beta\beta$ . The t.o.f. analysis is also very powerful to reject this background in the signal channels. Therefore the precision obtained on the activity measurements for this background model is sufficient, as will be showed in sections 5.4, 5.5 and 5.6.

Isotopes	Activity [Bq] Crossing	MC Efficiency Crossing	Events Crossing	MC Efficiency 1e1 $\gamma$	Events 1e1 $\gamma$
$^{214}\text{Bi}$ PMT	$556 \pm 21$	$4.2 \times 10^{-8}$	3982	$1.1 \times 10^{-8}$	1009
$^{40}\text{K}$ PMT	$1406 \pm 135$	$5.6 \times 10^{-9}$	1302	$1.3 \times 10^{-9}$	280
$^{208}\text{Tl}$ PMT	$52.2 \pm 1.8$	$2.3 \times 10^{-7}$	2025	$2.8 \times 10^{-8}$	233
$^{228}\text{Ac}$ PMT	$368 \pm 101$	$1.1 \times 10^{-8}$	660	$3.1 \times 10^{-9}$	136
SScint $^{40}\text{K}$	$9.02 \pm 0.75$	$9.0 \times 10^{-7}$	1345	$5.5 \times 10^{-9}$	7
SScint $^{152}\text{Eu}$	$18.1 \pm 2.1$	$3.7 \times 10^{-7}$	1096	$4.9 \times 10^{-8}$	129
SScint $^{210}\text{Bi}$	$17.8 \pm 1.4$	$1.3 \times 10^{-7}$	388	$6.8 \times 10^{-10}$	2
<b>Total MC</b>	-	-	10799	-	1798
<b>Data</b>	-	-	10824	-	1694

**Table 5.3.:** Summary of the measurement of the components of the effective external background model.

Isotopes	Activity [Bq]	$\Delta A$ (OCE)[Bq]	MC Efficiency	Events
$^{214}\text{Bi}$ PMT	$460 \pm 60$	96 (14%)	$1.1 \times 10^{-8}$	868
$^{40}\text{K}$ PMT	$1210 \pm 401$	196 (14%)	$1.3 \times 10^{-9}$	266
$^{208}\text{Tl}$ PMT	$46 \pm 8$	6.2 (12%)	$2.8 \times 10^{-8}$	214
$^{228}\text{Ac}$ PMT	$350 \pm 292$	18 (5%)	$3.1 \times 10^{-9}$	177
SScint $^{40}\text{K}$	$8.3 \pm 1.1$	0.72 (8%)	$5.5 \times 10^{-9}$	7
SScint $^{152}\text{Eu}$	$18 \pm 12$	0.1 (0.6%)	$4.9 \times 10^{-8}$	147
SScint $^{210}\text{Bi}$	$18 \pm 17$	0.2 (1%)	$6.8 \times 10^{-10}$	1
<b>Total MC</b>	-	-	-	1684
<b>Data</b>	-	-	-	1694

**Table 5.4.:** Result of the free fit in the 1e1 $\gamma$  (external) channel used for systematic uncertainty estimations.  $\Delta A$  (OCE) is the activity difference between this channel and the crossing electron channel (OCE) and the percentages are considered from the crossing electron channel activities.

### 5.3.2. 1 electron and 1 delayed $\alpha$ channel - $^{214}\text{Bi}$ - $^{214}\text{Po}$ background

As will be explained in further detail in Chapter 7, the so-called BiPo cascade can be used to measure contamination in  $^{214}\text{Bi}$ . The BiPo cascade considered here corresponds to a  $\beta$ -decay of  $^{214}\text{Bi}$  followed by a delayed  $\alpha$ -decay of  $^{214}\text{Po}$ . The half-life of the  $\alpha$ -decay of  $^{214}\text{Po}$  is 164  $\mu\text{s}$ . The time difference between the prompt electron and the delayed  $\alpha$ -particle is used to select events from this BiPo cascade. These events are studied in the 1 electron and 1 delayed  $\alpha$  channel (1e1 $\alpha$ ).

In this channel it is possible to identify the source of the contamination considering the length of the  $\alpha$ -track. These particles can come from the bulk of the source foil for an internal contamination or from the surface of the foil and of the tracker wires for radon deposition. Due to the very short mean free path of  $\alpha$ -particles in matter, the track length decreases with the amount of matter traversed. An  $\alpha$ -particle coming from inside the source will indeed lose more energy than one emitted from the surface of the foil or the surface of the tracker wires. Therefore the variable of interest that will be fitted here is the length of the  $\alpha$  track.

One electron and one  $\alpha$ -particle have to be reconstructed in this channel. The specific selection criteria for the 1e1 $\alpha$  channel are:

- The electron track is longer than 50 cm;
- The  $\alpha$ -particle and the electron vertices have to be within 5 cm in  $x, y, z$  if there are only two delayed hits and within 10 cm in  $x, y, z$  if there are more than three delayed hits. A stricter constraint is required for only two hits in order to reduce background.

Due to high radon activity in Phase 1 and a significant reduction of this background in Phase 2, the 1e1 $\alpha$  channel is studied in both phases separately for the internal contamination. A weighted average value is also obtained by the fit of the full statistics as the phases will not be separated in other analysis channels.

A refiring of the tracking cells can occur in the time window in which  $\alpha$ -particles are looked for. These events occur with a short delay and requiring at least two delayed hits allow them to be rejected [67]. In order to check that the selected events are compatible in time with  $^{214}\text{BiPo}$  events, the distribution of the time delay between

the two particles is studied. This delay time obeys the radioactive decay law as defined in section 5.1.5.

Figure 5.10 displays the result of the fit of the delay time in both phases together where the first bin is not included. Indeed, events with a very small delay time are not selected to reject background from refiring. Due to the low statistics, the half-life has been constrained to the expected value of  $164 \mu\text{s}$ . No data excess due to refiring above the fit is visible which confirms its proper rejection. The fit is compatible with an absence of random coincidences.

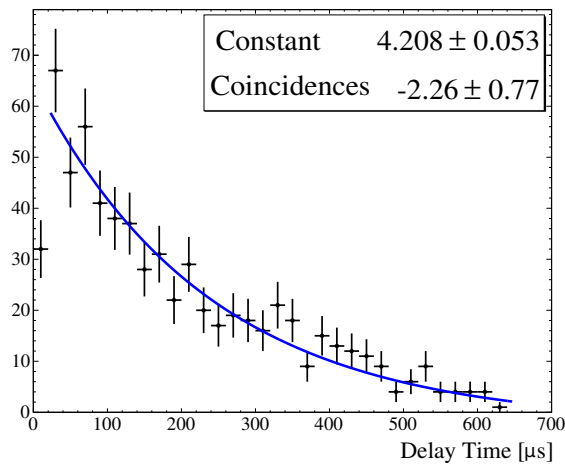


**Figure 5.10.:** *Fit of the delay time in both phases. The half-life has been set at the expected value of  $164 \mu\text{s}$  and the data are well-described. “Constant” stands for the scaling of the exponential. “Coincidences” describes the expected number of random coincidences per bin.*

Due to the low radon background in Phase 2, the sensitivity to internal contamination from the source itself and the Mylar it is wrapped in is much higher in this phase. Therefore their activities are measured with Phase 2 data only. As displayed in Figure 5.11, the internal contamination is clearly visible. In this figure, two types of distribution are identifiable. A peak at large track length, hence at high energy, is visible for the contamination from the surface of the wires and of the foil. It corresponds to events with an energy close to the  $\alpha$  energy in the decay of  $^{214}\text{Po}$  of  $7.69 \text{ MeV}$ . On the other hand, internal contamination almost only produce short tracks. It is even more visible for the contamination inside the bulk of the foil, having no contribution above  $20 \text{ cm}$  (in red in Figure 5.11).

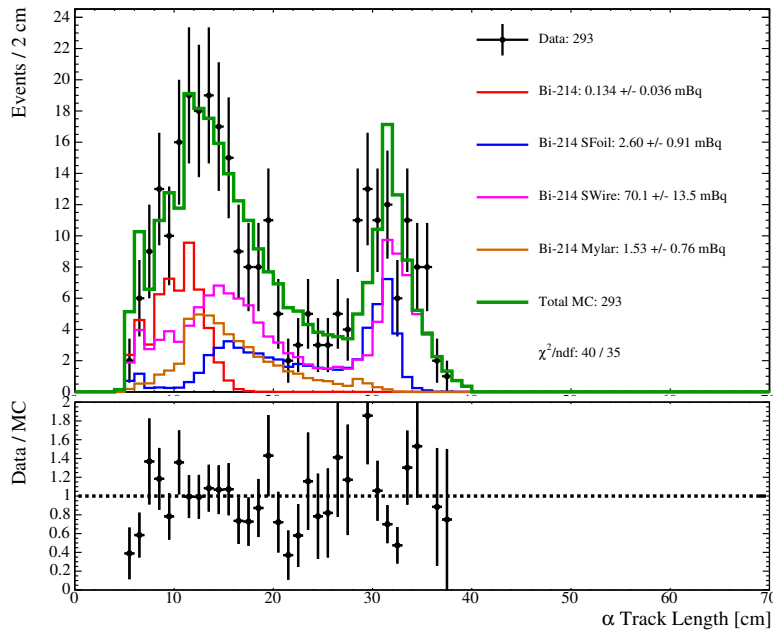


Figure 5.11.: *Fit of the  $\alpha$  track length in Phase 2*

These activities are fixed and used as an input to fit the  $\alpha$  track length in Phase 1 and in Phase 1+2. The results are displayed in Figure 5.12. The contamination in  $^{214}\text{Bi}$  from SFoil and SWire are the only free parameters in this case. In Phase 1, external backgrounds dominate and internal contamination is almost not visible.

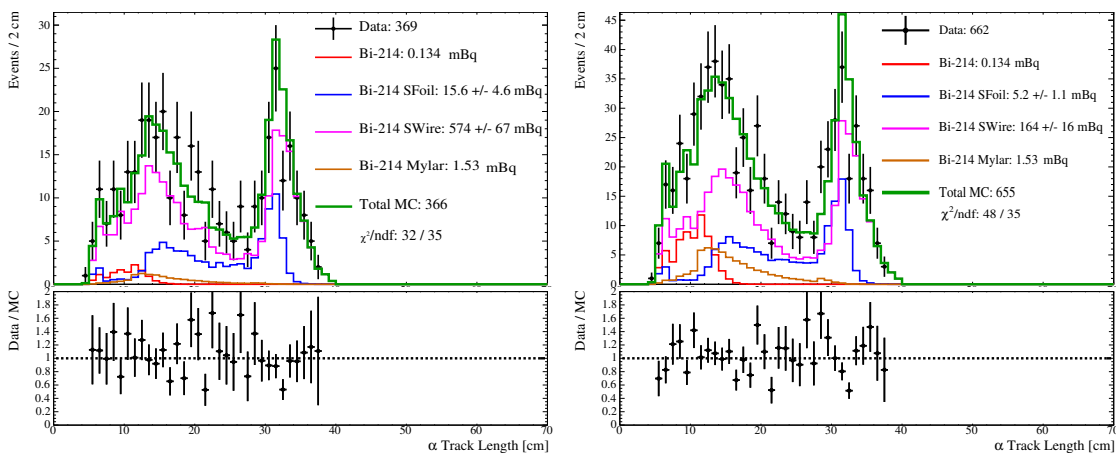


Figure 5.12.: *Fit of the  $\alpha$  track length in Phase 1 (left) and Phase 1 + Phase 2 (right)*

The activities of the different background components measured in the  $1e1\alpha$  channel are summarised in Table 5.5. The activities for  $^{214}\text{Pb}$  are assumed equal to the ones of  $^{214}\text{Bi}$  as they are in secular equilibrium in the decay chain of  $^{238}\text{U}$ <sup>1</sup>.

Origin of $^{214}\text{Bi}$	Events Both Phases	MC Efficiency	Activity [mBq]	Activity P1 [mBq]	Activity P2 [mBq]
Internal	65	$2.9 \cdot 10^{-3}$	-	-	$0.134 \pm 0.036$
Mylar	59	$2.3 \cdot 10^{-4}$	-	-	$1.53 \pm 0.76$
Surface of the foil	150	$1.7 \cdot 10^{-4}$	$5.2 \pm 1.1$	$15.6 \pm 4.6$	$2.6 \pm 0.9$
Surface of the wires	380	$1.4 \cdot 10^{-5}$	$164 \pm 16$	$573 \pm 67$	$70 \pm 13$
<b>Total MC</b>	655				
<b>Data</b>	662				

**Table 5.5.:** Summary of the  $^{214}\text{Bi}$  activity measurements in the 1 electron and 1  $\alpha$ -particle channel for both samples. The internal and Mylar contributions are fixed at their value in Phase 2.

Given that the two  $^{96}\text{Zr}$  samples in NEMO-3 have been produced separately, their internal contaminations are different. The same procedure has been performed for the two individual samples. The results for the contamination in  $^{214}\text{Bi}$  for the ITEP sample are presented in Table A.4 and in Table A.5 for the INR sample. The two samples are comprised of approximately the same mass of Mylar (4.1 g for ITEP and 4.2 g for INR), therefore a discrepancy in the Mylar contamination exist although not statistically significant. The efficiencies for the internal contamination are different since the two samples have different thickness.

The sum of the activities of the individual fit is in good agreement with the global fit. It has to be noted that the ITEP sample is around three times more contaminated in  $^{214}\text{Bi}$  than the INR one.

### 5.3.3. Internal background

Results on the contamination in  $^{214}\text{Bi}$  have already been provided in section 5.3.2. The internal background includes all of the contamination of the source foil itself. It

<sup>1</sup>The secular equilibrium in a decay chain implies that the activity of a radioactive isotope is equal to the activity of its decay products. It can be broken if long-lived isotopes exist in the chain.

can come from the Mylar, the outer part of the foil, during its preparation (mainly the drilling of the holes) or the installation in the detector. The other components such as the glue and the zirconium powder itself can also be contaminated. It turns out that the internal background is by far the most important contamination for the study of the double- $\beta$  decay of  $^{96}\text{Zr}$ . As for all of the other source foils installed in NEMO-3, the  $^{96}\text{Zr}$  samples have been measured in HPGe detectors. The two individual samples were produced separately and therefore measured separately. Table 5.6 summarizes these measurements.

Sample	Measured	Activity [mBq]				
	Mass [g]	$^{40}\text{K}$	$^{234m}\text{Pa}$	$^{214}\text{Bi}$	$^{228}\text{Ac}$	$^{208}\text{Tl}$
<b>ITEP</b>	13.7	< 2.97	< 3.04	< 0.22	< 0.32	< 0.14
<b>INR</b>	16.6	$9.7 \pm 2.8$	< 3.05	< 0.23	< 0.45	< 0.091

**Table 5.6.:** Summary of the HPGe measurements of the  $^{96}\text{Zr}$  samples. The error bars are given at  $1\sigma$  and the limits are set at  $2\sigma$  [68].

Several HPGe measurements were performed showing inconsistencies in the activity of  $^{40}\text{K}$ . A measurement carried out after the end of the NEMO-3 operation, showed a much higher activity (about a factor of 2) than the one presented here for the INR sample. Consequently these values will not be used as a constraint on the activity of the internal backgrounds. A comparison will be performed in section 5.3.4.

The source foil hosting  $^{96}\text{Zr}$  is surrounded by two other double- $\beta$  sources. On the side, a strip hosting  $^{150}\text{Nd}$  was installed and underneath several disks containing  $^{48}\text{Ca}$ . The contribution from  $^{48}\text{Ca}$  is negligible but that is not the case for  $^{150}\text{Nd}$ . An additional contribution from the internal backgrounds from  $^{150}\text{Nd}$  has therefore been considered in the internal background. The activities that were considered for these backgrounds were taken from a previous NEMO-3 analysis [84].

### 1 electron and 1 internal $\gamma$ channel

There are many  $\beta\gamma$ -emitters in natural radioactivity (see Table A.2.) Some of them are a background for  $0\nu\beta\beta$  and  $2\nu\beta\beta$  to excited states due to the high energy of the  $\gamma$ -particle they emit. The 1 electron and 1 internal  $\gamma$  channel (1e1 $\gamma$ ) enables

a precise measurement of the internal contamination in  $^{208}\text{Tl}$ . Indeed this isotope emits several  $\gamma$ -particles, one of which has a very high energy of 2.615 MeV. Other contamination can be measured in this channel, such as  $^{214}\text{Bi}$ , but  $1e1\alpha$  is purer. The activities of two other components of the internal background ( $^{212}\text{Bi}$ ,  $^{228}\text{Ac}$ ) can be inferred from the activity measured for  $^{208}\text{Tl}$ . This can be done since  $^{212}\text{Bi}$ ,  $^{228}\text{Ac}$  and  $^{208}\text{Tl}$  are supposed to be in secular equilibrium.

Pure  $\beta$ -emitters, such as  $^{40}\text{K}$ , can also be measured in this channel implying that a  $\gamma$ -particle from Bremsstrahlung in the source is detected along with the electron.

The activities of the external components of the background are set to the values previously measured in the crossing electron channel, and left free to fluctuate within  $1\sigma$  errors.

One electron and one  $\gamma$ -particle have to be reconstructed in this channel, as defined in sections 5.1.3 and 5.1.4. The specific selection criteria for the  $1e1\gamma$  channel are:

- The electron track is longer than 50 cm;
- The  $\gamma$  energy is higher than 300 keV in order to reject noise. The low-energy region is not necessary for the measurement of the activity of  $^{208}\text{Tl}$ , essentially constrained at high energy;
- No  $\alpha$ -particle has been reconstructed in the event;
- There is no non-associated Geiger cell within 15 cm in  $x, y$  of the electron vertex.

The total energy in the event is fitted here as presented in Figure 5.13. A good agreement is observed here and the high energy part of the spectrum enables the activity of  $^{208}\text{Tl}$  to be constrained.

Two other kinematic variables are available in this channel, the individual energies of the electron and of the  $\gamma$ . The distributions displayed in Figure 5.14 are normalised with the activities obtained from the fit of the total energy. The description of the individual energies also shows good agreement. However, the distribution of the cosine of the angle between the electron track and the  $\gamma$  trajectory shows a disagreement. It is mainly located at values close to 1, which means electrons and  $\gamma$ 's almost emitted in the same direction. This is probably due to an issue with the reconstruction of the angle between the electron and the  $\gamma$ . However, as will

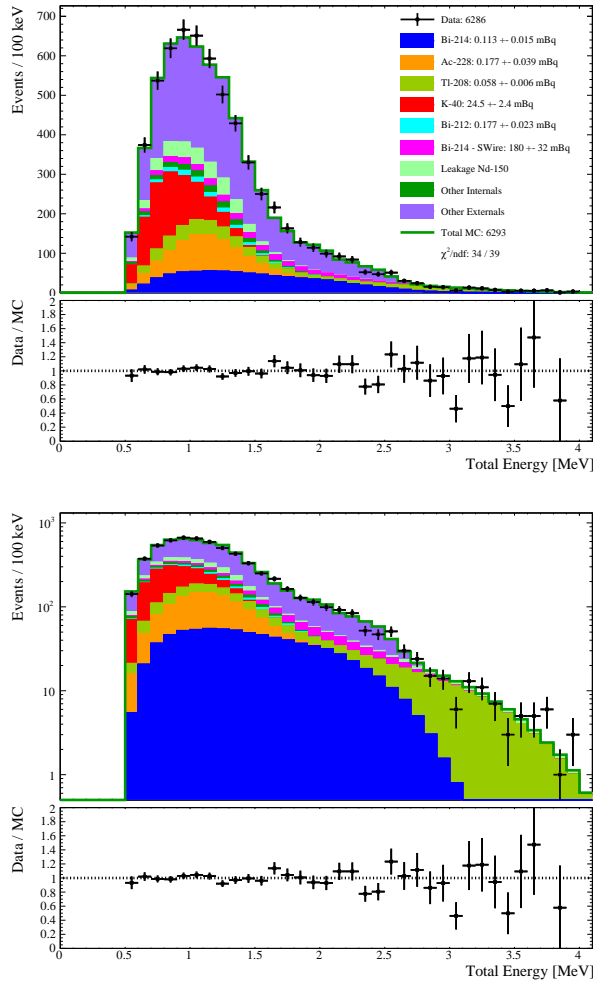


**Figure 5.13.:** *Distribution of the total energy in the  $1e1\gamma$  channel, on a linear scale (top) and on a logarithmic scale (bottom).  $^{208}\text{Tl}$  dominates at high energy.*

be seen, this should not impact the final results as the activities in  $1e1\gamma$  and  $2e$  are compatible (see section 5.4.1).

The activities of the different internal background components measured in the  $1e1\gamma$  channel are summarised in Table 5.7.

The measurements presented in this section have been performed for the two individual samples. The same activities have been assumed for the external background. This is a good approximation given that the two samples are very close to each other in the detector, therefore being essentially exposed to the same external background.

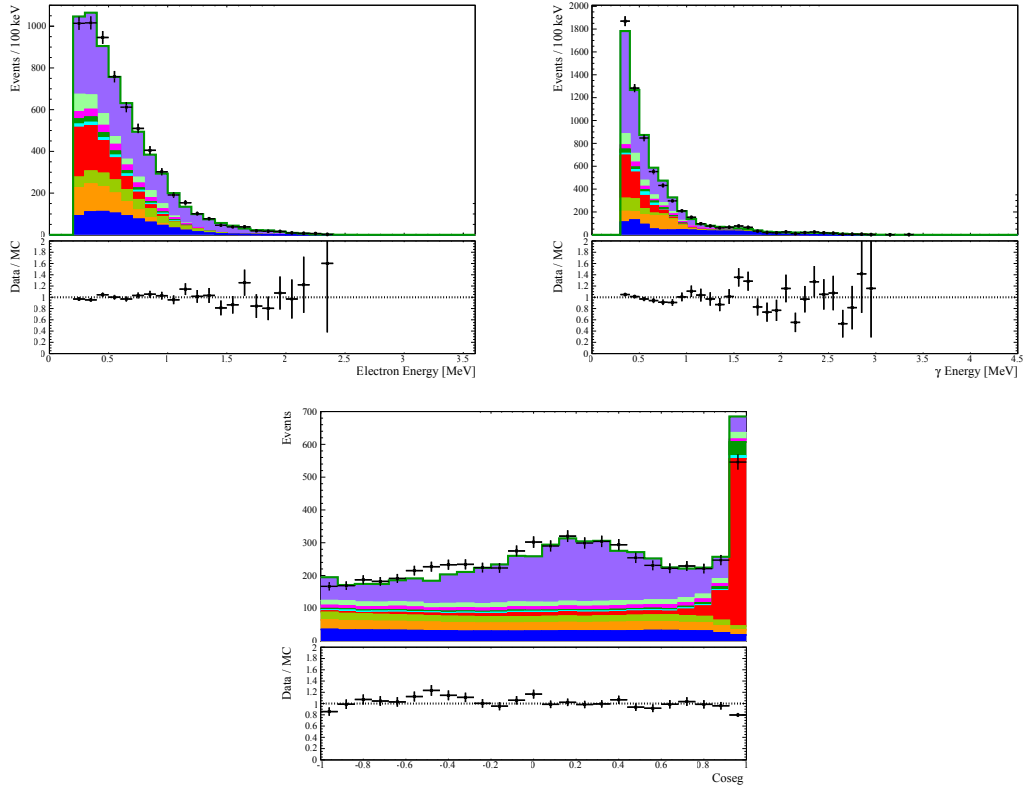


**Figure 5.14.:** Control distributions in the  $1e1\gamma$  channel: electron energy (top left),  $\gamma$  energy (top right), cosine of the angle between the electron and the  $\gamma$  (bottom).

Tables A.6 and A.7 present the results of these measurements for the ITEP and the INR sample respectively.

The activities obtained in the global fit and the sum of the activities of the individual samples are slightly different but compatible. This is due to the fact that a new fit is performed each time. It should be noted that the INR sample appears to have a lower contamination in  $^{208}\text{Tl}$  than the ITEP sample.

### 1 electron and 2 internal $\gamma$ channel

Most of the  $\beta\gamma$ -emitters in natural radioactivity not only emit one but several  $\gamma$ 's after their decay. It is the case for  $^{208}\text{Tl}$ ,  $^{214}\text{Bi}$  and  $^{228}\text{Ac}$ . This channel is also adapted for the measurement of the internal contamination in  $^{208}\text{Tl}$  due to the numerous high-energy  $\gamma$ -particles it emits ( see Table A.2). The fit of this channel is used as a cross-check of the  $1e1\gamma$  channel. The activity measurement will also be

Isotope	Events	Activity [mBq]	MC Efficiency
$^{208}\text{Tl}$	495	$0.058 \pm 0.006$	0.051
$^{228}\text{Ac}$	633	$0.177 \pm 0.039$	0.022
$^{212}\text{Bi}$	100	$0.177 \pm 0.023$	$3.4 \times 10^{-3}$
$^{214}\text{Bi}$	766	$0.113 \pm 0.015$	0.041
$^{40}\text{K}$	844	$24.5 \pm 2.4$	$2.1 \times 10^{-4}$
Other Internals	142		
Externals	2930		
Leakage $^{150}\text{Nd}$	381		
<b>Total MC</b>	6293		
<b>Data</b>	6286		

**Table 5.7.:** Summary of the activity measurements in the 1e1 $\gamma$  channel.

used as an estimation of the systematic uncertainty on the activity of  $^{208}\text{Tl}$ ,  $^{228}\text{Ac}$  and  $^{212}\text{Bi}$ .

One electron and two  $\gamma$ 's have to be reconstructed in this channel. The specific selection criteria for the 1 electron and 2 internal  $\gamma$  (1e2 $\gamma$ ) channel are:

- The electron track is longer than 50 cm;
- Each  $\gamma$  has an energy higher than 200 keV. A lower energy has been chosen here compared to 1e1 $\gamma$  to increase statistics.
- No  $\alpha$ -particle has been reconstructed in the event;
- There is no non-associated Geiger cell within 15 cm of the electron vertex.

The contributions of the external background are the same as for 1e1 $\gamma$ . The kinematic variable that has been fitted is the total energy available in the event, as displayed in Figure 5.15. Other kinematic variables are accessible in this channel, namely the energy of the electron and the individual energies of the  $\gamma$ . The distributions displayed in Figure 5.16 are normalised using the activities obtained from the fit of the total energy.

There is a good agreement of data with Monte-Carlo simulations given the low statistics available in this analysis channel. Again, the higher energy part of the

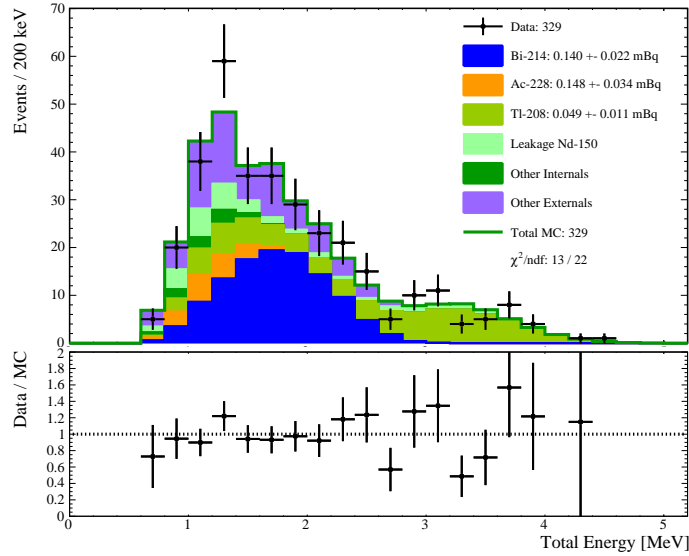


**Figure 5.15.:** *Distribution of the total energy in the  $1e2\gamma$  channel.*

spectrum is dominated by  $^{208}\text{Tl}$ , which enables a precise measurement of its activity. However, due to a lower statistics, the precision is lower than in  $1e1\gamma$ . The activities of the different internal background components measured in the  $1e2\gamma$  channel are summarised in Table 5.8. They are compatible with the results from  $1e1\gamma$ .

Isotope	Events	Activity [mBq]	$\Delta A$ ( $1e1\gamma$ ) [mBq]	MC Efficiency
$^{208}\text{Tl}$	80	$0.049 \pm 0.011$	0.009    16%	$9.9 \times 10^{-3}$
$^{228}\text{Ac}$	18	$0.148 \pm 0.034$	0.029    16%	$7.5 \times 10^{-4}$
$^{212}\text{Bi}$	2	$0.160 \pm 0.030$	0.017    10%	$7.6 \times 10^{-5}$
$^{214}\text{Bi}$	113	$0.140 \pm 0.022$	0.027    24%	$4.9 \times 10^{-3}$
Other Internals	7			
Externals	75			
Leakage $^{150}\text{Nd}$	32			
<b>Total MC</b>	<b>329</b>			
<b>Data</b>	<b>329</b>			

**Table 5.8.:** Summary of the activity measurements in the  $1e2\gamma$  channel.

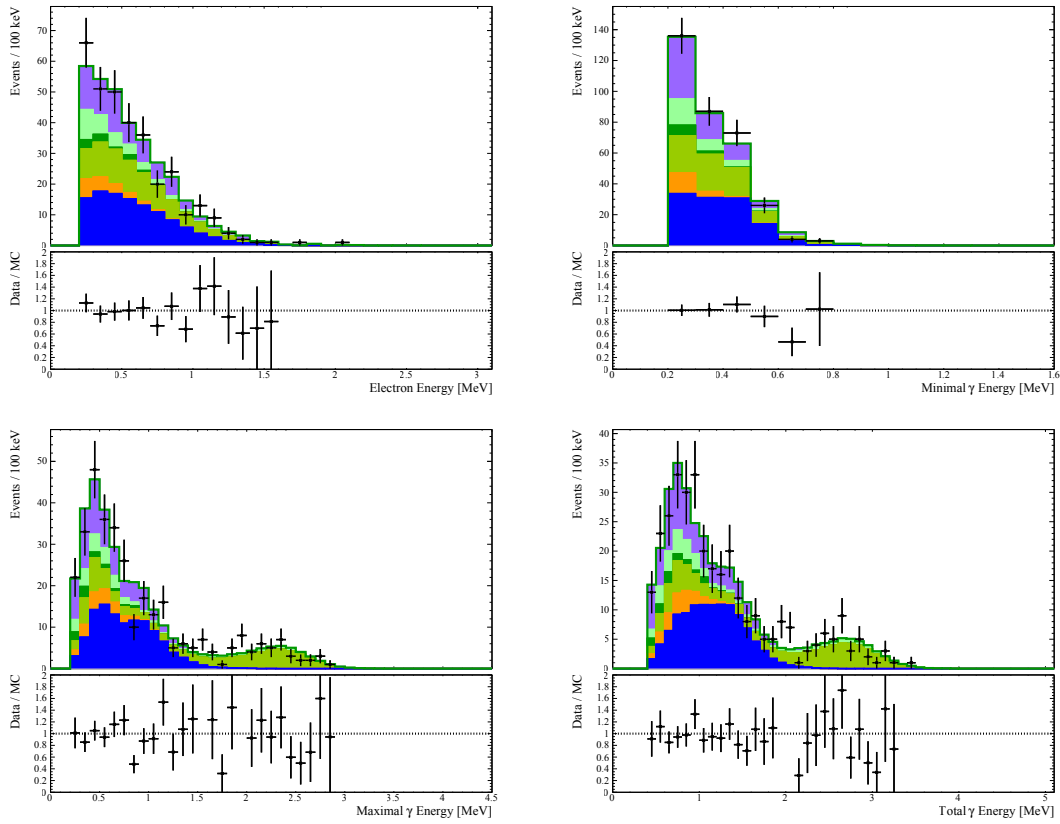


**Figure 5.16.:** Control distributions in the  $1e2\gamma$  channel: electron energy (top left), minimum  $\gamma$  energy (top right), maximum  $\gamma$  energy (bottom left) and total  $\gamma$  energy (bottom right).

The activity measurements have also been performed for the two individual samples. Tables A.8 and A.9 present the results of these measurement for the ITEP and the INR sample respectively.

The more important contamination in  $^{208}\text{Tl}$  that was visible in the  $1e1\gamma$  channel for the ITEP sample compared to INR does not appear here, presumably due to a statistical fluctuation. However an excess of  $^{214}\text{Bi}$  in the ITEP sample can still be seen as was observed in the  $1e1\alpha$  channel in section 5.3.2.

## 1 electron channel

Some of the isotopes contributing to the internal background are pure  $\beta$ -emitters. Therefore no  $\gamma$ -particle is emitted during their decays. It is the case for  $^{40}\text{K}$ ,  $^{234m}\text{Pa}$  and  $^{210}\text{Bi}$ . In order to measure their activity, the 1 electron ( $1e$ ) channel has been

investigated. It can also measure the contributions of other isotopes for decays where the  $\gamma$ -particle has been missed by the detector. It has very high statistics compared to channels involving  $\gamma$ 's.

One electron has to be reconstructed in this channel. The specific selection criteria for the 1e channel are:

- The track of the electron is longer than 50 cm;
- There is no non-associated Geiger cell within 15 cm in  $x, y$  of the electron vertex;
- The electron energy is higher than 400 keV. This energy selection has been made given that a lower energy cut has been made at 200 keV per electron to measure  $2\nu\beta\beta$  in the 2e channel. For a  $\beta$ -emitter to produce two electrons of at least 200 keV each, it requires a minimum energy of 400 keV for the electron emitted in the  $\beta$ -decay.
- No  $\alpha$ -particle is reconstructed in the event.

The energy of the electron is fitted here and the result is displayed in Figure 5.17. Although the fit is good, the measurement in the 2e channel raises some doubts regarding the Bremsstrahlung simulation in the Monte-Carlo (see section 5.4). The activities of the different internal background components measured in the 1e channel are summarised in Table 5.9.

Isotope	Events	Activity	MC Efficiency
$^{40}\text{K}$	613208	$19.38 \pm 0.05$ mBq	0.19
$^{234m}\text{Pa}$	25141	$0.60 \pm 0.01$ mBq	0.25
SWire $^{210}\text{Bi}$	80282	$17.1 \pm 0.7$ Bq	$2.8 \times 10^{-5}$
Other Internals	8848		
Other Externals	13431		
Leakage $^{150}\text{Nd}$	8366		
<b>Total MC</b>	749274		
<b>Data</b>	749147		

**Table 5.9.:** Summary of the activity measurements in the 1e channel.

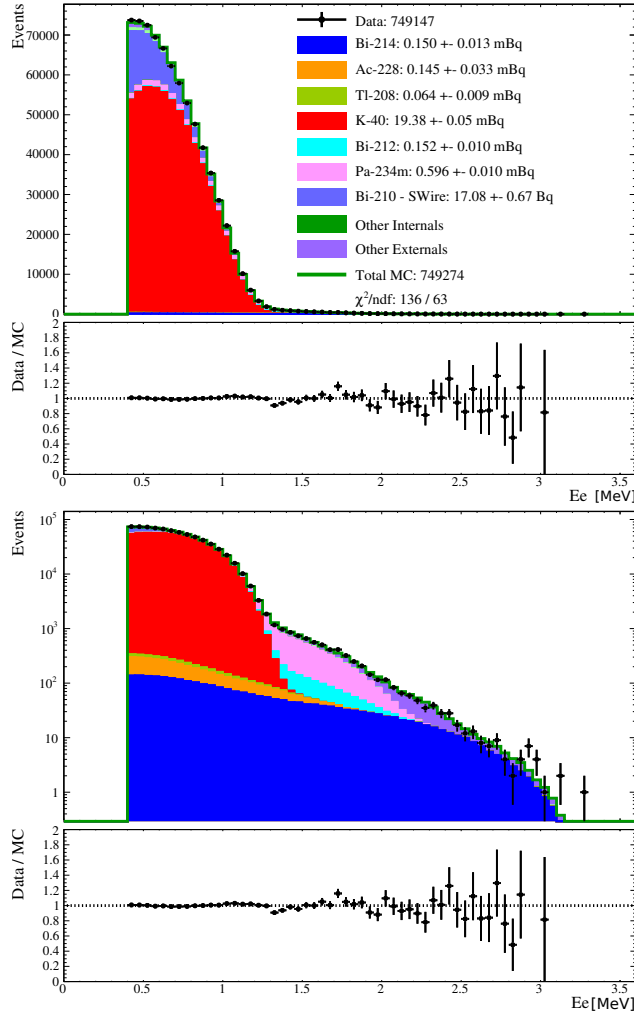


**Figure 5.17.:** *Fit of the electron energy in the one electron channel on a linear scale (top) and on a logarithmic scale (bottom).*

These measurement have also been performed for the individual samples. Tables A.10 and A.11 present the results of these measurement for the ITEP and the INR sample respectively. From these measurements, it is clear that both samples have been contaminated with  $^{40}\text{K}$  and the INR sample is about 5 times more contaminated than the ITEP one.

### 5.3.4. Summary of the internal background activities

Several analysis channels have been used in order to measure the different components of the internal background model. These results are summarised in Table 5.10.

The measurement of the background activities provides the input necessary for the search for double- $\beta$  decay processes.

Isotopes	Analysis Channel	Activity [mBq]	Activity ITEP [mBq]	Activity INR [mBq]
$^{214}\text{Bi}$	1e1 $\alpha$	$0.134 \pm 0.036$	$0.109 \pm 0.027$	$0.027 \pm 0.024$
$^{214}\text{Pb}$	1e1 $\alpha$	$0.134 \pm 0.036$	$0.109 \pm 0.027$	$0.027 \pm 0.024$
$^{208}\text{Tl}$	1e1 $\gamma$	$0.058 \pm 0.006$	$0.040 \pm 0.008$	$0.020 \pm 0.004$
$^{228}\text{Ac}$	1e1 $\gamma$	$0.177 \pm 0.039$	$0.097 \pm 0.023$	$0.064 \pm 0.027$
$^{212}\text{Bi}$	1e1 $\gamma$	$0.177 \pm 0.023$	$0.125 \pm 0.025$	$0.079 \pm 0.037$
$^{40}\text{K}$	1e	$19.38 \pm 0.05$	$3.26 \pm 0.02$	$15.34 \pm 0.04$
$^{234m}\text{Pa}$	1e	$0.60 \pm 0.01$	$0.29 \pm 0.02$	$0.30 \pm 0.01$

**Table 5.10.:** Summary of the measurements of the internal background model.

The activities summarised here are compatible with the HPGe measurements previously presented (Table 5.6). This is not the case for the contamination in  $^{40}\text{K}$  but as already mentioned this measurement has been problematic.

## 5.4. Measurement of two-neutrino double- $\beta$ decay of $^{96}\text{Zr}$ to the ground state of $^{96}\text{Mo}$

The target of this section is to measure the half-life of the  $2\nu\beta\beta$  of  $^{96}\text{Zr}$  to the ground state of  $^{96}\text{Mo}$ . Several measurements have already been performed with NEMO-2 [85] and NEMO-3 [86].

The 2 electron (2e) channel is used to perform the measurement of the half-life of  $2\nu\beta\beta$ . Two electrons have to be reconstructed in this channel. The specific selection criteria for the 2e channel are:

- The two electron vertices are within 2 cm in x,y and 4 cm in z;
- The two tracks are associated to two different calorimeter blocks;
- The two tracks are shorter than 30 cm. This is shorter than in the background channels in order to increase statistics and does not impact the half-life measurement;

- No  $\alpha$ -particle has been reconstructed in the event;
- There is no non-associated Geiger cell within 15 cm in  $x, y$  of the electron vertex.

The 2e channel offers several kinematic variables: the cosine of the angle between the two electrons tracks, the individual energy of the two electrons and the sum of these energies. The fit is performed on the sum of the electron energies, as displayed in Figure 5.18.

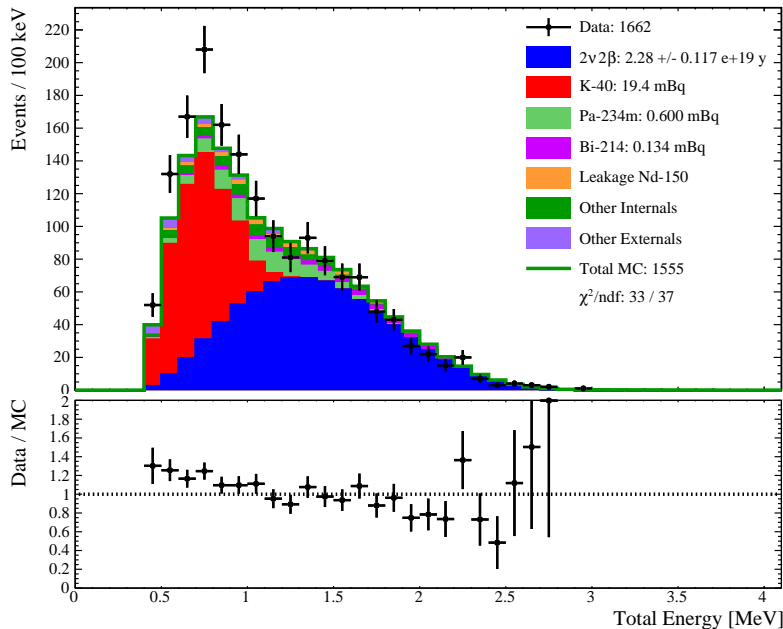


**Figure 5.18.:** *Fit of the total energy in the 2 electron channel.*

It is clearly visible that there is an excess in data below 1 MeV. This has only a small impact on the measurement of the  $2\nu\beta\beta$  half-life given that the signal exists at high energies, but it is necessary to explain this excess in order to be confident in our results. In Figure 5.18, 1662 data events and 1555 expected MC events are displayed, including signal and background.

As already briefly mentioned in section 5.3.3, this excess is likely due to an incorrect description of the  $^{40}\text{K}$  in the Monte-Carlo simulations. It can also be seen in other kinematic variables plotted in Figure 5.19 that the excess is in a region dominated by  $^{40}\text{K}$  background.

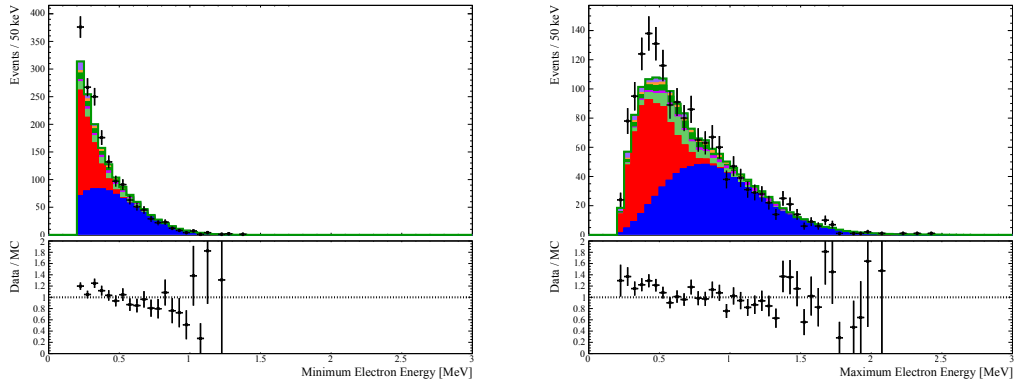


**Figure 5.19.:** *Control distributions in the 2 electron channel: minimum electron energy (left) and maximum electron energy (right). An excess at low energy is visible on both distributions.*

Given the shape and energies of the excess in data, the best hypothesis that was found was an underestimation of the  $^{40}\text{K}$  activity. A dedicated study has been performed in order to verify that this hypothesis is valid and is presented in the next section. A possible explanation is that the description of the Bremsstrahlung in GEANT-3 is not accurate and has been underestimated. This feature has already been observed in the analysis of a calibration source made of the pure  $\beta$ -emitters  $^{90}\text{Y}/^{90}\text{Sr}$ . This source was deposited on a  $^{100}\text{Mo}$  source foil and proved that the angle of emission of Bremsstrahlung was not accurately modelled. This does not have the same impact as in the 1e channel since the energies of the two electrons are lower and therefore the energies of the  $\gamma$ 's produced via Bremsstrahlung are lower.

There was already a slight excess in the previously published results in [86]. However, due to smaller statistics, this was probably considered as a statistical fluctuation of the background. The contribution of  $^{40}\text{K}$  will be left free in section 5.4.1. The result of the half-life measurement in the 2 electron channel with the activity set by the 1e channel and with the data excess shown in Figure 5.18 would be:

$$T_{1/2}^{2\nu 2\beta} (^{96}\text{Zr} \rightarrow ^{96}\text{Mo}) = 2.28 \pm 0.12 \text{ (stat.)} \times 10^{19} \text{ y} \quad (5.19)$$

### 5.4.1. Background identification and rejection for two-neutrino double- $\beta$ decay to ground state

The data excess in the 2e channel has been investigated in order to perform a more accurate measurement of the half-life of the  $2\nu\beta\beta$  decay. In order to verify the validity of the hypothesis that the activity of  $^{40}\text{K}$  is underestimated in 1e, the selection of  $^{40}\text{K}$  events has been optimised. The processes that produce the two electrons are different for double- $\beta$  decay and the  $^{40}\text{K}$  (a  $\beta$ -decay followed by a Møller scattering). Therefore their kinematics are different. Using kinematics provided by the detector, a two-dimensional study on Monte-Carlo simulations has been performed.

Figure 5.20 displays the maximum electron energy as a function of the minimum electron energy in the 2e channel for  $2\nu\beta\beta$  signal and  $^{40}\text{K}$  background. It is visible that the maxima of the distributions are not in the same region of this plane. Therefore it is possible to perform an elliptic cut selecting  $^{40}\text{K}$  and rejecting  $2\nu\beta\beta$ . The red ellipse has been optimised to select the majority of the Monte-Carlo events coming from  $^{40}\text{K}$  and is described by the equation (with energies in MeV):

$$\frac{(E_{min} - 0.2)^2}{0.3^2} + \frac{(E_{max} - 0.2)^2}{0.6^2} = 1 \quad (5.20)$$

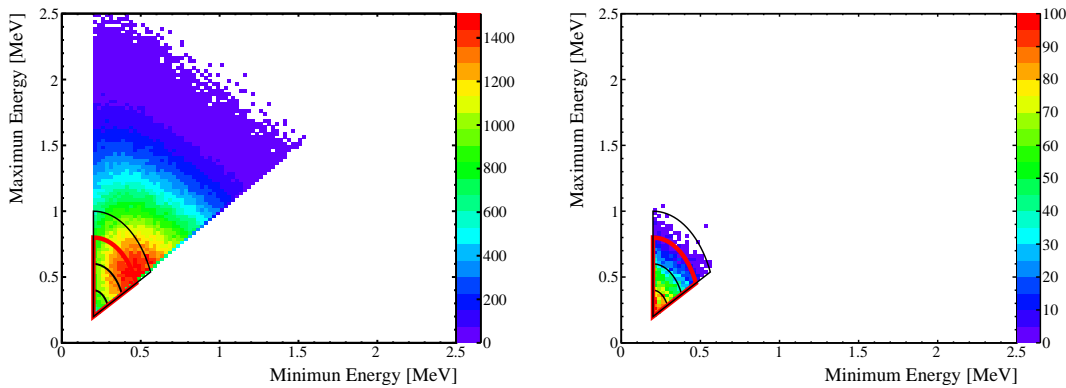


**Figure 5.20.:** *Distribution of the maximum energy as a function of the minimum energy in the 2 electron channel from Monte-Carlo simulations. The signal from  $2\nu\beta\beta$  is on the left and  $^{40}\text{K}$  is on the right.*

This selection allowed 96 % of  $^{40}\text{K}$  events to be selected. After this selection, the fit of the total energy has been performed again with  $^{40}\text{K}$  and  $2\nu\beta\beta$  left free. The result of the fit is displayed in Figure 5.21 along with the other available kinematic

variables. There is a good agreement between data and Monte-Carlo for these four variables.

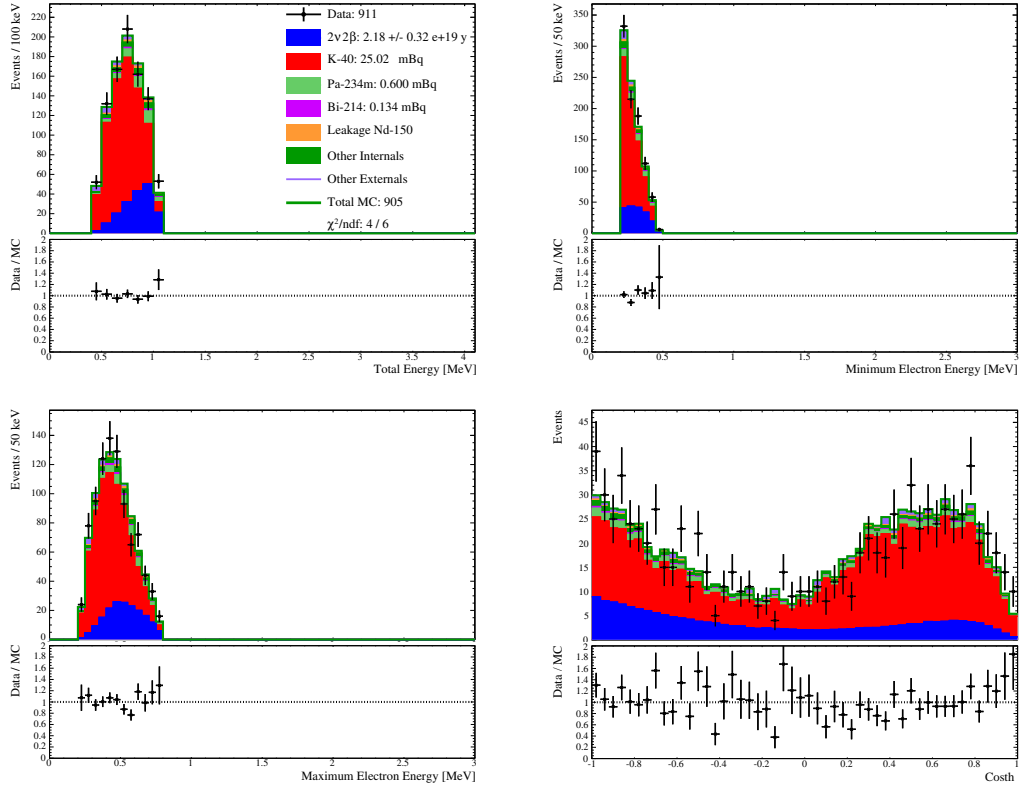


**Figure 5.21.:** *Fit of the total energy in the 2 electron channel (top left) and distributions of the minimum electron energy (top right), the maximum electron energy (bottom left) and the cosine of the angle between the electrons tracks (bottom right). The  $^{40}\text{K}$  and  $2\nu\beta\beta$  have been left free.*

Now that it has been proven that the observed excess could be explained by increasing the contribution from  $^{40}\text{K}$ , its activity can be fitted in the 2 electron channel. This is done as displayed in Figure 5.22 by releasing the constraint on the activity previously set in the 1e channel. The activity of  $^{40}\text{K}$  and the half-life of  $2\nu\beta\beta$  are the only free parameters in this fit. The other contributions, negligible here, are fixed at the central value determined in the control samples. The half-life is constrained at high energy and  $^{40}\text{K}$  at low energy. There is only little correlation between these two contributions that will be neglected here.

Both  $^{96}\text{Zr}$  samples have been analysed separately in order to obtain  $^{40}\text{K}$  activity from the 2e channel. The  $^{40}\text{K}$  activities used for the following steps of the analysis

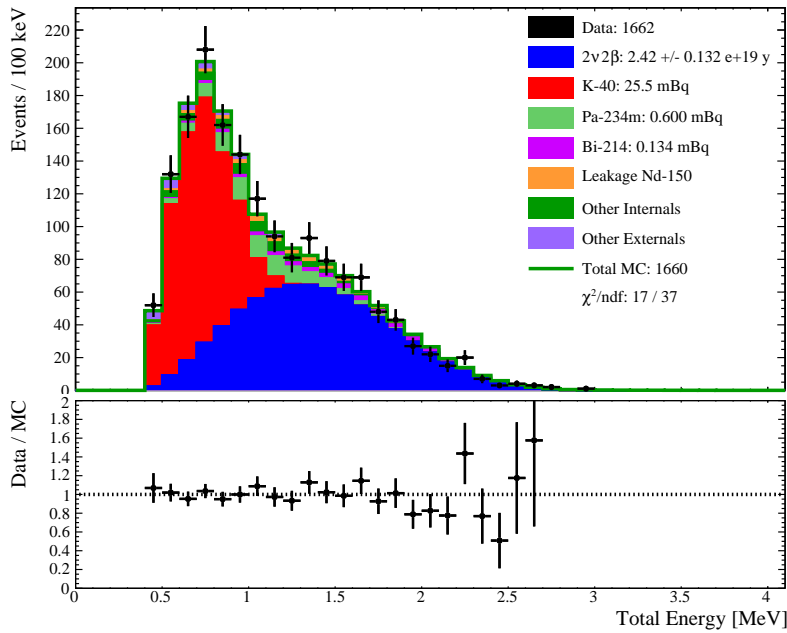


**Figure 5.22.:** *Fit of the total energy in the 2 electron channel. The activity of  $^{40}\text{K}$  is left free.*

are displayed in Table 5.11. Compared to the measurement in the 1e channel, the activities need to be increased by approximately 30 %.

Isotope	Activity [mBq]	MC Efficiency
$^{40}\text{K}$ - Total	$25.5 \pm 1.3$	$1.5 \cdot 10^{-4}$
$^{40}\text{K}$ - ITEP	$4.4 \pm 0.6$	$1.5 \cdot 10^{-4}$
$^{40}\text{K}$ - INR	$21.0 \pm 1.0$	$1.5 \cdot 10^{-4}$

**Table 5.11.:** Result of the  $^{40}\text{K}$  activity measurement in the 2 electron channel.

#### 5.4.2. Optimisation for two-neutrino double- $\beta$ decay

In order to optimise the signal to background ratio of 0.5, the selection using the ellipses from Figure 5.20 is now reversed. This has the effect of rejecting the  $^{40}\text{K}$ . Background activities are set at the central values measured in the control samples, left free to fluctuate within a  $1 \sigma$  range.

The activity measured in the 1e channel for  $^{40}\text{K}$  have not been used. For  $^{210}\text{Bi}$  and  $^{234m}\text{Pa}$ , the results of the 1e channel will be used in spite of this issue. The result of the final fit of the total energy in the 2e channel is displayed in Figure 5.23 and in Table 5.12.

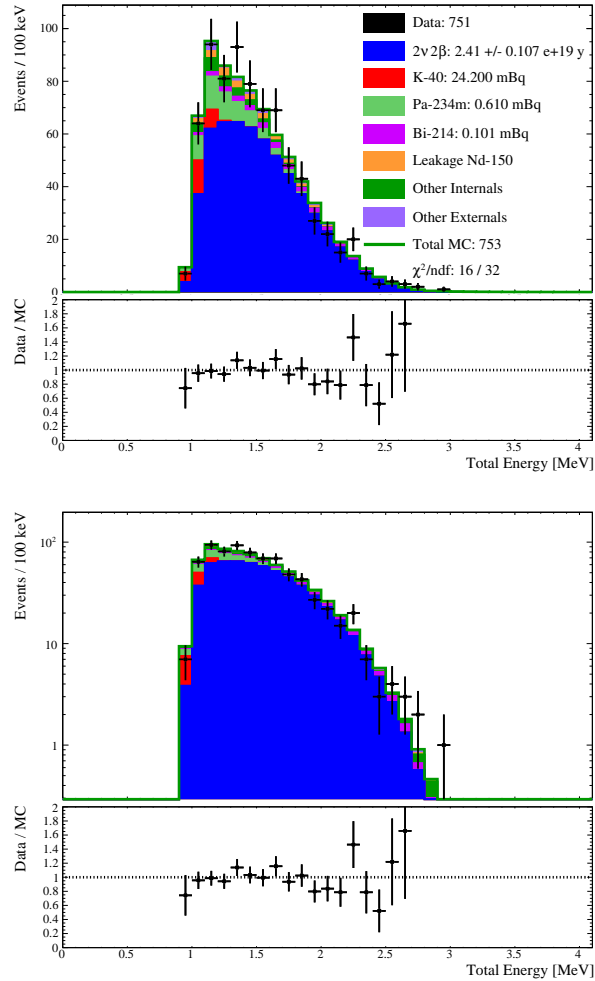


**Figure 5.23.:** *Fit of the total energy in the 2 electron channel after  $^{40}\text{K}$  rejection in linear scale (left) and logarithmic scale (right)*

Data and Monte-Carlo show good agreement. Using the background model defined in the previous sections, a measurement of the half-life of the  $2\nu\beta\beta$  of  $^{96}\text{Zr}$  to the ground state of  $^{96}\text{Mo}$  has been performed. The final result obtained for the combination of both samples with a signal over background of 3.3 is:

$$T_{1/2}^{2\nu 2\beta} (^{96}\text{Zr} \rightarrow ^{96}\text{Mo}) = 2.41 \pm 0.11 \text{ (stat.)} \times 10^{19} \text{ y} \quad (5.21)$$

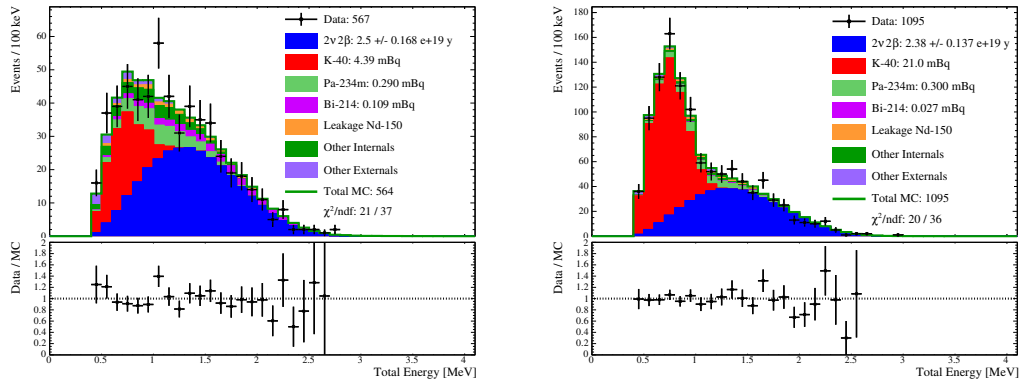
Isotopes	Selected MC Events	MC Efficiency	Expected Events
$2\nu 2\beta$	657565	0.066	583.3
$^{214}\text{Pb}$	0	$< 6.1 \times 10^{-7}$	$< 0.01$
$^{40}\text{K}$	244	$6.1 \times 10^{-6}$	24.5
$^{228}\text{Ac}$	1554	$3.9 \times 10^{-4}$	9.9
$^{234m}\text{Pa}$	4977	$5.5 \times 10^{-4}$	55.8
$^{212}\text{Bi}$	901	$2.3 \times 10^{-4}$	6.7
$^{214}\text{Bi}$	5778	$1.4 \times 10^{-3}$	26.2
$^{208}\text{Tl}$	8787	$8.8 \times 10^{-4}$	7.7
Mylar $^{214}\text{Bi}$	356	$3.6 \times 10^{-6}$	0.5
SFoil $^{214}\text{Bi}$	188	$1.7 \times 10^{-6}$	1.2
SWire $^{214}\text{Pb}$	0	$< 1.5 \times 10^{-9}$	$< 0.04$
SWire $^{210}\text{Bi}$	0	$< 3.1 \times 10^{-10}$	$< 0.8$
SWire $^{214}\text{Bi}$	214	$1.5 \times 10^{-7}$	4.4
$^{228}\text{Ac}$ PMT	0	$< 3.1 \times 10^{-11}$	$< 1.8$
$^{40}\text{K}$ PMT	1	$3.1 \times 10^{-12}$	0.7
$^{208}\text{Tl}$ PMT	27	$4.0 \times 10^{-10}$	3.3
$^{214}\text{Bi}$ PMT	18	$7.5 \times 10^{-11}$	7.2
SScint $^{40}\text{K}$	0	$< 1.2 \times 10^{-9}$	$< 2.4$
SScint $^{152}\text{Eu}$	0	$< 8.1 \times 10^{-10}$	$< 2.4$
Leakage $^{150}\text{Nd}$	-	-	21.6
<b>Total MC</b>	-	-	752.8
<b>Total Background</b>	-	-	169.5
<b>Data</b>	-	-	751

Table 5.12.: Result of the fit of the 2e channel after  $^{40}\text{K}$  rejection.

### 5.4.3. Measurement of two-neutrino double- $\beta$ decay to ground state for the individual samples

The external background model is the same for these two samples as they were placed almost at the same position in the detector. The internal backgrounds have been already measured in the previous sections in individual channels. One of the two samples has a higher contamination in  $^{40}\text{K}$  while the other one has a slightly

higher contamination in  $^{214}\text{Bi}$ . Unfortunately, separating the two samples increases statistical uncertainties. The results of the determination of the background models are summarised in Table A.12. Using these results and the external background model, the 2e channel has been analysed for both samples. Background activities have been set at the central values measured in the previous sections, left free to fluctuate within a  $1\sigma$  range. In Figure 5.24 are displayed the results of the fit of the total energy for the individual channels.



**Figure 5.24.:** *Fit of the total energy in the 2 electron channel for the individual samples. On the left the ITEP sample and on the right the INR sample.*

In order to reduce the impact of the  $^{40}\text{K}$  on the half-life measurement for  $2\nu\beta\beta$ , the same selection has been applied as explained previously. The results of the fit of the total energy in the 2 electron channel for the individual samples is displayed in Figure 5.25

The half-life has been measured for both samples individually and the result for the ITEP sample is:

$$T_{1/2}^{2\nu 2\beta}({}^{96}\text{Zr} \rightarrow {}^{96}\text{Mo}, \text{ITEP}) = 2.53 \pm 0.17 \text{ (stat.)} \times 10^{19} \text{ y} \quad (5.22)$$

and for the INR sample is:

$$T_{1/2}^{2\nu 2\beta}({}^{96}\text{Zr} \rightarrow {}^{96}\text{Mo}, \text{INR}) = 2.34 \pm 0.14 \text{ (stat.)} \times 10^{19} \text{ y} \quad (5.23)$$

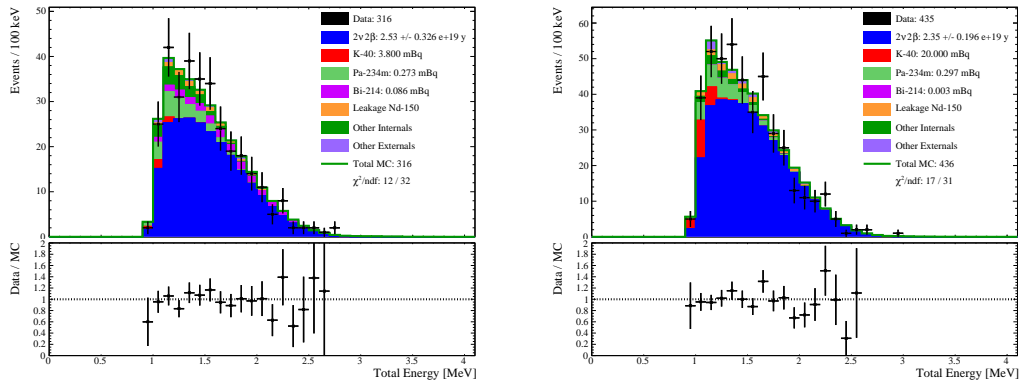


**Figure 5.25.:** *Fit of the total energy in the 2 electron channel for the individual samples after  $^{40}\text{K}$  rejection. On the left the ITEP sample and on the right the INR sample.*

#### 5.4.4. Estimation of the systematic uncertainties

There are several sources of systematic uncertainties to be considered. Some of them are not due to the analysis itself but to external causes, for example the enrichment fraction of the source foil. The precision on this fraction is known to 1.4 % for the  $^{96}\text{Zr}$  source foil [68]. This is directly applied to the half-life itself. Another indirectly measured uncertainty comes from the detector efficiency to detect two-electron events which has been estimated at 7% from the analysis of data from  $^{207}\text{Bi}$  sources compared to HPGE measurements [65].

The energy scale of the detector is known to a precision of 1%. In order to take into account this uncertainty, all of the energies from data events have been shifted by  $\pm 1\%$  and a half-life measurement re-done.

Another source of uncertainties comes from the background measurement procedures. Where possible, two independent analysis channels have been compared, such as  $^{208}\text{Tl}$  (1e1 $\gamma$  - 1e2 $\gamma$ ),  $^{214}\text{Bi}$  (1e1 $\alpha$  - 1e1 $\gamma$ ) and  $^{40}\text{K}$  (1e and 2e). The same uncertainties are assumed for isotopes in secular equilibrium, hence providing systematic uncertainties for  $^{212}\text{Bi}$  and  $^{228}\text{Ac}$  (from  $^{208}\text{Tl}$ ),  $^{214}\text{Pb}$  (from  $^{214}\text{Bi}$ ). The systematic uncertainty determined for  $^{40}\text{K}$  from the comparison between 1e and 2e channels accounts for the mismatch due to Bremsstrahlung. Therefore the same value has been used for  $^{234m}\text{Pa}$  and  $^{210}\text{Bi}$ . For the external background, the systematic uncertainty has been estimated from the comparison between the crossing electron channel and the 1e1 $\gamma$  (external) channel. No correlation has been assumed in the final analysis

channel between the different backgrounds. A systematic uncertainty is estimated for each of the contributions. For each isotope, the activities of all of the other backgrounds are left free within a  $1\sigma$  range determined from their individual measurement. Then a fit is performed with the activity of the considered isotope set at its measured value increased and decreased from its systematic uncertainty.

Source of Uncertainty	Absolute Uncertainty [%]	Half-life Uncertainty [%]
Isotope enrichment	$\pm 1.4$	$\pm 1.4$
Detection efficiency in 2e channel	$\pm 7$	$\pm 7$
Energy calibration	$\pm 1$	+1.9 -0.6
Internal $^{214}\text{Bi}$	$\pm 25$	+3.0 -0.1
Internal $^{208}\text{Tl}$	$\pm 9$	$\pm 2 \times 10^{-4}$
Internal $^{40}\text{K}$	$\pm 24$	+0.7 -0.3
Internal $^{234m}\text{Pa}$	$\pm 24$	+3.6 -2.0
Other Internals	-	$\pm 0.1$
External Background	$\pm 20$	+0.25 -0.35
Radon background	$\pm 21$	+0.02 -0.05
Total systematic uncertainty	-	+8.8 -7.5

**Table 5.13.:** Systematic uncertainties for  $2\nu\beta\beta$  half-life measurement.

Table 5.13 summarises the different contributions to the systematic uncertainty. A total uncertainty of  ${}^{+8.8}_{-7.5}\%$  has been estimated. This uncertainty will be used as the systematic uncertainty for both samples together as well as the individual samples. The final result on the half-lives are:

$$T_{1/2}^{2\nu 2\beta}({}^{96}\text{Zr} \rightarrow {}^{96}\text{Mo}, \text{Combined}) = 2.41 \pm 0.11 \text{ (stat.) } {}^{+0.21}_{-0.18} \text{ (syst.) } \times 10^{19} \text{ y} \quad (5.24)$$

$$T_{1/2}^{2\nu 2\beta}({}^{96}\text{Zr} \rightarrow {}^{96}\text{Mo}, \text{ITEP}) = 2.53 \pm 0.17 \text{ (stat.) } {}^{+0.22}_{-0.19} \text{ (syst.) } \times 10^{19} \text{ y} \quad (5.25)$$

$$T_{1/2}^{2\nu 2\beta}({}^{96}\text{Zr} \rightarrow {}^{96}\text{Mo}, \text{INR}) = 2.34 \pm 0.14 \text{ (stat.) } {}^{+0.21}_{-0.18} \text{ (syst.) } \times 10^{19} \text{ y} \quad (5.26)$$

## 5.5. Search for neutrinoless double- $\beta$ decay of $^{96}\text{Zr}$ to the ground state of $^{96}\text{Mo}$

$0\nu\beta\beta$  has never been observed yet and given the very low mass of  $^{96}\text{Zr}$  available this is even more challenging.

The fit of the total energy in the 2e channel is performed for the search for  $0\nu\beta\beta$  (see Figure 5.23). The different contributions to background have been estimated using the background model defined in the previous sections. In case no signal is observed, a limit on the half-life of the  $0\nu\beta\beta$  can be set using equation 5.27.

$$T_{1/2} > \frac{\ln(2) \times \mathcal{E}_{0\nu2\beta} \times m_{96\text{Zr}} \times N_A \times t_{\text{observation}}}{N_{\text{excluded}} \times M_{96\text{Zr}}} \quad (5.27)$$

where  $\mathcal{E}_{0\nu2\beta}$  is the detection efficiency for  $0\nu\beta\beta$ ,  $m_{96\text{Zr}}$  is the mass of  $^{96}\text{Zr}$ ,  $N_A$  is Avogadro's number,  $N_{\text{excluded}}$  is the number of excluded data events and  $M_{96\text{Zr}}$  the atomic mass of  $^{96}\text{Zr}$ . An expected half-life limit can be computed using Feldman-Cousins confidence intervals for a small number of expected background events [81].

In order to maximise the sensitivity, the lower cut on the total energy of the electrons has been optimised. This is performed on Monte-Carlo simulations without any comparison to data prior to the definition of the cut. For each value of the lower cut, the number of expected background events is calculated. Assuming no signal is observed, the number of excluded signal events is derived from Feldman-Cousins confidence interval at 90% C.L.. Figure 5.26 displays the result of the expected half-life limit computations. The criterion that maximises the half-life sensitivity is  $E_{\text{tot}} > 2.85$  MeV which corresponds to an expected half-life limit of:

$$T_{1/2}^{0\nu2\beta} (^{96}\text{Zr}) > 1.16 \times 10^{22} \text{ y @ 90\% C.L.} \quad (5.28)$$

After applying the lower energy cut, Table 5.14 displays the expected background in the region of interest. Only contributing sources of background are listed here. The number of excluded signal events is once again estimated from Feldman-Cousins

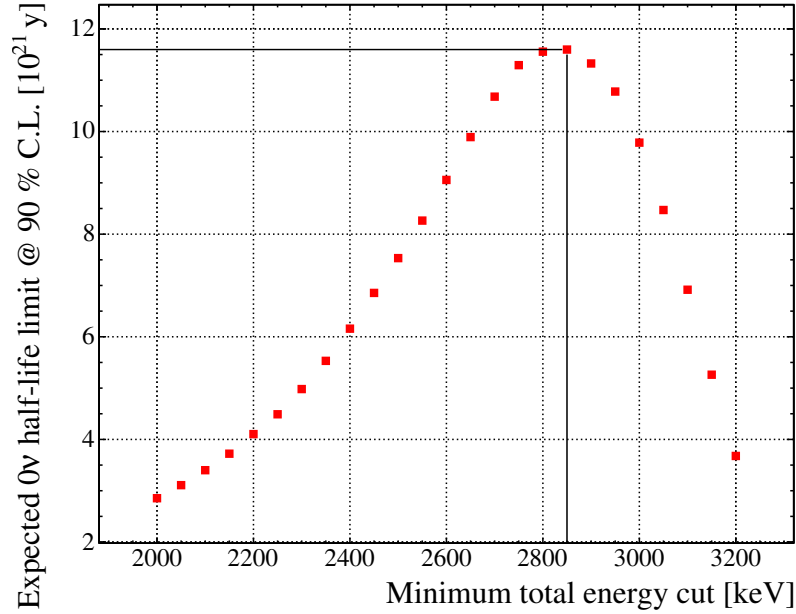


**Figure 5.26.:** *Expected  $0\nu\beta\beta$  half-life limit as a function of the lower cut on the total energy. A maximum in the expected half-life can be determined allowing an optimal lower energy cut to be defined.*

confidence intervals. Counting events above the lower energy cut, there are 1.2 expected background events and 1 data event. 3.17 signal events can therefore be excluded @ 90% C.L.. Therefore a lower limit on the half-life of  $0\nu\beta\beta$  is set at the value in equation 5.29 using equation 5.27 with  $\mathcal{E}_{0\nu2\beta} = 17.6\%$ ,  $m_{96\text{Zr}} = 9.4$  g,  $N_A = 6.022 \times 10^{23}$  mol $^{-1}$ ,  $t_{\text{observation}} = 5.25$  y,  $N_{\text{excluded}} = 3.17$  @ 90 % C.L. and  $M_{96\text{Zr}} = 96.0$  g.mol $^{-1}$ .

$$T_{1/2}^{0\nu2\beta}(^{96}\text{Zr}) > 1.19 \times 10^{22} \text{ y @ 90\% C.L.} \quad (5.29)$$

Using the nuclear matrix elements from [40], upper limits on the effective neutrino mass can be set at:

$$|m_{\beta\beta}| < 5.8 - 18.6 \text{ eV @ 90\% C.L.} \quad (5.30)$$

Isotopes	Selected MC Events	MC Efficiency	Expected Events
$2\nu2\beta$	237	$2.4 \times 10^{-5}$	0.211
$^{214}\text{Bi}$	12	$3.0 \times 10^{-6}$	0.067
$^{208}\text{Tl}$	809	$8.1 \times 10^{-5}$	0.782
Mylar $^{214}\text{Bi}$	6	$6.0 \times 10^{-8}$	0.015
SFoil $^{214}\text{Bi}$	1	$9.1 \times 10^{-9}$	0.008
SWire $^{214}\text{Bi}$	4	$2.8 \times 10^{-9}$	0.075
<b>Leakage <math>^{150}\text{Nd}</math></b>	-	-	0.014
<b>Total MC</b>	-	-	1.172
<b>Data</b>	-	-	1

**Table 5.14.:** Result of the fit of the 2e channel after the lower energy cut ( $E_{tot} > 2.85$  MeV) displaying the number of selected Monte-Carlo events, the Monte-Carlo efficiencies for each contribution and the number of expected background events in the region of interest. The leakage from  $^{150}\text{Nd}$  is the sum of all of the contamination.

The energy spectrum above 2 MeV is displayed in Figure 5.27 where the half-life of  $0\nu\beta\beta$  has been set at the limit for illustration. No excess above background is visible on this plot.

The laser correction system (see section 4.4.3) has been designed in order to check the proper calibration of the calorimeter. However, using these corrections reduces statistics by more than 25 %. In other NEMO-3 analyses on various isotopes with larger statistics, events due to a faulty calibration were detected in the region of interest. For  $^{96}\text{Zr}$ , no impact can be seen in the region of interest by applying the laser corrections. Given the very low mass of  $^{96}\text{Zr}$  present in NEMO-3, this cut has not been applied for the final estimation of the sensitivity to  $0\nu\beta\beta$ . As a comparison, applying the laser corrections and doing the same study as before provided an optimised expected half-life limit of  $T_{1/2}^{0\nu2\beta}(^{96}\text{Zr}) > 8.9 \times 10^{21}$  y. The lower limit on the half-life of  $0\nu\beta\beta$  of  $^{96}\text{Zr}$  would be  $T_{1/2}^{0\nu2\beta}(^{96}\text{Zr}) > 8.2 \times 10^{21}$  y which corresponds to a limit on the effective neutrino mass of  $|m_{\beta\beta}| < 7.8 - 20.6$  eV.

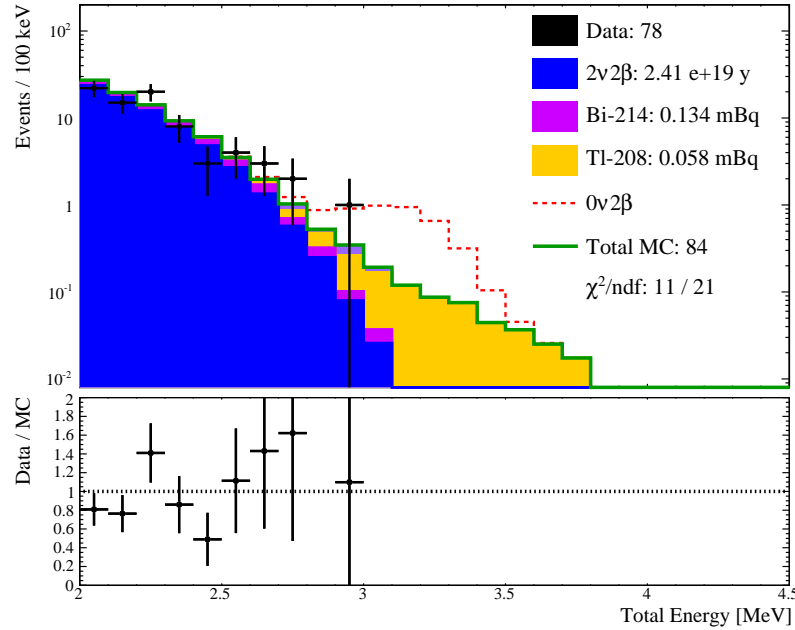


**Figure 5.27.:** High energy spectrum above 2 MeV in the 2e channel displaying the limit on the  $0\nu\beta\beta$  half-life. No excess above background is visible here.

### 5.5.1. Estimation of the systematic uncertainties

The same uncertainties as for the  $2\nu\beta\beta$  measurement have been considered. Thanks to the low-energy cut, most of the background have been removed. No contribution is now expected from external backgrounds,  $^{40}\text{K}$ ,  $^{210}\text{Bi}$ ,  $^{214}\text{Pb}$ ,  $^{212}\text{Bi}$  and  $^{228}\text{Ac}$ . The most important contribution to the uncertainties is due to  $^{208}\text{Tl}$ . Table 5.15 summarises the different contributions to the systematic uncertainty.

A total uncertainty of  $^{+9.8}_{-9.7}\%$  has been estimated. These systematic uncertainties were not used in the Feldman-Cousins method. Using ROOT TLimit CL<sub>s</sub> computation, including systematics and using the same energy region of interest, it has been possible to set a higher limit on  $0\nu\beta\beta$  half-life:

$$T_{1/2}^{0\nu2\beta}(^{96}\text{Zr}) > 1.29 \times 10^{22} \text{ y @ 90\% C.L. and } |m_{\beta\beta}| < 3.8 - 12.1 \text{ eV} \quad (5.31)$$

Source of Uncertainty	Absolute Uncertainty [%]	Half-life Uncertainty [%]
Isotope enrichment	$\pm 1.4$	$\pm 1.4$
Detection efficiency in 2e channel	$\pm 5$	$\pm 7$
Energy calibration	$\pm 1$	$+1.9$ $-0.6$
$2\nu\beta\beta$	$\pm 8$	$\pm 1.4$
Internal $^{214}\text{Bi}$	$\pm 25$	$\pm 1.4$
Internal $^{208}\text{Tl}$	$\pm 9$	$\pm 6.0$
Other Internals	-	$\pm 0.3$
Radon background	$\pm 21$	$\pm 1.4$
Total systematic uncertainty	-	$+9.8$ $-9.7$

**Table 5.15.:** Systematic uncertainties for the  $0\nu\beta\beta$  measurement.

## 5.6. Search for two-neutrino double- $\beta$ decay to excited states

$^{96}\text{Zr}$  is one of the double- $\beta$  decay isotopes that can undergo a double- $\beta$  decay to an excited state of  $^{96}\text{Mo}$ . The energy levels of  $^{96}\text{Mo}$  are displayed in Figure 5.28.

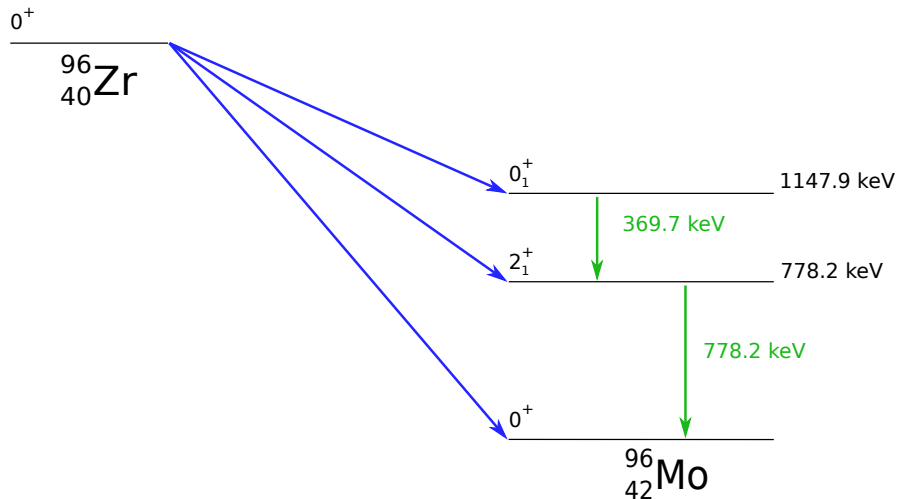


**Figure 5.28.:** Energy scheme for the double- $\beta$  decay of  $^{96}\text{Zr}$  to  $^{96}\text{Mo}$ . Two excited states are visible here along with the ground state.

Two energy levels were initially considered for this study,  $0^+$  and  $2^+$ . The decay to these excited states is strongly suppressed when compared to the double- $\beta$  decay to

the ground state. The  $2_1^+$  level is theoretically more suppressed than the  $0_1^+$  level [87]. Therefore the  $0_1^+$  level is of greater interest and the study will be performed assuming no contribution from the  $2_1^+$  level.

In a decay to excited states, the two electrons are emitted along with several  $\gamma$ 's. The efficiency to detect  $\gamma$ 's is much lower than for electrons but the distinctive event signature gives a further handle to reduce backgrounds. Given the decay scheme of  $^{96}\text{Zr}$  to the  $0_1^+$  excited state of  $^{96}\text{Mo}$ , a cascade of two  $\gamma$ 's is expected to be detected.

For this analysis, two electrons and one or two  $\gamma$ 's only have therefore been considered. Since the individual times of flight for each of the particles is available in NEMO-3, it is possible to follow the path of a single  $\gamma$ -particle that interacted several times in the calorimeter. This can be done thanks to a technique called  $\gamma$ -tracking. If the use of this method increases the statistics in all of the analysis channels involving  $\gamma$ 's (e.g.  $1e1\gamma$ ), it is primarily of importance for channels where statistics is very low. This technique has been employed for  $2e2\gamma$  events. Figure 5.29 gives an example of an event studied here.

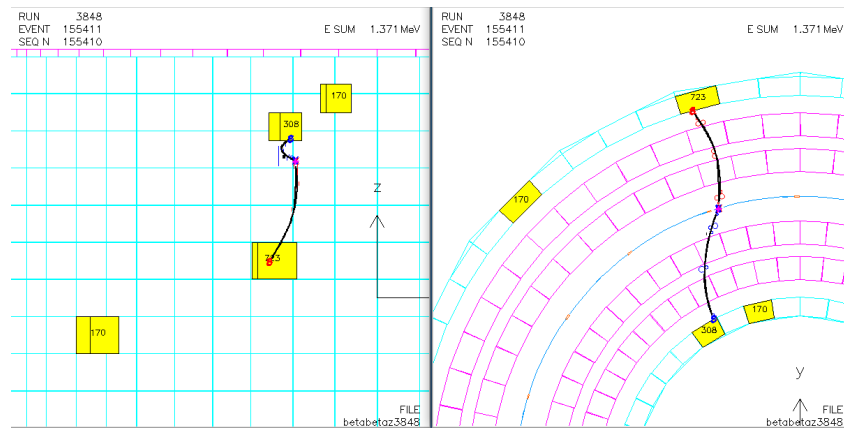


**Figure 5.29.:** *Example of a NEMO-3 event display in the 2 electrons  $N$   $\gamma$ 's channel. The two tracks correspond to two electrons. The unassociated calorimeter hits correspond to the  $\gamma$ -particles.*

T.o.f. cuts allow internal and external particles to be distinguished. The  $\gamma$ -tracking is of use when the t.o.f. of one of the  $\gamma$ 's is compatible with an internal origin and with an external origin for the other one. The standard cuts would reject this event. However, the  $\gamma$ -tracking enables another hypothesis for the external  $\gamma$  to be tested. If the times of flight are compatible with a first interaction of the internal  $\gamma$  followed



passing the analysis cuts. It has not been possible in the context of this work to generate more Monte-Carlo simulations due to the quantity that would have been necessary. In order to ensure that these isotopes cannot be expected to produce a significant amount of events,  $1e2\gamma$  and  $2e$  channels have been investigated since all of the backgrounds are single- $\beta$  emitters or  $\beta\gamma$  emitters.

For  $^{40}\text{K}$  on the surface of the scintillators, no MC event has been selected in  $2e$ . Given that producing a  $2eN\gamma$  event with two electrons from  $^{40}\text{K}$  requires that  $\gamma$ 's are produced via Bremsstrahlung, fewer events are expected. Therefore this contribution can be neglected in  $2eN\gamma$ .  $^{40}\text{K}$  in PMTs only contributes for a few events in the  $2e$  channel (2.4 events). The ratio of data events between  $2e$  and  $2eN\gamma$  is approximately 20 with similar analysis cuts except for the number of allowed  $\gamma$ 's. Hence, no significant number of events from  $^{40}\text{K}$  in the PMTs is expected.

A  $2eN\gamma$  event is a  $1e2\gamma$  event in which a second electron was produced via a Möller effect or a Compton scattering. Due to the probability of these interactions, it is a valid approach to consider that the number of expected MC events in the  $2eN\gamma$  channel is lower compared to  $1e2\gamma$ . Therefore, with no MC event selected for  $^{210}\text{Bi}$  on the surface of the wires in  $1e2\gamma$ , no contribution is expected in  $2eN\gamma$ . For  $^{214}\text{Pb}$  on the surface of the wires and in the source foil, less than 0.1 event is expected in  $1e2\gamma$ . Therefore it cannot significantly contribute in the  $2eN\gamma$  channel. For  $^{228}\text{Ac}$  from the PMTs and  $^{152}\text{Eu}$  on the surface of the scintillators, only few events are selected in  $1e2\gamma$  (2.3 and 1.8 respectively). There are 4 times less data events in  $2eN\gamma$  compared to  $1e2\gamma$ . Considering that another electron has to be produced for a  $2eN\gamma$  event, these two backgrounds can also be removed from the fit.

Finally, two isotopes have significant contributions in  $2eN\gamma$ :  $^{214}\text{Bi}$  from PMTs and internal  $^{40}\text{K}$ . However, two selections will be performed in order to reject background, as will be explained in the following sections. As visible in Table A.14, after the first selection only few expected events remain. Given that a stricter selection is performed, fewer events are expected. Hence these contributions will be assumed not to significantly contribute to the results in Table 5.16.

To summarize, no significant number of events can be expected from  $^{40}\text{K}$  (on the surface of the scintillators and in the PMTs),  $^{214}\text{Pb}$  (inside the foil and on the surface of the tracker wires),  $^{228}\text{Ac}$  (from the PMTs) and  $^{152}\text{Eu}$  (on the surface of the scintillators) in  $2eN\gamma$ .  $^{214}\text{Bi}$  (from the PMTs) and  $^{40}\text{K}$  (from the source foil) will

also be assumed not to contribute in the final fit.

Due to the low statistics in the  $2e2\gamma$  channel,  $2e1\gamma$  and  $2e2\gamma$  events will be treated together in a  $2eN\gamma$  channel ( $N \in \{1,2\}$ ). The total energy is therefore the sum of the electron energies and the  $\gamma$  energies. A fit of the total energy in the  $2eN\gamma$  channel is performed and displayed in Figure 5.32. The number of expected events are given in Table A.13.

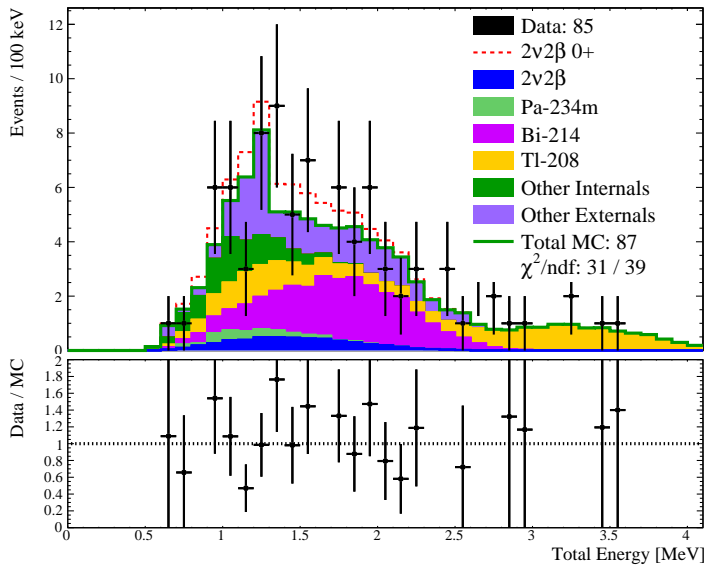


**Figure 5.32.:** *Distribution of the total electron energy in the  $2eN\gamma$ . Background activities have been fixed. No signal event is expected (see Table A.13) so an arbitrary scale has been applied on the signal distribution to make it visible.*

No signal is expected as a result of this fit. In order to reduce the impact of the uncertainties on the background, a selection optimising signal over background has been performed. It is based on Monte-Carlo simulations for each of the main background isotopes,  $2\nu\beta\beta$  and the potential signal. Once again, kinematic reconstruction in NEMO-3 is crucial. The energy of the unique  $\gamma$ -particle or the sum of the energies of the two  $\gamma$ 's is compared to the sum of the energies of the electrons. For this study, two-dimensional elliptic selections have been designed. The position of the ellipses in the plane  $(\Sigma_{E_\gamma}, \Sigma_{E_e})$  in Figure 5.33 illustrates the two cuts that have been performed in order to optimise the signal over background ratio.

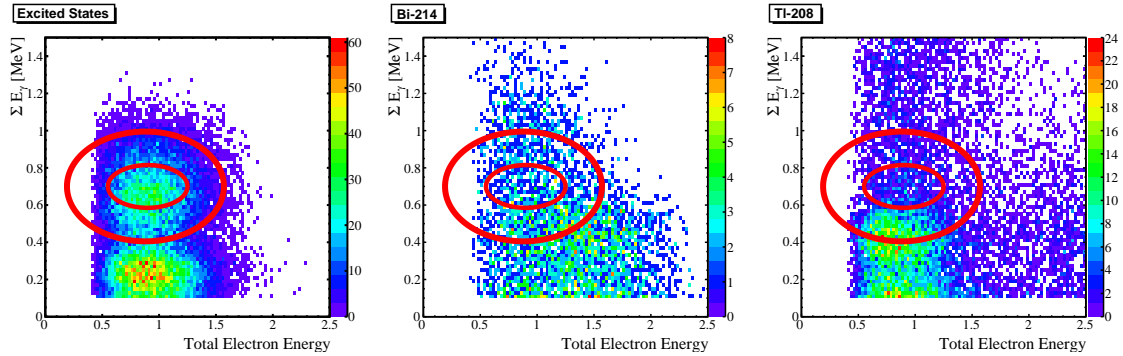


**Figure 5.33.:** Total  $\gamma$  energy as a function of total electron energy in  $2eN\gamma$  for, on the left the decay to the  $0_1^+$  excited state of  $^{96}\text{Mo}$ , in the middle  $^{214}\text{Bi}$  and on the right  $^{208}\text{Tl}$ . The red ellipses are the results of signal to background ratio optimisation with loose and strict conditions.

The first selection is aimed at selecting events with a large total  $\gamma$  energy in the signal distribution while rejecting contributions from the main backgrounds. It selects events in the largest of the two ellipses. It is important to note that although an essential part of the signal is expected at low energies, this cannot be selected. Indeed the background in this region is too large. As visible in Figure 5.33, this selection allows an essential part of the  $^{208}\text{Tl}$  background at low energies to be rejected. Figure 5.34 displays the results of the fit. The red dotted line illustrates the data excess over the expected background, assuming that all of these events come from the signal. The result of the fit of the total energy is presented in Table A.14.

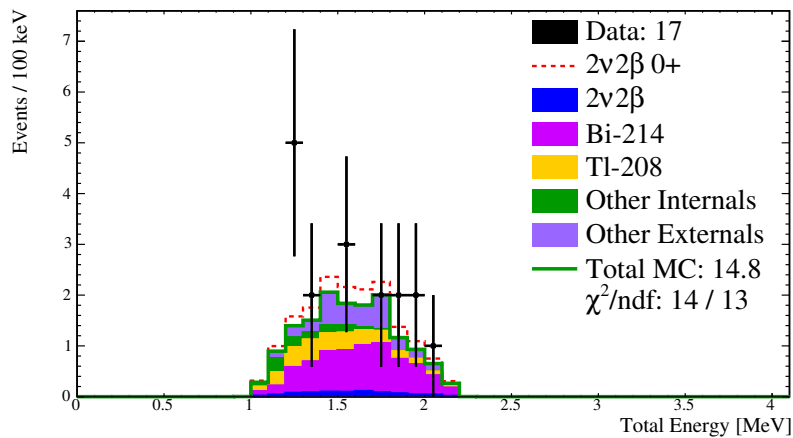


**Figure 5.34.:** Distribution of the total energy in the  $2eN\gamma$  channel after loose selection cut. No significant excess is visible here.

In order to further reject background, a stricter selection has been employed only considering events in the smallest ellipse in Figure 5.33. With a stricter selection, 17 % of the total number of MC signal events are kept. This drastically reduces all of the sources of background only keeping 6.5 % of  $^{214}\text{Bi}$ , 2.9 % of  $^{208}\text{Tl}$  and reducing the contribution from  $2\nu\beta\beta$  to ground state to only 3.9 %. A fit of the total energy available in the event is performed as illustrated in Figure 5.35. The results are displayed in Table 5.16.

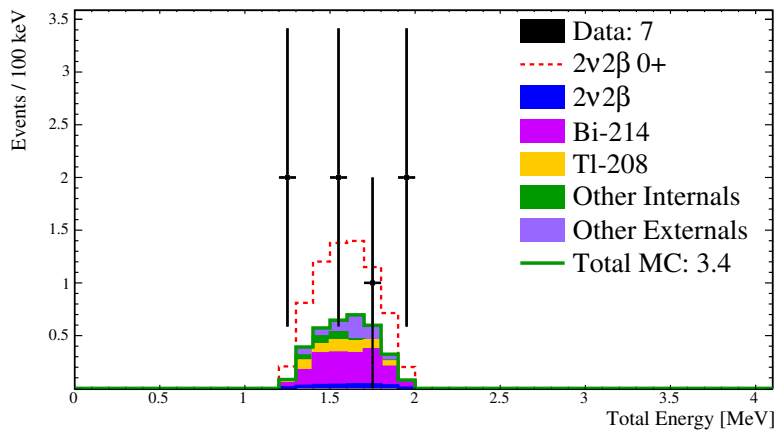


**Figure 5.35.:** *Distribution of the total energy in the  $2eN\gamma$  channel after strict selection cut. A small data excess is visible here, although not statistically significant.*

An excess in data is visible on this plot. The dotted red line corresponds to the distribution of the decay to excited states assuming that all of the events above background are signal events. The half-life that would correspond to this excess according to Feldman-Cousins 90% confidence intervals is:

$$T_{1/2}^{2\nu 2\beta}({}^{96}\text{Zr} \rightarrow {}^{96}\text{Mo}, 0_1^+) = 15.5_{-9.3}^{+101} \text{ (stat.)} \times 10^{19} \text{ y @ 90\% C.L.} \quad (5.32)$$

Using Poisson probabilities, there is a background fluctuation probability of 5.8 % which corresponds to a significance of approximately  $2\sigma$ . This is not enough to claim any indication on the observation of a signal, which would require at least  $3\sigma$ . A limit is set using the Feldman-Cousins confidence intervals. For that computation, 7 data events were available of which  $3.4 \pm 0.6$  (stat.) background events were expected. The worse case scenario has been assumed for the limit setting. The computation therefore assumes 7 data events and 4 background events.

Isotopes	Selected MC Events	MC Efficiency	Expected Events
$2\nu2\beta$	224	$2.2 \times 10^{-5}$	0.20
$^{228}\text{Ac}$	14	$3.5 \times 10^{-6}$	0.09
$^{234m}\text{Pa}$	2	$2.2 \times 10^{-7}$	0.02
$^{212}\text{Bi}$	17	$4.3 \times 10^{-6}$	0.13
$^{214}\text{Bi}$	298	$7.5 \times 10^{-5}$	1.70
$^{208}\text{Tl}$	601	$6.0 \times 10^{-5}$	0.58
Mylar $^{214}\text{Bi}$	33	$3.3 \times 10^{-7}$	0.08
SFoil $^{214}\text{Bi}$	15	$1.4 \times 10^{-7}$	0.12
SWire $^{214}\text{Bi}$	18	$1.2 \times 10^{-8}$	0.34
$^{208}\text{Tl}$ PMT	1	$1.5 \times 10^{-11}$	0.13
Leakage $^{150}\text{Nd}$	-	-	0.07
<b>Total Background</b>	-	-	3.4
$2\nu2\beta$ ( $0^+ \rightarrow 0_1^+$ )	5314	$2.7 \times 10^{-3}$	3.7
<b>Total MC</b>	-	-	7.1
<b>Data</b>	-	-	7

**Table 5.16.:** Result of the fit of the  $2eN\gamma$  channel after strict selection cuts. Number of selected Monte-Carlo events, Monte-Carlo efficiencies and number of expected background events. The number of events attributed to signal is the result of the fit. All of the activities have been fixed. When no Monte-Carlo events passed the selections, the isotope has not been taken into consideration.

Therefore the first limit with NEMO-3 data on the half-life of  $2\nu\beta\beta$  decay to excited states has been set assuming no signal has been observed at:

$$T_{1/2}^{2\nu2\beta} (^{96}\text{Zr} \rightarrow ^{96}\text{Mo}, 0_1^+) > 6.67 \times 10^{19} \text{ y @ 90\% C.L} \quad (5.33)$$

This value is comparable with the current best limit set at  $6.8 \times 10^{19}$  y [87]. It was obtained in a HPGe with an exposure of  $0.43 \text{ g} \cdot \text{y}$  while this analysis was performed with  $49.4 \text{ g} \cdot \text{y}$ . The limit set here is lower than the previous one due to the presence of the excess in data.



implied a difference of 25% in the number of events with a data excess of 79 events. Table 5.17 summarises the different contributions to the systematic uncertainty.

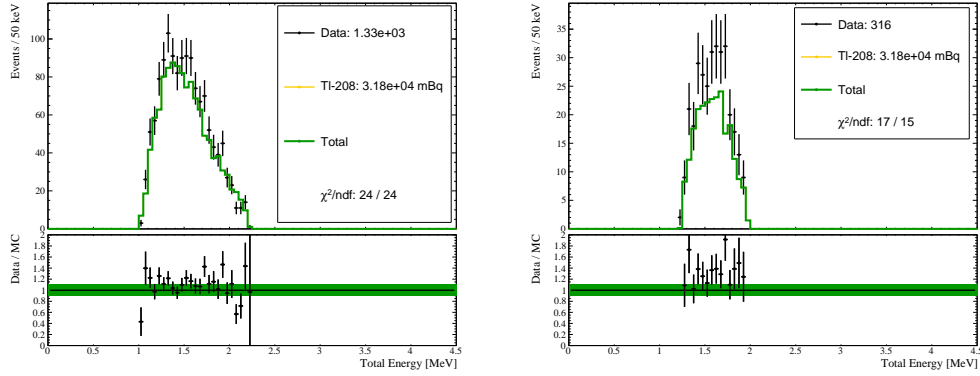


**Figure 5.37.:** *Distribution of the total energy in the 2 electrons and  $N$   $\gamma$ -particle channel after selection cuts in  $^{232}\text{U}$  (loose selection on the left and strict selection on the right).*

Source of Uncertainty	Absolute Uncertainty [%]	Half-life Uncertainty [%]
Isotope enrichment	$\pm 1.4$	$\pm 1.4$
Detection efficiency in 2e channel	$\pm 5$	$\pm 7$
Energy calibration	$\pm 1$	+1.9 -0.6
Strict selection	$\pm 25$	$\pm 25$
$2\nu\beta\beta$	$\pm 8$	$\pm 0.3$
Internal $^{214}\text{Bi}$	$\pm 25$	+9.5 -1.4
Internal $^{208}\text{Tl}$	$\pm 9$	$\pm 0.3$
Other Internals	-	+0.1 -0.3
External background	$\pm 20$	$\pm 0.4$
Radon background	$\pm 21$	+1.3 -1.2
Total systematic uncertainty	-	+27.7 -25.4

**Table 5.17.:** Systematic uncertainties for  $2\nu\beta\beta$  to excited states.

A total uncertainty of  $^{+27.7}_{-25.4}$  % has been estimated. Using ROOT TLimit CL<sub>s</sub> method and including these systematic uncertainties, a limit on the half-life of  $2\nu\beta\beta$  decay to excited states can be set at:

$$T_{1/2}^{2\nu\beta\beta} (^{96}\text{Zr} \rightarrow ^{96}\text{Mo}, 0_1^+) > 5.85 \times 10^{19} \text{ y @ 90\% C.L.} \quad (5.35)$$

This value is lower than the one set with the Feldman-Cousins since the systematic uncertainties are large.

# Chapter 6.

## The SuperNEMO experiment

*“As you cannot do what you want, want what you can do.” - L. da Vinci*

### 6.1. SuperNEMO and underground laboratories

As already explained in Chapter 4, NEMO detectors were installed underground in the LSM under 1700 m of rocks or 4800 m.w.e.. Several locations would be available for the construction of these detectors throughout the world (see Figure 6.1).

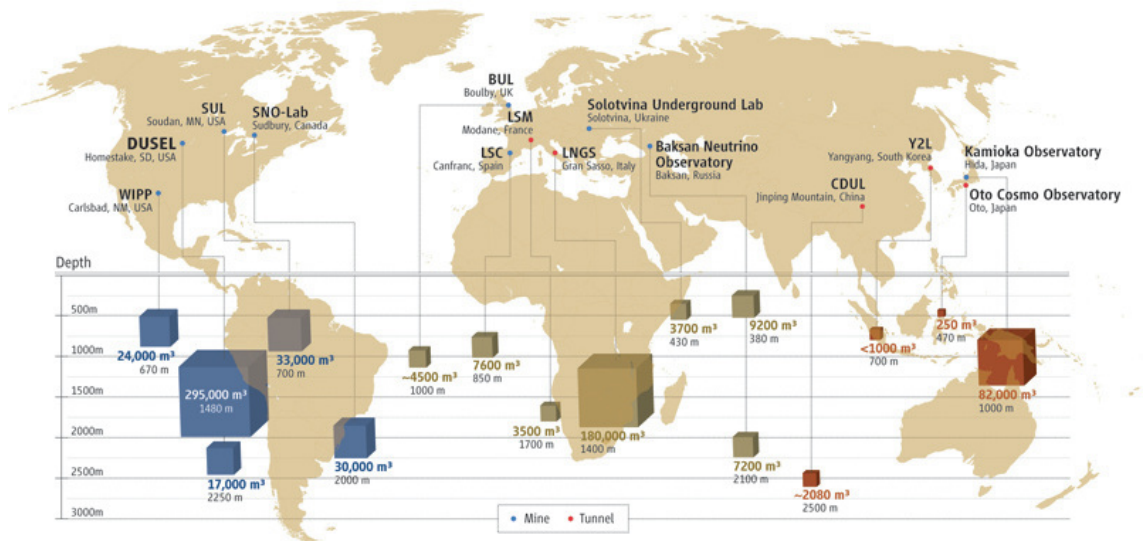


**Figure 6.1.:** *Underground facilities throughout the world, displaying depth and volume*

The LSM is one of the deepest laboratories in the world and an extension is about to be dug. As a reminder, cosmic rays fluxes are strongly reduced at a level of 4

$\text{m}^{-2} \cdot \text{d}^{-1}$ . The average level of radon in the air of the laboratory is  $15 \text{ Bq/m}^3$ . Due to this low background, NEMO-3 was installed at the LSM along with other detectors employed by the collaboration, like BiPo-1 (see Chapter 7) and several HPGe. The first SuperNEMO module, called *Demonstrator*, will be installed in this laboratory where NEMO-3 was located, and next modules in the extension (see Figure 6.2).

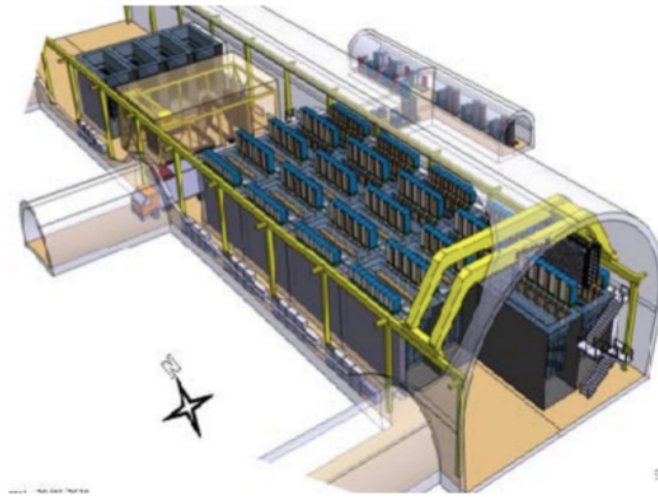


**Figure 6.2.:** *The 20 SuperNEMO modules in the extension of the LSM.*

Two other facilities host devices used by the SuperNEMO collaboration. The first one is the *Laboratorio Subterráneo de Canfranc* (LSC) under the Mount Tobazo in the Spanish side of the Aragon Pyrenees under 850 m of rock (2450 m.w.e.). The cosmic ray flux in this laboratory is around  $400 \text{ m}^{-2} \cdot \text{d}^{-1}$ . The preproduction module for BiPo-3 was operated in this laboratory. Today, the BiPo-3 detector (see Chapter 7) and several HPGe detectors are running at the LSC. Dark matter searches are also performed and a double- $\beta$  decay experiment (NEXT) is under construction in this laboratory. The average radon level is around  $80 \text{ Bq/m}^3$  which is significantly higher than the level in the LSM.

The second one is the Boulby Underground Laboratory. Boulby is a working potash and rock salt mine located in the North East of England. It is the deepest mine in the UK, at 1070 m (2805 m.w.e.), reducing cosmic ray muon flux to about  $30 \text{ m}^{-2} \cdot \text{d}^{-1}$ . The laboratory is built inside the mine tunnel surrounded by salt which is very low in natural radioactive elements. Hence radon level inside the laboratory is approximately  $2.5 \text{ Bq/m}^3$ . So far two HPGe detectors have been commissioned for material screening at Boulby. Dark matter research is also studied in this laboratory.

## 6.2. From NEMO-3 to SuperNEMO

### 6.2.1. Goals

Given the very good results of NEMO-3, a new-generation experiment has been designed: SuperNEMO. The SuperNEMO approach is unique being the only new-generation experiment that will fully reconstruct the topological signature of  $\beta\beta$  events and identify the different particles interacting in the detector. These advantages enable a high background rejection. Assuming appropriate statistics, the observation of a neutrinoless double- $\beta$  decay signal would also be accompanied by the identification of the physics mechanism involved. The expected sensitivity of SuperNEMO for  $^{82}\text{Se}$  assuming an exposure of 500 kg · y is:

$$T_{0\nu 2\beta}^{1/2} > 1.0 \times 10^{26} \text{ years @ 90\% C.L. and } \langle m_{\beta\beta} \rangle < 0.04 - 0.10 \text{ eV}$$

### 6.2.2. Design of SuperNEMO

SuperNEMO will further exploit the NEMO-3 *modus operandi*. The new detector will be planar and its most essential features have been improved. The baseline for the full detector is to be comprised of 20 independent modules, each with a source surface of  $5 \times 3 \text{ m}^2$  corresponding to 5 kg of  $^{82}\text{Se}$  with a thickness of 40 mg/cm<sup>2</sup>.

Each module will host 712 calorimeter blocks and 2034 tracking cells in 9 layers on both sides of the source foil (see Figure 6.3). Four C-sections will be assembled around the sources to form the complete tracker. The main walls of the calorimeter are constituted by 20 (horizontal)  $\times$  13 (vertical) calorimeter blocks. The complete  $4\text{-}\pi$   $\gamma$ -coverage represented a mechanical challenge. The other optical modules are comprised of two types of calorimeter blocks according to the part of the tracker they belong to: the so-called x-wall (vertical on the sides) and  $\gamma$ -veto (horizontal on top and bottom) frames. The 64  $\gamma$ -veto blocks and 128 x-wall blocks are made of 5" PMT re-used from NEMO-3, a new scintillator and light guides designed on the NEMO-3 principle. Only the x-wall blocks will be able to detect electrons, while tracking cells carriers will be located in front of the  $\gamma$ -veto blocks, making them only available for  $\gamma$ -detection. To compensate and increase the efficiency for the detection of double- $\beta$  decay electrons coming from the source

compared to NEMO-3, the height of the cells has been increased to more than 3 m. This also optimises the occupancy of the detector in the laboratory.

Given its good performance, the gas composition will not be changed compared to NEMO-3. As was the case for NEMO-3, the radiopurity of the detector is crucial. All of the components of the detector have been selected and most of them have been screened with HPGe. A new technology allows the emanation of the materials prior to their installation to be quantified and will be explained in the next section. Shielding has also been designed.

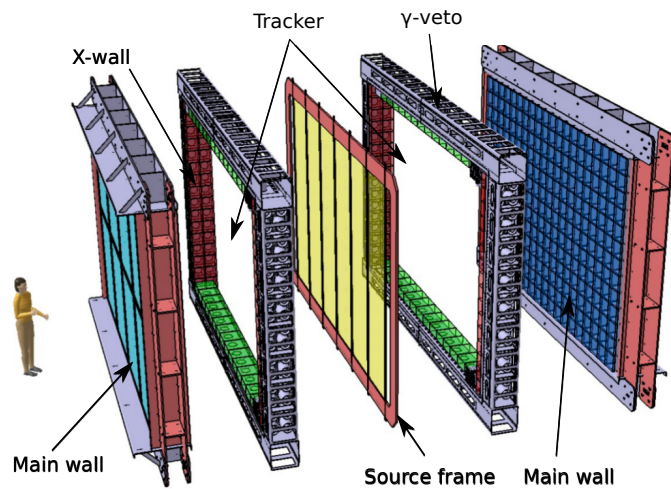


**Figure 6.3.:** *View of a SuperNEMO module. The frame holding the isotopic sources is in the centre. It is surrounded by the tracking chamber. The detector is closed by the two calorimeter walls.*

### 6.2.3. Improvements

Numerous improvements have been realised during five years of R&D for SuperNEMO. This was done to increase the half-life sensitivity to access rarer phenomena in the  $0\nu\beta\beta$  region. Figure 6.4 contains the final results of NEMO-3 on  $^{100}\text{Mo}$ .

Based on this measurement it is possible to identify the point of refinements explored for SuperNEMO. Considering equation 5.27 also enables to focus on three parameters to increase the half-life sensitivity: the mass, the number of background events and the energy resolution (background events in the ROI). The goals of these improvements, along with the general comparison between NEMO-3 and SuperNEMO are displayed in Table 6.1. Most of them are challenging and have already or will soon be completed.

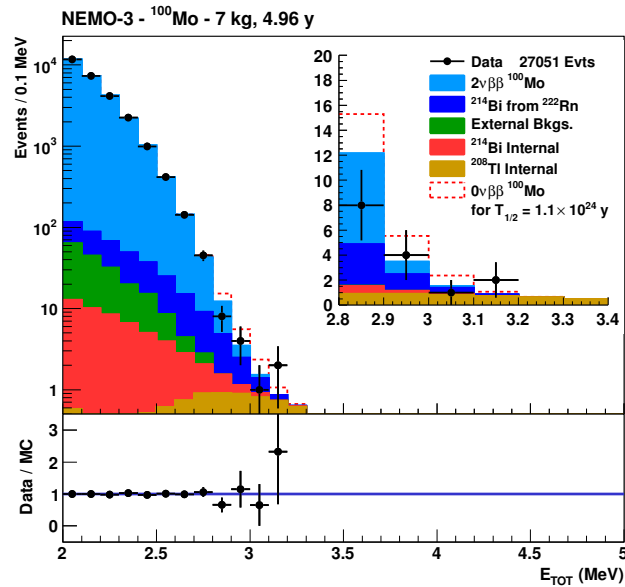


**Figure 6.4.:** Last results of the NEMO-3 experiment on  $^{100}\text{Mo}$ . The dashed red line corresponds to the limit on the neutrinoless double- $\beta$  decay [65].

### Isotopic sources and internal background

The first simple way to increase the sensitivity is to place a larger mass of isotope, up to 100 kg for SuperNEMO.  $^{82}\text{Se}$  has been selected because of its  $2\nu\beta\beta$  period approximately 13 times longer compared to  $^{100}\text{Mo}$ . This will contribute to reduce the number of background events. From Figure 6.4 it is visible that this was the dominant background above 2 MeV. The  $Q_{\beta\beta}$  values for  $^{82}\text{Se}$  and  $^{100}\text{Mo}$  are similar therefore the same isotopes are expected to contribute to the background. Moreover, strategies are currently being developed in order to enrich  $^{150}\text{Nd}$  and/or  $^{48}\text{Ca}$ . As they have a very high  $Q_{\beta\beta}$  value, they would have a very low background in the  $0\nu\beta\beta$  energy region.

One of the main points of refinement in SuperNEMO is about the contamination of the source foils (internal background). It can be seen on Figure 6.4 that  $^{208}\text{Tl}$  contamination inside the foil contributes to the background in the entire energy region of interest.  $^{214}\text{Bi}$  also contributes in almost all of this region. Therefore, the level of radiopurity required for SuperNEMO are extremely challenging (see Table 6.1). It is currently impossible to measure such levels with standard HPGe, and a dedicated detector has been designed and assembled by the collaboration (see Chapter 7). In order to achieve the purity requirements, several methods have been

		NEMO-3	SuperNEMO
Mass		6.9 kg	100 kg
Isotopes		$^{100}\text{Mo}$ 7 isotopes	$^{82}\text{Se}$ $^{150}\text{Nd}$ , $^{48}\text{Ca}$
Foil density		60 mg/cm <sup>2</sup>	40 mg/cm <sup>2</sup>
Energy resolution	@ 1 MeV	6.3   15 %	3.0   8 %
( $\sigma$   FWHM)	@ 3 MeV	3.4   8 %	1.7   4 %
Detector	tracking cells	6180	20 × 2034
	calorimeter blocks	1940	20 × 712
Radon in tracker	$\mathcal{A}(^{222}\text{Rn})$	5.0 mBq/m <sup>3</sup>	0.15 mBq/m <sup>3</sup>
Sources	$\mathcal{A}(^{208}\text{Tl})$	~ 100 $\mu\text{Bq/kg}$	< 2 $\mu\text{Bq/kg}$
contamination	$\mathcal{A}(^{214}\text{Bi})$	60 - 300 $\mu\text{Bq/kg}$	< 10 $\mu\text{Bq/kg}$
Total background (counts · keV <sup>-1</sup> · kg <sup>-1</sup> · y <sup>-1</sup> )		$1.3 \times 10^{-3}$	$5 \times 10^{-5}$
Sensitivity	$\mathcal{T}_{1/2}^{0\nu}$	> $1.1 \times 10^{24}$ y	> $1 \times 10^{26}$ y
(90 % CL)	$\langle m_{\beta\beta} \rangle$	< 0.33 - 0.87 eV	< 0.04 - 0.10 eV

**Table 6.1.:** Comparison between NEMO-3 performance and SuperNEMO requirements

tested. The same method of chemical purification as for NEMO-3 will be applied for the  $^{82}\text{Se}$  in SuperNEMO. Other possibilities based on distillation are currently being tested. These different solutions will be separately analysed in the Demonstrator. This will provide guidance for the next steps of the operation.

Concerning the source production, composite foils will be produced (see Chapter 4). Indeed the mechanical strength of  $^{82}\text{Se}$  metallic foils appeared not to be sufficient for 3 m-long sources. The irradiation method performed in NEMO-3 is still considered for the hole drilling in the backing film holding the  $\beta\beta$ -emitter in a mixture with PVA. This technique however needs to be improved, mainly the cleanliness conditions and the purity of the chemicals employed. Several source foils based on this irradiation method are already in measurement in the BiPo-3 detector (see Chapter 7). The PVA glue used for their assembling has also been tested and validated by BiPo-3. A laser-based technique has been tested and proved clean; however too few holes could be made for the correct drying of the sources. Therefore another technique has been studied using nylon or tulle netting. They are light material,

presenting holes naturally and enabling a good stiction of the composite samples. A measurement of tulle has been performed with the BiPo-3 detector proving it to be too contaminated but remains one of the current best solutions for the sources manufacturing. These sources will soon be screened in the BiPo-3 detector.

### Radon background reduction in the tracker

The radon contamination in the detector is another important point studied for the R&D of SuperNEMO. As visible on Figure 6.4,  $^{214}\text{Bi}$  events from radon represented an important contribution to the background. The two origins for radon are the diffusion from outside the tracking chamber and the internal emanation.

Two anti-radon tents (one inside the shielding and one outside) have been planed and will be installed right from the beginning of the experiment. This will reduce the amount of radon in the air surrounding the detector. The radon-free air factory based on radon trapping in charcoal and employed for NEMO-3 will be re-used in order to flush the tents and the air volumes next to the PMTs. Another step in the filtering of this air will be installed to increase the trapping capabilities. It has been thought of adding aerogel which has higher trapping capabilities than charcoal. Removing radon around the detector should reduce radon diffusion inside the tracking chamber.

In order to further isolate the detector it will be sealed with radon-tight materials. Diffusion setups have been developed by the collaboration to determine the tightest materials and several have been identified. A radon-tight glue (SBR) will seal the whole detector from the outside. In order to further reduce the radon diffusion in the tracker, the calorimeter walls will be covered with a 25  $\mu\text{m}$ -thick nylon foil in order to be isolated from the rest of the detector. This foil is thin enough not to degrade the energy resolution of the calorimeter and has a radon reduction factor of approximately 32000. It will be constituted of several bands glued together using STYCAST, another radon-tight glue.

The gas of the tracker will also be filtered before entering in SuperNEMO, as opposed to NEMO-3, in order to prevent any contamination from the gas containers. Given that this volume is not very large, a very efficient absorber can be purchased such as aerogel.

The detector itself can emanate radon and all of the internal materials have been selected. In addition, the size of the cells has been increased, reducing the number of wires by a factor of three. This reduces the amount of material inside the tracking chamber and therefore potential sources of background. Work has also been done in order to reduce the amount of material necessary to hold the tracker cells. Emanation measurements have been performed and are still carried out in order to measure the radon coming from all of the components of the tracker. Tests of emanation have also been realised for the two main potential sources of background in the calorimeter: the PMTs and the aluminised Mylar used for the calorimeter blocks wrapping. It appeared that no significant emanation was observed from the PMTs and only a small one coming from the Mylar. The total mass of Mylar being very small, this will not be an issue especially since they are located behind the nylon foil.

A radon concentration line has been developed in order to perform measurements of the emanation of the detector as the targeted levels are lower than measurable with standard radon detectors. The individual C-sections of the tracker are currently being successfully measured upon completion in emanation with this device. It will ultimately be installed at the LSM for radon contamination monitoring.

### Energy resolution of the calorimeter

An important parameter in double- $\beta$  decay experiments is the energy resolution. Indeed the signal being expected as a line, a good energy resolution produces a sharp peak. As visible in Figure 6.4, a relatively wide distribution was expected in NEMO-3 for  $0\nu\beta\beta$ . Moreover the backgrounds having a continuous energy spectrum, improving the energy resolutions tends to reduce their impact at high energy. It is the case of the contribution from  $2\nu\beta\beta$ , of  $^{214}\text{Bi}$  background inside the foil and from radon and of external backgrounds. As a result of the R&D program, the energy resolution for the main wall will be reduced by a factor of two thanks to improvements on several components of the detector.

First the source foils density has been reduced from  $60 \text{ mg/cm}^2$  to  $40 \text{ mg/cm}^2$  compared to NEMO-3 in order to reduce the energy losses inside the source. It should be noted that the Demonstrator will host sources with a density of  $53 \text{ mg/cm}^2$  in order to place a larger mass of  $^{82}\text{Se}$  (see section 6.3) as no event from  $2\nu\beta\beta$  is expected for an exposure of  $17.5 \text{ kg}\cdot\text{y}$ .

The  $\gamma$ -veto blocks have been optimised by removing one interface compared to NEMO-3 and by the polishing of their light guides. This decreases the energy resolution for  $\gamma$ -detection, however compensated by the use of larger blocks. The diminution of the number of tracking cells also limits potential electron scattering.

The main wall of the calorimeter is one of the parts of the detector that has been the most improved compared to NEMO-3. The performance of the low-radioactive PMTs have been increased by the use of 8" PMTs with a better quantum efficiency. Its value was 25% for NEMO-3 and is now above 30 % and on average around 37 % at 420 nm, knowing that it cannot exceed 50%. This corresponds to an increase of about 17 % in the number of photoelectrons detected. The high voltage dividers have also been improved in order to reduce the noise and increase the collection efficiency.

The scintillator blocks have also been optimised. The light collection is now better thanks to several improvements. One of them is the insertion of the PMTs inside the scintillator block. This allows the light-guides to be removed thus decreasing the number of interfaces and photon reflections. Their thickness has also been increased to about 15 cm in order to improve the  $\gamma$  detection efficiency. The chemical purity of the material constituting the scintillators has been improved, increasing the attenuation length for scintillation photons.

PVT (PolyVinylToluene) scintillators have been tested instead of PS (PolyStyrene), resulting in an increase in the light yield by 20 %. Due to a higher cost and the difficulty to manufacture calorimeter blocks of the required size, this solution has not been selected for the full detector. However, some PVT blocks will be installed in the Demonstrator to compare their performance.

The wrapping of the optical modules is similar to the one employed for NEMO-3. Teflon is wrapped around the sides of the scintillator block in order to entail the diffusion of the scintillation photons. This increases the number of photons reaching the photocathode of the PMT. The entrance face is also covered with aluminised Mylar, forming a mirror reflecting the light towards the PMT and also isolating the scintillator from possible light leaks. It also prevents UV light produced in the scintillator to enter the tracking chamber and to produce noise.

The average energy resolutions (FWHM) for the different calorimeter blocks in SuperNEMO will be 8 % for main walls, 12 % for x-walls and 20 % for  $\gamma$ -veto compared to 15 % for NEMO-3.

## 6.3. The SuperNEMO Demonstrator

### 6.3.1. Description of the detector

The construction of the successor to NEMO-3 has started with the first module, the Demonstrator. The aim of this Demonstrator is to reach NEMO-3's sensitivity in five months. The background should also be completely determined within a year of measurement. It will demonstrate the capability to produce the complete SuperNEMO detector, the purification of the source foils and finalise the technical aspects of the full detector. The measurement of the radon background, mainly from the emanation of the detector itself, is also one of the goals of the Demonstrator. Considering about 7 kg of  $^{82}\text{Se}$  placed in the Demonstrator (instead of the baseline 5 kg), it should be able to reach the same sensitivity as the phase I of the GERDA experiment. It should also be able to probe the effective neutrino mass region of Klapdor's claim [48].

Assuming no background in the  $0\nu\beta\beta$  region in 2.5 years, the sensitivity should reach, with an exposure of 17.5 kg·y:

$$T_{0\nu2\beta}^{1/2} > 6.5 \times 10^{24} \text{ years @ 90\% C.L. and } |m_{\beta\beta}| < 0.2 - 0.4 \text{ eV}$$

### 6.3.2. Demonstrator status

About 5.6 kg of enriched  $^{82}\text{Se}$  have already been produced and 4.6 kg have been purified. The purification process is now under testing with the BiPo-3 detector. It seems to be efficient but the first attempt at measuring it is with HPGe reached their sensitivity. The first four source foils in a baseline design have already been installed in the BiPo detector for qualification. The complete set of source foils are planned to be delivered at the LSM in 2016, assuming the purification techniques are proven to be efficient.

Another isotope has been investigated to be installed in the demonstrator:  $^{150}\text{Nd}$ . 37 g had already been measured in NEMO-3. Recent progress allowed several hundreds of gram to be made available which are going to be placed along with  $^{82}\text{Se}$ .

The calorimeter blocks are being assembled, both with 5" and 8" PMTs. The front-end electronic boards are already built, and control and trigger boards will be ready by the end the year. The magnetic shields for the PMTs have been manufactured. The main wall is being assembled under the form of calorimeter bricks. These bricks will be sent to the CENBG for the insertion of the PMTs and a first wall is about to be installed in summer 2015 at the LSM. The mechanical frame used to hold the calorimeter is already completed now. The second main wall is due to arrive at the LSM by the end of 2015.

All of the elements constituting the tracker frames have been produced and the 4 C-sections are assembled one by one. A wiring robot has been developed for automated drift cells production. The first and second C-section have been populated with tracker cells and are under commissioning at MSSL. They have also been successfully checked for radon emanation. The first two C-sections of the tracker should be at the LSM in autumn 2015 and the last two in spring 2016.

The commissioning of the different components of the full detector will be done along with their arrival at the LSM. The data taking is expected to start in 2016.

## 6.4. Future prospects

5 kg of  $^{150}\text{Nd}$  should be installed in the Demonstrator and solutions are investigated to operate SuperNEMO only with  $^{150}\text{Nd}$ . Its  $Q_{\beta\beta}$  is among the highest and its phase space factor is about 30 times more favourable compared to  $^{76}\text{Ge}$ . Therefore 5 kg of  $^{150}\text{Nd}$  is equivalent to 150 kg of  $^{76}\text{Ge}$ , more than GERDA phase II (not taking into consideration uncertainties on nuclear matrix elements computation).

Another opportunity would be that  $^{48}\text{Ca}$  becomes available, with the highest  $Q_{\beta\beta}$  of accessible  $\beta\beta$ -isotopes at 4.7 MeV. This implies that no background is expected in the energy region of interest which compensates a phase space factor less favourable than for  $^{150}\text{Nd}$ . However, new enrichment facilities would be required.

After the construction of the Demonstrator and the validation of the background level, the construction of the next modules could start in 2017.



## Chapter 7.

# BiPo prototypes and the BiPo-3 detector

*“You cannot test the suspension of a car with a seismometer.”*

- X. Sarazin, BiPo meeting

As already mentioned in Chapter 4, the two main background isotopes for  $0\nu\beta\beta$  are  $^{208}\text{Tl}$  and  $^{214}\text{Bi}$ . The radiopurity conditions for SuperNEMO are extremely severe (a few  $\mu\text{Bq}/\text{kg}$ ) for the  $\beta\beta$  source foil (see Chapter 6 (Table 6.1)). It is therefore currently impossible to measure such activities with HPGe (the best values are around 100  $\mu\text{Bq}/\text{kg}$  for a similar geometry and 33  $\mu\text{Bq}/\text{kg}$  for a raw copper sample without any mechanical or geometrical constraint [67]). HPGe detectors cannot reach higher sensitivities due to the surrounding  $\gamma$ -flux during the measurement and limited efficiencies at higher energies, even if promising improvements are realised. A more sensitive detector was thus designed as part of the R&D program of the SuperNEMO experiment: the BiPo detector. The aim of the BiPo-3 detector is to measure ultra-low contaminations in  $^{214}\text{Bi}$  and  $^{208}\text{Tl}$  inside SuperNEMO source foils (or any thin material). After validation of the manufacturing process and of the materials, this will provide an input for SuperNEMO. The principle of the BiPo detectors will be explained in the following sections, along with the construction, the calibration and the first measurements.

## 7.1. Principle of the BiPo detectors

### 7.1.1. Detection principle

**BiPo cascades** Both the decay chains of  $^{238}\text{U}$  and  $^{232}\text{Th}$  are comprised of a single  $\beta$ -decay of bismuth, followed by a delayed  $\alpha$ -decay of polonium (see Figure 7.1). Table 7.1 contains the important characteristics of these so-called *BiPo cascades*. Their existence has been at the origin of the BiPo detectors. The time-delayed coincidence provides a strong signature for BiPo events. This efficiently reduces background and therefore increases the sensitivity of these ultra-low contamination measurements.

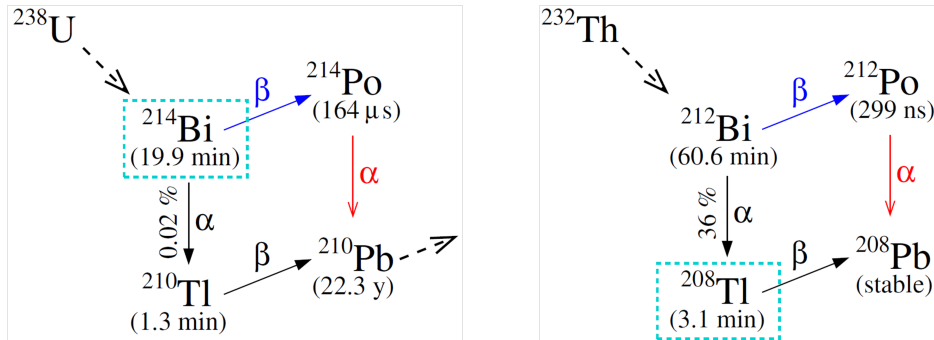


**Figure 7.1.:** *BiPo cascades in  $^{238}\text{U}$  (on the left) and  $^{232}\text{Th}$  (on the right) decay chains. The cyan boxed isotopes are the backgrounds for double- $\beta$  decay.*

	$^{212}\text{BiPo}$	$^{214}\text{BiPo}$
<b>Maximum energy of the electron (<math>Q_\beta</math>)</b>	2.25 MeV	3.27 MeV
<b>Energy of the <math>\alpha</math>-particle</b>	8.78 MeV	7.69 MeV
<b>Half-life of the <math>\alpha</math>-decay</b>	$^{212}\text{Po}$ : 299.2 ns	$^{214}\text{Po}$ : 164.3 $\mu\text{s}$

**Table 7.1.:** Characteristics of the BiPo cascades

**Detection method** The BiPo-3 detector consists of an array of face-to-face optical submodules made of 5" low-radioactivity PMTs coupled to ultra-radiopure organic polystyrene scintillators with a PMMA light guide (see Figure 7.2). The scintillator surface is covered with ultra-pure aluminium in order to enhance light collection. The light-guide collects the scintillation light toward the PMTs. It is wrapped with white Tyvek to improve further the light collection. Tyvek was used

instead of aluminised Mylar for its mechanical strength. A black film also wraps the optical submodules in order to prevent optical cross-talk from one to another. The measured samples are placed in the centre of the detector, sandwiched between the scintillators. In order to reduce the background, passive shielding has been designed to isolate the detector from radioactivity in its environment.

The BiPo-3 detector records events as presented in Figure 7.2 (left). A BiPo event originates from a contamination of the source foil in  $^{232}\text{Th}$  or  $^{238}\text{U}$  or their daughter nuclei. The different delay times between the two signals allows the distinction between  $^{212}\text{Bi}$  and  $^{214}\text{Bi}$  events. Several topologies are possible for the detection of a BiPo event. The two particles can enter the same scintillator or opposite ones. Only the *back-to-back* topology ( $\sim 50\%$  of all events) will be considered for the analyses presented in this chapter. This topology reduces the background by removing the contribution from the volume of the scintillators (see section 7.1.4). It has to be noted that in the first BiPo prototype, BiPo-1, the background in the same-side topology was estimated to be approximately six times higher than in the back-to-back topology [88].

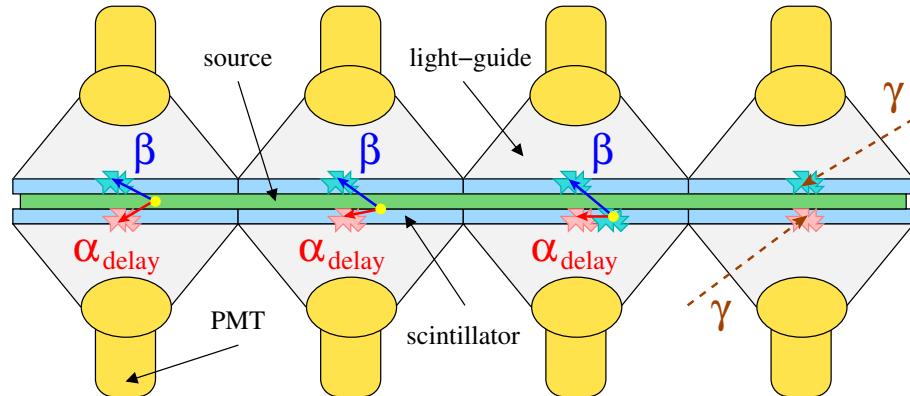


**Figure 7.2.:** *Detection principle of the BiPo detectors. On the left, a signal event coming from the source where the electron deposits its energy in one scintillator and the  $\alpha$ -particle in the opposite one. The three other are background events with in the middle left a surface contamination of the scintillators, in the middle right a contamination in the volume of the scintillator and on the right random coincidences due to two  $\gamma$ -particles.*

### 7.1.2. The data acquisition system

The data acquisition of the BiPo detectors has been designed to observe delayed coincidences. The acquisition chain consists of a trigger board, a delay function,

a Maticq board and a PC interface (see Figure 7.3). The interface, or controller board, sends instructions to all of the elements of the chain via a VME bus. The trigger board is designed to send a logic signal to the Maticq board to start the digitization of the pulse. It also sends the PMT signal through 30 m long cables used as a delay function to allow this digitization. The attenuation of the signal of 15 to 20% in these cables is not an issue for the performance of the acquisition system. After a first pulse is recorded, the trigger board waits for a second pulse to arrive and can be paused during up to 1 ms until a second trigger occurs for  $^{214}\text{Bi}$  study. If not, the system is reset.

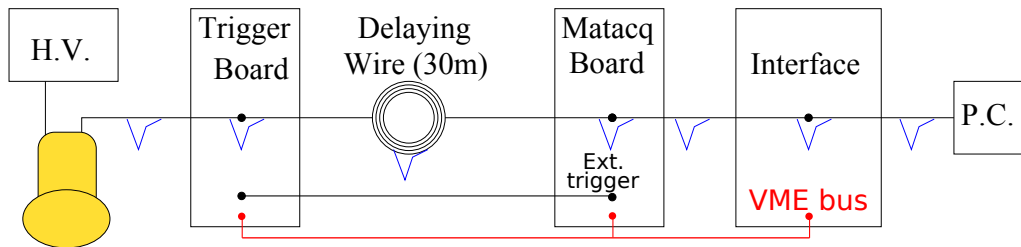


**Figure 7.3.:** Schematic of the acquisition chain used in BiPo detectors. In red the VME bus controlling all of the elements of the acquisition chain.

Pulse digitization is performed using VME sampling electronics, the Maticq boards, and allows all of the information about the signals to be kept. Three steps are necessary [89]. The first one is the acquisition phase for the sampling of the incoming analogue signal from the PMT and its storage in a circular analogue memory. 2460 data points are taken before the acquisition stops. The second phase is the conversion of the analogue signal into a digital one. The final phase is the reading of the memory during a few ms.

The precision of the sampling in amplitude is around 0.25 mV, thanks to a dynamic range in amplitude of 1 V ( [-100, 900] mV) available with a coding in 12 bits. This is also the average electronics noise level in the acquisition system. The digitization can be done within a 2.5  $\mu\text{s}$  time range thanks to a sampling of 1GS/s. 1500 points are used for the prompt particle energy deposit and 960 for the delayed particle energy deposit.

This acquisition system offers many advantages such as the individual particle energies and the arrival times. It has a very low threshold for the detection of the delayed  $\alpha$  at the level of a single photo-electron. Additional thresholds of approximately 100 keV (50 mV) for the prompt signal and 20 keV (10 mV) for the delayed

signal are imposed for noise rejection. The precision of the sampling enables a discrimination between electron and  $\alpha$ -particles. A survey of the performance of the PMTs can be done from the shape of the pulses. It can also be used to remove noise coming from the scintillation of the light guide thanks to a pulse-shape analysis (see section 7.8.1).

### 7.1.3. Event reconstruction

For each event detected in the BiPo detector, several pulses are sampled. The time of the pulse is determined using a constant fraction discrimination (cf) on the digitised pulses, which finds the time corresponding to a given percentage of the maximum amplitude (see Figure 7.4). A region of interest in time is also defined. The integral of the pulse over this region of interest, or charge, is directly proportional to the energy deposited in the scintillator. Two charges have been defined, the total charge (providing the energy after calibrations) and the tail charge. The tail time has been defined as part of the  $\beta/\alpha$  discrimination optimisation (see section 7.7.4). It corresponds to the starting time for the tail charge integration, a constant time after the cfd time. The amplitude of the pulse is also proportional to the energy and is kept at the reconstruction level. A pedestal value is calculated, corresponding to the average value of the amplitude over a few ns before the beginning of each pulse. Its value is subtracted from each sampling point for the computation of the charge and proved to be stable with time.

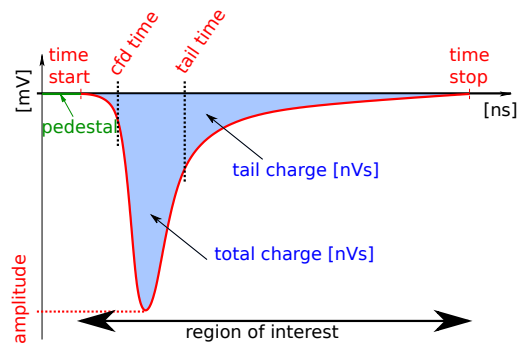


Figure 7.4.: Schematic of a sampled pulse in the BiPo detector.

#### 7.1.4. Background components

The three major backgrounds for the BiPo-3 detector are displayed in Figure 7.2. The middle-left plot depicts a surface contamination of the scintillator. This cannot be distinguished from events coming from the  $\beta\beta$ -source except for the  $\alpha$  energy. Indeed,  $\alpha$ -particles originating in the source foil lose part of their energy inside the foil and mainly contribute at low-energies. On the other hand, it is impossible for a surface contamination to cross the source foil, making these events contribute only as a peak at high energy.

Surface events can be due to a contamination of the scintillators or to a deposition of radon ( $^{222}\text{Rn}$ ) or thoron ( $^{220}\text{Rn}$ ). Radon is one of the main sources of background for BiPo events as it is very difficult to prevent it from entering the detector. It can diffuse between the source and the scintillator and mimic an event from the surface of the scintillator. To reduce this radon contamination as much as possible, the detector is flushed with radon-free nitrogen.

The second origin is the volume of the scintillator. Although the scintillators have been carefully selected for their radiopurity, some contamination might remain. This background can be rejected because there is a prompt signal in coincidence in both scintillators produced by the electron crossing both scintillators.

The last source of background corresponds to two  $\gamma$ 's hitting the scintillators (or a single  $\gamma$  after multiple Compton scattering) and creating random coincidences faking BiPo events. This is the dominant contribution to the counting rate. The lead shielding and the fact that the detector is placed in an underground laboratory reduce this counting rate. In addition, this kind of events has the signature of two electron events. In BiPo-1, a pulse shape analysis was used to decrease this background by a factor 10 (as BiPo events have an  $e^-/\alpha$  signature) [88]. This will also be applied in BiPo-3 (see section 7.9).

Figure 7.5 displays the pulses recorded in BiPo-3 for the different types of background. It has to be noted that for  $\alpha$ -particles, the charge of the pulse is higher than the one corresponding to an electron for a similar amplitude (see section 7.2).

The intrinsic background of the detector can be measured by the detector itself when no sample is placed between the scintillators leaving surface contamination

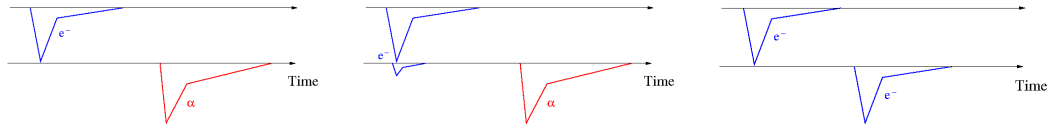


**Figure 7.5.:** Digitized PMT pulses recorded by the BiPo-3 detector. On the left in the case of a signal or surface contamination, in the middle for a bulk contamination and on the right for random coincidences from external  $\gamma$ s producing Compton electrons.

and radon as the only contributions at higher energies. An estimation of the random coincidences flux can also be made during this measurement.

## 7.2. Quenching of alpha-particles

The quenching of the energy of  $\alpha$ 's in plastic scintillators is due to their high ionization power. Birks' law [90] describes the relation between the energy deposition and the emitted light as in 7.1.

$$\frac{dL}{dx} = \frac{R_s \frac{dE}{dx}}{1 + kB \frac{dE}{dx}} \quad (7.1)$$

where  $\frac{dL}{dx}$  is the scintillation light output per unit of  $\alpha$ -track length,  $R_s$  is the scintillation efficiency defined as the ratio between the number of photons emitted and the deposited energy and  $kB$  is Birks' constant which can be interpreted as a saturation constant. As they intensely interact in the scintillator,  $\alpha$ -particles deposit their entire energy in a small volume. Therefore the scintillator is excited in a different way as for electrons and only part of their energy is visible through scintillation, the *quenched energy*. Energy levels with a longer de-excitation time are also excited producing a delayed scintillation. One of the direct consequence is to have a larger value for the tail charge (see Figure 7.4) of an  $\alpha$ -pulse due to the detection of this delayed scintillation in the tail of the main pulse.

The quenching factor is defined as  $E_Q = \frac{E_\alpha}{Q}$  where  $Q$  is the quenching factor,  $E_Q$  is the quenched energy and  $E_\alpha$  is the energy that would be reconstructed in the limit  $\frac{dE}{dx} \rightarrow 0$ . This energy-dependent factor also depends on the material. Figure 7.6 is the result of the measurements of the  $\alpha$ -quenching done at LAL. Blue points correspond to the measurement of an  $^{241}\text{Am}$  source emitting  $\alpha$ 's of 5.49 MeV with

Mylar absorbers of different thickness (1.5  $\mu\text{m}$  to 26.5  $\mu\text{m}$ ) to obtain  $\alpha$ 's with different energies. Red points were measured using Mylar as an absorber combined with the tagging of the  $\gamma$ -particle emitted during the  $\alpha$ -decay of  $^{241}\text{Am}$ . There is an important discrepancy between these two measurements at lower energies due to the use of two different functions for the fit; however a good agreement is reached at higher energies. The red curve is not constrained at lower energies as no measurement was performed below 3 MeV but due to the thresholds applied in the analysis, this will not have an important impact. The two points at high energy were determined with BiPo-3 data from aluminium foil. Data from  $^{212}\text{BiPo}$  events allowed a quenching for an energy of 8.78 MeV to be measured. As will be explained in section 7.9.1, the point at 7.69 MeV has been obtained from the measurement of radon deposited on the surface of the scintillators. Data are fitted by an approximate function describing Birks' law from the Mylar measurement and the BiPo points.

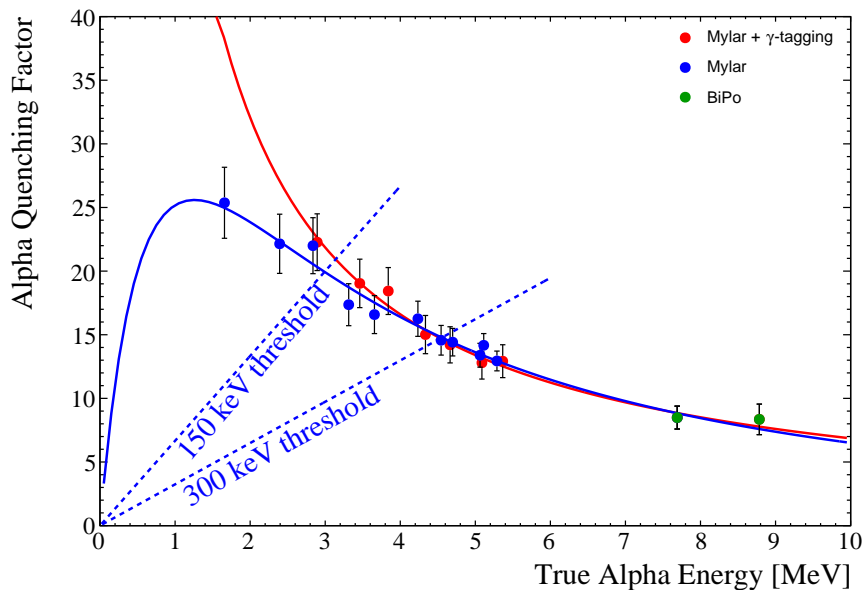


**Figure 7.6.:**  $\alpha$ -quenching factor in plastic scintillators. Two setups were designed. The blue points used for this analysis, are the measurement of an  $^{241}\text{Am}$  source with different thickness of Mylar. The red points were measured with air replacing Mylar. The green points were obtained with BiPo-3 data.

### 7.3. R&D for the BiPo detector

A R&D program started in 2006 and several prototypes have been designed at various stages of the development. The aim was to demonstrate the feasibility to

measure low-activities with the BiPo technique and to determine the achievable sensitivity for ultra-low measurements.

### 7.3.1. BiPo-1

The first prototype, BiPo-1, was installed at the LSM and acquired data from 2007 to 2011 [88]. It was made of 20 high-purity modules with aluminised scintillators, shielded against external backgrounds with passive lead walls. The background measurement was performed with an empty module. With an active surface of  $0.8 \text{ m}^2$  and with a measurement time of one year, a scintillator surface activity in  $^{208}\text{Tl}$  of  $1.4 \pm 0.2 \text{ } \mu\text{Bq}/\text{m}^2$  was measured. With this level of background, and extrapolated to a BiPo-3 detector with a  $12 \text{ m}^2$  surface, 6 months were estimated to be necessary to reach the required sensitivity of  $2 \text{ } \mu\text{Bq}/\text{kg}$ . This would have enabled the measurement of almost all of the sources of a SuperNEMO module at once. A surface contamination of  $150 \pm 20 \text{ } \mu\text{Bq}/\text{m}^2$  was measured in  $^{214}\text{Bi}$  [89]. The volume contamination was also studied thanks to 10 cm thick scintillators to maximise their detection efficiency. Finally the stability of the PMTs was monitored in dedicated modules using a deposited  $^{241}\text{Am}$   $\alpha$  source. The  $\beta/\alpha$  discrimination was implemented and greatly decreased the background level.

The validation of the BiPo measurement technique to measure the SuperNEMO  $\beta\beta$ -source foils was performed with a module equipped with a calibrated aluminium foil [88]. Thanks to this success, the full BiPo-3 detector has been based on the BiPo-1 technique. Using BiPo-1 results on background, the estimated sensitivity of BiPo-3 for SuperNEMO sources made of  $40 \text{ mg}/\text{cm}^2$  is  $\mathcal{A}(^{208}\text{Tl}) < 3 - 4 \text{ } \mu\text{Bq}/\text{kg}$  in 6 months [88]. Measuring  $10 \text{ } \mu\text{Bq}/\text{kg}$  in  $^{214}\text{Bi}$  required some improvements of the detector mainly concerning the radon background.

### 7.3.2. BiPo-2

The second BiPo prototype was made of two scintillator plates (see Figure 7.7). One of its advantage was a polishing making the surface aluminisation not necessary. The light emitted after the energy deposition was propagated by total internal reflection until the edges and collected by several 3" PMTs allowing a precise interaction position reconstruction. The other main advantage was the possibility to have a more compact detector.

This prototype was assembled in 2007 and installed at the LSM in 2008 and validated using an aluminium foil as was done in BiPo-1. The efficiency for back-to-back events was proved to be similar to the one obtained by BiPo-1.

No possibility of a  $\beta/\alpha$  discrimination was found to be possible. This was one of the limitations of this prototype. Optical cross-talk was also found to be too large, reducing the random coincidence rejection capability. This was the main issue as the coincidence rate was more than 40 times larger than for BiPo-1. As a consequence, the BiPo-2 design has not been selected for the construction of a large BiPo detector.

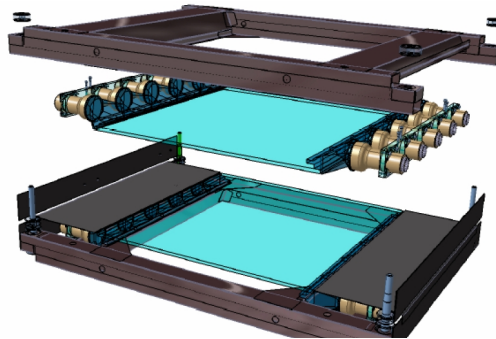


Figure 7.7.: Schematic of the BiPo-2 prototype.

### 7.3.3. Preproduction BiPo-3 module

#### Design

A preproduction module of BiPo-3 was built at LAL at the beginning of 2011 and set up in the LSC from March 2011 until July 2012. Indeed, there was not enough free space in the LSM to host the full BiPo-3 detector. It was aimed at measuring the background in this new environment and validating improvements necessary to reach the required sensitivities for SuperNEMO from BiPo-1. It was comprised of two face-to-face optical submodules (see Figure 7.8) for a total active surface of  $30 \times 30 \text{ cm}^2$ . The reduction of the radon background, the enhancement of the uniformity of the scintillator response and the cleanliness conditions for the assembly of the detector were tested.

It has been estimated that the radon background was high in BiPo-1 due to a lack of efficiency of the flushing system. A dedicated radon-free nitrogen gas flushing system was implemented in the preproduction module. It was proved that nitrogen coming

from the evaporation of liquid nitrogen is an appropriate gas for its radiopurity. Lead and water shielding was set up in order to reduce the background coming from the laboratory. The detector itself was placed inside an iron tank.

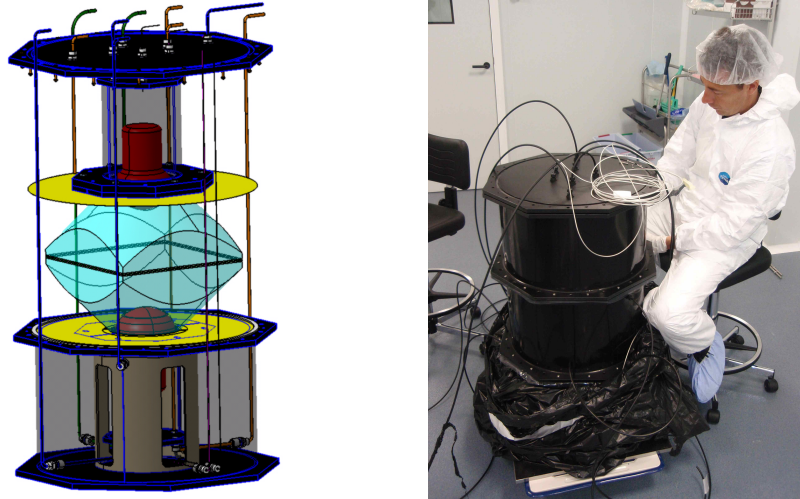


**Figure 7.8.:** *Left: Schematic of the BiPo-3 preproduction module, in red the PMTs, in cyan the light guides and the scintillators in between and in yellow a radon-tight film. Right: the BiPo-3 preproduction module in the LSC clean room.*

### Purpose and improvements

The first point was to determine the final detector design. The shape of the light guide was optimised thanks to optical simulations so as to maximise light collection. For BiPo-1, the non-uniformity between the centre and the edges of the scintillator could reach around 40% with smaller scintillators compared to BiPo-3. The use of hexagonal light guides instead of squares reduced the surface response non-uniformity to almost 15%, as will be demonstrated in section 7.6.

The thickness of the scintillators was also studied with two different scintillators (2 and 3 mm). It has to be small in order to limit the counting rate of the detector. The surface of the scintillators was increased from  $20 \times 20 \text{ cm}^2$  to  $30 \times 30 \text{ cm}^2$ . This reduced the cost of the detector for the same sensitive surface.

Special care was also taken in order to preserve the ultra-low radioactivity of the detector components during the construction. Compared to BiPo-1, a new device dedicated to evaporate only ultra-pure aluminium on the surface of the scintillators was employed.

The gas flushing system was optimised to reduce the radon background. There is internal emanation of radon in the detector and a high level of radon outside it (higher than in the LSM, see section 6.1). Therefore a radon-free gas flushing is compulsory.

Finally this preproduction module enabled the preparation of data analysis for the full detector and the optimisation of the tools for reconstruction, simulation and event selection and especially the  $\beta/\alpha$  discrimination.

## Operation

The preproduction module was calibrated using  $\gamma$  sources similarly to the full BiPo-3 detector (see section 7.7).

During the running of the prototype at the LSC several setups have been operated. The main results of this prototype concerns the measurement of the background and its reduction. Three phases have been realised:

- Phase 1: surface background measurement with the two scintillators in contact;
- Phase 2: radon background measurement with spacers between scintillators;
- Phase 3: aluminium calibration foil measurement.

**Phase 1: Background measurement** In this phase, no source foil has been introduced and the scintillators are in contact. No  $^{212}\text{BiPo}$  events were recorded for an exposure of  $5.3 \text{ m}^2 \cdot \text{d}$  and 29 d, yielding the limit on the surface contamination:

$$\mathcal{A}(^{212}\text{BiPo}) < 8.0 \text{ } \mu\text{Bq}/\text{m}^2 \text{ @ } 90\% \text{ C.L.} \quad (7.2)$$

This result can be compared to the  $1.5 \pm 0.3$  (stat.)  $\pm 0.3$  (syst.)  $\mu\text{Bq}/\text{m}^2$  [88] measured in BiPo1 with almost  $365 \text{ m}^2 \cdot \text{d}$  and does not indicate a higher surface contamination.

For the measurement in  $^{214}\text{BiPo}$ , one event has been observed corresponding to:

$$\mathcal{A}(^{214}\text{BiPo}) = 5.6 \text{ } \mu\text{Bq}/\text{m}^2 \in [0.6, 24.5] \text{ @ } 90\% \text{ C.L.} \quad (7.3)$$

This measurement shows a significant improvement compared to BiPo-1, with a factor 30 smaller. The raw counting rate was compared between the two scintillators and appeared to be too high for the 3 mm-thick scintillator [84]. Therefore 2 mm-thick scintillators have been selected for the full BiPo-3 detector.

**Phase 2: Radon Measurement** To optimize the gas flushing system, the radon level between the scintillators was increased by setting a 3 cm gap between scintillators with Teflon spacers. Teflon is a radiopure material and should not contribute to the background. In this phase, only  $^{214}\text{Bi}$  events were studied. Looking at the number of  $^{214}\text{BiPo}$  events versus time in Figure 7.9 several periods are identifiable.

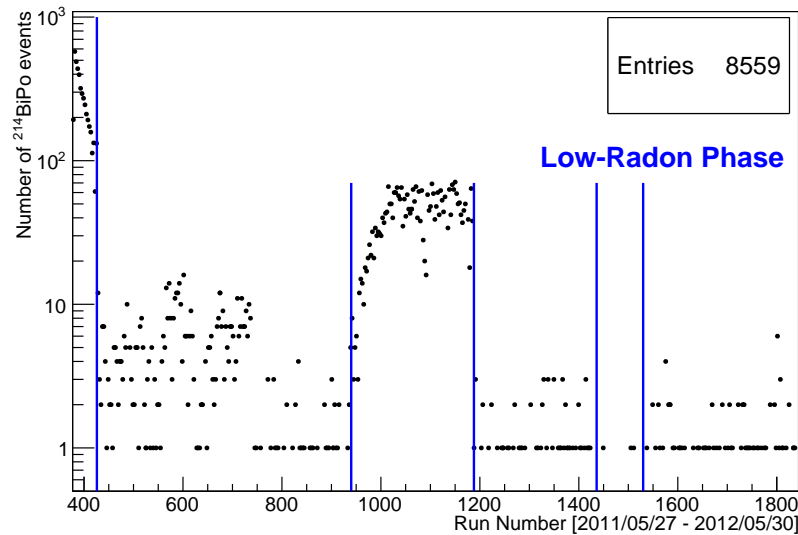


**Figure 7.9.:** *Number of  $^{214}\text{BiPo}$  events measured versus time (1 run  $\simeq$  6h) in the BiPo-3 preproduction module. A large number of events is visible in the first runs coming from the decay of radon trapped in the detector after its closure. Several other periods are due to the tests of the gas flushing. A low-radon phase was achieved setting the optimal flushing conditions.*

The first one corresponds to a period without nitrogen flushing and following the closure of the detector. A large number of  $^{214}\text{BiPo}$  events were recorded as some radon was trapped from the air in the clean room. The decrease with time is due to radon decay combined with the gas flushing. In the following periods, several gas flow tests have been performed, visible as the variations in the observed number of  $^{214}\text{BiPo}$  events. A low-radon phase was achieved defining an optimal flushing configuration. In this period only 3  $^{214}\text{BiPo}$  events were observed in 23.3 days for

an activity of:

$$\mathcal{A}({}^{214}\text{BiPo}) = 3.5 \in [1.3, 8.5] \text{ mBq/m}^3 \text{ @ 90\% C.L.} \quad (7.4)$$

The equivalent surface contamination in the baseline design with a gap between scintillators assumed to be 200  $\mu\text{m}$ -thick is:

$$\mathcal{A}({}^{214}\text{BiPo}) = 0.7 \in [0.4, 1.0] \text{ } \mu\text{Bq/m}^2 \text{ @ 90\% C.L.} \quad (7.5)$$

It is worth noting that flushing a single capsule is easier than the full detector and a higher surface activity can be expected.

**Aluminium foil measurement** This is a reference measurement already performed in the previous prototypes. It is designed to check the efficiencies from Monte-Carlo simulations, data reconstruction and the detector response. For this measurement the foil was sandwiched between the scintillators (see Figure 7.10). The foil was measured in HPGe detectors and more details will be given in section 7.9.1.

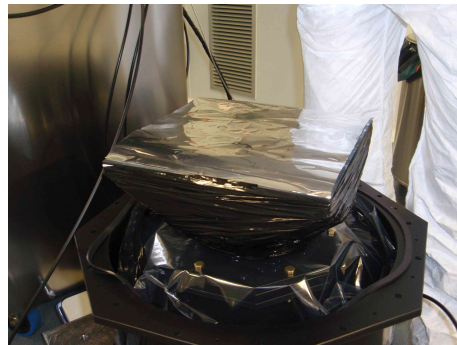


**Figure 7.10.:** *Aluminium calibration foil in the BiPo-3 preproduction module*

Due to the lack of statistics, the activity measurement was not very precise. One of the interesting outputs of this calibration was the design of a surface background rejection method. A radon source was introduced in the gas flushing system to increase the  ${}^{214}\text{Bi}$  background between the source and the scintillators. The energy spectrum for the  $\alpha$ 's that was obtained is displayed in Figure 7.11. Two distributions are visible here, the peak corresponding to the surface background and the lower energy part due to events inside the foil. Given the shape of these distributions, a rejection of the surface background was determined. Applying an upper energy

cut at 600 keV to the  $\alpha$ -energy enabled a reduction of a factor around 80 in the background efficiency while only reducing by 30% the source efficiency.

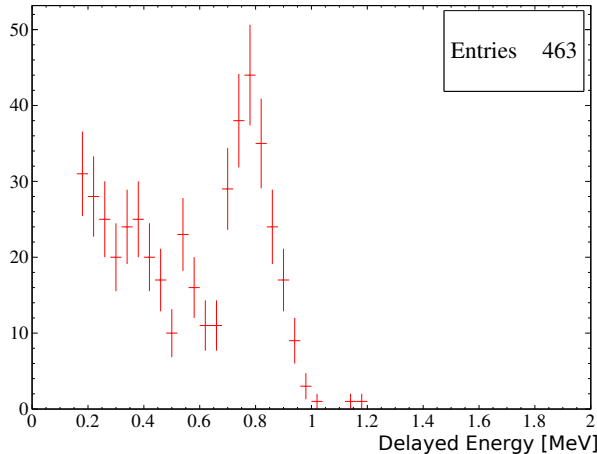


**Figure 7.11.:** *Delayed  $\alpha$  energy spectrum for  $^{214}\text{BiPo}$  events in phase 3 with the radon source. A peak is visible corresponding to the radon background. The low energy part is associated with the contamination coming from the aluminium calibration foil.*

## 7.4. GEANT4 Simulations

GEANT4 simulations have been produced with the SuperNEMO software, SN@ilWare. In particular, flexible geometry packages allowed us to accurately describe most of the features of the BiPo detectors. The BiPo simulations are used to understand the detector response and to compute the efficiencies for the detection of the different processes occurring in the detector: BiPo events from  $^{232}\text{Th}$  and  $^{238}\text{U}$  decay chains,  $\alpha$ - $\beta$  calibration for the optical submodules scans (see section 7.6),  $\gamma$ -calibration and external backgrounds such as  $\gamma$ 's from the laboratory and cosmic muons. They can be generated from any part of the detector. The BiPo-3 detector with its shielding and main elements has been simulated as in Figure 7.12.

## 7.5. The BiPo-3 detector

After the successful results obtained from the BiPo-3 preproduction module, the construction of the final BiPo-3 detector started in summer 2012. The first BiPo-3 module was installed at the LSC in June 2012 and the second one in early 2013. For the first time, the intrinsic background in 3 m long  $\beta\beta$  source foils can be measured

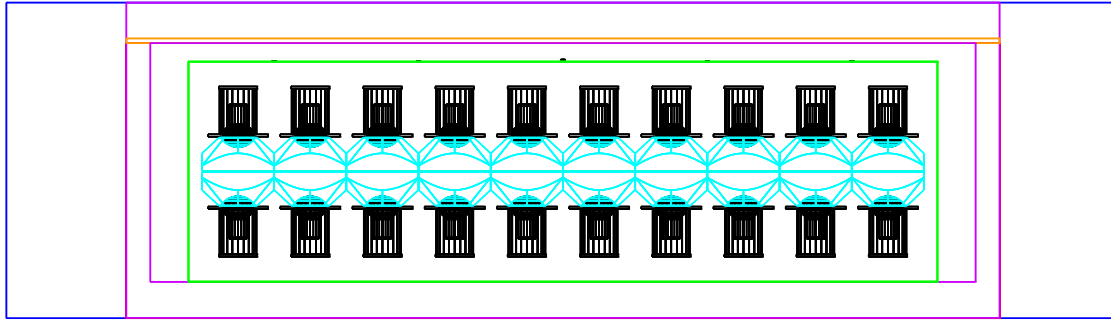


**Figure 7.12.:** *GEANT4 simulation of the full BiPo-3 module with the water shielding (blue), the lead shielding (magenta), the iron frame (green), the iron plate closing the detector (orange), the light guides (cyan) and the PMTs (black).*

prior to their installation in SuperNEMO. The detector is now taking data and several samples have already been measured.

### 7.5.1. Design

The final BiPo-3 detector is divided in two identical modules of  $3.0 \times 0.6 \text{ m}^2$ , each hosting 20 pairs of optical submodules. It has a total surface area of  $3.6 \text{ m}^2$  and can measure 1.44 kg of SuperNEMO source foil ( $40 \text{ mg/cm}^2$  which corresponds to a thickness of  $\sim 130 \text{ }\mu\text{m}$ ). The efficiency is only around few % due to the difficulty for  $\alpha$ -particles to escape the source foil. The design of the optical submodules is the same as for the preproduction module except that all of the scintillators are 2 mm thick.

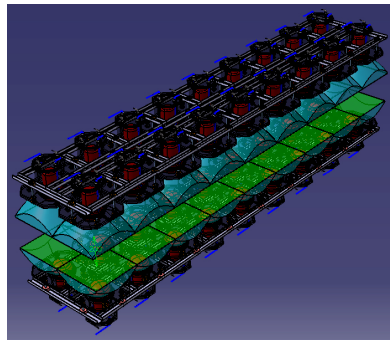


**Figure 7.13.:** *Schematic of one of the two modules of the final BiPo-3 detector.*

The full BiPo-3 detector can measure 8 strips of SuperNEMO source foils at the same time out of the 36 in total for one module. All of the optical submodules are assembled in a pure-iron mechanical frame closed by pure-iron plates and sealed to increase the efficiency of the gas system. All of the material inside the detector has been selected for their radiopurity.

High voltage is provided to both modules by a CAEN HV system. A VME crate was allocated to each of the modules for the acquisition Maticq boards, allowing them to be independent. The high voltages have been set on all of the PMTs at a nominal gain of  $G = 1 \times 10^6$ .

### Gas flushing

Radon is the most critical background for the BiPo detector. It has several possible origins, the main one being the high concentration of radon in the air of the laboratory. The average rate is around  $80 \text{ Bq/m}^3$  in the LSC to be compared to around  $15 \text{ Bq/m}^3$  in the open air. The second one is the internal emanation of the detector itself. The most important contribution is thought to come from the glass of the PMTs despite the fact that they have been selected for their radiopurity.

$\text{N}_2$  from liquid nitrogen evaporation is flushed in several independent volumes of the detector. A radon-tight plastic film (EVOH<sup>1</sup>) isolates the volume between the scintillators from the rest of the detector. It was placed around the light guides' collar near the PMTs to reduce the amount of radon in the most sensitive volume. PMTs have been encapsulated in polyethylene boxes flushed separately (see Figure 7.14). Thanks to this flushing, radon emanation from materials inside or radon diffusion from outside the detector are expected to be highly reduced.

### Shielding

Shielding is needed to reduce the external background from  $\gamma$ 's and neutrons. Temporary shielding was installed for the first module comprised of 20 cm of iron on top and bottom and 10 cm of lead on the lateral faces. A previous study was made with MC simulations of the BiPo-3 preproduction module in order to define an optimal shielding: it should be constituted of 15 cm of lead and 40 cm of water [84]. However the cost of such a shielding for the full BiPo-3 detector was too high. Data

---

<sup>1</sup>EVOH is a plastic film very gas-tight and used in food protection.

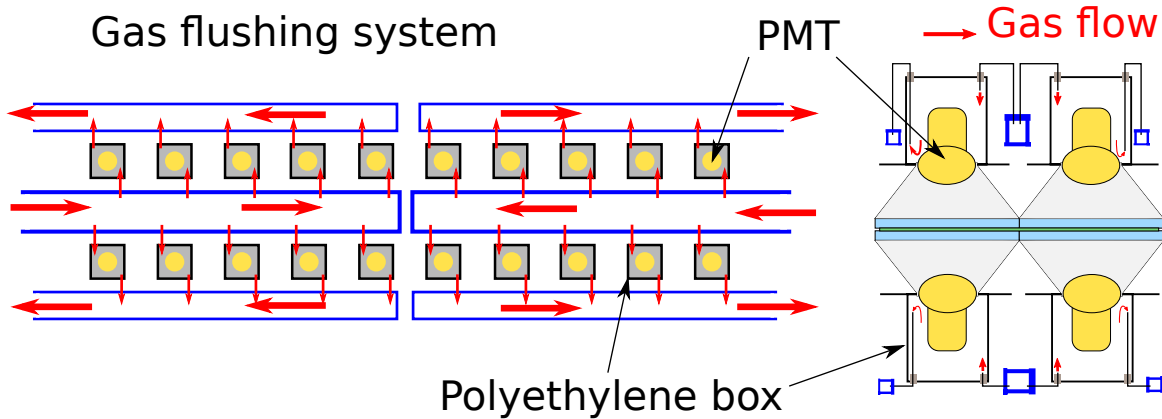


**Figure 7.14.:** *Schematic of the gas flushing system of the BiPo-3 detector*

analysis tools have been developed to compensate and reject external background (see section 7.8). A stainless steel tank capable of hosting the two modules of the BiPo-3 detector was installed in November 2012 and the new shielding is made of thick iron plates outside the tank and 5 cm of lead bricks inside the tank (see Figure 7.15). No water was used as shielding for the full detector.



**Figure 7.15.:** *Shielding of the BiPo-3 detector with iron plates outside the stainless steel tank. Lead bricks are placed inside the tank and on top of it.*

## 7.5.2. Construction and commissioning

### Detector assembly

All of the scintillator blocks were raw-machined at the INR and pre-cut at  $6 \times 30.5 \times 30.5$  mm<sup>3</sup>. They were then machined by a private company to the final dimensions of

$2 \times 30 \times 30 \text{ mm}^3$  with diamond tools under gas flushing to prevent contamination. The light guides were machined in France from PMMA selected for its UV transparency. All of the PMTs were new 5" PMTs specially ordered for the BiPo-3 detector.

The optical submodules were all assembled in a clean room at LAL. The scintillators and the light guides were first glued together. The surface of the scintillator is then aluminised in a dedicated clean device evaporating ultra-pure aluminium. The PMTs and the light guide are glued together with a transparent glue and white Tyvek (synthetic material from polyethylene fibers) is placed around the light guides.

The optical submodules were placed inside the mechanical frame in the underground clean room at the LSC. After the soldering of the cables onto the PMT dividers, their proper behaviour was checked after transportation. The tests were made using an  $\alpha$  source to observe the PMT signals and to check their shape.

A final cleaning of the scintillators surfaces was performed with pure acetic acid (remove surface dust), ultra-pure water (rinse the acid) and pure propan-2-ol (remove more dust and dry the surface). The flatness of the scintillators plane was finely tuned as any misalignment could damage the samples. Finally the detector was sealed with lateral iron plates (see Figure 7.16). This procedure only had to be done once as a dedicated opening system has been designed to replace the samples in the clean room.

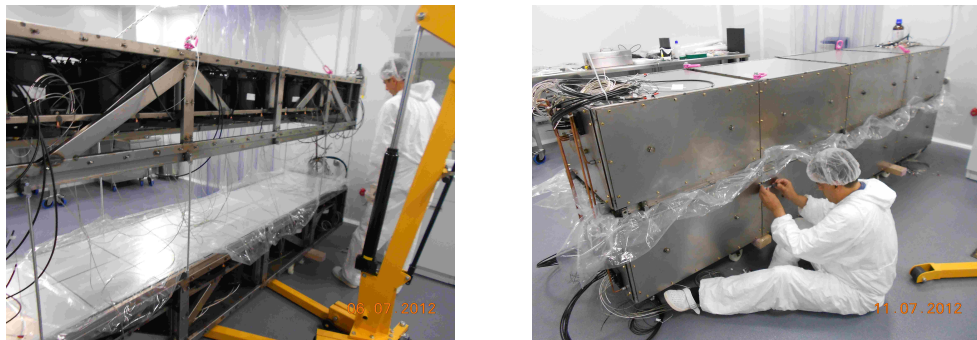


**Figure 7.16.:** *First BiPo-3 module at the LSC*

## 7.6. Uniformity of the surface response of the scintillators

All of the optical submodules have been tested at LAL for validation. An absolute measurement was performed with a  $^{207}\text{Bi}$  source emitting  $\gamma$ 's and conversion electrons (mainly at 976 keV and 482 keV) providing a reference in the centre of the scintillator. In Figure 7.17, the optimisation is only valid at high energy corresponding for the 976 keV conversion electron. At lower energies, contributions from the Compton scattering of low energy  $\gamma$ 's in the environment of the test bench have not been simulated. The retrodiffusion and the backscattering of these  $\gamma$ s probably explains part of the discrepancies observed below 800 keV.

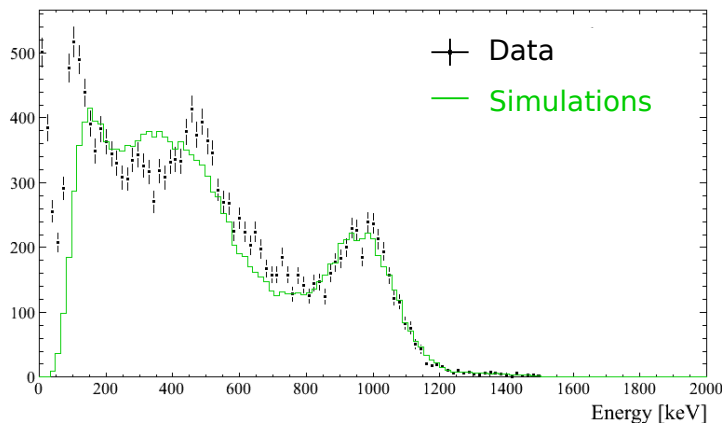


**Figure 7.17.:** *Electron energy spectrum from  $^{207}\text{Bi}$  at the centre of the scintillator*

Systematic scans of 25 points at the surface of the scintillators using an  $^{241}\text{Am}$  source emitting  $\alpha$ 's at an energy of 5.6 MeV were also part of the testing procedure. These scans were done in order to study the homogeneity of the surface response of the scintillators. The amount of scintillator scanned by each particle is illustrated in Figure 7.18. The  $\gamma$ -calibration performed at the LSC (see section 7.7) is also illustrated as a comparison on this figure. It is clear that  $\gamma$ 's can interact everywhere in the scintillator, while electrons and  $\alpha$ 's only test a limited volume.

There is a very good description of the  $\alpha$ -energy spectrum from the scans with the Monte-Carlo simulations in Figure 7.19. This also proves that the quenching factor applied to the simulations is correct at these energies.

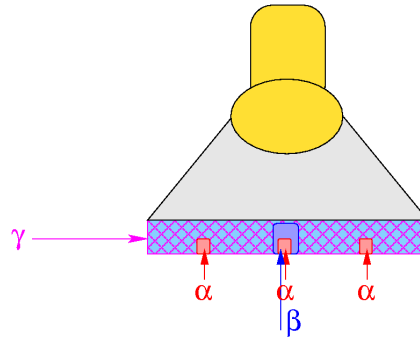


**Figure 7.18.:** Scan and qualification of the BiPo scintillators using electrons,  $\alpha$ 's and  $\gamma$ 's.

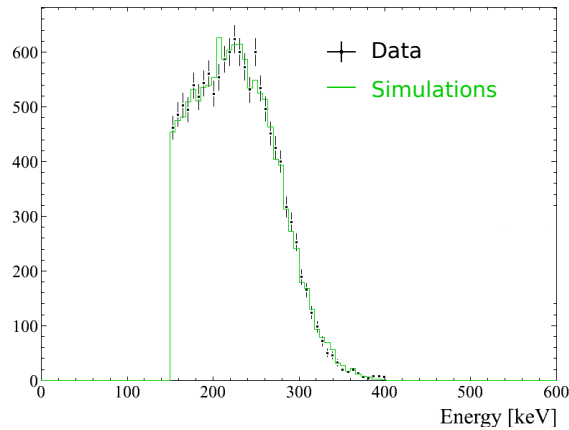


**Figure 7.19.:** Fit of the alpha energy spectrum from  $^{241}\text{Am}$  at the centre of the scintillator

From BiPo-1, it is known that the response of the scintillators is not uniform depending on the interaction point of the particle and that the light collection is more efficient at the centre. For each position of the source on the surface of the scintillators, the charge to energy conversion parameter (detailed in section 7.7.1) is determined from the comparison between data from the scans and Monte-Carlo. Values measured at the same distance to the centre of the scintillator are then averaged for all of the optical submodules in order to be fitted. Several fit methods of the scan data were compared. A global linear fit of the charge to energy conversion parameters for all of the optical submodules as a function of the distance to the centre of the scintillator was the simplest method and was chosen. Other methods, such as taking into account three symmetry axes of the scintillator and three independent second order fits, were also explored. These methods gave similar results to the global linear fit and gave results in agreement with previous optical simulations of the light guides [91]. From Figure 7.20, one can estimate that the amplitude of

the radial non-uniformity in the light collection between the centre and the edges of the scintillators is around 15%. This correction is applied to the simulations for every energy deposit according to its location in the scintillator.

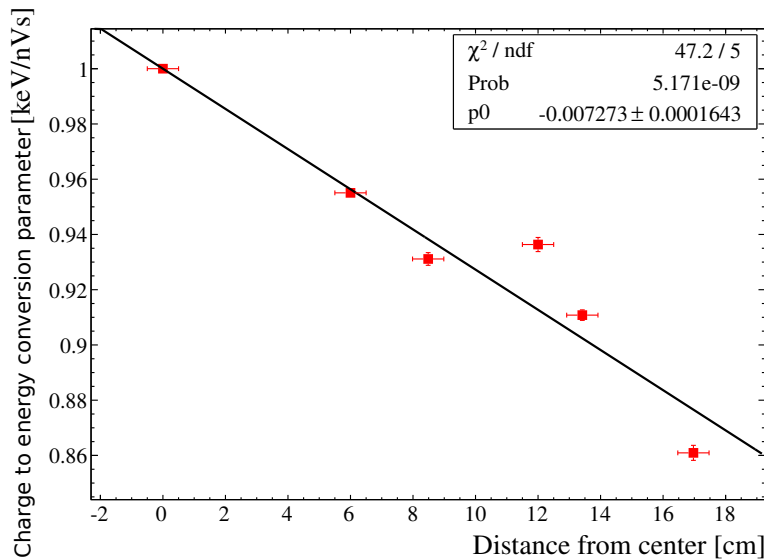


**Figure 7.20.:** *Linear law giving the radial non-uniformity of the scintillators of the BiPo-3 detector as a function of the distance to the centre of the scintillator.*

## 7.7. Calibration of the BiPo detectors

It is impossible to perform a calibration of the detector with a source between the scintillators since they are in contact. Indeed the insertion of a sample has to be done in a clean room and the detector is completely sealed before its operation. Therefore, a  $\gamma$ -calibration has been used as  $\gamma$ -particles from an external source can easily penetrate the detector.  $\gamma$ 's interact in the plastic scintillator by Compton scattering producing electrons. Several sources were considered and  $^{54}\text{Mn}$  was chosen since it emits  $\gamma$ 's in the proper energy range. The reference for the calibration is the Compton edge energy <sup>2</sup>.  $\gamma$ 's are emitted with an energy of 835 keV for a corresponding Compton edge energy of 639 keV. Given that only one calibration point is available with  $^{54}\text{Mn}$ , the energy calibration has been assumed linear with energy. On the other hand,  $^{54}\text{Mn}$  emitting only one  $\gamma$  particle, the observed energy spectrum is very pure and it is relatively easy to simulate.

<sup>2</sup>The energy of the Compton edge is defined as the maximum electron energy in the scattering of a  $\gamma$ -particle on an electron as follows  $E_{\text{Compton}} = \frac{2E_{\gamma}^2}{m_e c^2 + 2E_{\gamma}}$

In order to check that the detector is working properly, a  $\gamma$  calibration is done before each new measurement. This allows the proper behaviour of all of the optical submodules and the stability of the gain of the PMTs to be checked. The single counting rate also enables the stability of the detector to be checked.

### 7.7.1. Energy calibration and energy resolution

BiPo scintillators are very thin, therefore at energies of a few hundred of keV, only a small fraction of the Compton electrons are contained in the scintillator. Indeed their mean free path is of the order of a cm. Furthermore, at the energy of the Compton edge, electrons are the least contained. This makes this calibration quite time inefficient. To compensate, and given the large size of the detector, five sources are used simultaneously for the calibration as will be explained in section 7.7.2.

Data spectra are compared to Monte-Carlo with a Kolmogorov-Smirnov (KS) statistical test [92] to determine two parameters:

- the charge to energy factor which allows a pulse charge from data to be converted into an energy (in keV/nVs);
- the energy resolution, given by the FWHM at 1 MeV (in%), to be applied to the simulations.

The energy resolution of the optical submodules was measured before the installation of the detector and varies from one to another. The simulated energy spectra are produced without an energy resolution (see Figure 7.21) and the energy resolution is applied independently for each optical submodule. This energy resolution is re-measured during the  $\gamma$ -calibration as a cross-check and compared for each calibration. These measurements proved the overall stability of the detector so far. On the simulated spectrum in Figure 7.21, the energy of the Compton edge can be found at 639 keV. It can also be seen that the non-uniformity of the response of the scintillator reduces the detected energy as the MC are corrected taking into account the energy loss as a function of the interaction point on the surface of the scintillator.

Figure 7.22 presents the results of a KS test. The agreement between simulation and data is good at intermediate energies. Energy cuts have been applied to select only the Compton edge for the Kolmogorov test. Indeed at low energy the simulation

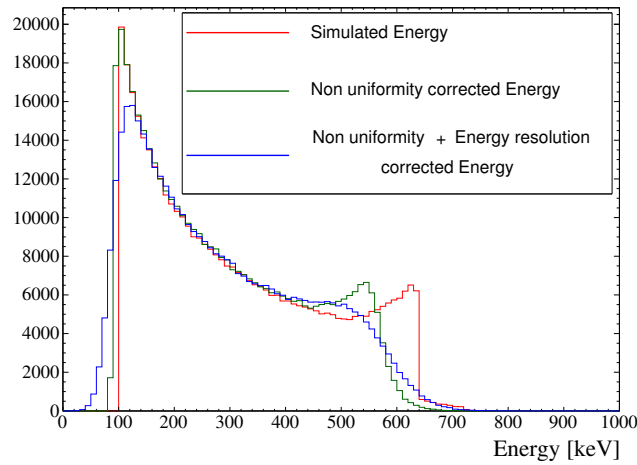


**Figure 7.21.:** *Simulation spectra for the  $^{54}\text{Mn}$   $\gamma$  calibration showing the ideal simulated spectrum, the energy corrected for the scintillators' non-uniformity with and without the energy resolution applied.*

is not accurate enough, due to the  $\gamma$  particles produced in the environment of the detector and not simulated here. Given that the geometry is a simplified model of the optical submodule environment, some interactions might not be properly described at low energy. It could be the case for example of the backscattering that occurs in the frame of the detector that is not simulated. Events at higher energy are due to contaminations inside the sample being measured in the detector. As an example the results of the calibration for this test are  $k_{calib} = 125.0$  keV/nVs and  $\text{FWHM} = 19.0\%$  for a probability of agreement of 99.7%.

### 7.7.2. Choice of the energy calibration procedure

A compromise had to be found between the position of the sources, the duration and the required statistics. This was optimised considering the detector geometry and five  $\gamma$ -sources. Several calibration scenarios were considered (see Figure 7.23):

- Top: 5 sources on top of the detector;
- Side: 5 sources on the side of the detector at the level of the scintillators;
- Top Side: 5 sources on top of the detector shifted to the side;
- Split Side: 3 sources on one side and 2 on the other side.

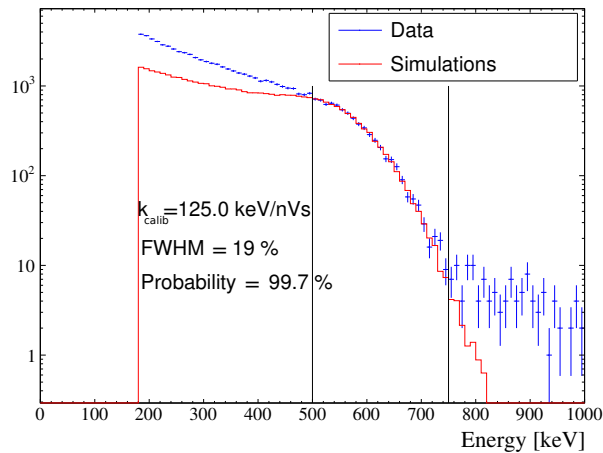


**Figure 7.22.:** Example of  $^{54}\text{Mn}$  energy calibration, the lines define the range of the KS test. A good agreement is observed in the Compton edge energy region but discrepancies exist at lower energies.

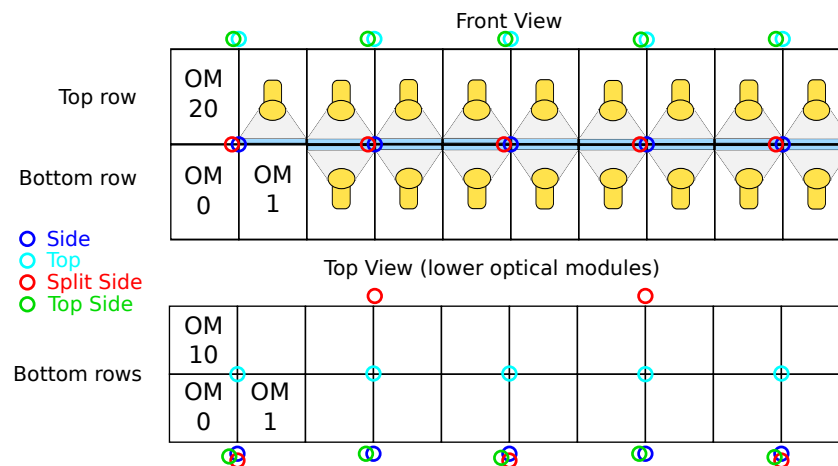


**Figure 7.23.:** Front and top view of the calibration scenarios for the BiPo-3 detector.

All of the optical submodules were taken into consideration to determine the required minimum exposure for all of them to be properly calibrated. The results of two optical submodules, labelled “OM 0” and “OM 10” have been taken as references (see Figure 7.23), the other being extrapolated from the symmetries of the detector. In the “split-side” and “side” scenarios, these two optical submodules represent the shortest and longest required exposure for the calibration. In the “top” and “top-side” scenarios, they require longer calibration times than the blocks in the upper rows (20 - 39). The criterion for an optical submodule to be calibrated was:

- Fully calibrated: at least 100,000 events have been recorded in the optical submodule;
- “Usefully” calibrated: at least 10,000 events have been recorded at an energy higher than 500 keV

The results of the different cases are presented in Table 7.2.

Scenario	Exposure Time (days)			
	Full		“Useful”	
	OM 0	OM 10	OM 0	OM 10
side	0.13	3.6	0.08	4.1
3-2 side	0.15	2.5	0.09	2.8
top	0.73	0.74	0.83	0.88
top side	0.91	1.4	0.96	1.5

**Table 7.2.:** Result of the exposure predictions from simulations in the different scenarios.

The calibration needs to be short due to manpower issues and to increase the available sample measurement time. Hence, calibrations requiring several days were rejected, making the “side” and “3-2 side” scenarios not suitable. The illumination of the detector also has to be as uniform as possible. Figure 7.24 displays the illumination profile along the y-axis in the “top” (left) and “top side” scenarios (right). The two scintillators rows are visible and  $y = 0$  corresponds to the separation between these two rows. It is possible to deduce that the “top side” scenario presents less discrepancies in the illumination of the scintillators between the centre and the edges compared to the “top” scenario. A larger illumination is also visible for the “top” scenario on the inner edges of the scintillator in Figure 7.25 (top).

### 7.7.3. Time calibration

The selection of the time coincident BiPo events requires the detector to be accurately calibrated in time. The time calibration consists in the measurement of the delay time for the response of two face-to-face optical submodules. These differences mainly come from the differences in high voltage between the PMTs, reduced thanks to a pairing of the PMTs according to their operating high voltage.

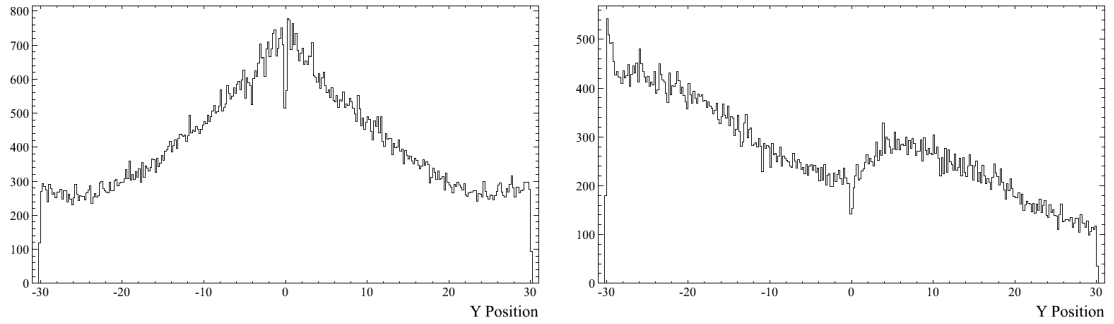


**Figure 7.24.:** Profile of the illumination of BiPo-3 in the “top side” (left) and “top” scenarios (right). A larger inhomogeneity in the illumination of the edges of the scintillators is visible for the “top” scenario.

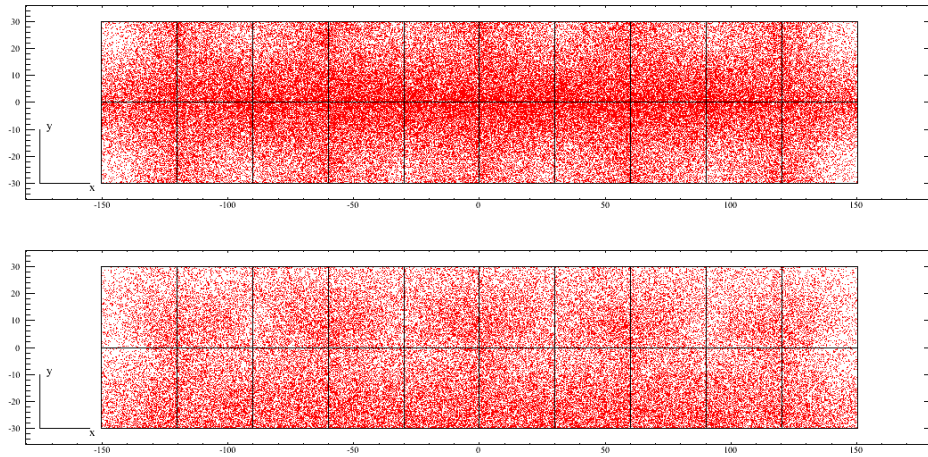


**Figure 7.25.:** Top view of a BiPo-3 module illustrating the interaction points of the  $\gamma$  calibration in the “top” scenario (top), a high radial non-uniformity is visible. The “top side” scenario (bottom) is one of the most uniform possibilities.

To perform this calibration, single crossing electron events are considered as shown in Figure 7.26. These events are the result of the Compton scattering of a  $\gamma$ -particle in one scintillator. The emitted Compton electron deposits part of its energy and then crosses the gap between the scintillators to deposit its energy in the opposite scintillator. One can consider that the two energy deposits occur at the same time in both scintillators. The measurement of the time delay between these energy deposits allows us to correct the time difference between the two optical submodules.

In Figure 7.27, an example of a Gaussian fit of the time difference between two optical submodules is displayed. This fit has been performed for all of the pairs of optical submodules. Given the half-life of the decay of  $^{212}\text{Po}$  of 299 ns, the precision

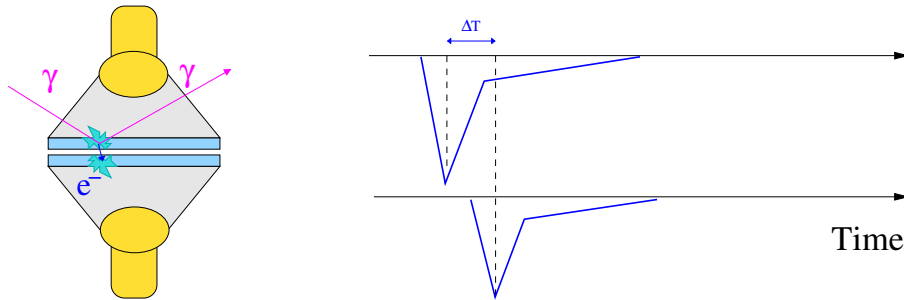


**Figure 7.26.:** *Crossing electron for time calibration and corresponding PMT pulses.*

that is required is of the order of a few ns. The observed time differences are close to zero with a deviation close to 1 ns. Therefore it is not an issue for the time measurements and the relative time differences are corrected in the analysis.

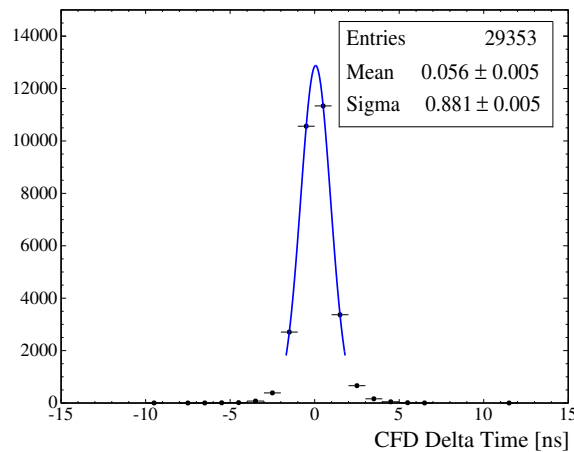


**Figure 7.27.:** *Example of a Gaussian fit of the time difference between two face-to-face optical submodules in the BiPo-3 detector.*

#### 7.7.4. $\beta$ - $\alpha$ discrimination

Pulse-shape discrimination was already implemented in BiPo-1 without the sampling capabilities of BiPo-3. The aim of the discrimination is to reduce the background level coming from random coincidences. As explained in section 7.2, the tail charge of an  $\alpha$ -pulse is larger compared to electrons. The delayed pulse in a BiPo event is produced by an  $\alpha$ -particle while it comes from a Compton electron for random coincidences. A discrimination factor different for electron and  $\alpha$ 's can be computed as in equation 7.6 where  $q_{tail}$  is the tail charge and  $Q_{total}$  is the total charge.

$$\chi = \frac{Q_{tail}}{Q_{total}} \quad (7.6)$$

It is difficult to select pure electron and  $\alpha$  event samples mainly due to random coincidences from  $\gamma$ 's. This was achieved with data from a calibrated aluminium foil producing a large number of  $^{212}\text{BiPo}$  events for which no random coincidence is expected. This study allowed a cut on the discrimination factor to be optimised and more details will be given in the section 7.9.1.

### 7.7.5. Detector stability

#### Counting rate

In order to check the proper behaviour of the detector, the raw counting rate has been studied for each analysis channel. It corresponds to the total number of events recorded, independently of the topology. It proved to be very stable apart from the last datasets. At that time, another experiment started its operation in the laboratory. One of the consequences was an increase in the temperature from 21 °C to 28 °C. Figure 7.28 displays on the left a normal counting rate throughout an entire dataset with a few runs with low counting rate due to a stop in the acquisition. On the right, one can see clear instabilities in the counting rate. The reason for this change has still not been understood. One of the main impacts on the measurements is the presence of pulses with very large charge and saturating the dynamic range in amplitude as displayed in figure 7.29.

#### Calibration parameters with time

The energy calibration procedure has been presented in section 7.7.1. In order to test the stability of this calibration, the energy spectra for each channel in the different calibrations are compared to each other. This also enables to identify issues in the energy calibration and to perform a new fit of the calibration parameters (charge to energy parameter and energy resolution) when necessary. Figure 7.30 illustrates the different calibrations of a given electronics channel. Changes in the energy thresholds explain the differences at low energy and a change in the position of the Compton edge would be due to a change in the gain of the PMT.

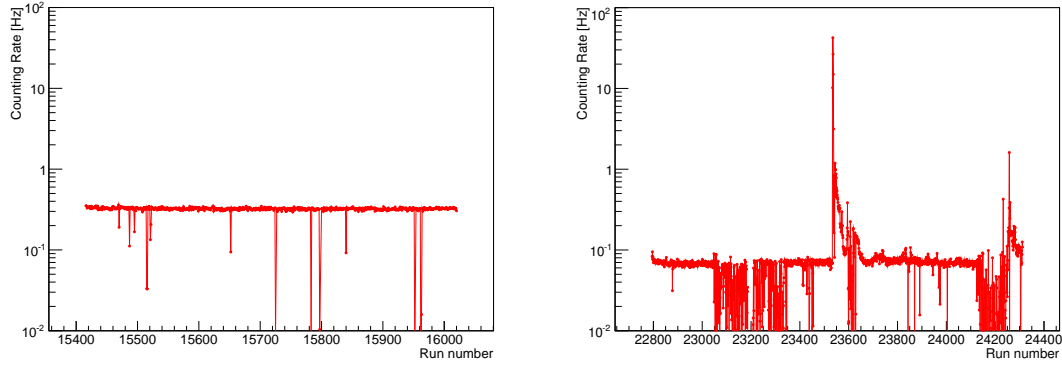


**Figure 7.28.:** *Left: Normal counting rate during the aluminium foil measurement. Right: Noisy counting rate during a selenium source foil measurement. The same electronics channel is displayed here. The average counting rate is higher on the left plot due to the presence of the aluminium foil.*

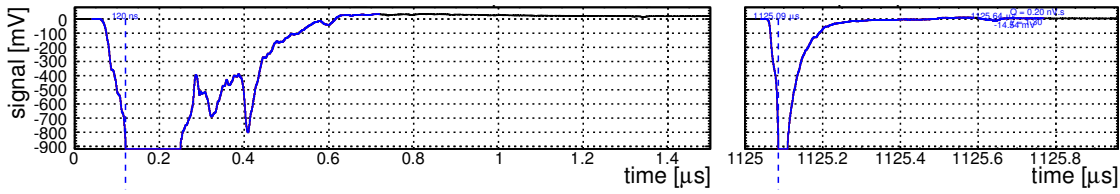


**Figure 7.29.:** *Example of a noisy pulse in the latest datasets of the BiPo-3 detector.*

## 7.8. Analysis techniques

### 7.8.1. Pulse shape analysis: noise rejection

Thanks to pulse digitization, it has been possible to reject pulses based on their shape in data. Given that both the amplitude and the charge are proportional to the energy, the charge over amplitude ratio ( $Q/A$ ) must be constant with the charge (see blue distribution in Figure 7.31). Some noise can come from the interaction of  $\gamma$ 's in the light guide instead of the scintillator. Even if it is not as efficient as in plastic scintillators, scintillation light can be produced in the light guide with a  $Q/A$  lower than in the scintillator [43]. Other noise pulses can be produced with a large charge or a deformed pulse. Their origin can be radio noise detected by the cables or the acquisition boards or noise coming from the PMTs. These noisy pulses can be identified thanks to the study of  $Q/A$  as a function of the charge. In Figure 7.31, signal and different noise events have been highlighted.

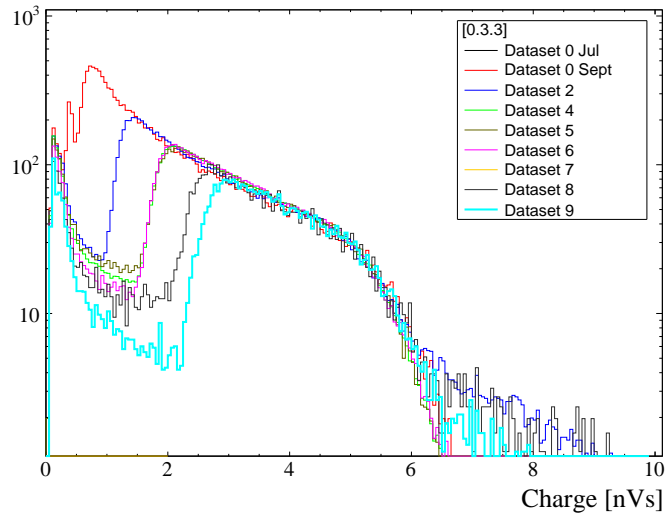


**Figure 7.30.:** *Successive  $\gamma$ -calibrations of an optical submodule. A change in the threshold of this channel can be seen at lower energies. A good agreement is visible in the Compton edge energy region proving a good stability of the calibration.*

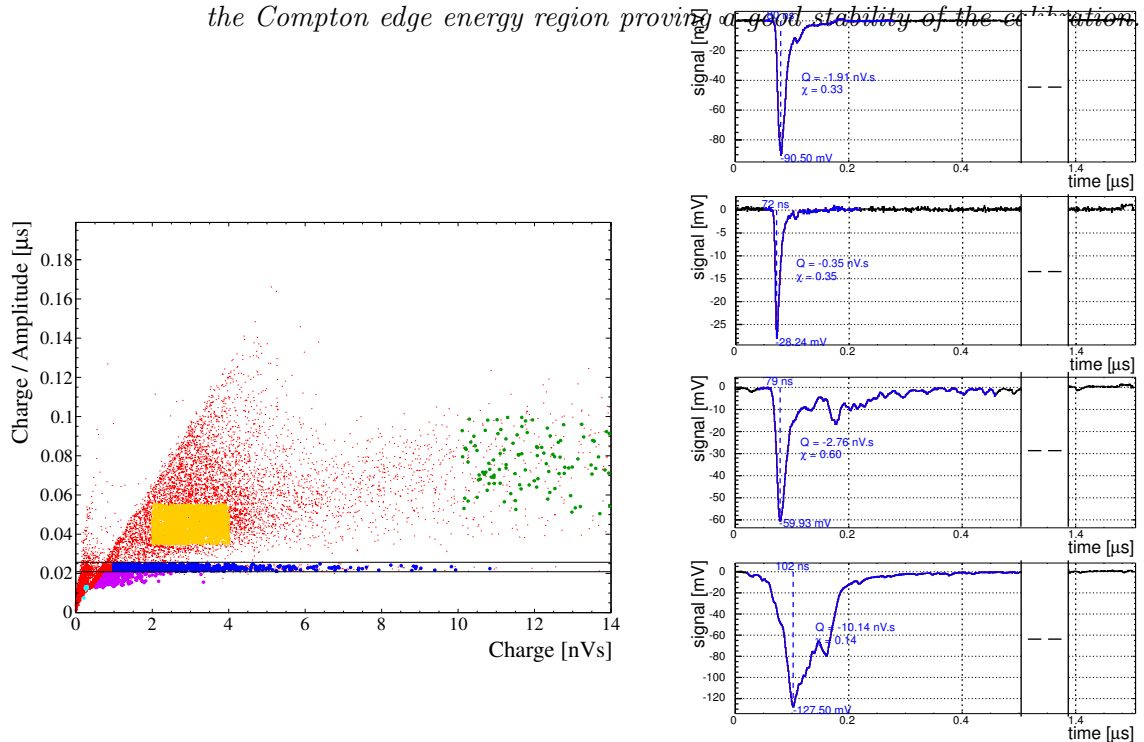


**Figure 7.31.:** *Left:  $Q/A$  of sampled pulses as a function of the charge. Several distributions have been identified: signal (blue), scintillation light in the light guide (violet and cyan) and noise (orange and green). Right: pulses examples are given for (from top to bottom) blue, violet, orange and green distributions.*

A criterion has been defined to select events with a proper pulse shape from  $Q/A$ . Two distributions are visible in Figure 7.32, one at lower  $Q/A$  values coming from

noise in the light guide and one at higher values for the signal. A dedicated study has been performed on all of the individual optical submodules of the two modules of the BiPo-3 detector in order to obtain the optimal parameters for the events selection. A Gaussian fit is performed on the signal distribution allowing events to be selected if their  $Q/A$  is within  $[\text{mean} - 3\sigma, \text{mean} + 3\sigma]$ . These distributions are fitted for all of the channels before the data analysis.

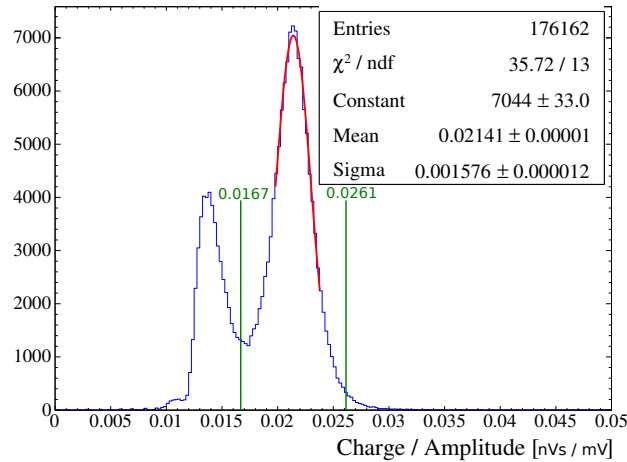


**Figure 7.32.:**  $Q/A$  values for one channel with two distributions visible. The signal is fitted and the other one is scintillation in the light guide.

### 7.8.2. Cross-talk rejection

It is possible to reject background from contamination in the volume of the scintillators as two prompt coincident pulses exist in these events (see Figure 7.33).

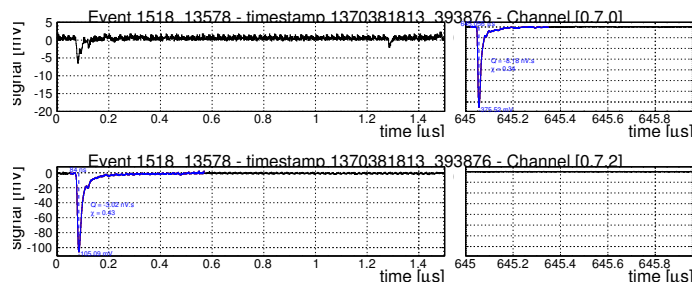


**Figure 7.33.:** Example of an event rejected due to a volume contamination in one of the scintillators. A pulse is visible opposite the prompt pulse.

Optical cross-talk can also produce a pulse in time coincidence with the prompt BiPo pulse, making it the limiting factor to the volume background rejection. The

black polyethylene wrapping the optical submodules is supposed to prevent this to happen however it could not be perfectly light-tight. This optical cross-talk produces coincident pulses with an amplitude corresponding to one photoelectron or 2 mV.

A volume contamination can result from the deposition of radon on the scintillators. Before decaying into  $^{214}\text{Bi}$  or  $^{212}\text{Bi}$ , several  $\alpha$ -decays occur. Each of them can entail a recoil of the daughter nucleus in the first  $\mu\text{m}$  of the scintillator. After the  $\beta$  decay of Bi, a coincident peak can therefore be observed with the electron pulse. An analysis was performed on background data in the  $^{214}\text{BiPo}$  analysis channel considering the period when radon trapped in the detector after its closure decays. The presence of coincidence pulses with the prompt BiPo pulse with an amplitude above 3 mV was associated to this signal [93].

A study on  $^{212}\text{BiPo}$  events from the calibration aluminium foil, where no signal is expected from the volume of the scintillator, showed the presence of coincident pulses with an amplitude lower than 3 mV. These events were associated to real BiPo events accompanied by an optical cross-talk. Only 4% of the coincident events had an amplitude larger than 3 mV. Therefore, rejecting the background coming from the volume of the scintillator by applying a higher coincident amplitude cut at 3 mV only reduces the BiPo efficiency by 4%.

This rejection is applied both for the delay and prompt pulses for  $^{214}\text{BiPo}$  events. However, the two pulses in  $^{212}\text{BiPo}$  events studies are in the same acquisition window. Therefore it is not possible to properly estimate a coincidence with the delayed pulse and the rejection is only applicable for the prompt pulse.

### 7.8.3. Activity measurements

#### Fit of the energy spectrum

The different contributions can be identified thanks to the binned likelihood method explained in Chapter 5 by comparing the shape of the backgrounds. Depending on its origin, the energy spectrum of the  $\alpha$ -particles is completely different. Figure 7.34 illustrates the different energy spectra. The source contaminations (at low energy) and the surface background (peak at high energy) are clearly identified.

The decay time of  $^{212}\text{Po}$  is too short compared to the counting rates around 10 Hz to allow significant contributions from the random coincidences in the time window [20, 1500] ns. For  $^{214}\text{BiPo}$  events, thanks to the high radiopurity of the detector and the gas flushing system, random coincidences are the dominant background (see section 7.1.4). No Monte Carlo simulations could be generated reproducing random coincidences as their origin is not precisely known, hence data have been used. The vast majority of the events recorded in the detector correspond to a single energy deposit from an electron in one optical submodule, or *single-electron events*. Random coincidences can be seen as two independent single-electron events occurring in the  $^{214}\text{BiPo}$  time window [10, 1000]  $\mu\text{s}$ . Additional criteria have been required to obtain the random coincidences spectrum such as Q/A selection (see section 7.8.1). No coincident pulse should have been seen on the opposite channel. Figure 7.34 displays the energy spectrum of single-electron events recorded in the detector. It can be seen that only random coincidences can produce events with an energy higher than 1.1 MeV in the aluminium foil.

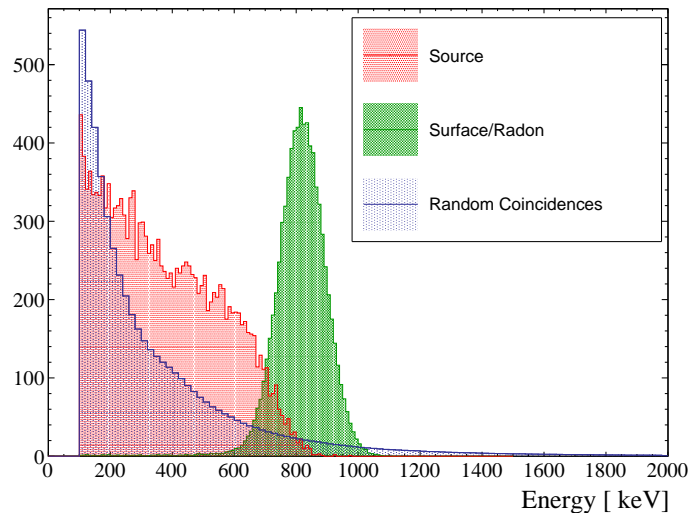


**Figure 7.34.:** *Monte Carlo simulations of BiPo events for an aluminium foil measurement. In red a contamination in the bulk of the aluminium source. In green a contamination on the surface of the scintillators or from radon. The normalisation is arbitrary.*

#### 7.8.4. Fit of the delay time

The time distribution of BiPo events follows the radioactive decay law with a different characteristic time for the two cascades. On the other hand, random coincidences

have a constant probability of occurring in time. A decreasing exponential combined with a constant function can therefore be used to describe the delay time such as in equation 7.7.

$$N = k \times e^{-\frac{\ln 2}{T_{1/2}} \Delta t} + N_{RC} \quad (7.7)$$

where  $N$  is the number of events,  $N_{RC}$  is the number of random coincidences,  $\Delta t$  is the delay time between the two pulses,  $T_{1/2}$  is the half-life of either  $^{212}\text{Po}$  or  $^{214}\text{Po}$  and  $k$  is a scaling factor.

The value of the ‘‘Coincidences’’ parameter in the fit provides the number of expected coincidence events. It can be subtracted to the total number of events to extract the number of BiPo events. An example of the global fit is displayed in Figure 7.35.

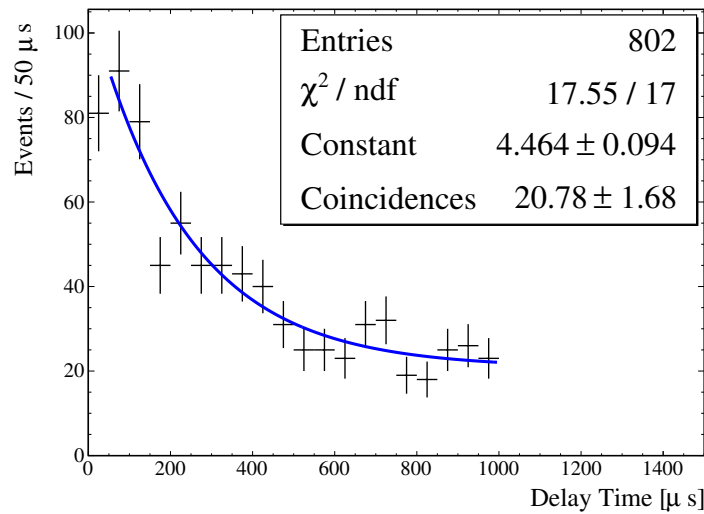


**Figure 7.35.:** *Fit of the delay time using a global fit combining an exponential and a flat distribution. ‘‘Coincidences’’ corresponds to the number of random coincidences per bin. ‘‘Constant’’ is the scaling parameter of the exponential.*

Given the flat distribution in time of the random coincidences, a delay time cut will be applied in  $^{214}\text{Bi}$  analysis in the following. This cut rejects any event with a delay time longer than three half-lives of  $^{214}\text{Po}$ , hence 492  $\mu\text{s}$ . This allows to remove 49% of random coincidences while keeping 88% of the BiPo events.

## 7.9. Measurements with BiPo-3

Since the beginning of its operation, BiPo-3 has participated in the material selection for SuperNEMO source foils. The measurement of an aluminium calibration foil allowed the response of the detector and the simulations to be understood, the detection technique to be validated and the  $\beta/\alpha$  discrimination to be developed. An intrinsic background measurement has also been necessary. In the next sections, several of these measurements will be presented along with results for the first SuperNEMO source foils.

General analysis criteria have been applied for the following measurements. Two pulses have to be selected in the following time windows:  $[20, 1500]$  ns for  $^{212}\text{BiPo}$  events and  $[10, 1000]$   $\mu\text{s}$  for  $^{214}\text{BiPo}$  events. The Q/A of the pulses have to meet the requirements defined in section 7.8.1. A prompt and delayed threshold are applied, with different values depending on the measurement. For  $^{214}\text{BiPo}$  events, the first 15 days after the closure of the detector are rejected due to the remaining radon background on the surface of the scintillators. Figure 7.36 illustrates the rejection of this background.

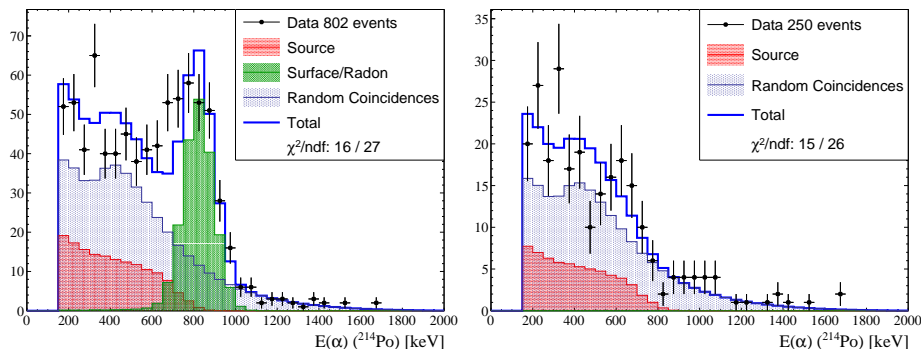


**Figure 7.36.:** Energy of the  $\alpha$ 's from the one-foil aluminium sample before radon decay (left) and after radon decay (right). The peak on the surface due to radon on the surface of the scintillators disappears after the decay. The scaling factors are left free for the fit.

### 7.9.1. Aluminium foil

As already mentioned in section 7.3.3, an aluminium foil 88  $\mu\text{m}$ -thick, with a mass of  $214 \pm 10$  g for a 3 m-long sample, has been measured as part of the validation and calibration process of the BiPo-3 detector (see Figure 7.37). It comes from the same

batch as used for BiPo-1 and for the BiPo-3 preproduction module. Several HPGe measurements provided information on the contaminations in  $^{208}\text{Tl}$  and  $^{214}\text{Bi}$ . The latest HPGe results with 48.3 g in January 2014 for a total exposure time of 41 d revealed the following contamination:

$$\begin{aligned}\mathcal{A}(^{208}\text{Tl}) &= 109 \pm 2 \text{ (stat.)} \pm 8 \text{ (syst.) mBq/kg} \\ \mathcal{A}(^{214}\text{Bi}) &= 13.2 \pm 2.6 \text{ (stat.)} \pm 1.0 \text{ (syst.) mBq/kg}\end{aligned}\tag{7.8}$$

These results were only revealed after a blind analysis of BiPo data. Two different samples were placed in BiPo-3 in both modules successively and were comprised of one and two aluminium foils respectively. They were wrapped in 4  $\mu\text{m}$ -thick polyethylene to avoid contaminating the detector. These samples were measured during 25 days in the first module and 40 days in the second one. The analysis of the aluminium foil was useful for numerous aspects now in use for the BiPo-3 analysis such as the  $\beta/\alpha$  discrimination and an improvement of the  $\alpha$ -quenching measurement. It should be noted that as opposed to low-activity analyses, the aluminium is a high-activity sample with  $\beta - \gamma$  contamination producing most of the random coincidences.



**Figure 7.37.:** *Aluminium calibration foil in a BiPo-3 module*

### Quenching factor

As introduced in section 7.2,  $\alpha$ -particles undergo a quenching of their scintillation while interacting in plastic scintillators. Several studies have been carried out to measure the value of this quenching factor as a function of the  $\alpha$  energy. No  $\alpha$ -source was available with a sufficient energy to measure the quenching of the  $\alpha$ -particles produced by the decays of the polonium ions in the BiPo cascade (7.6 MeV and 8.9 MeV). Therefore BiPo-3 data during the first 15 days of the measurement with a higher amount of  $^{222}\text{Rn}$  were used. A peak in the energy of  $\alpha$ 's, visible in Figure 7.38, around 800 keV corresponds to events originating from radon deposition. A lower

delay time cut at  $10\ \mu\text{s}$  is applied to reject  $^{212}\text{BiPo}$  events. Selecting events with a delay time lower than three  $^{214}\text{Po}$  half-lives allows half of the random coincidences to be rejected while keeping about 90% of BiPo events. As visible in Figure 7.38 (right), this selection significantly reduces the background at the peak energy producing a narrower signal distribution.

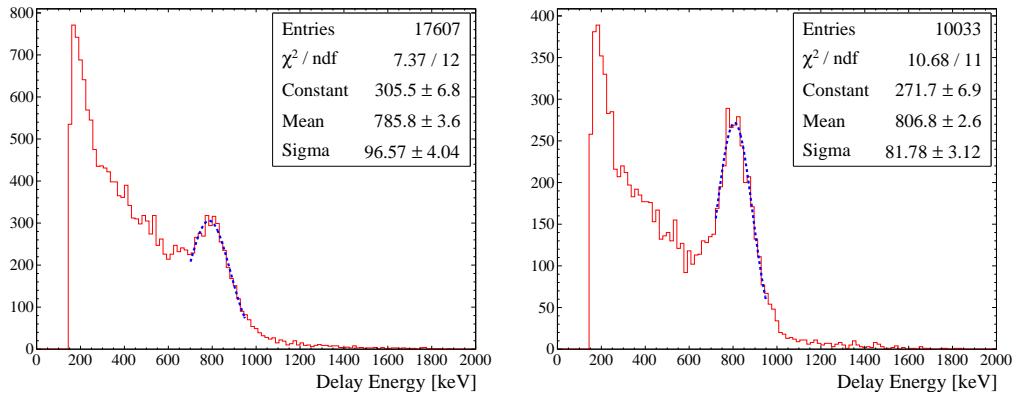


**Figure 7.38.:** *Distribution of  $\alpha$  energy in the aluminium foil in a period with high radon level. On the left, an important number of random coincidences contribute in the peak energy region. An upper cut on the delay time between the two pulses allows half of these events to be rejected.*

In order to enhance random coincidences rejection, the  $\alpha$  energy spectrum of events with a delay time above  $492\ \mu\text{s}$  was subtracted from the  $\alpha$  energy spectrum of the other events. This has only little impact on the BiPo events since only 12% of these events have a longer delay time. A Gaussian fit of the peak in Figure 7.39 gives the new value of 8.49 for the  $\alpha$ -quenching at 7.69 MeV. This value takes into account the non-uniformity of the scintillator response that decreases the maximum energy of the  $\alpha$ -particle from 7.69 MeV to 6.89 MeV and was used for the fit on Figure 7.6.

### $^{208}\text{Tl}$ measurement

The energy thresholds have been chosen at 200 keV for the prompt pulse and 150 keV for the delayed pulse. The two samples of different thickness have been studied separately to perform a cross-check. The results for the two modules and the two individual samples are presented in Figures 7.40 and 7.41. On the left the delay times reproduce well the expected  $^{212}\text{Po}$  half-life of 299 ns. The middle plot illustrates the delayed energy spectrum, showing a relatively good data description. Discrepancies at higher energies in the delayed energy spectrum are probably due to issues in the description of the quenching of  $\alpha$ 's. No surface contamination of the foil could

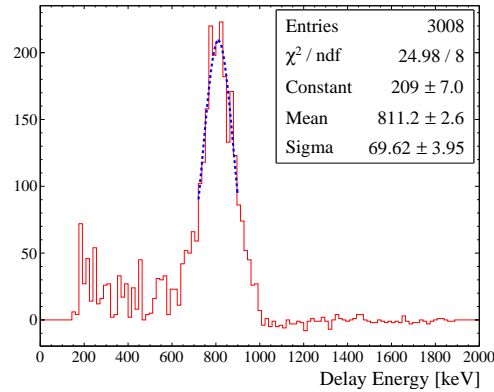


**Figure 7.39.:** *Distribution of  $\alpha$ 's energy in the aluminium foil in a period with high radon level after random coincidences subtraction.*

be identified and the expected background from the surface of the scintillators is negligible. On the right, the proper description of the electron energy from  $^{212}\text{Bi}$   $\beta$ -decay is highlighted.

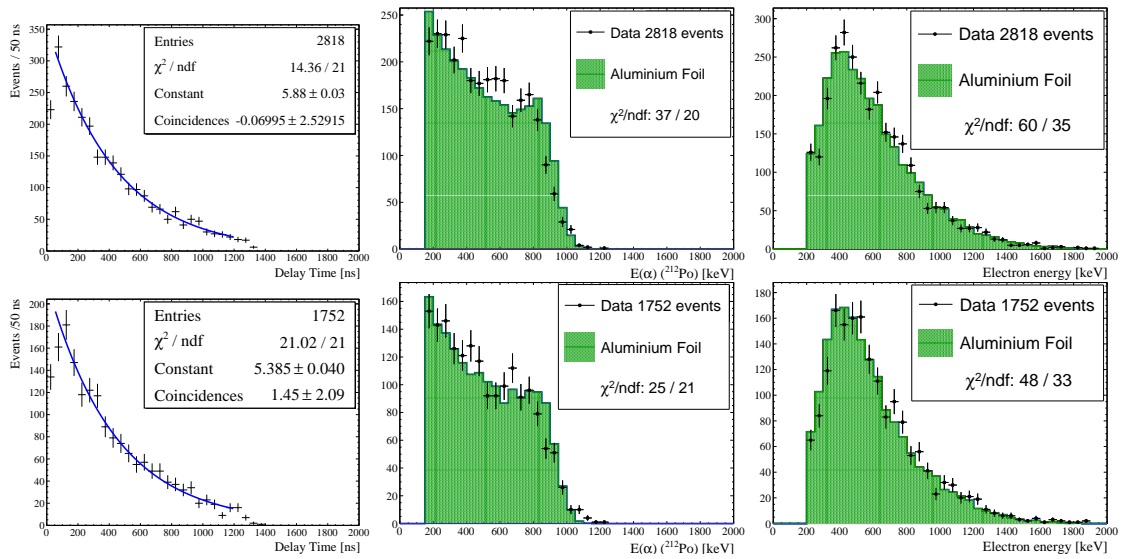


**Figure 7.40.:** *Time and energy distributions in the first module for one foil (top) and two foils (bottom). Left: Time between prompt and delayed pulses. The half-life is fixed at the expected value of 299 ns. Middle: Energy of the  $\alpha$ . Right: Energy of the electron. The high energy discrepancy in  $E_\alpha$  is probably due to a quenching issue.*

Table 7.3 contains the activities for the different samples and modules with a  $1\sigma$  statistical uncertainty. The results are in good agreement with each other. The efficiency for two foils is much lower than for one foil given that the centre of sample cannot be probed due to  $\alpha$  energy losses as illustrated in Figure 7.42.

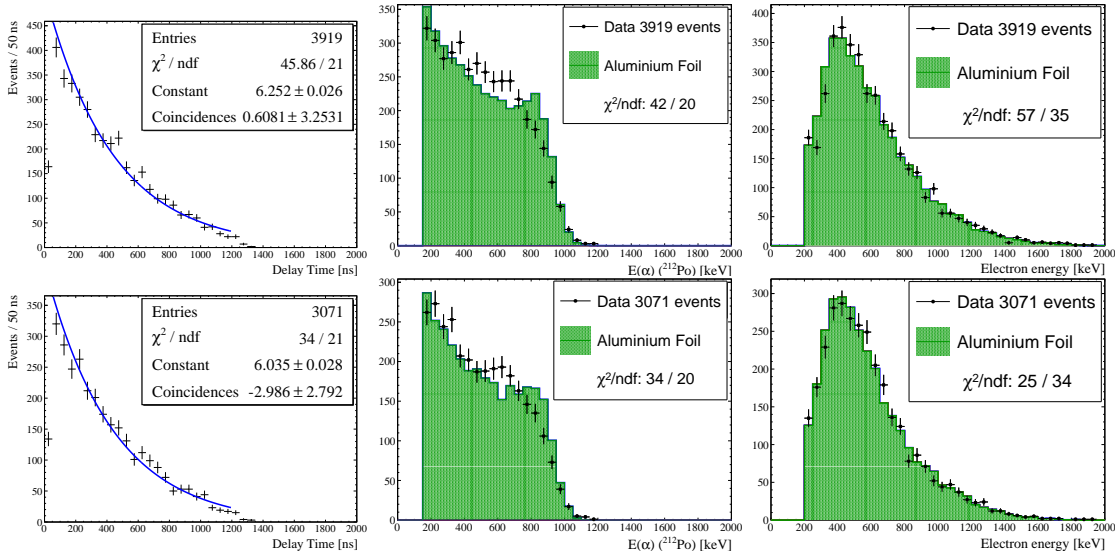


**Figure 7.41.:** Time and energy distributions in the second module for one foil (top) and two foils (bottom). Left: Time between prompt and delayed pulses. The half-life is fixed at the expected value of 299 ns. Middle: Energy of the  $\alpha$ . Right: Energy of the electron.

Samples	Efficiency [%]	Module 1	Module 2	Both modules
One foil	5.22	$74.3 \pm 1.4$	$70.8 \pm 1.1$	$72.6 \pm 0.9$
Two foils	2.29	$71.1 \pm 1.7$	$65.8 \pm 1.2$	$68.5 \pm 1.0$
Both	-	$72.7 \pm 1.1$	$68.3 \pm 0.8$	$70.5 \pm 0.7$

**Table 7.3.:**  $^{208}\text{Tl}$  activities in the aluminium foil (in mBq/kg). Only statistical uncertainties are given.

The different contributions to the systematic uncertainty on the activity have been estimated. The two samples show different activities, therefore a systematic uncertainty of 3% has been associated to the effect of the thickness. The activity measurement has been carried out for several values of the lower cut on the delayed energy (from 100 to 600 keV) and of the prompt energy (from 200 to 600 keV). 6 % systematic uncertainty on the lower cut on the delayed energy and 5 % on the prompt energy have been estimated. Due to the time window available from the acquisition system, the energy measurement is less accurate for pulses with a very high delay time. A systematic uncertainty of 2 % has been associated to a high delay time selection by changing the selection in the maximum delay time from 1200 to 1500 ns. Two experimental setup were employed for the  $\alpha$ -quenching determination yielding

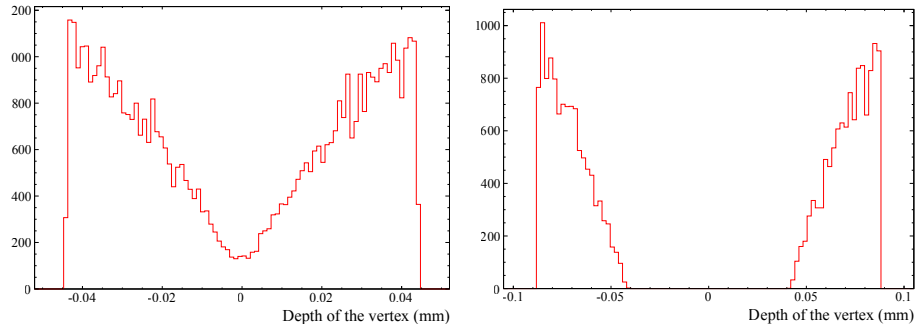


**Figure 7.42.:** *Vertices of the simulated events in the one-foil (left) and two-foil (right) aluminium samples. The centre of the two-foil sample cannot be measured due to  $\alpha$  energy losses in the foil.*

different results (see section 7.2). When compared, the activity measurements differ by 1 %. The error on the non-uniformity of the surface response of the scintillators implies an additional  ${}^{+5}_{-4}$  % contribution to the systematic uncertainties. This was set by varying the fit to the non-uniformity (see section 7.6) to two extreme cases. Finally, a systematic uncertainty between the two modules has been estimated at 6 % from the different activity measurements. This adds up to a total systematic uncertainty of  ${}^{+12}_{-11}$  %.

The final result of the blind analysis in  ${}^{208}\text{Tl}$  is therefore:

$$\mathcal{A}({}^{208}\text{Tl}) = 70.5 \pm 0.7 \text{ (stat.) } {}^{+8.5}_{-7.8} \text{ (syst.) mBq/kg} \quad (7.9)$$

These activity measurements represent a discrepancy of approximately 30%, corresponding to about  $3\sigma$ , with HPGe. Several cross-checks leading to a better understanding of the samples and of the detector have therefore been necessary. In order to test the homogeneity of the contaminations, activity measurements have been carried out on individual pairs of optical submodules (or *capsules*). Figure 7.43 displays the comparison of the activities in the two modules for the one-foil sample. The same comparison is performed for the two-foil sample in Figure 7.44. When a capsule was rejected from the analysis, its activity was set to 0 in these two Figures. Inhomogeneities are clearly visible with a rather large amplitude from one capsule (a pair of face-to-face optical submodules) to another and similar variations appear in the two modules.

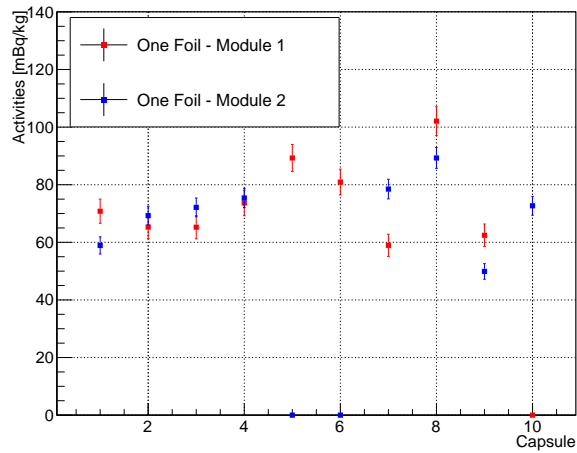


**Figure 7.43.:** Comparison of the activities measured in the two BiPo-3 modules for the one-foil sample. A similar inhomogeneity is visible.

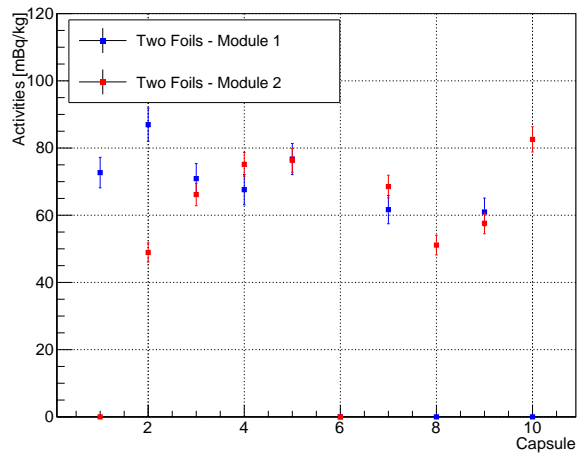


**Figure 7.44.:** Comparison of the activities measured in the two BiPo-3 modules for the two-foils sample. As for the one-foil sample, compatible inhomogeneities can be observed.

Despite the similar behaviour between the modules, possible detector effects leading to these inhomogeneities were looked for. The calibration constant converting the pulse's charge into an energy could be a source of inhomogeneity between capsules and was investigated. This constant has been determined independently for each of the optical submodules. Figure 7.45 demonstrates that no correlation between the calibration parameter and the measured activity can be identified. Therefore, this cannot explain the difference observed here.

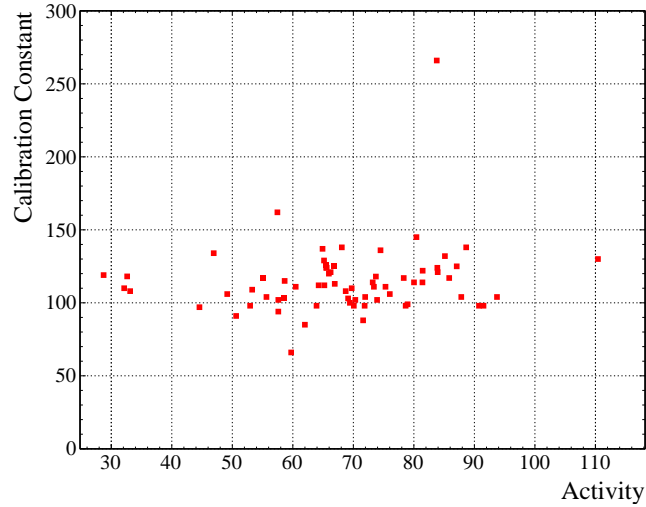


**Figure 7.45.:** *Calibration constant as a function of the activity measured in each of the electronic channel. No correlation is visible.*

No other significant detector effect being identified, it seems that a non homogeneous contamination exists in the aluminium foil in  $^{208}\text{Tl}$  which could explain the difference with HPGe. Another possible reason would be the contamination of the HPGe sample before its measurement. It is worth noting that the sample measured in HPGe is not the same as the ones measured in BiPo-3. The simulation of the sample and the background level estimation in the HPGe measurement might also contribute to this difference. Further investigations are in progress and a HPGe measurement of the foils that were installed in BiPo-3 has been planned to help understanding a possible inhomogeneity.

### $\beta/\alpha$ discrimination

The  $^{212}\text{BiPo}$  channel provides us with a very pure sample of real BiPo events, with a prompt electron pulse and a delayed  $\alpha$ -pulse. Indeed due to the high activity of the foil compared to the radiopurity of the detector, the source was the only contribution. This was illustrated in Figures 7.40 and 7.41, where the delay time distribution is compatible with  $^{212}\text{BiPo}$  events and no random coincidence is expected.

In order to differentiate these two particles, the distributions of the discrimination factors, introduced in section 7.7.4, are compared in Figure 7.46. A larger discrimination factor  $\chi$  is expected for  $\alpha$  pulses. Setting a lower cut on the delayed  $\chi$  variable of 0.32 entailed a rejection of 82% of pulses produced by electron while keeping 81%

of those associated to  $\alpha$ 's. This discrimination is necessary for  $^{214}\text{Bi}$  measurements of aluminium and all of the other samples.

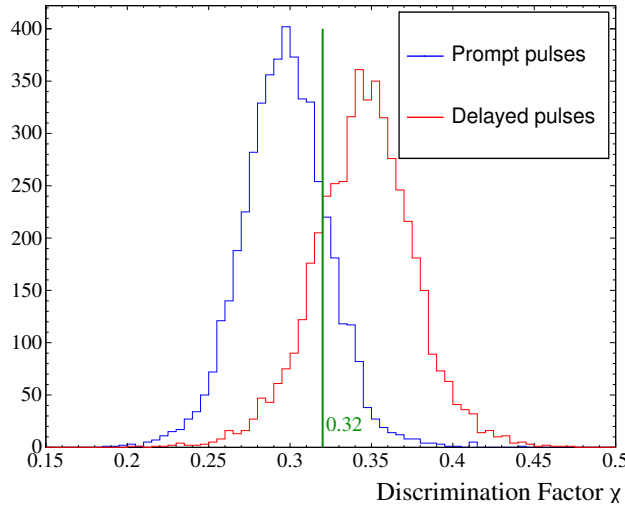


**Figure 7.46.:** *Discrimination factors for  $^{212}\text{BiPo}$  events from the aluminium foil. The prompt pulses (blue) and delayed pulses (red) are relatively well separated allowing a cut to be performed rejecting delayed pulses produced by electrons.*

### $^{214}\text{Bi}$ measurement

A larger background from random coincidences and radon is expected in this analysis channel. As will be explained later, it has not been possible to measure the source contamination for the two-foil samples from the energy spectra due to the high level of random coincidences and only an estimation of this activity will be provided from the delay time studies.

**Delay time study** As explained in section 7.8.4, a global delay time fit has been performed here. The number of random coincidences is extracted from the constant distribution in this fit and the number of events from the source is derived as the subtraction of these coincidences from the number of data. As visible in Table 7.4, a significantly lower activity has been measured in Module 2 compared to Module 1. This will be confirmed using the energy spectra fit method. A much larger contribution from random coincidences also appears in the two-foil sample.

**Energy spectra study** The second method used to extract the activity of the aluminium foil is based on the energy spectra. For this measurement, a lower en-

Modules	Samples	Efficiency	Origin	Events	Activity mBq/kg
Module 1	One foil	3.1	Signal	98.1	$16.5 \pm 1.7$
			Coincidences	255.9	
Module 1	Two foils	1.3	Signal	67.7	$17.4 \pm 2.1$
			Coincidences	592.3	
Module 2	One foil	3.1	Signal	146.1	$11.2 \pm 0.9$
			Coincidences	496.9	
Module 2	Two foils	1.3	Signal	86.6	$7.9 \pm 0.9$
			Coincidences	1532.4	

**Table 7.4.:**  $^{214}\text{Bi}$  activities in the aluminium foil (in mBq/kg) from global delay time fit. Only statistical uncertainties are given. 11.6 d of data were available for Module 1 and 25.8 d for Module 2.

ergy cut on the electron energy has been applied at 300 keV to reject noise. A lower threshold of 150 keV has been chosen for  $\alpha$ -energies since no other significant contribution is expected at low energies. The external radon that will be mentioned in the background level in section 7.9.2 cannot play a role here due to the presence of the aluminium foils. Contributions from the source, the surface of the scintillators and random coincidences are considered.

An important contribution from random coincidences can be seen in the delay time distribution in Figure 7.36 (top, left) with  $10.36 \pm 1.08$  events per bin . It should be noted that the half-life of the exponential decay, fixed at  $164.3 \mu\text{s}$ , is compatible with the observed value. For module 2 (Figure 7.36 (bottom)), a surface contamination seems to exist although not significant.

Several options are available in order to reject the random coincidences. As previously mentioned, these events have a flat distribution in time. Therefore, selecting only events with a delay time smaller than  $492 \mu\text{s}$  rejects about half of the random coincidences in the  $[10, 1000] \mu\text{s}$  time window as illustrated in Figure 7.48.

The  $\beta/\alpha$  discrimination can also contribute to the rejection of the random coincidences. Applying this selection results in the distributions in Figures 7.49. Table 7.5 summarises the reconstructed activities with the different selections.

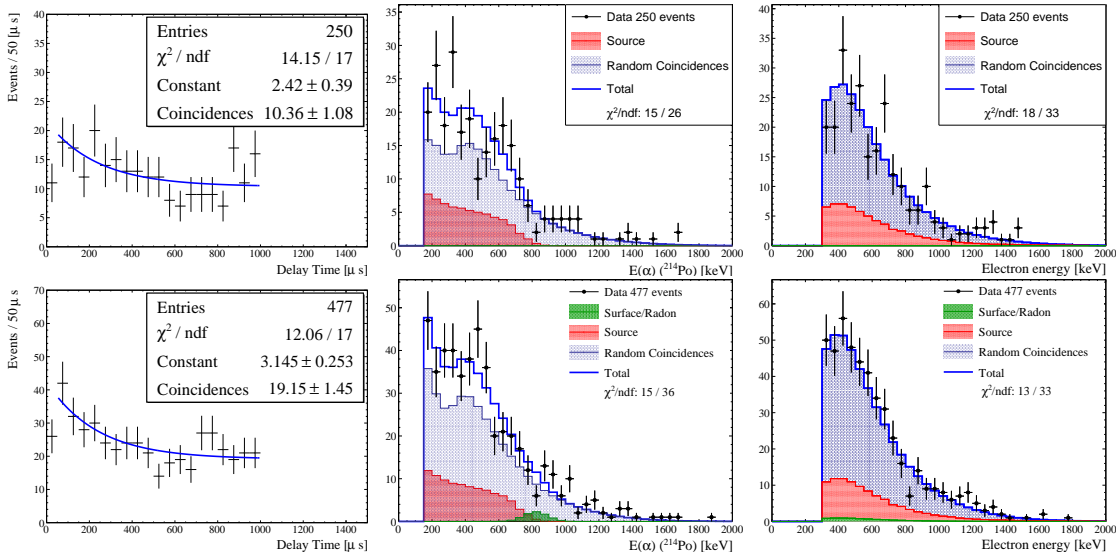


**Figure 7.47.:** Time and energy distributions for one aluminium foil after radon decay in module 1 (top) and module 2 (bottom). Left: Time between prompt and delayed pulses. The half-life is fixed at the expected value of  $164.3 \mu\text{s}$ . Middle: Energy of the  $\alpha$ . Right: Energy of the electron.

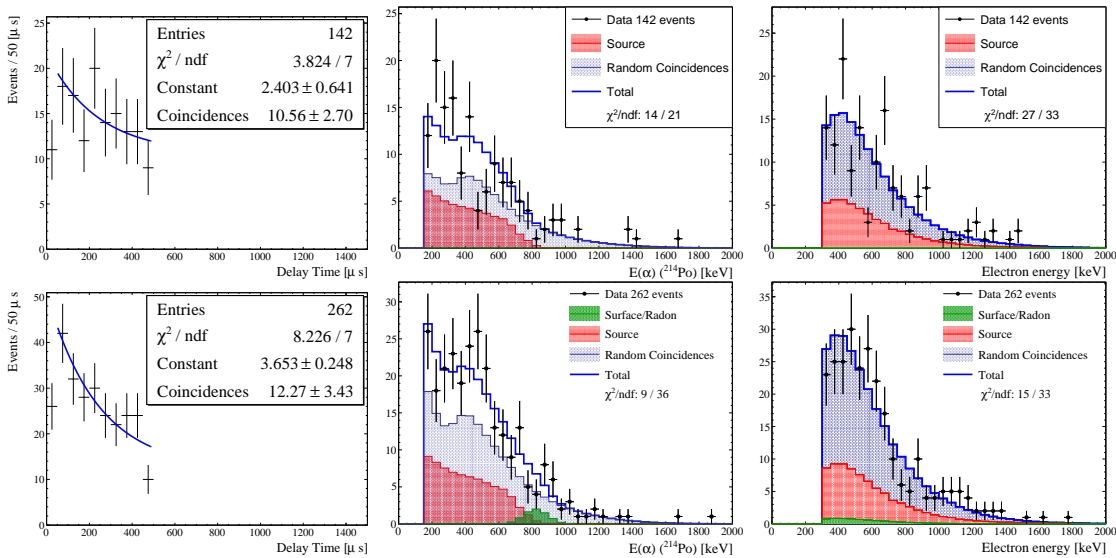


**Figure 7.48.:** Time and energy distributions for one aluminium foil in module 1 (top) and module 2 (bottom) applying an upper delay time cut. Left: Time between prompt and delayed pulses. The half-life is fixed at  $164.3 \mu\text{s}$ . Middle: Energy of the  $\alpha$ . Right: Energy of the electron.

No sign of a non-homogeneous contamination has been observed; however the statistics is much lower than for  $^{208}\text{Tl}$  and the random coincidences background is very high. The signal to background ratio is lower than 0.1 in the two-foil sample. It is

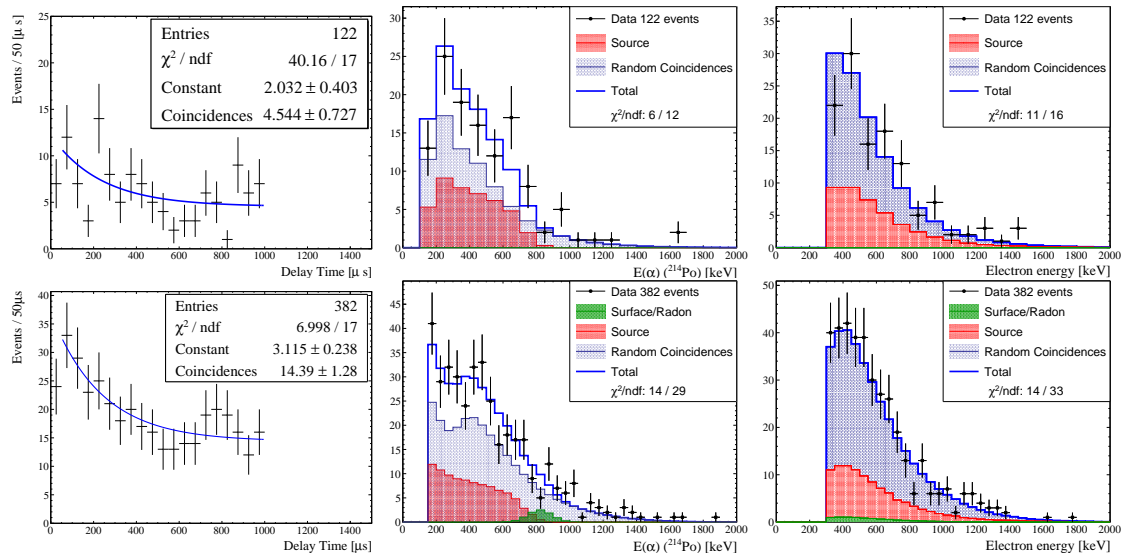


**Figure 7.49.:** Time and energy distributions for one aluminium foil in module 1 (top) and module 2 (bottom) applying the  $\beta/\alpha$  discrimination. Left: Time between prompt and delayed pulses. The half-life is fixed at  $164.3 \mu\text{s}$ . Middle: Energy of the  $\alpha$ . Right: Energy of the electron.

clear from the delay time distribution in Figure 7.50 that most of the events come from random coincidences.

Therefore, the two-foil sample does not allow an accurate measurement of the contamination. This  $^{214}\text{Bi}$  measurement is less accurate compared to  $^{280}\text{Tl}$  for both samples. It is important to note that if 80% of random coincidences are supposed to be removed with  $\beta/\alpha$  discrimination, it is not the case here (only approximately 40%). This probably means that this discrimination can be improved. Therefore the final measurement of the contamination will consider the activity after random coincidences rejection with the delay time fit.

The measurement in Module 2 is systematically lower for the measurement of the same sample as for Module 1. This difference will be included as a systematic uncertainty of  ${}^{+20}_{-12}\%$  due to the detector and the weighted average value between Module 1 and Module 2 will be adopted. Other than that, similar systematic uncertainties have been calculated: 12% for the lower cut on the delayed energy (between 100 and 300 keV), 10% for the lower cut on the prompt energy (between 150 keV and 450 keV) and 20% for the non-uniformity of the surface response of the scintillators. An uncertainty of 18% on the quenching factor was found, much larger compared to  $^{208}\text{Tl}$  measurements. This is due to the fact that there is only the source con-

	Selection	$\mathcal{E}$ [%]	Data	Events	S/B	Activity [mBq /kg]
Module 1	Standard	2.7	250	Source: 62.0 Random: 185.6	0.33	$11.9 \pm 2.8$
	Low $\Delta t$	2.4	142	Source: 49.4 Random: 92.8	0.53	$10.7 \pm 2.4$
	$e^-/\alpha$	2.2	122	Source: 42.5 Random: 76.3	0.69	$10.1 \pm 2.5$
Module 2	Standard	2.7	477	Source: 95.5 Random: 354.0 Surface: 8.4	0.26	$8.5 \pm 1.8$
	Low $\Delta t$	2.4	262	Source: 73.9 Random: 177.0 Surface: 7.4	0.40	$7.5 \pm 1.5$
	$e^-/\alpha$	2.2	382	Source: 91.8 Random: 262.2 Surface: 9.2	0.35	$10.6 \pm 2.0$

**Table 7.5.:**  $^{214}\text{Bi}$  activities in the aluminium foil (in mBq/kg) from energy spectra fit for the one foil sample. Only statistical uncertainties are given. Random coincidences have been constrained from the delay-time fit. The selection that was made, the efficiency for events from the source, the number of data events and the signal over background are also provided.

tribution in  $^{212}\text{BiPo}$  while several exist for  $^{214}\text{Bi}$ . The binned likelihood method compares histograms shapes and changing the quenching changes the shape of the energy spectra. Therefore it has a strong impact in  $^{214}\text{BiPo}$ . A total systematic uncertainty of  ${}_{-33}^{+37}\%$  has therefore been associated to this measurement.

The final result of the contamination of the aluminium foil in  $^{214}\text{BiPo}$  is:

$$\mathcal{A}(^{214}\text{Bi}) = 8.4 \pm 1.3 \text{ (stat.) } {}_{-2.7}^{+3.1} \text{ (syst.) mBq/kg} \quad (7.10)$$

This result presents a discrepancy of 36% with HPGe, although they are in agreement within a  $1\sigma$  uncertainty. The difference can come from the difficulty to measure such a contaminated source due to random coincidences. It could also be caused

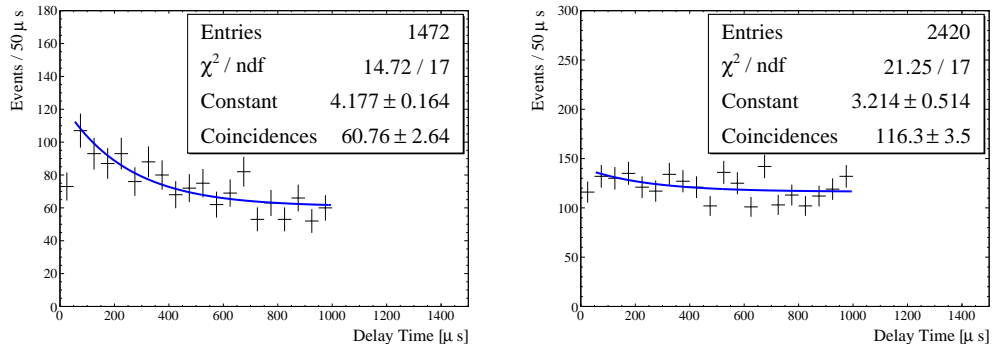


**Figure 7.50.:** *Distributions of the delay time for  $^{214}\text{BiPo}$  events from the two-foils sample in module 1 (left) and module 2 (right). Most of the events come from random coincidences, making the source activity measurement impossible.*

by the presence of a radon background around the HPGe during its measurement, which would increase the activity of the source. This is one of the main reasons why measurements in  $^{214}\text{Bi}$  in HPGe are not as accurate as they are for  $^{208}\text{Tl}$ .

### 7.9.2. Background level

Before any radiopure sample can be measured, the background level of the detector itself needs to be determined. From the measurements performed with the preproduction module, we know that the detector only suffers from extremely low contaminations. Several background runs have been performed so far, showing a good stability of the intrinsic background level of the detector. The background activities for  $^{208}\text{Tl}$  and  $^{214}\text{Bi}$  have been measured for the two modules individually and combined. Monte Carlo simulations provided the efficiencies.

#### $^{208}\text{Tl}$ measurement

The energy thresholds that have been considered here are 200 keV for the prompt signal and 100 keV for the delayed signal. Two contributions have been taken into consideration for the surface contamination. A nitrogen gap exists between the two scintillators and some background can originate in these 50  $\mu\text{m}$ . The second origin considered for the background is the 200 nm thick aluminium reflector deposited on the surface of the scintillator which represents either a surface contamination of the scintillators or a deposition of thoron. The efficiency for this measurement is 32% for both origins due to the limited energy losses in nitrogen and the expected energy spectra are almost identical. Therefore all of the events will be assumed to

come only from the surface of the scintillators. The proper description of the time delay with the half-life of the exponential function set at 299 ns ensures the proper selection of  $^{212}\text{BiPo}$  events as shown in Figure 7.51.

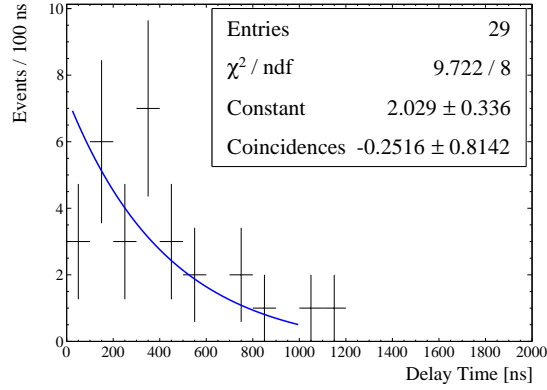


**Figure 7.51.:** *Fit of the delay time in the  $^{212}\text{BiPo}$  channel for all of the background runs recorded by the detector.*

The result of the fits of the electron and  $\alpha$  energy are displayed in Figure 7.52 for the sum of all of the background data recorded by the BiPo-3 detector so far. There is only one low-energy event that can be associated to a random coincidence. The other events are compatible with the surface background of the detector.

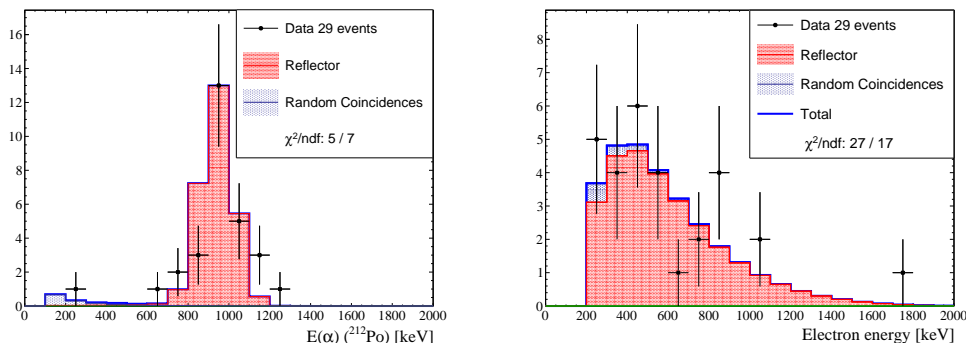


**Figure 7.52.:** *Distributions of the  $\alpha$  and electron energies for the background runs in the  $^{212}\text{BiPo}$  channel with all of the data available.*

Table 7.6 displays the results of the different background runs. A good stability is observed in these activity measurements independently of the module or the shielding that is considered. In order to reduce the statistical uncertainty, a combination of all of the measurements has therefore been performed. During the first measurement of a  $^{82}\text{Se}$  source foil in the detector (see section 7.9.3), half of the first module

was left empty. This enabled a background measurement in sample screening conditions and a cross-check of the activity measurements. It appeared that the activity was compatible with the averaged background activity measurements (last column in Table 7.6) but it has not been included in the background measurement here.

The same  ${}_{-11}^{+12}$  % systematic uncertainty as for the  ${}^{208}\text{Tl}$  measurement has been used here. The final result on the intrinsic background measurement in  ${}^{208}\text{Tl}$  of BiPo-3, expressed in scintillator surface activity for an exposure of 64.6 d/m<sup>2</sup>, is:

$$\mathcal{A}({}^{208}\text{Tl}) = 0.90 \pm 0.17 \text{ (stat.) } {}_{-0.10}^{+0.11} \text{ (syst.) } \mu\text{Bq/m}^2 \quad (7.11)$$

This measurement is similar to the activity measured in BiPo-1 at  $1.4 \pm 0.2 \mu\text{Bq/m}^2$  and compatible with the limit set in the BiPo-3 preproduction module.

	Module 1 Temporary shielding	Module 1 Final shielding	Module 2 Final shielding	<b>Total</b>	Module 1 Run <sup>82</sup> Se
Run time [d]	73.5	51.2	75.7	200.4	74.2
Data events	9	8	12	29	5
Signal events	7.4	8.0	12.0	27.7	5.0
Coincidences	1.6	0.0	0.0	1.3	0.0
Available Surface [m <sup>2</sup> ]	2.7	3.06	3.42	3.10	1.26
Activity [ $\mu\text{Bq/m}^2$ ]	$0.76 \pm 0.28$	$1.04 \pm 0.37$	$0.95 \pm 0.27$	$0.90 \pm 0.17$	$1.09 \pm 0.49$

**Table 7.6.:** Results of the surface background measurement in  ${}^{208}\text{Tl}$ .

### ${}^{214}\text{Bi}$ measurement

The minimal prompt energy is set here at 200 keV. A lower cut on the delayed energy at 300 keV has been applied in order to reject random coincidences and contribution from external radon as will be explained later. For a background measurement, essentially high energy deposits are observed. The remaining contribution from the random coincidences at these energies is almost negligible and the surface background efficiency has been estimated at 28%. The fit of the delay time with a half-life constrained at 164.3  $\mu\text{s}$  proves the proper selection of  ${}^{214}\text{BiPo}$  events as shown in Figure 7.53.

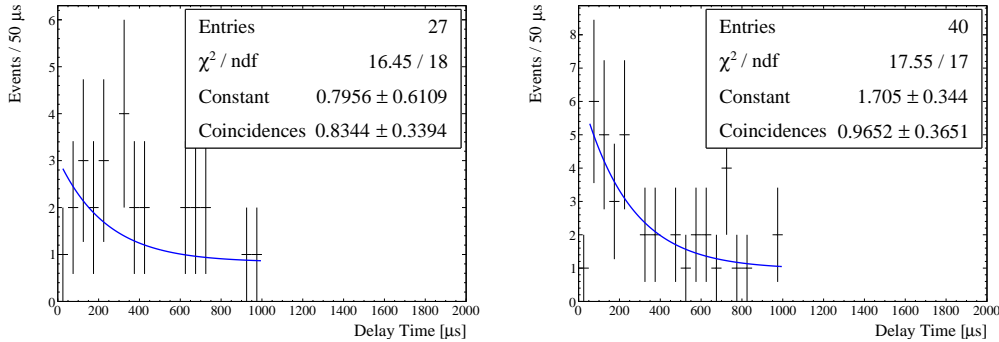


**Figure 7.53.:** Delay time fit in the  $^{214}\text{BiPo}$  channel. The half-life is set at  $164.3 \mu\text{s}$ . Left: first module in temporary shielding, right: both modules in final shielding.

The result of the fits of the electron and  $\alpha$  energy are displayed in Figure 7.54. The top two plots correspond to the first module in its temporary shielding. The bottom plots are the gathering of the background run in the final shielding for the two modules. The lower energies correspond to random coincidences while a peak is visible at high energies due to the surface/radon background. An important radon background can be seen on the surface of the scintillators for the temporary shielding (Figure 7.54 (top, left)).

Table 7.7 contains the results of the activity measurements. Since the temporary shielding was not gas tight, a higher background is observed. Therefore, this measurement will not be taken into consideration for the estimation of the detector surface background.

A cross-check of this background measurement is also performed during the  $^{82}\text{Se}$  source foil measurement and a higher activity can be observed. The source foil could have been contaminated in a  $\beta$ -emitter or the presence of a larger gap between the scintillators due to the presence of the source foil in the other half of the module may allow more radon to diffuse between the scintillators. This value is not included in the final measurement of the background.

It turns out that another source of background might exist. As visible in Figure 7.54, considering events with an energy lower than 600 keV leaves only random coincidences. However, when studying the time difference between prompt and delayed pulses, an exponential distribution with a half-life compatible with  $^{214}\text{Po}$  half-life can be observed as in Figure 7.55 (left). This shows the existence of an

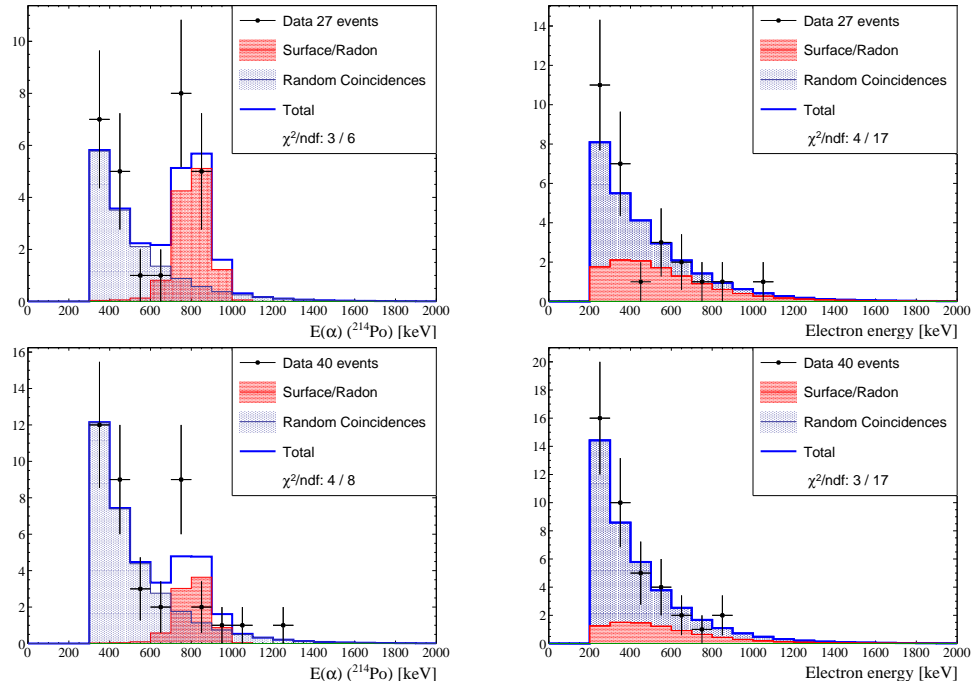


**Figure 7.54.:** *Distribution of the  $\alpha$  and electron energies for the background runs in the  $^{214}\text{BiPo}$  channel. Top: first module in temporary shielding and bottom both modules in final shielding.*

	Module 1 Temporary shielding	Module 1 Final shielding	Module 2 Final shielding	<b>Total Final shielding</b>	Module 1 Run $^{82}\text{Se}$
Run time [d]	73.5	36.2	75.7	111.9	61.5
Data events	27	18	22	40	16
Signal events	11.7	2.5	6.4	8.3	2.6
Coincidences	15.3	15.5	15.7	31.7	13.4
Surface [m <sup>2</sup> ]	2.7	3.06	3.42	3.24	1.26
S/B	0.76	0.16	0.41	0.26	0.19
Activity [ $\mu\text{Bq}/\text{m}^2$ ]	$2.48 \pm 0.73$	$0.95 \pm 0.61$	$1.03 \pm 0.41$	$0.96 \pm 0.33$	$1.43 \pm 0.92$

**Table 7.7.:** *Results of the background measurement in the  $^{214}\text{BiPo}$  analysis channel. Only statistical errors are given.*

external source of radon around the scintillators, contributing with an  $\alpha$  energy below 300 keV. As it is negligible above 300 keV (see Figure 7.55 (right)), this lower cut will be applied for the selenium measurement.

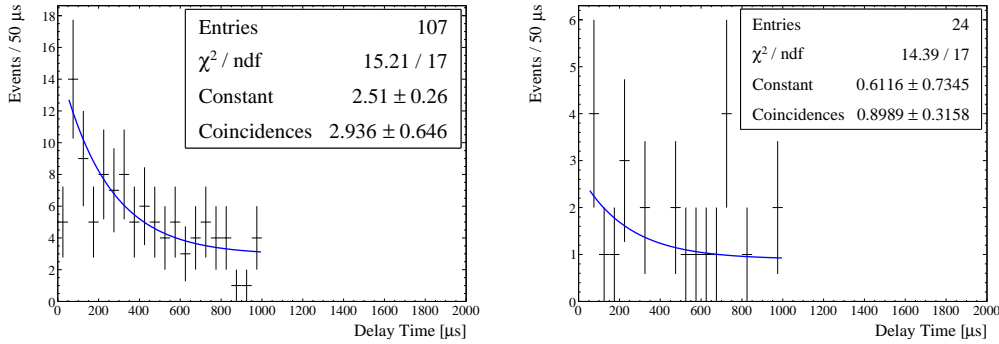


**Figure 7.55.:** *Time difference distribution for events with the energy of the alpha below 600 keV. On the right plot, a lower cut at 300 keV is also applied, rejecting most of the radon events.*

The result of the comparison of the measurement of the aluminium foil with HPGe measurements allowed a 36% uncertainty on the overall detector efficiency to be set. This uncertainty will be propagated to the selenium measurement. An additional 7% uncertainty was associated to the lower energy cuts. A total systematic uncertainty of 37% has been associated to this measurement.

The final result on the intrinsic background measurement in  $^{214}\text{Bi}$  of BiPo-3, expressed in scintillator surface activity and for an exposure of  $34.5 \text{ d/m}^2$ , is:

$$\mathcal{A}(^{214}\text{Bi}) = 0.96 \pm 0.33 \text{ (stat.)} \pm 0.36 \text{ (syst.) } \mu\text{Bq/m}^2 \quad (7.12)$$

This is 100 times better than what was done for BiPo-1 and 5 times better than the BiPo-3 preproduction module. With a lower delay energy cut at 300 keV,  $0.022 \text{ event d}^{-1} \cdot \text{m}^{-2}$  or 0.3 BiPo event per module per month and  $0.087 \text{ d}^{-1} \cdot \text{m}^{-2}$  or 1.3 random coincidences per module per month are expected.

### Estimated sensitivity

From the background measurements, it is possible to determine the sensitivity of the detector. This has been done in  $^{208}\text{Tl}$  and  $^{214}\text{Bi}$  based on the previous surface activity measurements. In order to measure the sensitivity of the  $^{82}\text{Se}$  foil measurements, the background efficiency has been estimated considering the analysis cuts performed for the activity measurement of the source foil in section 7.9.3. The background activity measurement and the uncertainties associated to it are used to obtain the number of excluded events assuming no signal is observed with the Feldman-Cousins. From

these estimations, one year would be necessary to reach the required sensitivity. It could be improved in  $^{214}\text{Bi}$  with proper surface background rejection cuts but random coincidences, not included here, can significantly reduce the sensitivity.

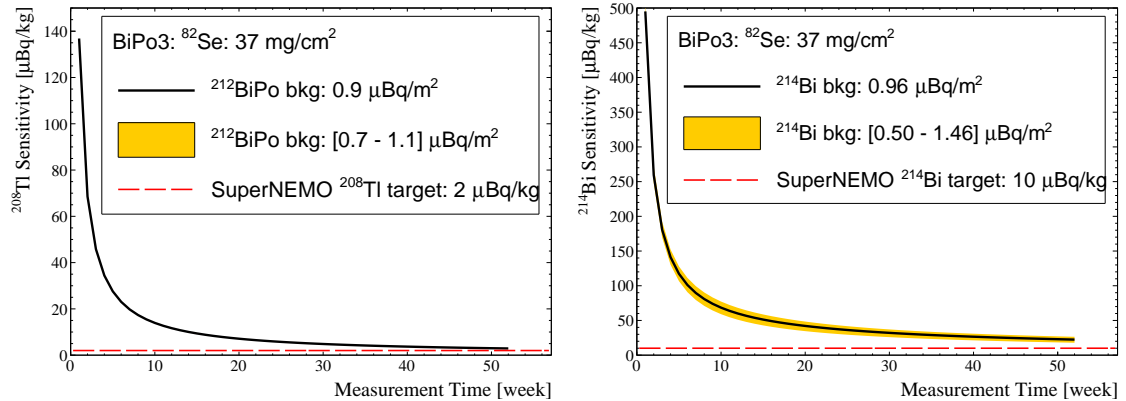


Figure 7.56.: Left: Sensitivity in  $^{208}\text{Tl}$ . Right: Sensitivity in  $^{214}\text{Bi}$ .

### 7.9.3. Selenium foils

After all of the cross-check measurements used for the qualification and the calibration of the detector, sources in the final SuperNEMO Demonstrator design have been installed in the BiPo-3 detector. The first two foils were installed in August 2014 and two more were installed in December 2014 (see Figure 7.57) as a result of two years of material selection.

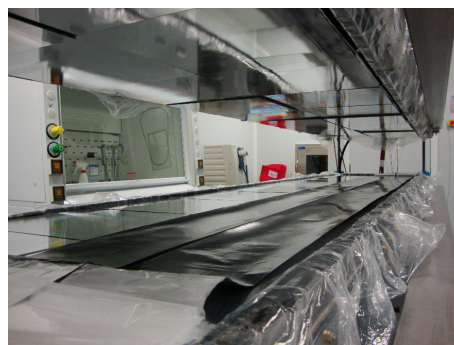
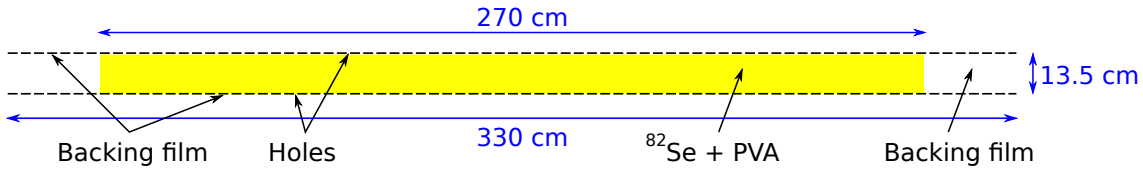


Figure 7.57.: First enriched and purified selenium source foils in a BiPo-3 module.

The foils were assembled with a backing film for a total length of 3.3 m (2.7 m around the selenium) and a width of 13.5 cm (see Figure 7.58). The total mass of selenium was 539 g and 45.9 g of PVA glue was used to hold the selenium inside 46.8 g of backing film, for a selenium density around  $37 \text{ mg/cm}^2$ . No assumption of

the PVA contamination will be made, leading to the measurement of the activities of its mixture with selenium.



**Figure 7.58.:** Schematic of the four  $^{82}\text{Se}$  source foils installed in BiPo-3.

2 pairs of optical submodules have not been filled with selenium and will therefore not be part of the measurement. An extra 3 pairs of optical submodules were not operational, two of which were switched off for hardware issues and the third one rejected from the analysis from Q/A selections (see section 7.8.1). An important contamination (of the order of 10 mBq/kg possibly from the foil itself) has also been observed in the  $^{214}\text{BiPo}$  analysis channel (and not in the  $^{212}\text{BiPo}$  channel) for one pair of optical submodules leading to its removal from this analysis. Further investigations of the origin of this contamination have to be performed.

This analysis is crucial as it determines if the foils are suitable for use in the Demonstrator and for the full SuperNEMO. It is aimed at checking if the purification of the selenium has been efficient enough. The binned likelihood method will be employed here for the measurement of the contaminations.

Previously measured contaminations have been used as inputs. A separate study of the backing film with the BiPo-3 detector resulted in the following contaminations:

$$\begin{aligned} \mathcal{A}(^{208}\text{Tl}) &= 104_{-57}^{+67} \mu\text{Bq/kg} \\ \mathcal{A}(^{214}\text{Bi}) &= 797_{-431}^{+334} \mu\text{Bq/kg} \end{aligned} \quad (7.13)$$

In the following, the activity of the backing film has been allowed to fluctuate around the central values within the errors. Similarly, the results on the surface background measurements presented in equations 7.11 and 7.12 are used to constrain the intrinsic background. The energy spectrum of random coincidences will be estimated from data and the number of coincidences will be constrained from the delay time fit. As previously explained, no random coincidence is expected for  $^{208}\text{Tl}$  measurements.

$^{208}\text{Tl}$  measurement

This measurement was performed with 127 days of data. Similar cuts as for the aluminium foils have been applied, namely 150 keV for  $\alpha$ 's and 200 keV for electrons. The different expected sources of events are clearly identifiable in the delayed energy spectrum in Figure 7.59 (middle). The high energy is dominated by the surface background and the backing film. It should be noted that the presence of the source foil in the detector reduces the surface background efficiency.

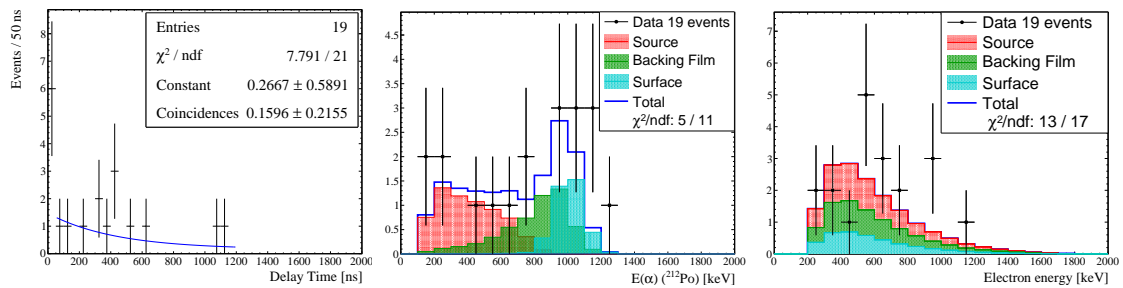


**Figure 7.59.:** *Left: Time difference between prompt and delayed pulses. Middle: Energy of  $\alpha$ 's. Right: Energy of electrons. The standard cuts have been applied.*

19 events are selected here, of which 4.8 are associated to the backing film and 3.8 to the surface for 15.6 Monte-Carlo events in total. The missing events at high energies could indicate a too strong energy quenching at these energies in MC compared to data. Given that the source only contributes at lower energies, an upper delayed energy cut at 600 keV has been applied. It is derived from the surface background rejection already presented in section 7.3.3 and has not been based on data events but on Monte-Carlo selections. The efficiencies for this measurement were:  $\mathcal{E}_{\text{source}} = 2.9 \%$ ,  $\mathcal{E}_{\text{backing}} = 3.7 \%$  and  $\mathcal{E}_{\text{surface}} = 0.2 \%$ . Almost all of the surface background is therefore rejected as visible in Figure 7.60.

9 events are now selected of which 2.5 background events are expected from the backing film and 0.1 from the surface of the scintillators. This corresponds to an activity of 171  $\mu\text{Bq}/\text{kg}$  for the backing film which is the maximum value allowed by the  $1\sigma$  error on the independent measurement. It indicates that the backing film used for the source might be more contaminated than the previous one. A surface activity of 1.07  $\mu\text{Bq}/\text{m}^2$  is expected by the fit, which is in good agreement with the surface background measurement. 6.3 events are expected to come from the source foil itself. This corresponds to an activity of the source foil of  $23.6 \pm 10.5 \mu\text{Bq}/\text{kg}$  ( $1\sigma$  statistical error from the fit). The same systematic uncertainties

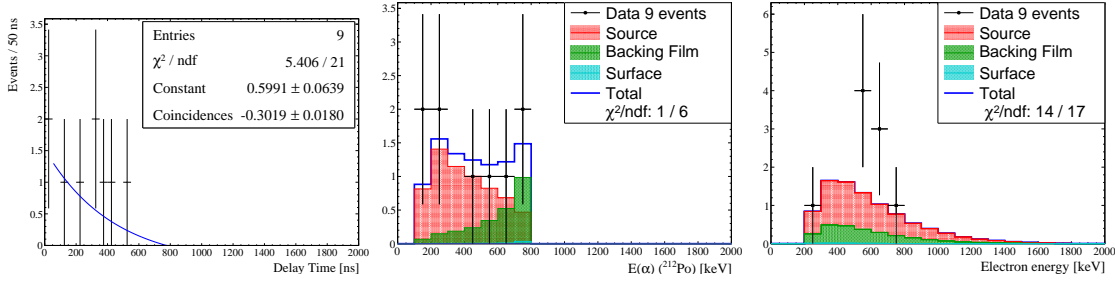


**Figure 7.60.:** *Left: Time difference between prompt and delayed pulses. Middle: Energy of  $\alpha$ 's. Right: Energy of electrons. An upper cut of 800 keV has been applied on the energy of  $\alpha$ 's.*

as for the aluminium foils of  $^{+12}_{-11}$  % will be used here. Given the very small number of events, the Feldman-Cousins confidence interval is computed for 9 data events and 2.8 background events, taking into consideration the systematic uncertainties. With an exposure of  $0.17 \text{ kg} \cdot \text{y}$  it allows us to set the following activity measurement:

$$\mathcal{A}(^{208}\text{Tl}) = 23.6 \in [7.2, 48.3] \text{ } \mu\text{Bq/kg} \text{ @ } 90\% \text{ C.L.} \quad (7.14)$$

This would suggest a contamination of the foils at levels acceptable for the Demonstrator, producing less than 1 event in the  $0\nu\beta\beta$  region of interest with an exposure of  $21 \text{ kg} \cdot \text{y}$  [94]. However, for the final detector, it would imply that further improvements in the source manufacturing and purification are necessary to reach the target of  $2 \text{ } \mu\text{Bq/kg}$ . An important point here, is that the manufacturing method is the same as for NEMO-3 and other solutions are being considered for source production. It is important to recall that this measurement could not have been performed in HPGe which has a maximum sensitivity of around  $50 \text{ } \mu\text{Bq/kg}$ . In order to constrain further this activity measurement, it would be interesting to keep on measuring these sources for longer. Assuming twice as much time, for the same background level and twice as many data events this measurement would become:  $\mathcal{A}(^{208}\text{Tl}) = 23.6 \in [10.7, 40.2] \text{ } \mu\text{Bq/kg} \text{ @ } 90\% \text{ C.L.}$ .

### $^{214}\text{Bi}$ measurement

Two contributions to the fit in energy have already been constrained: the backing film and the surface background. The random coincidences and the contamination

of the source foil itself still need to be determined. The contamination of the source is unknown and from the aluminium measurement it has been shown that random coincidences can be produced by a sample contaminated in  $\beta$ - $\gamma$  emitters. The source contribution is left free and the random coincidences are constrained by the delay time for the fit of the energy of  $\alpha$ 's in Figures 7.61, 7.62 and 7.63.

This measurement is performed with 124 d of data and due to the small statistics no individual measurement of the different foils will be performed.

With standard cuts from aluminium measurement (300 keV for  $\alpha$ 's and 200 keV for electrons), an efficiency of 0.8% for events coming from the foils has been determined from simulations. As expected, the surface background does not produce any significant number of events. The random coincidences are the dominant contribution at lower energies while higher energy events are produced by the backing film.

In Figure 7.61, the delay time is compatible with the expected value of 164.3  $\mu$ s. The fit of the  $\alpha$  energy shows the presence of a possible contamination of the source foil, however due to the shape of the random coincidences distribution, no clear conclusion can be made. The distribution of the electron energy shows good agreement.

In order to reject random coincidences, an upper delay time cut is applied at 492  $\mu$ s. As visible in Figure 7.62, a source contribution still exists and could imply a contamination of the source foil.

No contribution from the foil is expected from the fit after  $\beta/\alpha$  discrimination in Figure 7.63. This shows that the uncertainties on this measurement are too large to set a value for the activity.

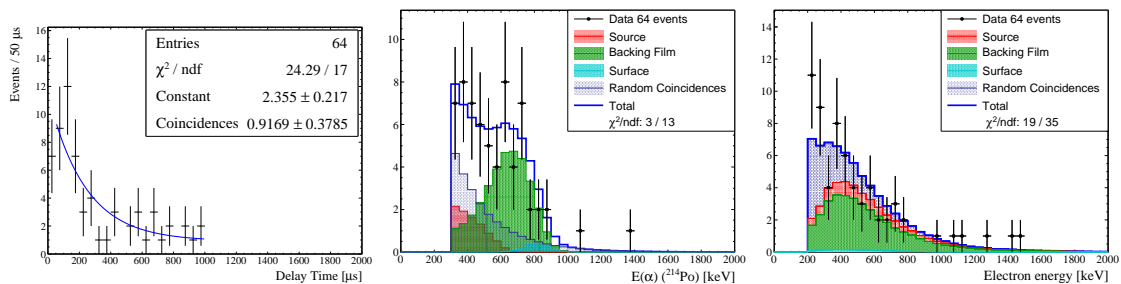


**Figure 7.61.:** Standard cuts have been applied. Left: Time difference between prompt and delayed pulses. Middle: Energy of  $\alpha$ 's. Right: Energy of electrons.

Table 7.8 displays the result of the different selections performed for the activity measurements. Due to the large uncertainties on the source contamination, it has

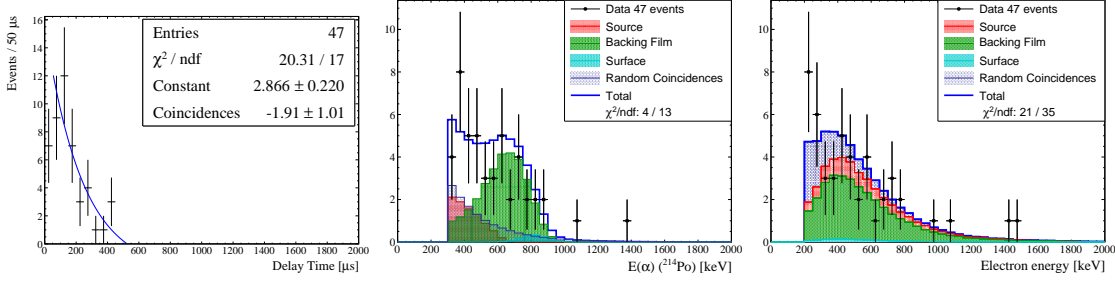


**Figure 7.62.:** An upper time difference cut has been applied in addition to the standard set of cuts. Left: Time difference between prompt and delayed pulses. Middle: Energy of  $\alpha$ 's. Right: Energy of electrons.

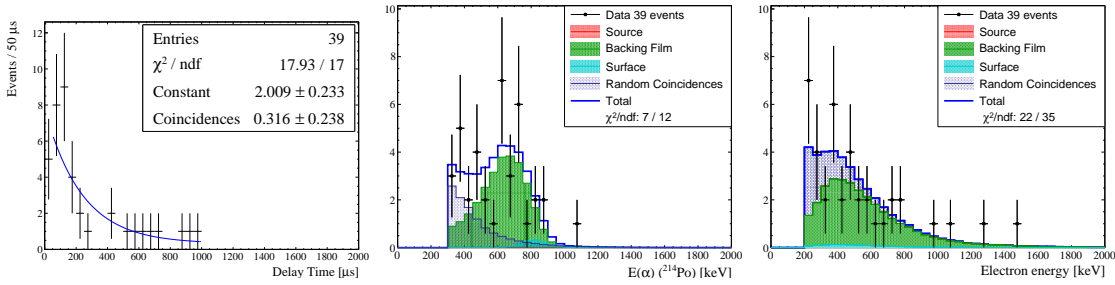


**Figure 7.63.:** The  $\beta/\alpha$  discrimination has been applied in addition to the standard set of cuts. Left: Time difference between prompt and delayed pulses. Middle: Energy of  $\alpha$ 's. Right: Energy of electrons.

been decided to set a limit on the source activity. It has not been possible to set a strict limit on the contamination of the selenium and PVA mixture due to the large background. The three limits set here are compatible and due to the uncertainties on  $\beta/\alpha$  discrimination, the delay time cut will be considered as it reduces by half the number of random coincidences events. A limit has therefore been set at:

$$\mathcal{A}(^{214}\text{Bi}) < 340 \text{ } \mu\text{Bq/kg} \text{ @ } 90\% \text{ C.L.} \quad (7.15)$$

## Summary

The measurement of the contamination in  $^{208}\text{Tl}$  proved to be acceptable for the requirements of the Demonstrator module. However a reduction of about one order of magnitude of this contamination seems necessary to reach the required contamination of  $2 \text{ } \mu\text{Bq/kg}$  for SuperNEMO.

Selection	$\mathcal{E}$ [%]	Events	Activity [ $\mu\text{Bq} / \text{kg}$ ]
Standard	0.8	Source: 8.1	< 348
	6.6	Backing film: 28.5	
	9.8	Surface: 1.5	
	-	Coincidences: 25.9	
Low $\Delta t$	0.7	Source: 12.4	< 340
	5.8	Backing film: 18.4	
	8.7	Surface: 2.2	
	-	Coincidences: 12.9	
$e^-/\alpha$	0.6	Source: < 10.2	< 335
	5.3	Backing film: 25.5	
	7.9	Surface: 1.2	
	-	Coincidences: 11.1	

**Table 7.8.:**  $^{214}\text{Bi}$  activities in the selenium foils (in  $\mu\text{Bq}/\text{kg}$ ) for an exposure of  $0.17 \text{ kg} \cdot \text{y}$  from energy spectra fit. Limits are set at 90% C.L..

The contamination in the backing film is higher than the requirements for SuperNEMO for the complete source foil. Given the mass and the density of this backing film, a constraint 10 times higher than the constraint on the foil is acceptable. However, if the current level of contaminations are acceptable for the Demonstrator, it is not the case for SuperNEMO. Therefore, further improvements have to be performed on its radiopurity, or other solutions have to be found.

The measurement of  $^{214}\text{Bi}$  contamination in the BiPo-3 detector is challenging. Due to the very small activities that have to be measured, any source of background can become critical. It is the case here of random coincidences and external radon background. Due to the different selections and cuts required for background rejection, a very small efficiency of 0.8% remains for the source foil. A factor of 2 in this efficiency could be gained by setting a lower energy cut on the energy of  $\alpha$ 's at 150 keV instead of 300 keV. One of the most important task for the continuation of these measurements is the design of methods to properly identify the backgrounds allowing the cuts to be loosened.



# Conclusion

*“Measure what is measurable, and make measurable what is not so.” -  
Galileo*

Neutrinoless double- $\beta$  decay ( $0\nu\beta\beta$ ) is a process beyond the Standard Model since it violates total lepton number conservation. If discovered, it would prove the Majorana nature of the neutrino ( $\nu=\bar{\nu}$ ) and provide a measurement of a model-dependent absolute mass for neutrinos. Mass mechanism is the most common mechanism for  $0\nu\beta\beta$  based on a flip of the neutrino helicity and the exchange of a Majorana neutrino. It is the only process studied here but other may exist.

Two-neutrino double- $\beta$  decay ( $2\nu\beta\beta$ ) has already been observed for several isotopes. The study of this process is important as it is a source of background for  $0\nu\beta\beta$  but can also help tuning nuclear models providing essential information on the nuclear matrix elements for the determination of the mass if  $0\nu\beta\beta$  is observed.

In this thesis, the double- $\beta$  decay of  $^{96}\text{Zr}$  has been studied with data from NEMO-3 acquired between 2003 and 2011. The most precise half-life of  $2\nu\beta\beta$  has been measured to be:

$$T_{1/2}^{2\nu2\beta}(^{96}\text{Zr}) = 2.41 \pm 0.11 \text{ (stat.) } {}_{-0.18}^{+0.21} \text{ (syst.) } \times 10^{19} \text{ y} \quad (7.16)$$

This measurement is in agreement with previous measurements obtained in NEMO-3. The  $2\nu\beta\beta$  half-life was used for the search for  $0\nu\beta\beta$ . No evidence has been found for this process, allowing a lower limit to be set:

$$T_{1/2}^{0\nu2\beta}(^{96}\text{Zr}) > 1.29 \times 10^{22} \text{ y @ 90\% C.L.} \quad (7.17)$$

This result allows upper limits on the effective neutrino mass to be extracted:

$$|m_{\beta\beta}| < 3.8 - 12.1 \text{ eV @ 90\% C.L.} \quad (7.18)$$

The range in values accounts for the different models used for nuclear matrix elements computation. Due to the small mass of  $^{96}\text{Zr}$  measured in the detector (9.4 g) with an enrichment fraction of only 57.3 % yielding an exposure of 49.4 g·y, this result is not competitive with the current best searches. However, due to its high  $Q_{\beta\beta}$  value above most of the background,  $^{96}\text{Zr}$  is a very interesting candidate for future experiments.

A search for  $2\nu\beta\beta$  decay of  $^{96}\text{Zr}$  to excited states has also been carried out for the first time with NEMO-3. It exploits the capabilities of NEMO-3 to measure the full kinematics of the decays occurring in the source foils and to tag all of the emitted particles. Due to very small mass and the rareness of the searched process, very low statistics was available. No significant measurement could be made, and only a limit comparable to the current best limits on the process could be set:

$$T_{1/2}^{2\nu 2\beta} (^{96}\text{Zr} \rightarrow ^{96}\text{Mo}, 0_1^+) > 5.85 \times 10^{19} \text{ y @ 90\% C.L.} \quad (7.19)$$

According to theoretical predictions, the half-life of this process should be several orders of magnitude longer than this limit. However, with a larger mass it is very likely that a measurement could be made in a detector like SuperNEMO.

SuperNEMO is the successor to NEMO-3 designed to reach higher sensitivities in the search for  $0\nu\beta\beta$  of  $^{82}\text{Se}$ :

$$T_{1/2}^{0\nu 2\beta} > 1.0 \times 10^{26} \text{ y @ 90\% C.L. and } \langle m_{\beta\beta} \rangle < 0.04 - 0.10 \text{ eV} \quad (7.20)$$

The same detection principle as NEMO-3 will be employed, combining tracking and calorimetry. In order to reach the required sensitivities, one of the main constraints was set on the radiopurity of the source foils at 2  $\mu\text{Bq/kg}$  in  $^{208}\text{Tl}$  and 10  $\mu\text{Bq/kg}$  in  $^{214}\text{Bi}$ .

These constraints are so strict that it would be impossible to measure the source foils with standard techniques, such as HPGe  $\gamma$ -spectroscopy. Therefore, an ultra-low radioactivity measurement detector has been designed by the collaboration: the

BiPo-3 detector. It is aimed at measuring contamination in  $^{214}\text{Bi}$  and  $^{208}\text{Tl}$ , the two main backgrounds for  $0\nu\beta\beta$ .

BiPo-3 should be able to measure in less than a year the contamination inside thin source foils as used for SuperNEMO at these levels.

After several prototypes, the BiPo-3 detector was constructed and installed in the *Laboratorio Subterraneo de Canfranc* (LSC, Spain) in 2012.

The commissioning, the qualification of the detector response and an intrinsic background measurement were realised prior to the measurement of any source foils. Analysis techniques have been developed in order to reach the required sensitivities in spite of the ultra-low contaminations to be measured. With a few signal events per month expected, a precise knowledge of the background is essential.

After participating in the material selection for the manufacturing of the source foils, the first SuperNEMO isotopic sources have been measured. The current sensitivities allowed a contamination of the source foils in  $^{208}\text{Tl}$  to be measured:

$$\mathcal{A}(^{208}\text{Tl}) = 23.6 \in [7.2, 48.3] \mu\text{Bq/kg} @ 90 \% \text{ C.L.} \quad (7.21)$$

which is close to the requirements for the SuperNEMO demonstrator. Other sources production techniques are being investigated and samples will be measured in BiPo-3 to check the possible radiopurity improvements.

On the other hand, due the much higher background for the detection of events from  $^{214}\text{Bi}$ , only a limit has been set on these contaminations:

$$\mathcal{A}(^{214}\text{Bi}) < 340 \mu\text{Bq/kg} @ 90 \% \text{ C.L.} \quad (7.22)$$

In spite of the current performance of the analysis in the  $^{214}\text{BiPo}$  channels, a larger exposure and further optimisation of the analysis tools ( $\beta$ - $\alpha$  discrimination and low-energy background understanding) will be necessary to obtain a real measurement.

The BiPo-3 detector clearly achieves its target of providing competitive measurements of levels of contaminations never reached before with a thin foil geometry. It was decisive to prepare the production of the  $\beta\beta$ -sources for SuperNEMO.



# Appendix A.

## NEMO-3 analysis tables

Isotopes	Processes	Locations in NEMO-3	Generated events
$^{96}\text{Zr}$	$2\nu 2\beta$	Zr foil	$1 \times 10^7$
	$2\nu 2\beta (0^+ \rightarrow 0_1^+)$		$2 \times 10^6$
	$2\nu 2\beta (0^+ \rightarrow 2_1^+)$		$2 \times 10^6$
	$0\nu 2\beta$		$5 \times 10^6$
$^{214}\text{Pb}$ $^{40}\text{K}$ $^{228}\text{Ac}$ $^{234m}\text{Pa}$ $^{212}\text{Bi}$ $^{214}\text{Bi}$ $^{208}\text{Tl}$	background	Zr foil	$4 \times 10^6$ $4 \times 10^7$ $4 \times 10^6$ $9 \times 10^6$ $4 \times 10^6$ $4 \times 10^6$ $1 \times 10^7$
$^{214}\text{Bi}$	background	mylar of Zr foil	$1 \times 10^8$
$^{214}\text{Bi}$	background	surface of Zr foil	$1.1 \times 10^8$
$^{214}\text{Pb}$ $^{210}\text{Bi}$ $^{214}\text{Bi}$	background	surface of wires	$1.6 \times 10^9$ $8.0 \times 10^9$ $1.4 \times 10^9$
$^{40}\text{K}$ $^{228}\text{Ac}$ $^{214}\text{Bi}$ $^{208}\text{Tl}$	background	PMTs	$3.2 \times 10^{11}$ $7.8 \times 10^{10}$ $2.4 \times 10^{11}$ $6.8 \times 10^{10}$
$^{40}\text{K}$ $^{152}\text{Eu}$	background	surface of scintillators	$2.0 \times 10^9$ $3.0 \times 10^9$

**Table A.1.:** Detail of the generated Monte-Carlo simulations for the searched signals and the backgrounds.

Isotopes	Decay mode	Q-value in keV	Branching ratio in%	Main $\gamma$ -rays in keV	Intensities in%
$^{214}\text{Pb}$	$\beta^-$	1024	100	242	7.43
				295	19.3
				352	37.6
$^{40}\text{K}$	$\beta^-$ <i>e.c.</i> / $\beta^+$	1311 1505	89.3 10.7	-	-
				1461	11
$^{210}\text{Bi}$	$\beta^-$	1162	100	-	-
$^{152}\text{Eu}$	$\beta^-$	1819	27.9	344	26.5
				411	2.23
				779	12.9
	<i>e.c.</i> / $\beta^+$	1874	72.1	122	28.6
				244	7.58
				444	2.82
				867	4.25
				964	14.6
				1086	10.2
				1112	13.6
1408	21.0				
$^{228}\text{Ac}$	$\beta^-$	2127	100	129	2.42
				209	3.89
				270	3.46
				328	2.95
				338	11.3
				463	4.40
				795	4.25
				911	25.8
				965	4.99
				969	15.8
1588	3.22				
$^{234m}\text{Pa}$	$\beta^-$	2196	99.8	-	-
$^{212}\text{Bi}$	$\beta^-$	2254	64.1	727	6.58
	$\alpha$	6207	35.9	-	-

**Table A.2.:** Summary of decay modes and  $\gamma$ -rays of the internal and external backgrounds considered for the zirconium double- $\beta$  decay analysis. Only the significant decay modes are presented in this table. The main  $\gamma$ -rays are considered with total intensities greater than few percent.

Isotopes	Decay mode	$Q$ -value in keV	Branching ratio in%	Main $\gamma$ -rays in keV	Intensities in%
$^{214}\text{Bi}$	$\beta^-$	3272	99.98	609	46.1
				768	4.94
				934	3.03
				1120	15.1
				1238	5.79
				1378	4.00
				1408	2.15
				1509	2.11
				1730	2.92
				1765	15.4
				1847	2.11
2204	5.08				
$^{208}\text{Tl}$	$\beta^-$	5001	100	277	6.31
				511	22.6
				583	84.5
				861	12.4
				2615	99.0

**Table A.3.:** Summary of decay modes and  $\gamma$ -rays of the internal and external backgrounds considered for the zirconium double- $\beta$  decay analysis. Only the significant decay modes are presented in this table. The main  $\gamma$ -rays are considered with total intensities greater than few percent.

Origin of $^{214}\text{Bi}$	Number of events	MC Efficiency	Activity [mBq]	Activity Phase 1 [mBq]	Activity Phase 2 [mBq]
Internal	48	$2.6 \cdot 10^{-3}$	-	-	$0.109 \pm 0.027$
Mylar	9	$9.0 \cdot 10^{-5}$	-	-	$0.57 \pm 1.21$
Surface of the foil	79	$6.6 \cdot 10^{-5}$	$7.2 \pm 1.9$	$20.7 \pm 7.4$	$3.7 \pm 1.5$
Surface of the wires	154	$5.6 \cdot 10^{-6}$	$167 \pm 26$	$625 \pm 105$	$62.1 \pm 20.5$
<b>Total MC</b>	290				
<b>Data</b>	293				

**Table A.4.:** Summary of the  $^{214}\text{Bi}$  activity measurements in the 1 electron and 1  $\alpha$ -particle channel for the ITEP sample. The internal and mylar contribution are fixed at their value in phase 2.

Origin of $^{214}\text{Bi}$	Number of events	MC Efficiency	Activity [mBq]	Activity Phase 1 [mBq]	Activity Phase 2 [mBq]
Internal	15	$3.3 \cdot 10^{-3}$	-	-	$0.027 \pm 0.024$
Mylar	56	$1.4 \cdot 10^{-4}$	-	-	$2.36 \pm 0.98$
Surface of the foil	67	$1.1 \cdot 10^{-4}$	$3.8 \pm 1.3$	$13.1 \pm 5.7$	$1.8 \pm 1.1$
Surface of the wires	228	$8.4 \cdot 10^{-6}$	$164 \pm 20$	$529 \pm 84$	$75.4 \pm 17.5$
<b>Total MC</b>	366				
<b>Data</b>	369				

**Table A.5.:** Summary of the  $^{214}\text{Bi}$  activity measurements in the 1 electron and 1  $\alpha$ -particle channel for the INR sample. The internal and mylar contribution are fixed at their value in phase 2.

Isotope	Events	Activity [mBq]	MC Efficiency	Selected MC Events
$^{208}\text{Tl}$	316	$0.040 \pm 0.008$	0.048	877577
$^{228}\text{Ac}$	318	$0.097 \pm 0.023$	0.020	264767
$^{212}\text{Bi}$	68	$0.125 \pm 0.025$	0.003	345415
$^{214}\text{Bi}$	520	$0.083 \pm 0.045$	0.038	378269
$^{40}\text{K}$	423	$9.4 \pm 1.7$	$2.7 \times 10^{-4}$	4668622
Other Internals	53			
Externals	1016			
Leakage $^{150}\text{Nd}$	141			
<b>Total MC</b>	2856			
<b>Data</b>	2852			

**Table A.6.:** Summary of the activity measurements in the 1 electron and 1  $\gamma$  channel for the ITEP sample.

Isotope	Events	Activity [mBq]	MC Efficiency	Selected MC Events
$^{208}\text{Tl}$	183	$0.020 \pm 0.004$	0.054	951731
$^{228}\text{Ac}$	247	$0.064 \pm 0.027$	0.023	290029
$^{212}\text{Bi}$	46	$0.079 \pm 0.037$	0.004	376559
$^{214}\text{Bi}$	321	$0.044 \pm 0.011$	0.044	411743
$^{40}\text{K}$	461	$19.3 \pm 3.5$	$1.4 \times 10^{-4}$	5114072
Other Internals	129			
Externals	1809			
Leakage $^{150}\text{Nd}$	241			
<b>Total MC</b>	3439			
<b>Data</b>	3434			

**Table A.7.:** Summary of the activity measurements in the 1 electron and 1  $\gamma$  channel for the INR sample.

Isotope	Events	Activity [mBq]	MC Efficiency	Selected MC Events
$^{208}\text{Tl}$	34	$0.023 \pm 0.008$	$8.8 \times 10^{-3}$	877577
$^{228}\text{Ac}$	9	$0.079 \pm 0.030$	$7.4 \times 10^{-4}$	264767
$^{212}\text{Bi}$	1	$0.048 \pm 0.016$	$7.1 \times 10^{-5}$	345415
$^{214}\text{Bi}$	73	$0.103 \pm 0.015$	$4.3 \times 10^{-3}$	378269
Other Internals	11			
Externals	28			
Leakage $^{150}\text{Nd}$	12			
<b>Total MC</b>	168			
<b>Data</b>	168			

**Table A.8.:** Summary of the activity measurements in the 1 electron and 2  $\gamma$  channel for the ITEP sample.

Isotope	Events	Activity [mBq]	MC Efficiency	Selected MC Events
$^{208}\text{Tl}$	46	$0.026 \pm 0.005$	0.011	951731
$^{228}\text{Ac}$	9	$0.072 \pm 0.023$	$7.6 \times 10^{-4}$	290029
$^{212}\text{Bi}$	1	$0.088 \pm 0.017$	$8.1 \times 10^{-5}$	376559
$^{214}\text{Bi}$	35	$0.040 \pm 0.011$	$5.4 \times 10^{-3}$	411743
Other Internals	1			
Externals	49			
Leakage $^{150}\text{Nd}$	21			
<b>Total MC</b>	162			
<b>Data</b>	161			

**Table A.9.:** Summary of the activity measurements in the 1 electron and 2  $\gamma$  channel for the INR sample.

Isotope	Events	Activity	MC Efficiency	Selected MC Events
$^{40}\text{K}$	97735	$3.26 \pm 0.02$ mBq	0.18	$3.6 \times 10^6$
$^{234m}\text{Pa}$	11548	$0.29 \pm 0.02$	0.24	$1.2 \times 10^6$
$^{210}\text{Bi}$ Surface of the wires	37895	$21.4 \pm 0.5$ Bq	$1.1 \times 10^{-5}$	85542
Other Internals	5562			
Other Externals	5455			
Leakage $^{150}\text{Nd}$	3125			
<b>Total MC</b>	161322			
<b>Data</b>	161326			

**Table A.10.:** Summary of the activity measurements in the 1 electron channel for the ITEP sample.

Isotope	Events	Activity [mBq]	MC Efficiency	Selected MC Events
$^{40}\text{K}$	511286	$15.34 \pm 0.04$ mBq	0.20	$4.0 \times 10^6$
$^{234m}\text{Pa}$	13429	$0.30 \pm 0.01$ mBq	0.27	$1.1 \times 10^6$
$^{210}\text{Bi}$ Surface of the wires	47631	$16.3 \pm 0.5$ Bq	$1.8 \times 10^{-5}$	141236
Other Internals	3170			
Other Externals	7111			
Leakage $^{150}\text{Nd}$	5241			
<b>Total MC</b>	587870			
<b>Data</b>	587821			

**Table A.11.:** Summary of the activity measurements in the 1 electron channel for the INR sample.

Isotopes	ITEP			INR		
	Selected MC Events	MC Efficiency	Expected Events	Selected MC Events	MC Efficiency	Expected Events
$2\nu 2\beta$	317082	0.063	235.1	340484	0.068	350.3
$^{214}\text{Pb}$	0	$< 6.1 \times 10^{-7}$	$< 0.01$	0	$< 6.1 \times 10^{-7}$	$< 0.01$
$^{40}\text{K}$	128	$6.4 \times 10^{-6}$	4.0	116	$5.8 \times 10^{-6}$	19.2
$^{228}\text{Ac}$	781	$3.9 \times 10^{-4}$	6.8	773	$3.9 \times 10^{-4}$	3.9
$^{234m}\text{Pa}$	2621	$5.2 \times 10^{-4}$	23.7	2356	$5.9 \times 10^{-4}$	29.0
$^{212}\text{Bi}$	444	$2.2 \times 10^{-4}$	5.9	457	$2.3 \times 10^{-4}$	3.2
$^{214}\text{Bi}$	2889	$1.4 \times 10^{-3}$	20.5	2889	$1.4 \times 10^{-3}$	0.7
$^{208}\text{Tl}$	4286	$8.6 \times 10^{-4}$	5.4	4501	$9.0 \times 10^{-4}$	4.6
Mylar $^{214}\text{Bi}$	149	$1.5 \times 10^{-6}$	0.1	207	$2.1 \times 10^{-6}$	1.1
SFoil $^{214}\text{Bi}$	73	$6.7 \times 10^{-7}$	0.9	115	$1.1 \times 10^{-6}$	0.9
SWire $^{214}\text{Pb}$	0	$< 1.5 \times 10^{-9}$	$< 0.04$	0	$< 1.5 \times 10^{-9}$	$< 0.04$
SWire $^{210}\text{Bi}$	0	$< 3.1 \times 10^{-10}$	$< 0.8$	0	$< 3.1 \times 10^{-10}$	$< 0.8$
SWire $^{214}\text{Bi}$	82	$5.7 \times 10^{-8}$	1.7	132	$9.1 \times 10^{-8}$	2.8
$^{228}\text{Ac}$ PMT	0	$< 3.1 \times 10^{-11}$	$< 1.8$	0	$< 3.1 \times 10^{-11}$	$< 1.8$
$^{40}\text{K}$ PMT	0	$< 7.6 \times 10^{-12}$	$< 1.6$	1	$3.1 \times 10^{-12}$	0.6
$^{208}\text{Tl}$ PMT	10	$1.5 \times 10^{-10}$	1.2	17	$2.5 \times 10^{-10}$	2.2
$^{214}\text{Bi}$ PMT	7	$2.9 \times 10^{-11}$	2.9	11	$4.6 \times 10^{-11}$	4.4
SScint $^{40}\text{K}$	0	$< 1.2 \times 10^{-9}$	$< 2.434$	0	$< 1.2 \times 10^{-9}$	$< 2.434$
SScint $^{152}\text{Eu}$	0	$< 8.1 \times 10^{-10}$	$< 2.440$	0	$< 8.1 \times 10^{-10}$	$< 2.440$
Leakage $^{150}\text{Nd}$	-	-	8.3	-	-	13.3
<b>Total MC</b>	-	-	316.4	-	-	436.1
<b>Total Background</b>	-	-	81.3	-	-	85.8
<b>Data</b>	-	-	316	-	-	435

**Table A.12.:** Result of the fit of the 2e channel after  $^{40}\text{K}$  rejection for the individual samples.

Isotopes	Selected MC Events	MC Efficiency	Expected Events
$2\nu 2\beta$ ( $0^+ \rightarrow 0_1^+$ )	31027	$1.6 \times 10^{-2}$	0.0
$2\nu 2\beta$	5780	$5.8 \times 10^{-4}$	5.1
$^{40}\text{K}$	20	$5.0 \times 10^{-7}$	2.0
$^{228}\text{Ac}$	830	$2.1 \times 10^{-4}$	6.3
$^{234m}\text{Pa}$	209	$2.3 \times 10^{-5}$	2.3
$^{212}\text{Bi}$	116	$2.9 \times 10^{-5}$	0.9
$^{214}\text{Bi}$	4604	$1.2 \times 10^{-3}$	25.5
$^{208}\text{Tl}$	20517	$2.1 \times 10^{-3}$	22.3
Mylar $^{214}\text{Bi}$	417	$4.2 \times 10^{-6}$	1.1
SFoil $^{214}\text{Bi}$	273	$2.5 \times 10^{-6}$	2.1
SWire $^{214}\text{Bi}$	336	$2.3 \times 10^{-7}$	6.3
$^{40}\text{K}$ PMT	1	$3.1 \times 10^{-12}$	0.7
$^{208}\text{Tl}$ PMT	19	$2.8 \times 10^{-10}$	2.4
$^{214}\text{Bi}$ PMT	20	$8.3 \times 10^{-11}$	7.6
Leakage $^{150}\text{Nd}$	-	-	2.4
<b>Total MC</b>	-	-	87.1
<b>Total Background</b>	-	-	87.1
<b>Data</b>	-	-	85

**Table A.13.:** Result of the fit of the  $2eN\gamma$  channel before selection cuts displaying the number of selected Monte-Carlo events, the Monte-Carlo efficiencies for each contribution and the number of expected background events. For the leakage from  $^{150}\text{Nd}$ , all of the contaminations have been added. All of the activities have been fixed at their values from the background model.

Isotopes	Selected MC Events	MC Efficiency	Expected Events
$2\nu 2\beta$	829	$8.3 \times 10^{-5}$	0.70
$^{40}\text{K}$	2	$5.0 \times 10^{-8}$	0.20
$^{228}\text{Ac}$	72	$1.8 \times 10^{-5}$	0.48
$^{234m}\text{Pa}$	8	$8.9 \times 10^{-7}$	0.09
$^{212}\text{Bi}$	44	$1.1 \times 10^{-5}$	0.30
$^{214}\text{Bi}$	1205	$3.0 \times 10^{-4}$	6.70
$^{208}\text{Tl}$	2879	$2.9 \times 10^{-4}$	3.10
Mylar $^{214}\text{Bi}$	106	$1.1 \times 10^{-6}$	0.27
SFoil $^{214}\text{Bi}$	59	$5.4 \times 10^{-7}$	0.46
SWire $^{214}\text{Bi}$	83	$5.7 \times 10^{-8}$	1.60
$^{208}\text{Tl}$ PMT	4	$5.9 \times 10^{-11}$	0.51
$^{214}\text{Bi}$ PMT	1	$4.2 \times 10^{-12}$	0.38
Leakage $^{150}\text{Nd}$	-	-	0.36
<b>Total Background</b>	-	-	14.84
$2\nu 2\beta$ ( $0^+ \rightarrow 0_1^+$ )	13230	$6.6 \times 10^{-3}$	2.26
<b>Total MC</b>	-	-	17.10
<b>Data</b>	-	-	17

**Table A.14.:** Result of the fit of the  $2eN\gamma$  channel after loose selection cuts displaying the number of selected Monte-Carlo events after analysis cuts, the Monte-Carlo efficiencies for each contribution and the number of expected background events. The number of events attributed to signal is the result of the fit. For the leakage from  $^{150}\text{Nd}$ , all of the contaminations have been added. All of the activities have been fixed at their values from the background model.



# References

- [1] J. Chadwick, *The intensity distribution in the magnetic spectrum of beta particles from radium (B + C)*, Verh.Phys.Gesell. **16** (1914) 383–391.
- [2] C. D. Ellis and W. A. Wooster, *The Continuous Spectrum of  $\beta$ -Rays.*, Nature **119** (1927) no. 2998, 563.
- [3] W. Pauli, *On the Earlier and more recent history of the neutrino*, Cambridge Monogr. Part. Phys. Nucl. Phys. Cosmol. **14** (2000) 1–22.
- [4] N. Bohr, H. Kramers, and J. Slater, *LXXVI. The quantum theory of radiation*, Philosophical Magazine Series 6 **47** (1924) no. 281, 785–802.
- [5] E. Fermi, *Versuch einer Theorie der  $\beta$ -Strahlen.*, Zeitschrift fur Physik **88** (1934) 161–177.
- [6] H. Bethe and R. Peierls, *The Neutrino*, Nature **133** (1934) 532.
- [7] F. Reines, C. L. Cowan, F. B. Harrison, A. D. McGuire, and H. W. Kruse, *Detection of the Free Antineutrino*, Phys. Rev. **117** (1960) 159–173.
- [8] T. D. Lee and C. N. Yang, *Question of Parity Conservation in Weak Interactions*, Phys. Rev. **104** (1956) 254–258.
- [9] R. P. Feynman and M. Gell-Mann, *Theory of the Fermi Interaction*, Phys. Rev. **109** (1958) 193–198.
- [10] M. Goldhaber, L. Grodzins, and A. W. Sunyar, *Helicity of Neutrinos*, Phys. Rev. **109** (1958) 1015–1017.
- [11] Particle Data Group, K. Olive et al., *Review of Particle Physics*, Chin.Phys. **C38** (2014) 090001.
- [12] B. Pontecorvo, *Electron and muon neutrinos*, Sov. Phys. JETP **10** (1960)

- 1236–1240.
- [13] G. Danby, J. Gaillard, K. A. Goulianos, L. Lederman, N. B. Mistry, et al., *Observation of High-Energy Neutrino Reactions and the Existence of Two Kinds of Neutrinos*, Phys.Rev.Lett. **9** (1962) 36–44.
- [14] *Precision electroweak measurements on the Z resonance.*, Physics Reports **427** (2006) 257 – 454.
- [15] K. Kodama et al., *Observation of tau neutrino interactions*, Physics Letters B **504** (2001) no. 3, 218 – 224.
- [16] B. Pontecorvo, *Mesonium and anti-mesonium*, Sov.Phys.JETP **6** (1957) 429.
- [17] Z. Maki, M. Nakagawa, and S. Sakata, *Remarks on the Unified Model of Elementary Particles*, Progress of Theoretical Physics **28** (1962) 870–880.
- [18] Super-Kamiokande, Y. Fukuda et al., *Evidence for oscillation of atmospheric neutrinos*, Phys.Rev.Lett. **81** (1998) 1562–1567.
- [19] C. Giunti and C. W. Kim, *Fundamentals of Neutrino Physics and Astrophysics*. Oxford University Press, Oxford, UK, 2007.
- [20] E. Majorana, *Teoria simmetrica dell'elettrone e del positrone*, Il Nuovo Cimento **14** (1937) 171–184.
- [21] LSND Collaboration, A. Aguilar et al., *Evidence for neutrino oscillations from the observation of  $\bar{\nu}_\mu \rightarrow \bar{\nu}_e$  appearance in a  $\bar{\nu}_\mu$  beam*, Phys. Rev. D **64** (2001) 112007.  
<http://link.aps.org/doi/10.1103/PhysRevD.64.112007>.
- [22] G. Drexlin, V. Hannen, S. Mertens, and C. Weinheimer, *Current direct neutrino mass experiments*, Adv.High Energy Phys. **2013** (2013) 293986.
- [23] V. N. Aseev et al., *Upper limit on the electron antineutrino mass from the Troitsk experiment*, Phys. Rev. D **84** (2011) .
- [24] K. N. Abazajian et al., *Cosmological and astrophysical neutrino mass measurements*, Astroparticle Physics **35** (nov, 2011) 177–184.
- [25] C. F. V. Weizsacker, *Zur Theorie der Kernmassen*, Z. Phys. **96** (1935) 431–458.

- [26] M. Goeppert-Mayer, *Double beta-disintegration*, Phys. Rev. **48** (1935) 512–516.
- [27] V. Tretyak and Y. Zdesenko, *Tables Of Double Beta Decay Data - An Update*, Atomic Data and Nuclear Data Tables **80** (2002) 83.
- [28] J. Kotila and F. Iachello, *Phase space factors for double- $\beta$  decay*, Phys.Rev. **C85** (2012) 034316, [arXiv:1209.5722 \[nucl-th\]](#).
- [29] S. Stoica and M. Mirea, *New calculations for phase space factors involved in double- $\beta$  decay*, Phys.Rev. **C88** (2013) no. 3, 037303, [arXiv:1307.0290 \[nucl-th\]](#).
- [30] NEMO, R. Arnold et al., *Measurement of double beta decay of Mo-100 to excited states in the NEMO 3 experiment*, Nucl.Phys. **A781** (2007) 209–226.
- [31] M. Aunola and J. Suhonen, *Systematic study of beta and double beta decay to excited final states*, Nuclear Physics A **A602** (1996) 133 – 166.
- [32] J. Suhonen and M. Aunola, *Systematic study of neutrinoless double beta decay to excited  $0+$  states*, Nuclear Physics, Section A **723** (2003) 271 – 288.
- [33] W. Furry, *On transition probabilities in double beta-disintegration*, Phys.Rev. **56** (1939) 1184–1193.
- [34] P. Vogel, *Nuclear structure and double beta decay*, J.Phys. **G39** (2012) 124002, [arXiv:1208.1992 \[nucl-th\]](#).
- [35] W. Rodejohann, *Neutrinoless double beta decay and neutrino physics*, J.Phys. **G39** (2012) 124008.
- [36] P. Bamert, C. Burgess, and R. Mohapatra, *Multi - Majoron modes for neutrinoless double beta decay*, Nucl.Phys. **B449** (1995) 25–48.
- [37] R. Barbier, C. Berat, M. Besancon, M. Chemtob, A. Deandrea, et al., *R-parity violating supersymmetry*, Phys.Rept. **420** (2005) 1–202.
- [38] K. Zuber, *Consensus Report of a Workshop on 'Matrix elements for Neutrinoless Double Beta Decay'*, [arXiv:nucl-ex/0511009](#).
- [39] S. R. Elliott and J. Engel, *Double beta decay*, J.Phys. **G30** (2004) R183–R215.

- [40] J. Yao and others., *Systematic study of nuclear matrix elements in neutrinoless double- $\beta$  decay with a beyond-mean-field covariant density functional theory*, Phys.Rev. **C91** (2015) no. 2, 024316.
- [41] J. Engel, *Uncertainties in nuclear matrix elements for neutrinoless double-beta decay*, Journal of Physics G: Nuclear and Particle Physics **42** (2015) .
- [42] P. Guzowski et al., *A Combined Limit on the Neutrino Mass from Neutrinoless Double-Beta Decay and Constraints on Sterile Majorana Neutrinos*, (2015) , arXiv:1504.03600 [hep-ex].
- [43] SuperNEMO Collaboration, X. Sarazin, *Habilitation à Diriger les Recherches: Recherche de la Double Désintégration Beta sans Émission de Neutrino*, .
- [44] GERDA, M. Agostini et al., *The background in the  $0\nu\beta\beta$  experiment GERDA*, Eur.Phys.J. **C74** (2014) no. 4, 2764.
- [45] M. Agostini et al., *Pulse shape discrimination for GERDA Phase I data*, Eur.Phys.J. **C73** (2013) no. 10, 2583.
- [46] H. Klapdor-Kleingrothaus et al., *Latest results from the Heidelberg-Moscow Double Beta Decay Experiment*, Eur.Phys.J. **A12** (2001) 147–154, arXiv:hep-ph/0103062.
- [47] IGEX Collaboration, C. Aalseth et al., *The IGEX Ge-76 neutrinoless double beta decay experiment: Prospects for next generation experiments*, Phys.Rev. **D65** (2002) 092007, arXiv:hep-ex/0202026 [hep-ex].
- [48] H. Klapdor-Kleingrothaus, I. Krivosheina, A. Dietz, and O. Chkvorets, *Search for neutrinoless double beta decay with enriched  $^{76}\text{Ge}$  in Gran Sasso 1990-2003*, Phys.Lett. **B586** (2004) 198–212, arXiv:hep-ph/0404088.
- [49] GERDA Collaboration, M. Agostini et al., *Measurement of the half-life of the two-neutrino double beta decay of Ge-76 with the Gerda experiment*, J.Phys. **G40** (2013) 035110, arXiv:1212.3210 [nucl-ex].
- [50] GERDA Collaboration, M. Agostini et al., *Results on neutrinoless double beta decay of  $^{76}\text{Ge}$  from GERDA Phase I*, Phys.Rev.Lett. **111** (2013) 122503, arXiv:1307.4720 [nucl-ex].
- [51] B. Majorovits, *Phase II Upgrade of the GERDA Experiment for the Search of*

- Neutrinoless Double Beta Decay*, Physics Procedia **61** (2015) 254 – 259.  
International Conference on Topics in Astroparticle and Underground Physics,  
TAUP 2013.
- [52] C. Macolino and the Gerda Collaboration, *The GERDA experiment: results and perspectives*, Journal of Physics: Conference Series **556** (2014) 012063.  
<http://stacks.iop.org/1742-6596/556/i=1/a=012063>.
- [53] E. Andreotti, C. Arnaboldi, F. Avignone, M. Balata, I. Bandac, et al.,  $^{130}\text{Te}$  *Neutrinoless Double-Beta Decay with CUORICINO*, Astropart.Phys. **34** (2011) 822–831, [arXiv:1012.3266](https://arxiv.org/abs/1012.3266) [nucl-ex].
- [54] CUORICINO Collaboration, E. Andreotti et al., *Double-beta decay of  $^{130}\text{Te}$  to the first  $0^+$  excited state of  $^{130}\text{Xe}$  with CUORICINO*, Phys.Rev. **C85** (2012) 045503, [arXiv:1108.4313](https://arxiv.org/abs/1108.4313) [nucl-ex].
- [55] L. Canonica et al., *First CUORE-0 Performance Results and Status of CUORE Experiment*, Journal of Low Temperature Physics **176** (2014) no. 5-6, 986–994.
- [56] CUORE, D. Artusa et al., *CUORE-0 results and prospects for the CUORE experiment*, [arXiv:1502.02576](https://arxiv.org/abs/1502.02576) [physics.ins-det].
- [57] CUORE, K. Alfonso et al., *Search for Neutrinoless Double-Beta Decay of  $^{130}\text{Te}$  with CUORE-0*, [arXiv:1504.02454](https://arxiv.org/abs/1504.02454).
- [58] CUORE, M. Sisti et al., *Status of the CUORE and results from the CUORE-0 neutrinoless double beta decay experiments*, Nuclear Physics B Proceedings Supplement (2015) , [arXiv:1502.03653](https://arxiv.org/abs/1502.03653).
- [59] J. Beeman et al., *Current Status and Future Perspectives of the LUCIFER Experiment*, Adv.High Energy Phys. **2013** (2013) 237973.
- [60] EXO Collaboration, J. B. Albert et al., *Improved measurement of the  $2\nu\beta\beta$  half-life of  $^{136}\text{Xe}$  with the EXO-200 detector*, Phys. Rev. C **89** (2014) 015502.
- [61] EXO-200 Collaboration, J. Albert et al., *Search for Majorana neutrinos with the first two years of EXO-200 data*, Nature **510** (2014) 229–234, [arXiv:1402.6956](https://arxiv.org/abs/1402.6956) [nucl-ex].
- [62] KamLAND-Zen Collaboration, A. Gando et al., *Measurement of the double- $\beta$*

- decay half-life of  $^{136}\text{Xe}$  with the KamLAND-Zen experiment*, Phys.Rev. **C85** (2012) 045504, arXiv:1201.4664 [hep-ex].
- [63] KamLAND-Zen, *Results from KamLAND-Zen*, arXiv:1409.0077 [physics.ins-det]. XXVI Conference on Neutrino Physics and Astrophysics (Neutrino 2014).
- [64] KamLAND-Zen Collaboration, A. Gando et al., *Limit on Neutrinoless  $\beta\beta$  Decay of  $^{136}\text{Xe}$  from the First Phase of KamLAND-Zen and Comparison with the Positive Claim in  $^{76}\text{Ge}$* , Phys.Rev.Lett. **110** (2013) no. 6, 062502, arXiv:1211.3863 [hep-ex].
- [65] NEMO-3, R. Arnold et al., *Search for neutrinoless double-beta decay of  $^{100}\text{Mo}$  with the NEMO-3 detector*, Phys.Rev. **D89** (2014) no. 11, 111101.
- [66] J. Mott, *Search for double beta decay of  $^{82}\text{Se}$  with the NEMO-3 detector and development of apparatus for low-level radon measurements for the SuperNEMO experiment*. PhD thesis, University College London, 2013.
- [67] NEMO Collaboration, J. Argyriades et al., *Measurement of the background in the NEMO 3 double beta decay experiment*, Nucl.Instrum.Meth. **A606** (2009) 449–465.
- [68] R. Arnold, C. Augier, A. Bakalyarov, J. Baker, A. Barabash, et al., *Technical design and performance of the NEMO 3 detector*, Nucl.Instrum.Meth. **A536** (2005) 79–122.
- [69] R. Arnold et al., *Performance of a prototype tracking detector for double beta decay measurements*, Nucl. Instrum. Meth. A **354** (1995) 338 – 351.
- [70] G. Audi and A. Wapstra, *The 1995 update to the atomic mass evaluation.*, Nuclear Physics A **A595** (1995) no. 4, 409 – 480.
- [71] R. Arnold et al., *Chemical purification of molybdenum samples for the NEMO 3 experiment*, Nucl. Instrum. Meth. A **474** (2001) 93–100.
- [72] R. Arnold et al., *Double beta decay of  $^{96}\text{Zr}$* , Nuclear Physics A **658** (1999) 299 – 312.
- [73] G. Charpak and F. Sauli, *Multiwire chambers operating in the Geiger-Müller mode; new simple method of particle localization*, Nuclear Instruments and

- Methods **96** (1971) 363 – 367.
- [74] F. Sauli, *Principles of Operation of Multiwire Proportional and Drift Chambers*, CERN-77-09 (1977) .
- [75] W. R. Leo, *Techniques for Nuclear and Particle Physics Experiments*. Springer, 1987.
- [76] R. Brun, F. Bruyant, M. Maire, A. McPherson, and P. Zancarini, *GEANT3 user's guide*, tech. rep., CERN DD/EE/84-1, 1987.
- [77] O. Ponkratenko, V. Tretyak, and Y. Zdesenko, *The Event generator DECAY4 for simulation of double beta processes and decay of radioactive nuclei*, Phys.Atom.Nucl. **63** (2000) 1282–1287.
- [78] C. Hugon, *Data analysis of the NEMO3 experiment for the neutrinoless double beta decay search. Study of the systematics errors of the calorimeter and analysis tools developments*. PhD thesis, Université Paris Sud - Paris XI, 2012.
- [79] J. Mott and S. Blot, *New model for the electron-gamma time-of-flight hypothesis in NEMO-3*, Internal Note **DocDB:3343** (2014) .
- [80] F. James and M. Roos, *Minuit: A System for Function Minimization and Analysis of the Parameter Errors and Correlations*, Comput.Phys.Commun. **10** (1975) 343–367.
- [81] G. J. Feldman and R. D. Cousins, *Unified approach to the classical statistical analysis of small signals*, Phys. Rev. D **57** (1998) 3873–3889.  
<http://link.aps.org/doi/10.1103/PhysRevD.57.3873>.
- [82] S. S. Wilks, *The Large-Sample Distribution of the Likelihood Ratio for Testing Composite Hypotheses*, Ann. Math. Statist. **9** (1938) 60–62.
- [83] T. Junk, *Confidence level computation for combining searches with small statistics*, Nucl.Instrum.Meth. **A434** (1999) 435–443.
- [84] S. Blondel, *Optimisation du blindage contre les neutrons pour le démonstrateur de SuperNEMO et analyse de la double désintégration  $\beta$  du néodyme-150 vers les états excités du samarium-150 avec le détecteur NEMO-3*. PhD thesis, Université Paris Sud - Paris XI, 2013.

- [85] NEMO Collaboration, A. Barabash, *Investigation of double beta decay of Se-82 and Zr-96 with tracking detector NEMO-2*, Nucl.Phys. **A629** (1998) 517C–522C.
- [86] J. Argyriades et al., *Measurement of the two neutrino double beta decay half-life of Zr-96 with the NEMO-3 detector*, Nuclear Physics A **847** (2010) 168–179.
- [87] A. S. Barabash et al., *Investigation of the  $\beta\beta$  decay of  $^{96}\text{Zr}$  to excited states in  $^{96}\text{Mo}$* , Journal of Physics G: Nuclear and Particle Physics **22** (1996) no. 4, 487–496.
- [88] J. Argyriades et al., *Results of the BiPo-1 prototype for radiopurity measurements for the SuperNEMO double beta decay source foils*, Nucl. Instrum. Meth. A **622** (2010) 120–128, [arXiv:1005.0343](https://arxiv.org/abs/1005.0343) [physics.ins-det].
- [89] A. Chapon, *Mesure des processus de double-désintégration  $\tilde{\beta}\beta$  du  $^{100}\text{Mo}$  vers l'état excité  $0_1^+$  du  $^{100}\text{Ru}$  dans l'expérience NEMO3. Programme de R & D SuperNEMO : mise au point d'un détecteur BiPo pour la mesure de très faibles contaminations de feuilles sources*. PhD thesis, Université de Caen Basse-Normandie, 2011.
- [90] C. Leroy and P.-G. Rancoita, *Principles of radiation interaction in matter and detection; 2nd ed.* World Scientific, 2009.
- [91] E. Chauveau, *Développement de compteurs à scintillation hautes performances et de très basse radioactivité pour le calorimètre du projet SuperNEMO*. PhD thesis, Université de Bordeaux1, 2010.
- [92] Chakravarti et al., *Handbook of Methods of Applied Statistics*, John Wiley and Sons **I** (1967) 392–394.
- [93] X. Sarazin, *Results of BiPo-3 measurements*, Internal Note **DocDB:3029** (2014) .
- [94] A. S. Barabash, *Se-82 purification and source production in SuperNEMO: present status*, Internal Note **DocDB:3222** (2014) .